

EXPERIMENTAL AND MODELING STUDIES OF
CONTAMINANT TRANSPORT IN CAPPED SEDIMENTS
DURING GAS BUBBLE EBULLITION

A Dissertation

Submitted to the Graduate Faculty of the
Louisiana State University and
Agricultural and Mechanical College
in partial fulfillment of the
requirements for the degree of
Doctor of Philosophy

in

The Cain Department of Chemical Engineering

By
Qingzhong Yuan
B.E., Tianjin Institute of Light Industry, China, 1982
May, 2007

ACKNOWLEDGMENTS

I would like to sincerely appreciate my advisor Dr. Valsaraj for giving me this opportunity to pursue this degree and to do this project. I am also grateful to Drs. Valsaraj, Reible, and Thibodaux for their guidance during my research. I would like to thank Dr. Ravikrishna for his help and beneficial discussions. I also appreciate Dr. Willson for his guidance to digitalize the sediment tomography images with BLOB3D and T3D softwares. I wish to recognize the efforts of Joel Leger, a student worker who performed the extractions of some water samples. Special acknowledgments are extended to Dr. Constant and Dr. Rouse for being my committee members.

I am indebted to my parents, my brothers and my sister for being always there for me whenever I needed them. I would like to thank my wife Jinhui Liu and my daughter Yunan Yuan for their love and encouragement. Without their encouragement and understanding, my research would not have been possible.

This research was supported by a grant from the U. S. Environmental Protection Agency through the Hazardous Substance Research Center (South and Southeast) situated at Louisiana State University, Baton Rouge.

TABLE OF CONTENTS

| | |
|--|-----|
| ACKNOWLEDGMENTS | ii |
| ABSTRACT | vii |
| CHAPTER 1. INTRODUCTION | 1 |
| CHAPTER 2. LITERATURE REVIEW | 6 |
| 2.1 Transport and Fate Processes in Capped Contaminated Sediments | 6 |
| 2.1.1 Partition | 6 |
| 2.1.2 Diffusion | 7 |
| 2.1.3 Advection | 8 |
| 2.1.4 Degradation | 8 |
| 2.1.5 Bioturbation | 9 |
| 2.1.6 Characteristic Time of Transport Processes | 10 |
| 2.2 Oxygen Behaviors in Sediment | 10 |
| 2.3 Bubble-Facilitated Contaminant Transport in Sediment | 12 |
| 2.3.1 Formation and Growth of Bubble in Sediment | 12 |
| 2.3.2 The Role of Gas Ebullition in Contaminant Transport | 13 |
| 2.4 Computerized Tomography and Its Application to Investigation of Sediment Structure | 13 |
| 2.5 Summary and Objectives | 14 |
| CHAPTER 3. CONTAMINANT TRANSPORT IN CAPPED SEDIMENTS | 16 |
| 3.1 Studies of Organics Release in Lab-Contaminated University Lake Sediment | 16 |
| 3.1.1 Experimental Materials and Methods | 17 |
| 3.1.1.1 Tracers | 17 |
| 3.1.1.2 Sediment | 18 |
| 3.1.1.3 Capping Material--Sand | 18 |
| 3.1.1.4 Gypsum | 18 |
| 3.1.1.5 Tracer Flux Measurement | 18 |
| 3.1.1.6 Mass Transfer Coefficient at the Sediment-Water Interface | 23 |
| 3.1.2 Mathematical Modeling | 24 |
| 3.1.2.1 Governing Equations for Contaminant Transport in Capped Sediment | 24 |
| 3.1.2.2 Initial and Boundary Conditions for Uncapped System | 26 |
| 3.1.2.3 Initial and Boundary Conditions for Capped System | 27 |
| 3.1.2.4 Numerical Method | 27 |
| 3.1.3 Results and Discussion | 28 |
| 3.1.3.1 Sediment Consolidation | 28 |
| 3.1.3.2 Mass Transfer Coefficient at the Sediment-Water Interface | 30 |
| 3.1.3.3 Tracer Flux and Capping Effectiveness | 30 |
| 3.1.3.4 Model Applications | 33 |
| 3.2 Studies of Metals Release and Oxygen Distribution in Anacostia River Sediment | 37 |
| 3.2.1 Experimental Materials and Methods | 37 |
| 3.2.1.1 Sediment and Metal Concentrations | 37 |

| | |
|--|----|
| 3.2.1.2 Sand and Metal Concentrations | 37 |
| 3.2.1.3 Metal Flux Measurement | 39 |
| 3.2.1.4 Sediment Oxygen Demand (SOD)..... | 39 |
| 3.2.1.5 Oxygen and Redox Potential in Sediment/Cap..... | 40 |
| 3.2.2 Results and Discussion | 41 |
| 3.2.2.1 pH..... | 41 |
| 3.2.2.2 Metal Flux..... | 41 |
| 3.2.2.3 Metal Concentration Profiles in Sediment/Cap | 42 |
| 3.2.2.4 Oxygen Distribution in Sediment/Cap..... | 42 |
| 3.3 Summary..... | 45 |

CHAPTER 4. BUBBLE-FACILITATED CONTAMINANT TRANSPORT IN CAPPED SEDIMENT

| | |
|---|----|
| 4.1 Sediment and Contaminant Release during Gas Ebullition..... | 47 |
| 4.1.1 Experimental Materials and Methods | 47 |
| 4.1.1.1 Materials | 47 |
| 4.1.1.2 Setup | 48 |
| 4.1.1.3 Experimental Operation and Conditions..... | 49 |
| 4.1.1.4 Sample Collection and Measurements..... | 50 |
| 4.1.2 Results and Discussion | 54 |
| 4.1.2.0 Determination of k_1 for Water Solution and Sediment Slurry | 54 |
| 4.1.2.1 Effects of Methane Flux on TSS or Sediment Flux..... | 56 |
| 4.1.2.2 Effects of Methane Flux and TSS on Contaminant Release..... | 56 |
| 4.1.2.3 Effects of Consolidation on Contaminant Release | 60 |
| 4.1.2.4 Effects of Cap on Contaminant Release | 60 |
| 4.1.2.5 Contaminant Concentration Profiles in Sediment Cores | 62 |
| 4.1.2.6 Mass Balance | 62 |
| 4.1.2.7 Void Size Distribution in Sand and Sediment | 66 |
| 4.1.2.8 Contaminant Transport Pathway..... | 71 |
| 4.2 Measurement of Methane-Water Henry's Law Constants of PAHs and Their Temperature Dependence between 5 and 30 °C..... | 73 |
| 4.2.1 Theoretical Background..... | 74 |
| 4.2.1.1 Henry's Law..... | 74 |
| 4.2.1.2 van't Hoff Equation | 75 |
| 4.2.2 Materials and Methods..... | 76 |
| 4.2.2.1 Chemicals..... | 76 |
| 4.2.2.2 Experimental Setup and Operations..... | 76 |
| 4.2.2.3 Sample Collection and Analysis | 78 |
| 4.2.2.4 Calculations of Henry's Law Constants | 79 |
| 4.2.3 Results and Discussion | 79 |
| 4.2.3.1 Method Verification..... | 79 |
| 4.2.3.2 Correlation between log H and Molar Volume at 25 °C | 81 |
| 4.2.3.3 Determination of Enthalpy and Entropy of Phase Change | 82 |
| 4.2.3.4 The Enthalpy-Entropy Compensation Analysis..... | 84 |
| 4.2.4 Summary | 85 |
| 4.3 Mathematical Modeling..... | 85 |

| | |
|--|------------|
| 4.3.1 Model Development..... | 85 |
| 4.3.1.1 Assumptions..... | 85 |
| 4.3.1.2 Uncapped Sediment..... | 86 |
| 4.3.1.3 Capped Sediment..... | 90 |
| 4.3.2 Results and Discussion..... | 91 |
| 4.3.2.1 Model Verification..... | 91 |
| 4.3.2.2 Model Performance under Field Conditions..... | 98 |
| 4.3.2.3 Effects of Gas Flux, TSS and Cap on Contaminant Flux..... | 100 |
| 4.3.2.4 Sensitivity Analysis..... | 102 |
| 4.4 Summary..... | 105 |
| CHAPTER 5. CONCLUSIONS AND RECOMMENDATIONS..... | 106 |
| 5.1 Conclusions..... | 106 |
| 5.1.1 Capping Contaminated Sediments..... | 106 |
| 5.1.2 Bubble-Facilitated Contaminant Transport..... | 107 |
| 5.2 Recommendations..... | 108 |
| 5.2.1 Capping Contaminated Sediments..... | 108 |
| 5.2.2 Bubble-Facilitated Contaminant Transport..... | 109 |
| BIBLIOGRAPHY..... | 111 |
| APPENDIX A: ANALYTICAL PROCEDURES FOR SEDIMENT AND AQUEOUS SAMPLES..... | 127 |
| A1 PAH Analysis (US EPA Method 8270 and 8310)..... | 127 |
| A1.1 Sediment Samples..... | 127 |
| A1.2 Aqueous Samples..... | 127 |
| A2 Metal Analysis (US EPA Method 6020 and 200-8)..... | 128 |
| A2.1 Sediment Samples..... | 128 |
| A2.2 Aqueous Sample..... | 129 |
| APPENDIX B: MATHEMATICAL METHODS AND DERIVATIONS..... | 130 |
| B1 Diffusion, Advection and Reaction in a Two-layer Finite System..... | 130 |
| B1.1 Coordinates..... | 130 |
| B1.2 Model..... | 130 |
| B1.3 A Numerical Algorithm-----Fully Implicit Method..... | 132 |
| B2 Runge-Kutta and Adams-Moulton Numerical Methods..... | 135 |
| B3 Penetration Theory..... | 136 |
| APPENDIX C: COMPUTER (MATLAB) CODES..... | 138 |
| C1 Fully Implicit Method to Solve Partial Differential Equations (PDEs)..... | 138 |
| C2 Runge-Kutta and Adams-Moulton Methods to Solve Ordinary Differential Equations (ODEs)..... | 148 |
| APPENDIX D: CONCENTRATION PROFILES IN SEDIMENTS AND METAL FLUXES..... | 154 |
| D1 Tracer Concentration Profiles in the U.L. Sediment..... | 154 |
| D2 Metal Flux from A.R. Sediment with and without Sand Cap..... | 157 |

| | |
|---|-----|
| D3 Metal Concentration Profiles in A.R. Sediment | 168 |
| D3.1 Uncapped Sediment | 168 |
| D3.2 Capped Sediment (4 mm sand cap)..... | 177 |
| D3.3 Capped Sediment (8 mm sand cap)..... | 186 |
| APPENDIX E: FILTRATION LOSS FACTORS | 195 |
| APPENDIX F: MASS TRANSFER COEFFICIENT BETWEEN THE ORGANIC AND AQUEOUS PHASES | 199 |
| F1 Water Solution..... | 199 |
| F2 Sediment Slurry | 202 |
| VITA..... | 206 |

ABSTRACT

Fluxes of the three organics and eighteen metals from sediments were measured with diffusion chambers, and the effectiveness of a sand cap ascertained. The influence of sediment consolidation on contaminant flux and the mass transfer coefficient at the sediment-water interface was studied. A two-layer diffusion-advection model and consolidation model were coupled to elucidate the effect of sediment consolidation on chemical transport in the sediment-cap system. The model was tested and verified by the experimental data from microcosms, and then was used to predict phenanthrene flux under field conditions. The simulation results showed that consolidation could accelerate phenanthrene breakthrough and enhance the initial phenanthrene flux. At the same time, oxygen distribution in both cap and sediment were studied with microelectrodes.

A bubble column was employed to investigate sediment and phenanthrene release from sediment with methane injection. The experiments indicated that significant amounts of both solid particulate matter and phenanthrene could be released from a sediment bed by gas movement with the amount of release related to the volume of gas released. The effective mass transfer coefficient of gas bubble facilitated contaminant release was estimated under field conditions, being around three orders of magnitude smaller than that of bioturbation. A thin sand cap layer (2 cm) was found to dramatically reduce the amount of phenanthrene or particles released with the gas. X-ray computerized tomography was used to investigate the void space distribution in the sediment penetrated by gas bubbles. The results showed that gas bubble migration could redistribute the sediment void spaces and facilitate pore water circulation in the sediment. A model was developed for bubble-facilitated contaminant release from sediments. The model was first verified by experimental data and then was used to calculate the

contaminant flux into the air under field conditions. It was also used to investigate the effects of total suspended soil, gas flux and sand cap on the contaminant flux into the air. Model sensitivity analysis suggested that the cap thickness and its organic carbon content be two important parameters for the effectiveness of a cap to control the contaminant flux into the atmosphere.

CHAPTER 1. INTRODUCTION

Contaminated sediments resulted from past discharge to surface waters. The Environmental Protection Agency (US, EPA) has estimated that 1.2 billion cubic meters of contaminated surficial sediments pose a risk to environmental health (EPA, 1997). Major sediment contaminants include: mercury, polychlorinated biphenyls (PCBs), dioxins, DDT, polycyclic aromatic hydrocarbons (PAHs), and metals. These contaminants remain in the environment long after their sources have been removed. With the implementation of the Clean Water Act (CWA), contaminated sediments have converted from being a sink to a source. The sediment pollutants can transport into water and air, and constitute threats to plants, animals and human life. For example, the Anacostia River (Washington, D. C) was polluted due to agricultural, industrial and urban development in past decades. High levels of hazardous substances, including PCBs; pesticides; lead and other heavy metals; and PAHs have been found in sediment throughout the Anacostia River. Toxicity studies of the Anacostia River sediment show that some of these hazardous substances have been found in fish at concentrations exceeding the Food and Drug Administration (FDA) Action Levels. The US EPA identified the Anacostia River as one of the most contaminated rivers in the Chesapeake Bay watershed, and its contaminated sediment poses a significant risk to aquatic life (Reible et al., 2003; Beyer et al., 2000; Phelps, 1993; Mason and Sullivan, 1998; Velinsky et al., 1994; Wade et al., 1994; Schlekot et al., 1994). Thus, sediment contamination is recognized as one of the most serious environmental problems, and the management of contaminated sediments presents significant challenges (Thoma, et al., 1993; TechData Sheet, 2002; U. S. EPA, 2004).

Polycyclic aromatic hydrocarbons (PAHs) are hydrocarbon compounds with multiple benzene rings. PAHs are typical components of asphalts, fuels, oils, and greases; they are formed

during the incomplete burning of coal, oil and gas, garbage, or other organic substances like tobacco or charbroiled meat. These compounds are widespread pollutants in contaminated sediments (Wang et al., 1991; Ravikrishna, 2000) and have been found in at least 600 of the 1,430 National Priorities List sites identified by the Environmental Protection Agency (US, EPA), particularly at creosote wood treatment facilities and industrial activities involving the processing, combustion and disposal of fossil fuels or fossil-fuels-derived products (Wilson and Jones, 1993). With benzene as their fundamental building block, these compounds have very low water solubility. Due to hydrophobicity, PAHs in soil are mainly associated with the solid phase, or as a separate hydrocarbon phase in the subsurface, or may even be present with solid particles (Grimberg et al., 1995; Mulder et al., 1997). In test animals, PAHs can harm their reproductive system and interfere with normal development of a fetus. The World Health Organization (WHO) and the Department of Health and Human Services (DHHS) have determined that some PAHs may reasonably be expected to be carcinogens (ATSDR, 1995).

Heavy metals or heavy elements are chemical elements with a specific gravity that is at least five times the specific gravity of water (Lide, 1992). Heavy metals are another one of the most prevalent contaminants in contaminated sediments. There are 35 metals that concern us because of occupational or residential exposure; twenty-three of these are the heavy metals: antimony, arsenic, bismuth, cadmium, cerium, chromium, cobalt, copper, gallium, gold, iron, lead, manganese, mercury, nickel, platinum, silver, tellurium, tin, uranium, vanadium, and zinc (Glanze, 1996). In cooperation with the U.S. EPA, the Agency for Toxic Substances and Disease Registry (ATSDR) has compiled a Priority list for 2001 called "Top 20 Hazardous Substances." The heavy metals arsenic (No.1, Specific Gravity $\rho=5.7$), lead (No.2, $\rho=11.34$), mercury (No.3, $\rho=13.546$), and cadmium (No.7, $\rho=8.65$) appear on this list. In small quantities, certain heavy

metals are nutritionally essential for a healthy life. Some of these are referred to as trace elements (e. g., iron, copper, manganese, and zinc). But heavy metals become toxic when they are not metabolized by the body and accumulate in the soft tissues. Large amounts of any of them may cause acute or chronic toxicity (poisoning). Heavy metal toxicity can result in many severe problems or diseases and may even cause cancer (International Occupational Safety and Health Information Center, 1999).

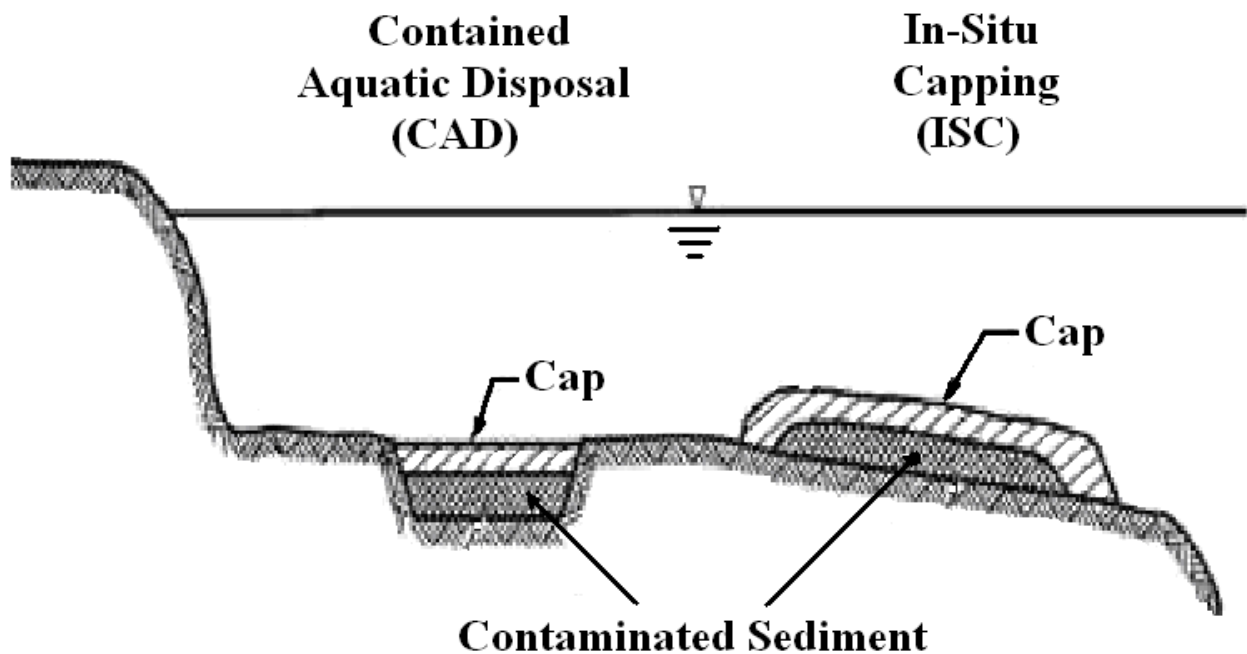


Figure 1.1 Conceptual illustration of dredge material capping and *in situ* capping.

Dredging and capping are two remediation technologies employed to treat and manage contaminated sediments. Dredging is a process of excavating materials underwater. Since dredging needs removal of contaminated sediments from the aquatic environment, it is costly and only used in specific situations (TechData, 2002). Capping with clean sand or uncontaminated sediment is often an economically sound management technique. Figure 1.1 illustrates the schematics of contained aquatic disposal (CAD) and *in situ* capping (ISC) (U. S. EPA, 2004; Palermo, et al. 1998 b). By comparison, *in situ* capping is more attractive, which is a process of

underwater containment of contaminated sediments using layers of clean sediment, sand, and natural minerals. Besides lower cost, this technique also has many advantages such as: (a) reduction and elimination of the potential for contaminated sediment suspension and transport, (b) reduction or elimination of the advection or diffusion of contaminants to the water column; some active capping materials can react with pollutants and mineralize them into environment-friendly substances, (c) elimination of direct contact between contaminated sediment and surface water, and (d) recreation of a healthy benthic environment (TechData, 2002; U. S. EPA, 2004; Palermo, et al. 1998 b).

Conventional capping materials are sand or clean sediment. These materials can passively slow the contaminant migration. Recently, “active” capping techniques have been proposed by Reible et al. (HSRC/S&SW, Research Brief #23, 2002). These techniques use innovative “active” cap materials to implement containment and treatment of contaminated sediments. The goal of such a cap is to ensure reduction or elimination of migration through the cap by sorption, chemical fixation or degradation of any contaminants that may migrate. A variety of active capping materials have been proposed, which include: (a) AquaBlokTM, significantly reducing advective contaminant transport and maybe mixing with other constituents to encourage degradation or sorption for any material that diffuse into the cap, (b) BionSoilTM, encouraging sorption and degradation of organic contaminants, (c) Zero-valent iron, encouraging dechlorination and metal reduction, (d) Apatite, encouraging precipitation and sorption of metals, (e) other potential cap materials including organo-modified clays, coke breeze, Ambersorb, and coal-based sorbents. Some active materials have already been tested in the field (www.hsrtc-ssw.org/ana-index.html). The work on the Anacostia River Active Capping Demonstration Project and the results have been well documented by Reible et al. (2003, 2004, and 2005).

On the other hand, contaminated sediments often contain high organic matter content. Both oxygen profiles and redox potential data show that anaerobic conditions exist in capped sediments (Valsaraj and Yuan, 2004). Under anaerobic conditions, organic matter is converted into methane and carbon dioxide by bacterial and microbial activities (Di Toro, 2001). Gas bubbles form when the gas reaches saturation in the porewater. Methane gas plumes (so-called gas flares) are found to form on the seafloor (Klaucke et al., 2005). As previously discussed by Martens et al. (1980) and Hovland and Judd (1992), the movement of bubbles in sediments may cause a destabilization of the sediment and/or stripping of volatile pollutants out of contaminated sediments and subsequent release into the water column. Both theoretical modeling study and experimental work are needed to assess the effects of gas bubble on pollutant transport and sediment/cap integrity.

As stated above, although capping is an effective way to retard the transport of chemicals from contaminated sediment to the natural environment (Wang et al., 1991; Thoma et al., 1993; Ravikrishna, 2000), little is known about degradation mechanisms of organics, soil respiration, and metal oxidation in both sediment and cap (Lee et al., 2003; Revsbech, et al., 1980). There are also concerns about the impacts of methane migration on the pollutant transport and the cap integrity (Baudo and Muntau, 1990; Johnson et al., 2002; Jepsen et al., 2000). Thus there are two main objectives of this work: (1) to quantify and model the transport and degradation of hazardous chemicals, and oxygen behavior in cap and sediment systems and (2) experimentally and mathematically to investigate the effects of gas bubble ebullition on pollutant transport and cap and/or sediment integrity. This can provide the basis on which suitable remediation methods can be developed.

CHAPTER 2. LITERATURE REVIEW

Boudreau (1996) used a figure to illustrate some processes in sediment during diagenesis. The figure included such processes as diffusive boundary layer, resuspension, flow through sediment, biological irrigation, release and consumption of solutes, bioturbation, mineral precipitation/dissolution, and molecular diffusion. After cap placement, the important processes are chemical partition, diffusion, advection, degradation, bioturbation and bubble movement in sediment/cap. To provide a background understanding of these processes relative to this research, they are briefly discussed below. More complete discussions are available elsewhere (Thoma, 1994).

2.1 Transport and Fate Processes in Capped Contaminated Sediments

2.1.1 Partition

Adsorption/desorption partitioning of contaminants between pore water and solid phase has a significant effect on their fates, transport, and ecotoxicological risks. The sorption between the pore-water and the sand or the soil particles in the sediment retards the contaminant transport, which capping relies on for its effectiveness. The equilibrium partition coefficient of an organic chemical between the aqueous solution and soil particles in a sediment is defined as

$$K_d = \frac{w_A}{C_A} \quad (2.1)$$

where w_A is the sediment contaminant loading (mg/kg) and C_A is the aqueous phase concentration (mass/volume) (Thibodeaux, 1996; Valsaraj, 1995b). Curtis et al. (1986) suggested that the overall partition coefficient of hydrophobic organic compounds, including both organic carbon fraction and mineral sorption, be given by

$$K_d = f_{\min} S_a K_{d,\min} + f_{oc} K_{oc} \quad (2.2)$$

where f_{\min} , f_{oc} are the mineral and organic carbon fraction in the sediment ($f_{\min} + f_{oc} = 1$), S_a is the specific surface area (area/mass), $K_{d,\min}$ and K_{oc} are the mineral and organic carbon partition coefficient respectively. For $f_{oc} > 0.1\%$, the mineral sorption contributes little ($f_{\min} S_a K_{d,\min} \ll f_{oc} K_{oc}$) and can be usually neglected. Thus,

$$K_d = f_{oc} K_{oc} \quad (2.3)$$

The above equation has been widely accepted and used for several decades.

Partition in soils and sediments with greater than 0.1% organic carbon is considered to be through hydrophobic interaction as it is in octanol water systems. To quantify a chemical's hydrophobicity, octanol-water partition coefficient (K_{ow}) was introduced, which is defined as a ratio of the octanol phase activity to the water phase activity at equilibrium (Valsaraj, 1995b). Based on a linear free energy relationship between K_{oc} and K_{ow} , Curtis et al. (1986) obtained the following semi-empirical correlation for adsorption on the natural organic matter of soils

$$\log K_{oc} = 0.92 \log K_{ow} - 0.23 \quad (2.4)$$

Recently a growing body of evidence shows that the simple equation (2.3) does not always apply (Allen-King et al., 2002; Weber et al., 2001). Other kinds of carbons such as black carbon and unburned coal carbon can also have influence on the partition process in sediment (Lohmann et al., 2005; Cornelissen et al., 2005). Nguyen et al. (2005) reviewed polyparameter linear free energy relationships (pp-LFER) and presented more accurate correlations to estimate K_{oc} .

2.1.2 Diffusion

The driving force of molecular diffusion is the concentration gradient. Contaminant diffusion in capped sediment is essentially diffusion in a porous media. The effective diffusivity

in porous media can be calculated by correcting water diffusivity with porosity and tortuosity. McDuff et al. (1979) and Oelkers et al. (1991) suggested some methods to estimate the diffusion coefficients in porous media. Several researchers studied sulfate reduction and diffusion (Urban et al., 1994; Goldhaber et al., 1977) and radionuclide diffusion (Meier et al., 1992; Anderson, et al., 1992) in sediments. Wang et al. (1991) and Thoma et al. (1994) measured diffusion flux of some organic compounds from capped sediments with diffusion chambers. Valsaraj et al. (1997) investigated the effects of porewater ionic strength on the diffusion of dissolved organic carbon (DOC) in sediment using two different electrolytes and laboratory microcosms. Choy et al. (1999), Di Toro (2001) and Boudreau (1989, 1996, 2000) completed many relevant modeling work.

2.1.3 Advection

Natural processes such as strong current/storm and active groundwater seepage may result in the water flow through the pores in sediments. Capping causes sediment consolidation that can also lead to porewater advection. Thibodeaux et al. (1987) investigated flow through the bedforms (dunes) induced by wake separation. Boudreau, et al. (2001c) edited a general review which included a lot of information about porewater flow in sediments. Wilson (1986) used the diagenetic model to study porewater advection in deep-ocean sediments. Moo-Young (2001, 2002) conducted experiments to study the environmental impact of consolidation induced convective transport through capped sediment.

2.1.4 Degradation

Conventional capping materials such as sand and clean sediments can retard the contaminant transport and give more time for fate processes to degrade or detoxify the contaminants in capped sediments. Levitt et al. (2003) conducted laboratory experiments to

elucidate the degradation of α -methylnaphthalene in lake sediments using an advanced oxidation process. The experiments showed fast degradation and products were most likely biodegradable. The degradation of dioxins with a mechanochemical process was investigated by Nomura et al. (2005). Lei et al. (2005) reported that the biodegradation of PAHs occurred under aerobic, sulfate reducing and denitrifying conditions. Wammer et al. (2005) performed experiments to examine the role of molecular structure in determining the biodegradation rates of PAHs. Although no significant correlations were found, biomass-normalized first-order rate coefficients of 22 PAHs were reported. Tang et al. (2005) reported that controlled-release electron acceptors such as nitrate and sulfate could enhance the rates of in-situ microbial anaerobic biodegradation of phenanthrene in undisturbed marine sediments. With the experimental results, Tungittiplakom et al. (2005) showed that engineered polymeric nanoparticles could not only enhance the release of sorbed and NAPL-sequestered phenanthrene but also increase its mineralization rate. Although contaminant degradation in sediment has received considerable attention, the degradation rates in sediments are still uncertain. Determining degradation rates of contaminants in sediments can be very difficult for degradation rate dependent on bioavailability limitations from physical-chemical processes (Wammer et. al., 2005).

2.1.5 Bioturbation

The term bioturbation implies turbulence or mixing brought about by the activity of organisms, specifically particles and porewater in the upper layers (ca. 10 cm) of the sediment (Thibodeaux, 1996). Lee (1980) and Bosworth and Thibodeaux (1990) published reviews about the effect of bioturbation on contaminant transport. Ciutat and Boudou (2003) studied bioturbation effects on metal transfers from a contaminated sediment into the water column, and they concluded that bioturbation produces a significant metal release into the water column

through the resuspended sediment particles. Anderson et al. (2001) conducted experiments to investigate the effect of polychaete bioturbation on sediment-water fluxes of pyrene and cadmium. Cunningham et al. (1999) reported that native oligochaetes could enhance natural attenuation of contaminated sediment in the field. Kamp-Nielsen et al. (1982) used a multilayer sediment-water exchange model to evaluate the importance of bioturbation in lake sediments. Recently, Boudreau et al. (2001d) and Choi et al. (2002) suggested a lattice-automaton model to simulate the bioturbation in sediments.

2.1.6 Characteristic Time of Transport Processes

Reible et al. (1991) defined a characteristic time for leaching of the contaminant from a finite layer, H , as the time required to achieve a concentration at depth H equal to 84% of its original value. Based on the definition, the order-of-magnitude estimates of the characteristic times of several transport processes in sediment were made (Table 2.1; please note that the characteristic times for the advective processes represent complete removal times). Processes with a shorter characteristic time are likely to be the most important transport processes. They concluded that the processes with particle movement dominate over pore-water processes for hydrophobic contaminants.

2.2 Oxygen Behaviors in Sediment

Sediment redox potential ($Eh = -\Delta G/nF$, where F is the Faraday constant, n is the number of electrons exchanged in the half-cell reactions and ΔG is the Gibbs free energy) characterizes the intensity of reduction or oxidation and relates many processes occurring in the sediment such as biological, microbial and meiofaunal distribution, transformation and transport of hydrophobic pollutants and trace metals etc (Callebaut et al. 1982; Malicki et al. 1990; Shaikh et al. 1985). Aerated soils have characteristic redox potentials in the range of +400 to +700 mV.

Sediments have a broader range of redox potentials since they function as both oxidized (+400 to +700 mV) and reduced (-250 to -300 mV) forms (Gambrell et al., 1984).

Table 2.1 Comparison of the characteristic times of sediment transport processes for trichlorobiphenyl (TCPB) (H=10 cm)

| Mechanism | Formula | Characteristic time |
|--|--|----------------------------------|
| Molecular diffusion (Unretarded by sorption) | $H^2 / 4D_s$ ^(a) | 0.5 years (Hypothetical) |
| Retarded diffusion | $H^2 / 4D_{sr}$ ^(b) | 1,900 years |
| Colloidally enhanced diffusion | $H^2 / 4D_{sc}$ ^(c) | 1,500 years |
| Erosion (U=1 cm/yr) | H^2 / U | 10 years ($N_{pe} \gg 1$) |
| Capped sediment (L=30 cm effective cap) | L^2 / D_{sc} | 21,000 years |
| Sediment movement (Bed load transport) | $\frac{0.7hl(1-\varepsilon)}{4u_{b1}C_{p,b1}d_p}$ ^(d) | 42 hours (Rapid desorption) |
| Aquifer interactions (Advection, V=10 cm/yr) | $\frac{H(\varepsilon + \varepsilon K_c C_c + \rho_b K_s)}{V}$ | 4,000 years ($N_{pe} > 1$) |
| Local advection (Surface roughness, V=11.7 cm/yr) | $\frac{l(\varepsilon + \varepsilon K_c C_c + \rho_b K_s)}{V}$ | 69,000 years ($N_{pe} > 1$) |
| Bioturbation | H^2 / D_{bio} ^(e) | 10 years |

(a) $D_s = D_w \varepsilon^{4/3}$, where D_w is the diffusivity (m^2/s) in water and ε is the sediment porosity.
(b) $D_{sr} = D_s / (\varepsilon + \rho_b K_d)$, where ρ_b is the bulk density of sediments (kg/m^3).
(c) $D_{sc} = (D_s + D_s^{(c)} K_c C_c) / (\varepsilon + \rho_b K_d + \varepsilon K_c C_c)$, where $D_s^{(c)}$ is the effective diffusivity of the colloid, K_c is the contaminant partition coefficient between the pore water and the colloids in the pore space, and C_c is the organic colloid concentration in the pore water. (d) h is the height of sediment dune (m), l is the length of the sediment dune (m), u_{b1} is the bed load velocity (m/s), $C_{p,b1}$ is the fraction of exposed particles carried in the bed load layer, and d_p is the particle diameter (m). (e) D_{bio} is the effective bioturbation diffusion coefficient.

The sediment oxygen demand (SOD) is the rate of oxygen consumption in the overlying water due to the biological and chemical processes in sediment. SOD is the largest dissolved

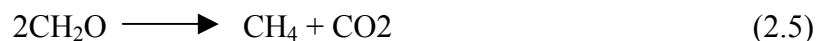
oxygen (DO) sink within natural water. The substantial SOD can lead to severe oxygen depletion, constituting a threat to the health or life of aquatic organisms. SOD studies are useful in determining waste load allocations and measuring the depletion of oxygen in waters when there are concerns about nutrient regeneration and loss of aquatic life. Nalan and Johnson (1979) developed a method to measure SOD. Rounds and Doyle (1997) measured sediment oxygen demand of river sediment. Shin (1998) conducted experiments to measure sediment SOD and developed a SOD model.

Revsbech et al. (1980a, b) measured oxygen distribution in marine sediments with microelectrodes. Burke (1999) measured profiles of oxygen concentration in sediment cores and reported that oxygen typically penetrated less than 3 mm into the sediment. Lee et al. (2003) studied microbial respiration and diffusion of oxygen in unsaturated soils and geologic sediments. Bouldin (1968) and Di Toro (2001) assumed that the consumption of oxygen was zero-order and constant with respect to depth below the sediment-water interface.

2.3 Bubble-Facilitated Contaminant Transport in Sediment

2.3.1 Formation and Growth of Bubble in Sediment

Usually contaminated sediment is rich in organic compounds. Volatile substances such as methane and carbon dioxide can be produced by organic matter decomposition in anaerobic sediment layer (Di Toro, 2001; Kuivila et al., 1989). The overall reaction of methanogenesis is



where CH_2O is the stoichiometric organic matter. Johnson et al. (2002) observed that bubbles in sediments are non-spherical and often disk-shaped, with their long axis in a near-vertical orientation. Boudreau et al. (2001a, b) and Gardiner et al. (2003) simulated the process by coupling a reaction-diffusion model and a linear elastic fracture mechanics (LEFM) model. The

model results conclude that the bubble growth rate is strongly dependent on bubble aspect ratio and the eccentric bubbles grow 2-4 times faster than spherical bubbles for an equivalent volume of gas. Furthermore, isolated bubble growth may become arrested so that small bubbles can cease to grow in sediments; isolated bubbles can easily rise in sediments by a buoyancy-driven fracture mechanism. Most recently, they observed that bubbles in sand are essentially spherical away from mud contacts (Boudreau et al., 2005).

2.3.2 The Role of Gas Ebullition in Contaminant Transport

A number of papers have been published about gas bubble ebullition rates from wetland sediments (Tanner et al., 1997), paddy soil (Rothfuss and Conrad, 1998) and other sediments (Henry et al., 1999; Adams et al., 1987). The gas fluxes from these observations vary largely from 0.3 to 2640 mL/m²-day due to the different local conditions. Recently, Himmelheber and Hughes (2005) measured the methane generation from the Anacostia River sediment in the laboratory and reported that the gas generation rates normalized to sediment-water interfacial area were near 0, 341, and 917 mL/day-m² at 4, 22 and 35 °C respectively. Fendinger et al. (1992) estimated the overall pesticide contaminant fluxes by measuring the gas bubble flux and assuming equilibrium between the gas bubble and water. They noted that because the estimation is only approximate, more research is needed to understand the gas bubble/water partitioning. Huls et al. (2003 and 2005) conducted bench and field studies to investigate the gas generation and the PAHs migration from capped contaminated sediments. They concluded that gas release rates are highly dependent on sediment temperature, and significant insulation will have to be added to lower sediment temperatures and terminate gas production when a sand cap is placed on the sediment.

2.4 Computerized Tomography and Its Application to Investigation of Sediment Structure

As discussed before, nucleation of gas bubbles occurs when gases saturate in the pore water. During their growth, bubbles push aside the surrounding sediment grain matrix. Resulting

stresses may initiate cracks around bubbles. If these cracks join, they may form channels stretching to the sediment surface and along which gas may escape. Van Kessel et al. (2002) reported that accumulation of gas in sludge may continue until a bulk density less than that of water is attained, and only then can gas escape as a result of instabilities in the sediment matrix. The resulting gas movement can influence sediment structure.

X-ray computerized tomography (CT) is a nondestructive visualization and characterization technique that creates three-dimensional images that map the variation of X-ray attenuation within objects. The X-ray attenuation is a function of the X-ray energy and the atomic number and density of the material being scanned. Ketcham and Carlson (2001) provided an excellent review of the principles of CT and application to geosciences. Due to its non-destructive nature and the large differences in X-ray attenuation between the sediment and the gas bubbles, CT is an excellent tool for investigating the distribution and impact of gas bubbles in sediment systems. Jepsen et al. (2000) studied the effects of gas generation on sediment density and erosion. Many others (Selomulya, et al., 2005; Anderson, et al., 1988) have employed CT techniques to investigate the sediment structure nondestructively. The method could capture the influence of gas release on sediment structure.

2.5 Summary and Objectives

For capping contaminated sediments, Wang et al. (1991) and Thoma et al. (1993) have done fundamental work of organic contaminant diffusion in capped sediments. Based on their work, advection due to sediment consolidation was added to the diffusion model herein; boundary conditions and mass transfer coefficient at the sediment-water interface became time dependent. The experiments were carried out and the data supported the model results. The effects of consolidation and degradation on contaminant flux in capped sediment were also

simulated. Metals fluxes from the field contaminated Anacostia River sediment were measured, and oxygen distribution in the sediment was investigated. These results are given in Chapter 3.

The literature review shows that the influence of gas bubbles on contaminant transport in sediments and sediment/cap integrity is not fully understood. Both experimental and modeling work are needed to answer some questions regarding the process. Experiments were conducted to find out what factors are responsible for the bubble-associated contaminant transport in sediments. A sand cap was tested and the cap effectiveness was ascertained. CT techniques were used to study the effects of bubble movement on the sediment/cap integrity. All the experimental results are given in sections 4.1 and 4.2. In section 4.3, a model was developed, verified with the experimental data, and used to predict the contaminant flux during bubble ebullition under field conditions. Finally, Chapter 5 offers some conclusions and recommendations.

CHAPTER 3. CONTAMINANT TRANSPORT IN CAPPED SEDIMENTS

One primary objective of this work is to develop and experimentally verify the mathematical models which describe the dynamics of contaminant diffusion and advection from both capped and uncapped sediments. Experiments were performed to investigate diffusion and advection of three organic compounds from lab-contaminated University Lake (Baton Rouge, LA) sediment, and eighteen metals release and oxygen distribution in field-contaminated Anacostia River (Washington, D. C) sediment with diffusion chambers. This chapter consists of two sections, one focusing on organics release in lab-contaminated University Lake (U.L.) sediment and the other focusing on metals transport and oxygen distribution in field-contaminated Anacostia River (A.R.) sediment.

3.1 Studies of Organics Release in Lab-Contaminated University Lake Sediment

Surface fluxes of organics from both capped and uncapped systems were measured. In order to observe the influence of sediment consolidation on contaminant flux, mass transfer coefficients with consolidation at the sediment-water interface were measured using a gypsum-wafer method (Birdwell and Thibodeaux, 2005; Santschi et al., 1991; Santschi and Bower, 1983; Marshal and Slusher, 1966). A transport (diffusion and advection) model was employed to simulate the processes with and without sediment consolidation. The experimental data satisfactorily support the transport model. The transport model and consolidation model were coupled to predict the chemical flux with and without sediment consolidation under field conditions, which is necessary before an actual field trial. The model (diffusion and reaction) was used to simulate the impacts of degradation on contaminant flux, which shows that

degradation in sediment/cap can substantially reduce the contaminant flux or enhance the cap effectiveness.

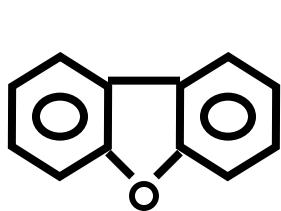
3.1.1 Experimental Materials and Methods

3.1.1.1 Tracers

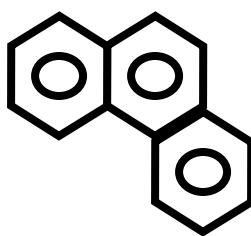
Dibenzofuran (DBF) of 99+% purity, and phenanthrene (PHE) and pyrene (PYR) of 98% purity were purchased from Aldrich Chemicals, Milwaukee, WI. Table 3.1 lists the relevant properties of these compounds. Figure 3.1 shows their structures.

Table 3.1 Physico-chemical properties of three tracers

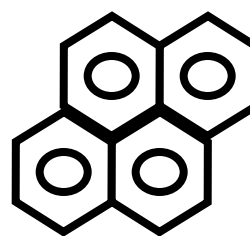
| Property | Dibenzofuran | Phenanthrene | Pyrene |
|---|----------------------|----------------------|----------------------|
| λ_{\max} (nm) | 217 | 252 | 240 |
| Solubility in water (mg/L) | 10 | 1 | 0.15 |
| Log K_{oc} | 4±0.1 | 4.4 | 4.8 |
| Log K_{ow} | 4.15 | 4.5 | 5.1 |
| Henry's Constant (atm m ³ /mol) | 7.9×10 ⁻⁵ | 6.0×10 ⁻⁵ | 1.0×10 ⁻⁵ |
| Diffusivity in water (cm ² /s, 20°C) | 6.0×10 ⁻⁶ | 5.8×10 ⁻⁶ | 5.5×10 ⁻⁶ |



Dibenzofuran
CAS#: 192-64-9
MW: 168.20
Formula: C₁₂H₈O



Phenanthrene
CSA#: 85-01-8
MW: 178.24
Formula: C₁₄H₁₀



Pyrene
CSA#: 129-00-0
MW: 202.26
Formula: C₁₆H₁₀

Figure 3.1 Chemical structures of three tracers.

3.1.1.2 Sediment

The sediment was collected from the University Lake (LSU, Baton Rouge, LA). The sediment was sieved using a grid with $10 \times 10 \text{mm}^2$ openings and a fine sieve (No.10: 2 mm openings, U. S. A. Standard testing sieve). The sieved sediment was inoculated with the three tracers using a procedure described already in the literature (Thoma, 1994). The initial tracer concentrations in the sediment are listed in Table 3.2.

Table 3.2 Initial tracer loading for the University Lake sediment

| Chemicals | Loading (mg/kg) | Measured (mg/kg) (n=3) | Stdev | Water (w%)(n=9) |
|--------------|-----------------|------------------------|-------|-----------------|
| Dibenzofuran | 117.7 | 118.4 | 3.0 | 57.0 |
| Phenanthrene | 118.2 | 118.6 | 0.9 | |
| Pyrene | 118.1 | 110.9 | 5.4 | |

3.1.1.3 Capping Material---Sand

The sand used was play sand (QUIKRETE[®]). Before use, it was sieved through two sieves (No.20 and No.70, U. S. A. Standard testing sieve) to remove larger and smaller particles, washed several times with tap water and then with de-ionized water, and dried in the oven at 100 °C.

3.1.1.4 Gypsum

Calcium sulfate, hemihydrate ($\text{CaSO}_4 \cdot 1/2\text{H}_2\text{O}$, CAS#10034-76-1) was purchased from VWR Scientific, Buffalo Grove, IL. It was used to measure mass transfer coefficient (MTC) at the sediment-water interface.

3.1.1.5 Tracer Flux Measurement

Setup: The experimental cell described previously (Thoma et al., 1993; Wang et al., 1991; Palermo et al., 1998) was modified for these experiments. The diffusion chamber consists

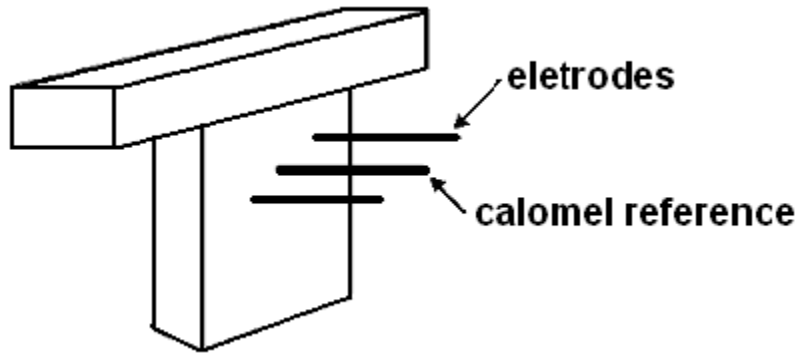


Figure 3.2 Diffusion chamber equipped with electrodes.

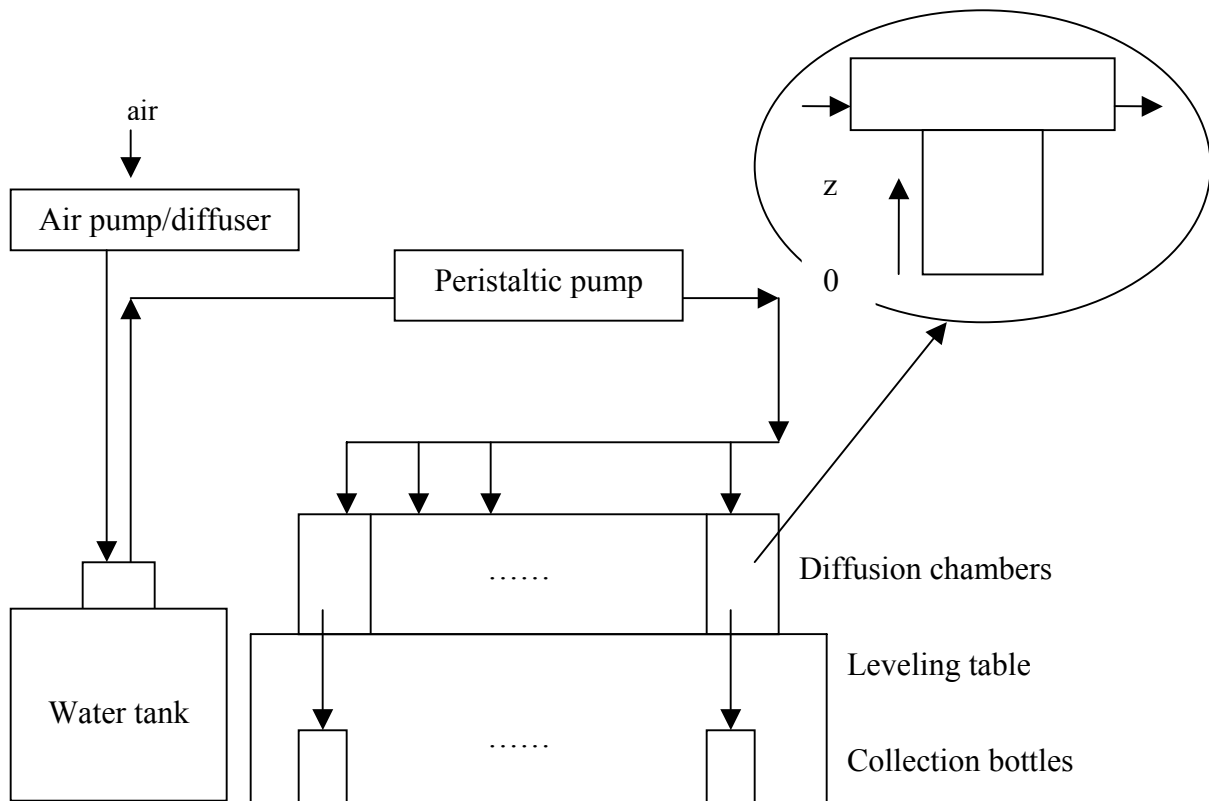


Figure 3.3 Experimental setup for capping project.

of two parts. The top part (with dimension $200 \times 50 \times 50 \text{ mm}^3$) is for water flow. The bottom part ($100 \times 50 \times 150 \text{ mm}^3$) holds the contaminated sediment and sand. Figures 3.2 and 3.3 show the diffusion chamber and the coordinate system used in the model work, and the whole setup for capping experiment.

Material Loading, Operation and Sample Collection: The contaminated sediment was gently placed in the bottom part of the diffusion chamber, and leveled with a spatula. Then the capping material (sand) was carefully placed on the top of the contaminated sediment, and leveled using a machined skimmer. The cap thickness was determined from the weight and the bulk density of the material, and cross section area of the diffusion chamber.

Air was diffused into the water in the tank by an air pump. A peristaltic cassette pump (Masterflex[®], Cole-Parmer, No.7520-35) was used to pump water into the diffusion chambers. The flow rate for each diffusion chamber was measured from the measurement of the weight of the sample collected in a certain period of time (t). The volume (v) of the sample was determined by the weight with the assumed density of 1 g/cm^3 . Then the flow rate was calculated by v/t . In the experiment, six identical diffusion chambers were used. One was for the uncapped sediment and the other two were capped but they had different cap thickness. Duplicate chambers were used for each experiment. Table 3.3 lists the experimental conditions.

Glass bottles (500 mL, PYREX[®], Germany) were used to collect samples at the outlet of the diffusion chambers. The connection between the glass bottle and the exit of the diffusion chamber was plastic tubing. Samples were collected at defined time intervals and analyzed for tracer concentrations that were used to calculate the tracer flux.

After the experiment run for a predetermined time, the contaminated sediment/cap in the diffusion chamber was sliced with a skimmer. The sediment/cap from the same sliced layer

(usually 2 mm) was mixed thoroughly and split into two subsamples for moisture and tracer analysis respectively. The sediment loading concentrations were calculated and the concentration profiles in the sediment/cap were obtained.

Table 3.3 Conditions for experiment with the U.L. sediment
 Sediment inoculation: 06/20/2003
 Start of run: 08/25/2003 End of run: 11/26/2003

| Chamber | Cap material | Cap depth (mm) | Contaminated sediment depth (mm) | Average flow rate with stdev. (mL/hr) |
|---------|--------------|----------------|----------------------------------|---------------------------------------|
| A1 | No cap | 0 | 150 | 9.2±0.7 |
| B1 | No cap | 0 | 150 | 8.7±0.6 |
| C1 | Sand | 8 | 142 | 8.4±0.4 |
| D1 | Sand | 8 | 142 | 9.9±1.2 |
| E1 | Sand | 12 | 138 | 10.1±1.0 |
| F1 | Sand | 12 | 138 | 9.6±1.0 |

Analytical Methods: PAHs in both water and sediment were determined using a Hewlett-Packard liquid chromatograph (HP 1100) equipped with an UV/Visible diode array detector. The column used was Phenomenex Envirosep-pp (125×3.2mm). Since the concentrations of PAHs in the water sample were very low, a solvent extraction was carried out before HPLC (High Performance Liquid Chromatography) analysis. Extraction procedures for both water and sediment samples, the parameters and HPLC conditions for the analysis were the same as the US EPA Standard Method 8270 (APHA/AWWA/WEF, 1991). The extraction procedure was summarized in Appendix A.

Quality Assurance (QA)/Quality Control (QC): Aqueous samples and most of the sediment samples were analyzed on the same day as they were collected. Some of the sediment samples that could not be analyzed immediately after the collection were kept in a refrigerator and extracted within 3 days. For aqueous samples, typical sample volumes collected from each

channel were around 400 mL. The sample was split into three subsamples. One of the subsamples was spiked by adding a concentrated solution of the analytes in acetonitrile. The mass of spiked analyte was adjusted to be approximately equal to the expected mass of analyte in the sample. Analysis of the spiked samples followed the same procedure. Spike recovery was calculated by the analyte mass recovered from the spiked sample, from the background sample and the actual mass of analyte added to the spiked sample. The QA acceptance criteria for spike recovery were generated from statistical control charts prepared and updated, for each analyte, as the experiment progressed. The second subsample was treated as a duplicate. The average value obtained from the duplicate analysis was used as the background level in calculation of spike recovery. The method blank was a reagent water sample taken through the entire analytical extraction and analysis procedure; this served to monitor for glassware contamination. Only a few anthracene surrogate samples were used in the initial stage of the experiment. Acetonitrile and standard solution were used in every HPLC run. The method detection limit (MDL) by HPLC was evaluated from the standard deviation of replicate analyses of spiked reagent water. The spike level was near, but above the anticipated detection limit. The MDL was then calculated by multiplying the standard deviation of the replicate measurements by the Student's t value with 99% confidence (or $t_{(n-1, \alpha=0.01)}$).

Data Reduction: Tracer flux was calculated from

$$F = \frac{WC}{d\Delta tA} \quad (3.1)$$

where F is the flux (ng/cm²-day), W is the weight of aqueous sample (g), d is the density of water (g/cm³), C is the concentration of the sample (ng/cm³), Δt is the period of time (day), and A is the exposed sediment or sand surface area (50 cm²).

3.1.1.6 Mass Transfer Coefficient at the Sediment-Water Interface

Gypsum-doublon wafers were used to quantify advective mass transfer coefficient (MTC) at the sediment-water interface (Birdwell and Thibodeaux, 2005; Santschi et al., 1991, 1983; Marshal et al., 1966). The following steps were used for the measurement and calculation.

Step1---Preparation of gypsum wafer devices (GWDs): Put ½ tablespoon of water in a cup or container, than add about ½ tablespoon of gypsum power into the water and mix with a spatula. Continue to add small amount of water or power with continuous mixing until continuous consistency is achieved. Apply the paste to the clean surface of a doublon. The gypsum layer thickness should be that of the doublon thickness. After about ½ hour, GWDs harden enough to be weighed and deployed.

Step2---Deployment of GWDs: Gently place GWDs at the interface between water and sediment in the diffusion chamber.

Step 3---Recovery of GWDs: Recover and reweigh GWDs after predetermined time in the diffusion chamber.

Step 4---Calculation of MTC: According to the definition, MTC can be calculated by the equation:

$$k_m = \frac{\Delta m}{\Delta t \cdot A \cdot C^*} \quad (3.2)$$

where Δm is the change in mass of gypsum (kg), Δt is the elapsed time (s), $A = \pi r^2$ is the surface area (m²), and C^* is the solubility of gypsum (0.0151 mol/l, at 25°C).

MTCs of PAHs can be calculated from the following equation (Deen, 1998; Thibodeaux, 1996):

$$k_{m1} = k_{m2} \sqrt{\frac{D_1}{D_2}} \quad (3.3)$$

where D_1 is the diffusivity of gypsum in water. The diffusivity of gypsum is $8.12 \times 10^{-10} \text{ m}^2/\text{s}$ at 25°C . D_2 is the diffusivity of a PAH (m^2/s). k_{m2} is the MTC of gypsum under identical conditions.

Sediment consolidation creates a trough region for sediment in the diffusion chamber. The trough depth has a significant influence on the MTC (Thibodeaux, 1996). Since the trough depth increases with time, the MTC is a function of time.

3.1.2 Mathematical Modeling

3.1.2.1 Governing Equations for Contaminant Transport in Capped Sediment

Based on mass balance in a differential volume element, the conservation equations for minor components may be written as (Deen, 1998; Choy and Reible, 1999)

$$\frac{\partial C_A'}{\partial t} = -\vec{\nabla} \cdot \vec{N}_A + R_{Vi} \quad (3.4)$$

where C_A' is the total concentration of species A, \vec{N}_A is the total flux of species A, and R_{Vi} is the source term, representing the net rate of formation of species A by reactions, per unit volume,

and the gradient operator or 'del' $\vec{\nabla} = i \frac{\partial}{\partial x} + j \frac{\partial}{\partial y} + k \frac{\partial}{\partial z}$.

The total flux of species A including advection and diffusion of mobile phase can be expressed as

$$\vec{N}_A = C_A \vec{v} - D_A \vec{\nabla} C_A \quad (3.5)$$

where C_A is the concentration of species A in the mobile phase, \vec{v} is the advection velocity, and D_A is the diffusivity of species A.

For a specific one-dimensional case where the reaction is a first-order degradation (Wammer and Peters, 2005), combining equations (3.4) and (3.5) yields the governing equation for the contaminant dynamics (Choy and Reible, 1999) as follows.

$$R_f \frac{\partial C_A}{\partial t} = D_{A(eff)} \frac{\partial^2 C_A}{\partial z^2} - v \frac{\partial C_A}{\partial z} - kC_A \quad (3.6)$$

where R_f is the retardation factor defined as a ratio of total concentration to mobile phase concentration of species A, $D_{A(eff)}$ is the effective diffusivity, and k is the first-order degradation rate coefficient.

Retardation Factor: For water-saturated sediment, the following equation can be developed from the definition of the retardation factor

$$R_f = \varepsilon + \rho_b K_d \quad (3.7)$$

where ε is the sediment porosity, ρ_b is the sediment bulk density (kg/m^3), and K_d is the partition coefficient (m^3/kg), defined as a ratio of the sediment loading to equilibrium aqueous concentration.

Diffusion in Porous Medium: The effective diffusivity in porous medium is usually a function of porosity and tortuosity. For such a porous medium as sediment, the following equation is used to calculate the effective diffusivity (Millington and Quirk, 1961; Thibodeaux, 1996)

$$D_e = D_w \varepsilon^{\frac{4}{3}} \quad (3.8)$$

where D_w is the diffusivity in water.

3.1.2.2 Initial and Boundary Conditions for Uncapped System

For the uncapped sediment, the general governing equation (3.6) is applied to the sediment layer with the following initial and boundary conditions.

$$\text{Initial condition: 1) } C_A(z, t)|_{t=0} = C_{A0}$$

$$\text{Boundary conditions: 1) } \left. \frac{\partial C_A}{\partial z} \right|_{z=0} = 0$$

$$2) D_{A(eff)} \left. \frac{\partial C_A}{\partial z} \right|_{z=b} + k_a C_A|_{z=b} = 0$$

where $k_a = \frac{q(k_m + v)}{q + k_m A}$, q is water flow rate (m³/s), A is the exposed sediment-water interface area (m²), v is advection velocity (m/s) and k_m is the mass transfer coefficient at the sediment-water interface (m/s).

The initial condition 1) is based on the assumption that the sediment is initially uniformly contaminated. The boundary condition 1) means that there is no downward contaminant flux at the bottom of the contaminated sediment ($z=0$, see Figure 3.3). The boundary condition 2) is from the mass balance at the sediment-water interface ($z=b$). Thus, the mass diffused from the sediment must be equal to the mass carried away by flushing of the overlying water, and it must also be equal to the mass transported through the benthic boundary layer.

$$-AD_{A(eff)} \left. \frac{\partial C_A}{\partial z} \right|_{z=b} + AvC_A|_{z=b} = qC_{Aw} = Ak_m(C_A|_{z=b} - C_{Aw}) + AvC_A|_{z=b} \quad (3.9)$$

where C_{Aw} is the background concentration in the overlying water. Solving the right equality for C_{Aw} , then substituting it into the left equality and rearranging yields the boundary condition 2).

3.1.2.3 Initial and Boundary Conditions for Capped System

For the capped system, equation (3.6) can be applied to both the cap and sediment layers (see Appendix B). The initial and boundary conditions are written as

$$\text{Initial conditions: 1) } C_{A1}(z, t)|_{t=0} = C_{A0}$$

$$2) C_{A2}(z, t)|_{t=0} = 0$$

$$\text{Boundary conditions: 1) } \left. \frac{\partial C_{A1}}{\partial z} \right|_{z=0} = 0 \text{ (} z=0, \text{ at the bottom of the chamber)}$$

$$2) C_{A1}(z, t)|_{z=a} = C_{A2}(z, t)|_{z=a}$$

($z=a$, at the sediment-cap interface)

$$3) D_{A(eff)1} \left. \frac{\partial C_{A1}}{\partial z} \right|_{z=a} = D_{A(eff)2} \left. \frac{\partial C_{A2}}{\partial z} \right|_{z=a}$$

$$4) D_{A(eff)2} \left. \frac{\partial C_{A2}}{\partial z} \right|_{z=b} + (k_a - v)C_{A2}|_{z=b} = 0$$

($z=b$, at the water-sediment/cap interface)

The coordinate system is given in Appendix B. The subscripts 1 and 2 refer to the sediment and cap respectively. Initial condition 1) means that the sediment is initially uniformly contaminated and initial condition 2) that the cap is initially free of contamination. Boundary conditions 1) and 4) here have the same meanings as the boundary conditions 1) and 2) for the uncapped system. The boundary conditions 2) and 3) state continuity of concentration and flux at the sediment-cap interface.

3.1.2.4 Numerical Method

It is difficult to find analytical solutions to the above models. There are several numerical methods such as explicit, fully implicit and Crank-Nicolson methods to solve the partial

differential equations. Here the fully implicit method is chosen, which has been shown to be totally unconditionally stable (Chapra, 2002; Chandra and Singh, 1994). The mathematical method and derivation is given in Appendix B, and computer (MATLAB) codes in Appendix C.

3.1.3 Results and Discussion

3.1.3.1 Sediment Consolidation

Consolidation is defined as the compaction of sediment under the weight of the overlying layers and self-weight. The contaminated sediments are usually fine grained and contain a large amount of water. When capping materials are placed on the contaminated sediments, they are often susceptible to consolidation. A digital caliper was used to measure the sediment consolidation. Figure 3.4 shows the U.L. sediment consolidation with time. The consolidation is very sharp in the beginning and approaches to a plateau after a month. The total consolidation depth is around 9 mm. A Langmuir-like expression is employed to fit the data. The equation (3.10) is the regression relationship between sediment consolidation and time.

$$z = 150 - \frac{1.1t}{1 + 0.11t} \quad (3.10)$$

where z is the coordinate of the sediment-water interface or sediment height (mm), and t is the time (day).

The pore water advection velocity due to sediment consolidation is the derivative of z with respect to t :

$$v = -\frac{dz}{dt} = \frac{1.1}{(1 + 0.11t)^2} \quad (3.11)$$

where t is the time (day), and v is the advection velocity (mm/day).

Based on the definition of sediment porosity, the equation below can be developed, which gives the porosity as a function of consolidation depth.

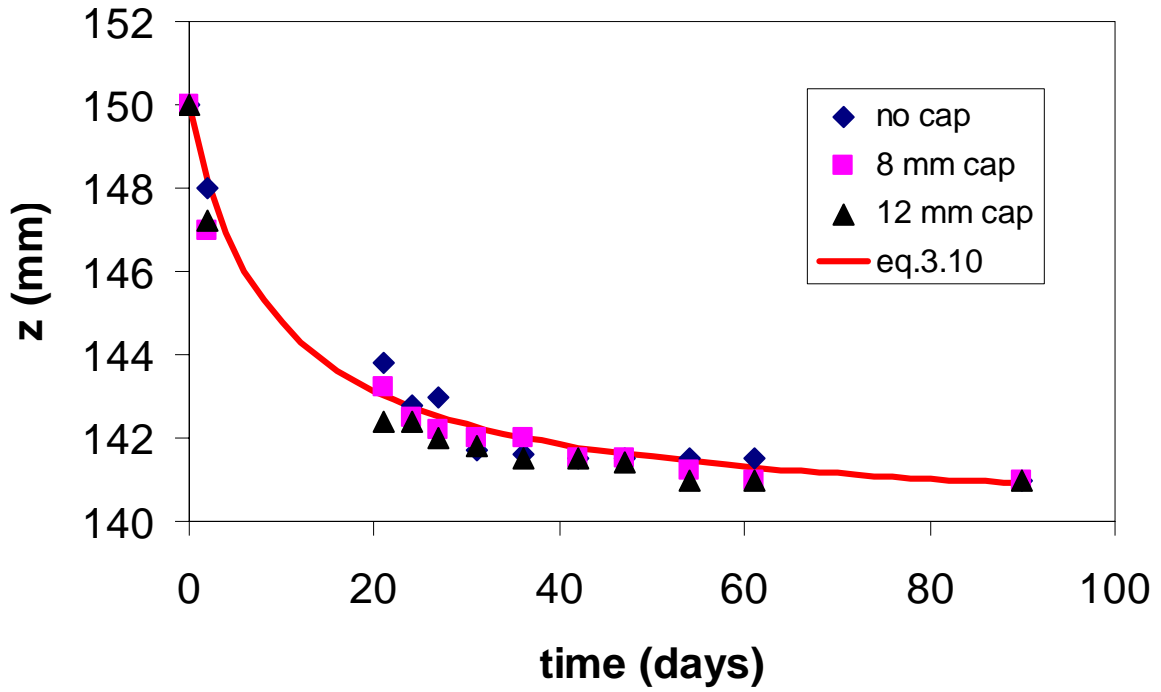


Figure 3.4 U.L. sediment consolidation with time.

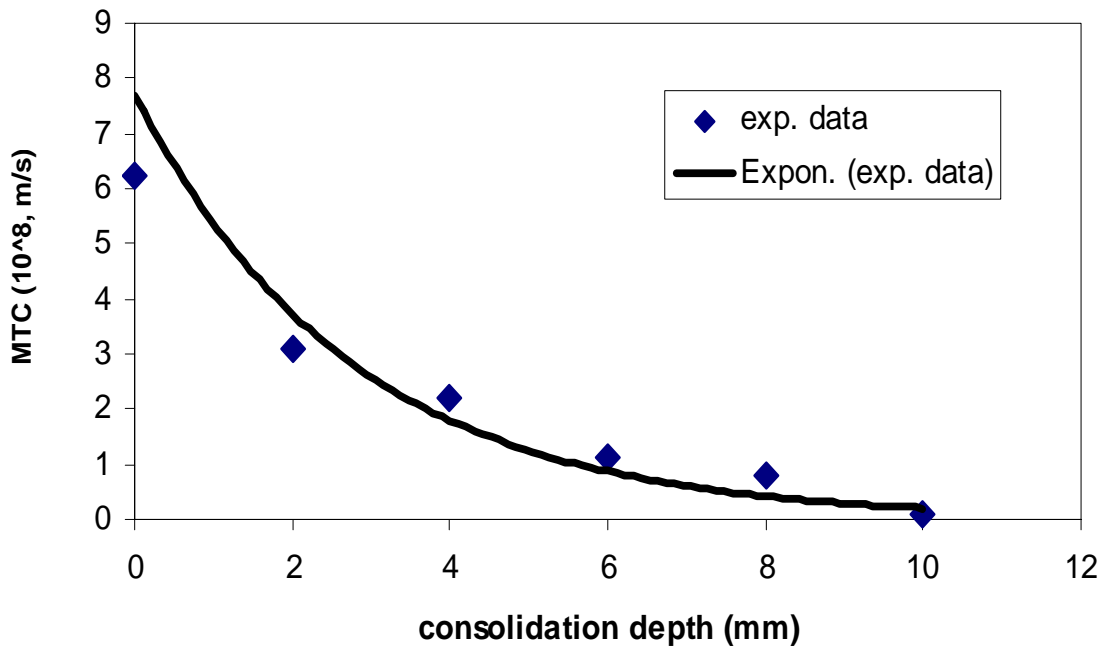


Figure 3.5 MTC of gypsum with depth.

$$\varepsilon = \varepsilon_0 + \frac{z}{H_0} - 1 \quad (z \geq 141\text{mm}, \quad d \leq 9\text{mm}, \quad H_0 = 150\text{mm}) \quad (3.12)$$

where ε , ε_0 are the porosity and initial porosity, and H_0 is the initial sediment height (150 mm).

3.1.3.2 Mass Transfer Coefficient at the Sediment-Water Interface

Gypsum wafer devices (GWDs) were employed to measure the MTC at different consolidation depth as described in 3.1.1.6. Figure 3.5 gives the experimental MTC results for gypsum. It shows that the MTC decreases with consolidation. In fact, sediment consolidation increases the depth within the small diffusion chamber, from which the concentration difference is derived. Usually the MTC is inversely proportional to the diffusion depth. This explains why the MTC decreases with consolidation in our experimental chambers.

By regression of the experimental data using Microsoft Excel (exponential trendline), the following equation was obtained.

$$k_{mg} = 8 \cdot 10^{-8} e^{-0.3633(150-z)} \quad (3.13)$$

where k_{mg} is the mass transfer coefficient of gypsum (m/s), and z is the height of sediment (mm) that is a function of time quantified by equation (3.10). Equation (3.3) can correct MTC of gypsum to those of PAHs.

3.1.3.3 Tracer Flux and Capping Effectiveness

Figures 3.6 to 3.8 are fluxes of DBF, phenanthrene and pyrene with time for capped and uncapped systems. The cap effectiveness is clearly shown, especially in the early stage of the experiment. For the uncapped situation, the initial flux is very large because of large contaminant concentration gradient at the sediment-water interface. With time, the concentration gradient decreases due to contaminant loss in the top of the sediment and leads to flux decrease. For the capped case, initial flux of contaminants is zero due to the clean sand cap. As contaminants move

Table 3.4 Other parameters used in the simulation

| | Sediment | Sand |
|---------------------------------------|--------------------------------|-------|
| Thickness (m) | 0.138 | 0.012 |
| Porosity (ϵ) | 0.69 | 0.5 |
| Bulk density (kg/m^3) | 725.5 | 1541 |
| Fractional organic carbon (%) | 5 | 0.001 |
| Mass transfer region (m^2) | $W \times L = 0.05 \times 0.1$ | |

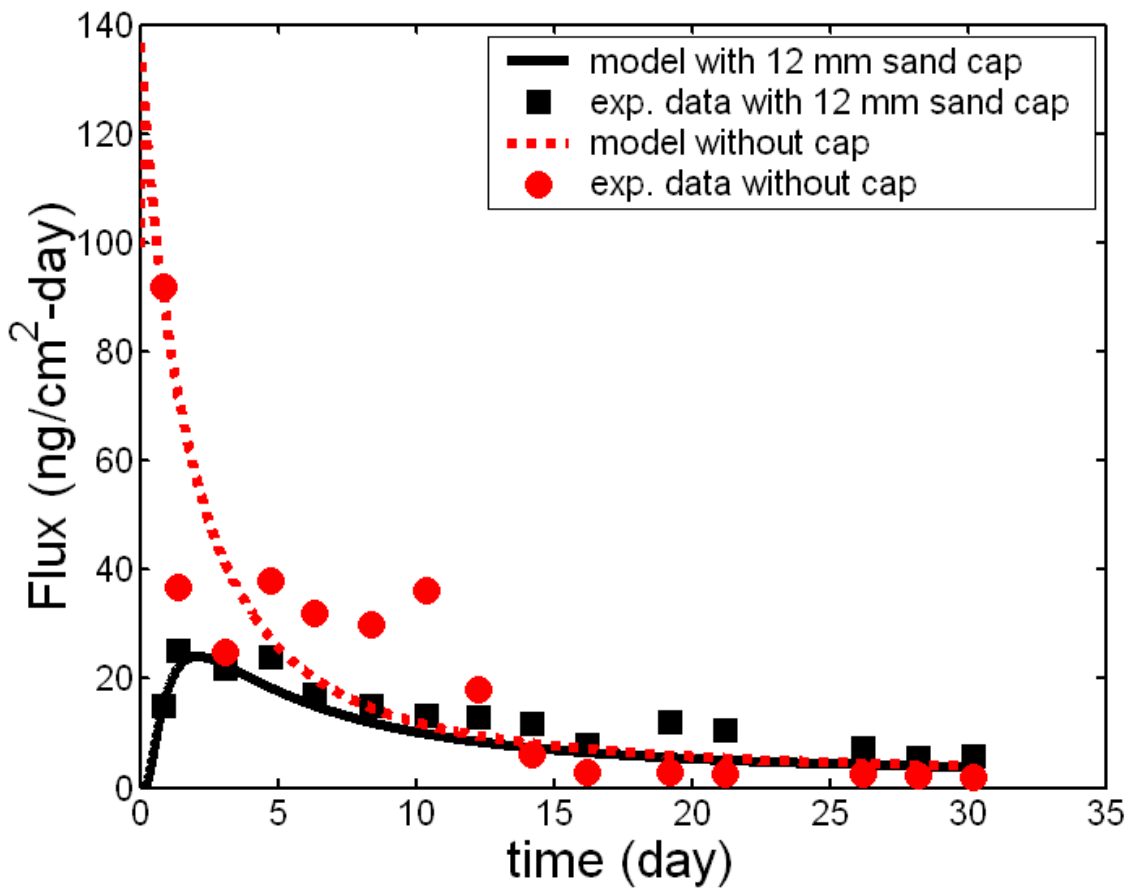


Figure 3.6 Flux of DBF with time.

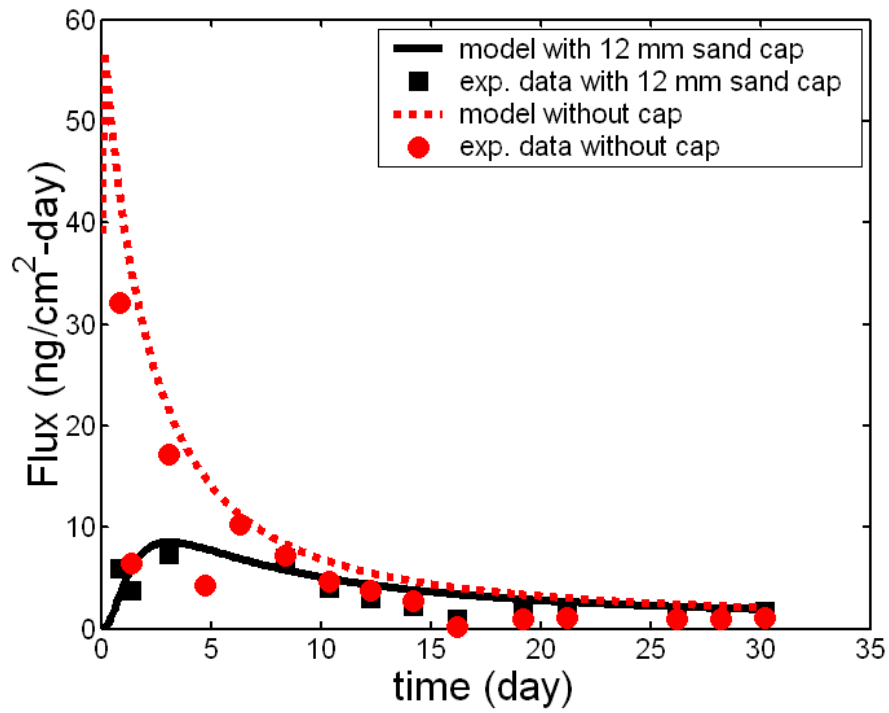


Figure 3.7 Flux of phenanthrene with time.

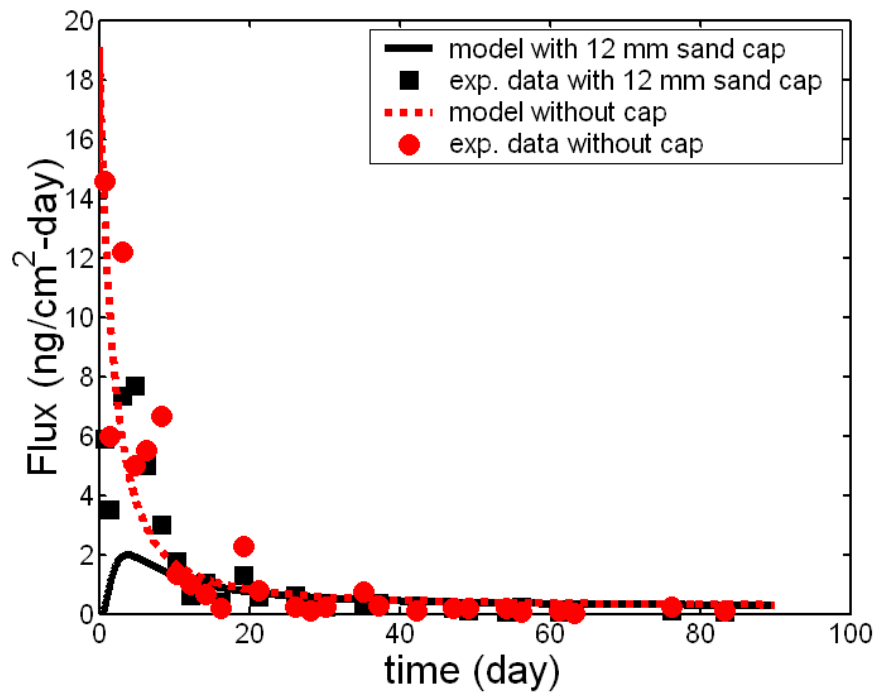


Figure 3.8 Flux of pyrene with time.

into the cap layer from contaminated sediment and finally saturate the sorption sites on the sand, breakthrough occurs and the flux increases with time. Theoretically flux from both capped and uncapped systems should be proportional to $t^{-1/2}$ (Formica et al., 1988). This has also been observed by the previous researchers (Thoma et al., 1993; Wang et al., 1991). The difference is that flux from the chamber with sediment consolidation falls more sharply with time than that without consolidation. This is because the MTC decreases with consolidation in the experimental chamber. Figures 3.6 to 3.8 also show that the model satisfactorily describes the experimental data. The parameters used in the simulation are from Tables 3.1 to 3.4. The concentration profiles in sediment/cap are summarized in Appendix D.

3.1.3.4 Model Applications

Effects of Sediment Consolidation on Contaminant Flux: Sediment consolidation is significant after the cap placement, especially during the initial stage. During this process, pore water is driven out. This may also enhance the migration of pollutants. Akram et al. (2005) and Rahbar (2003) suggested a model for contaminant flux in capped sediment under consolidation by coupling the Terzaghi consolidation theory and transport equations. Fox (2003) developed a numerical model for contaminant transport in consolidating sediments. This model does not consider the mass transfer resistance in the overlying water that is especially important for contaminant transport in capped sediments. Although some experimental methods have been developed to monitor and measure sediment consolidation (Galyin, 1996; Maus et al., 1973), there have been very few experimental studies verifying the consolidation effects on contaminant transport during the capping process.

The large strain consolidation theory has been used for analyzing consolidation of capped sediments (Cargill, 1985; Poindexter-Rolling, 1990). The computer models have been developed

such as PCDDF (Primary Consolidation and Desiccation of Dredged Fill) (Cargill, 1985), MOUND and CONSOL (Gibson and Cargill, 1981; Wong and Duncan, 1984). The MOUND and CONSO models were used to predict consolidation of three capped dredged material mounds in Long Island Sound (Silva et al. 1994). The results showed that the two models were reasonably accurate (Palermo et al., 1998). Basically the consolidation model and transport model can be coupled to simulate the effects of consolidation on the contaminant flux under field conditions.

Let us assume that the sediment consolidation follows the trend such as given by Palermo (Palermo, 1998), i.e., $s = 53t / (1 + 0.03t)$ where s is the settlement (mm) and t is the time (day). The area covered by the contaminated sediment is $180 \times 180 \text{ m}^2$. The depth of the contaminated sediment is 3 meters, the sand cap 0.5 meters and the overlying water 5 meters. The gypsum MTC and the river friction velocity are 0.592 mm/hr and 2.32 cm/s measured in the Mississippi River (Birdwell and Thibodeaux, 2005). The other parameters used in the simulation are from Tables 3.1 to 3.4. Figure 3.9 demonstrates that sand cap is effective in retarding phenanthrene transport even though the sediment consolidation would lead to an acceleration of this process. From Figure 3.10, we can see that sediment consolidation can shorten the breakthrough time and enhance the initial flux. In this case, it is obvious that consolidation has a profound influence on the cap design. The sediment consolidation data used in this example were from dredged sediment. For real capping projects, consolidation is not necessarily this large since contaminated sediments are usually consolidated before cap placement. Figure 3.10 here is only used to show the trend that sediment consolidation affects the breakthrough and initial flux of contaminants.

Effects of Degradation on Contaminant Flux: An active capping material contains a substance that can react with or degrade contaminants when they migrate through the cap. This

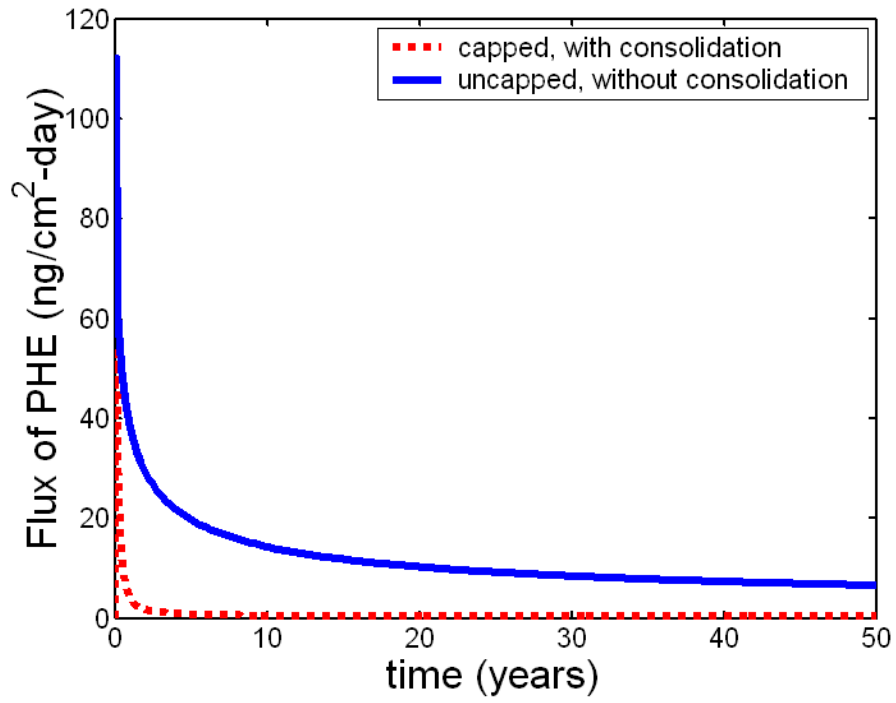


Figure 3.9 Simulation results for capped and uncapped systems under field conditions.

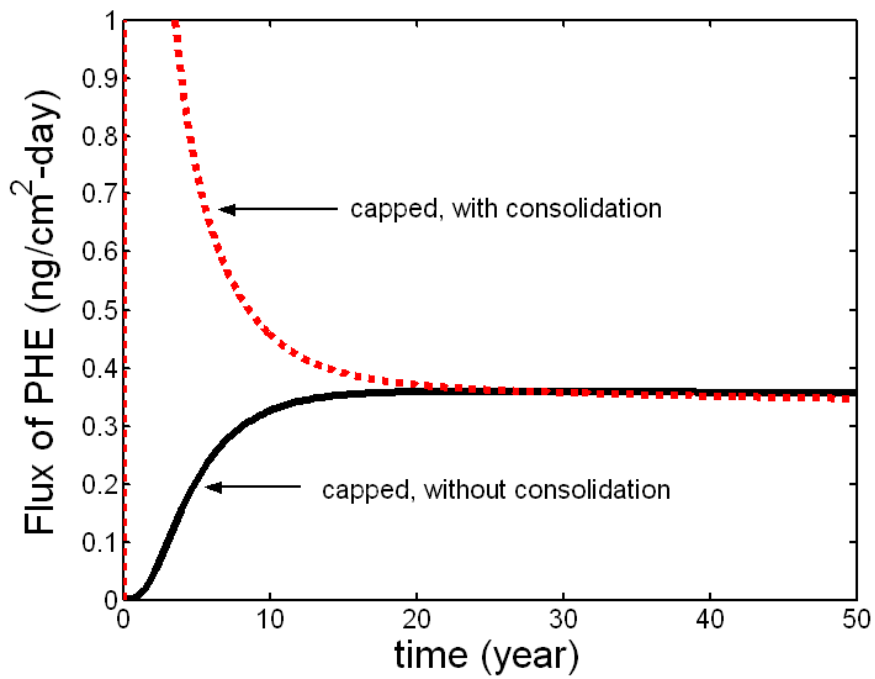


Figure 3.10 Simulation results for capped systems with and without consolidation under field conditions.

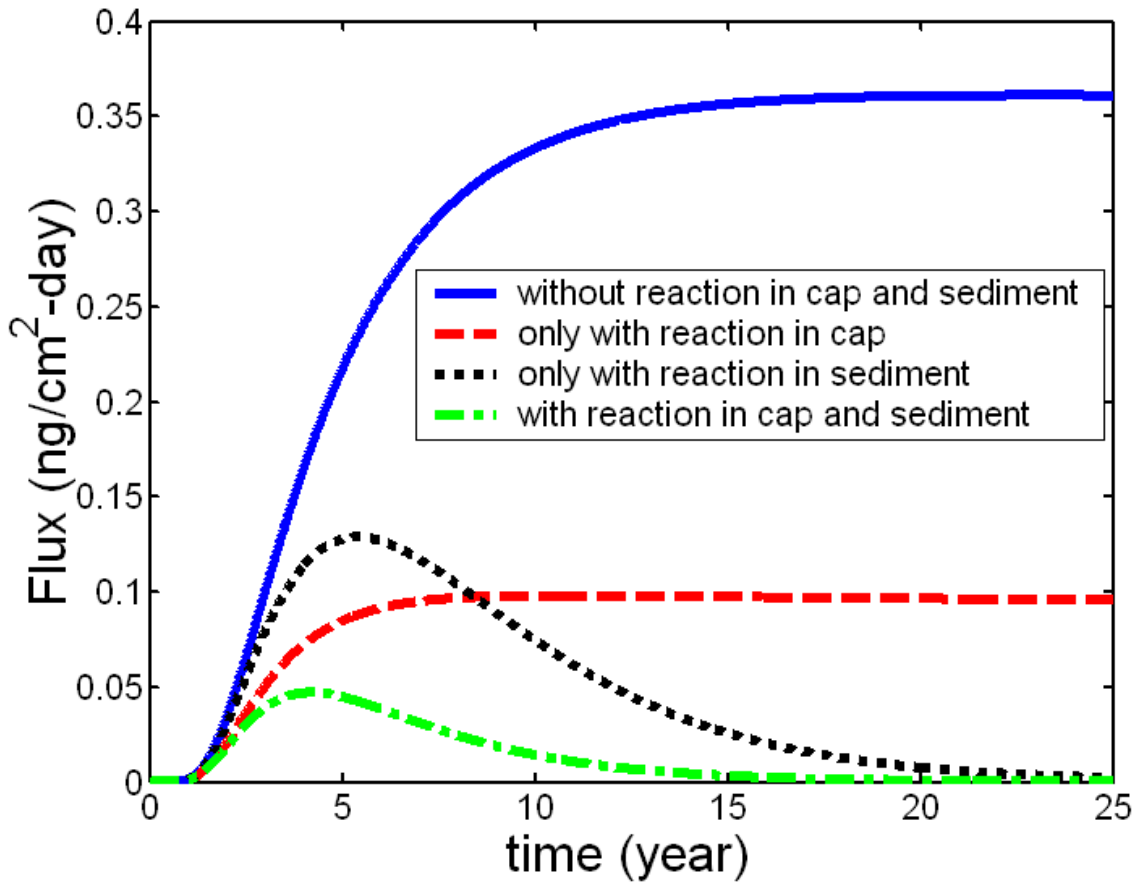


Figure 3.11 Comparison of PHE flux among (a) without reaction in both cap and sediment ($k_1 = k_2 = 0$), (b) only with reaction in cap ($k_1 = 0$ and $k_2 = 1 \times 10^{-8}$ 1/s), (c) only with reaction in sediment ($k_1 = 1 \times 10^{-8}$ 1/s and $k_2 = 0$), and (d) with reaction in both cap and sediment ($k_1 = k_2 = 1 \times 10^{-8}$ 1/s).

kind of cap can not only retard the release of the contaminants, but also reduce the contaminant flux. The contaminant flux from a reactive cap can be quantified by the diffusion-reaction model. For the above field conditions, if the first-order reaction rate constant in the cap (k_2) is 1×10^{-8} s⁻¹, the phenanthrene flux at steady state would be three times less than that without reaction in the cap (Figure 3.11(a) and (b)). Wammer and Peter (2005) reported that the first-order biodegradation rate constant of phenanthrene is around 1.12×10^{-4} s⁻¹ in aqueous systems (independent of bioavailability limitations from physical-chemical processes). Substituting this

rate constant into the model gives a zero PHE flux (about 10^{-81} ng/cm²-day at steady state). For a conventional sand cap, the PHE flux largely decreases if the degradation occurs in sediment (Figure 3.11(c)). Figure 3.11 (d) also demonstrates that PHE flux is minimal if there are reactions in both cap and sediment.

3.2 Studies of Metals Release and Oxygen Distribution in Anacostia River Sediment

Fluxes of eighteen metals were measured and fit with penetration theory. Oxygen probe and SOD chamber were used to measure the sediment oxygen demand (Nolan and Johnson, 1979; Rounds and Doyle, 1997; Shin, 1998). Redox potentials were measured with platinum electrode and calomel reference electrode (Patrick *et al.*). With the help of microelectrodes (Ferrell and Himmelblau, 1967; Revsbech *et al.*, 1980), oxygen profiles in sediment were measured, which were simulated by a steady state diffusion and zero-order reaction model. A good match was found between the oxygen profiles and redox potential data at different depths.

3.2.1 Experimental Materials and Methods

3.2.1.1 Sediment and Metal Concentrations

The sediment was from the Anacostia River (point 2, Washington, D. C) (<http://www.hsrb-ssw.org/ana-index.html>). In order to keep its original properties, it was only sieved by grid with 10mm×10mm openings for removal of twigs, leaves, etc. Then it was rotated on a tumbler for two weeks. The initial metal compositions are shown in Figure 3.12.

3.2.1.2 Sand and Metal Concentrations

The same kind of sand as described in 3.1.1.2 was used in the experiment. The initial concentrations of metals in the sand were measured; the metal zinc had the largest concentration (<1.7 mg/kg). Compared with the metal concentrations in sediment, they can be neglected.

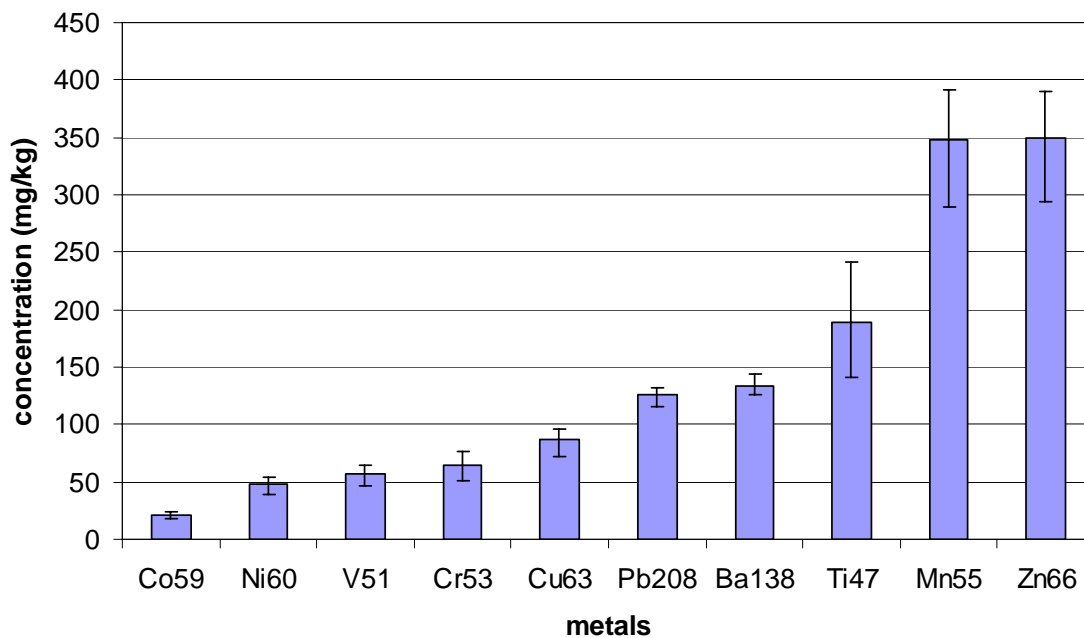
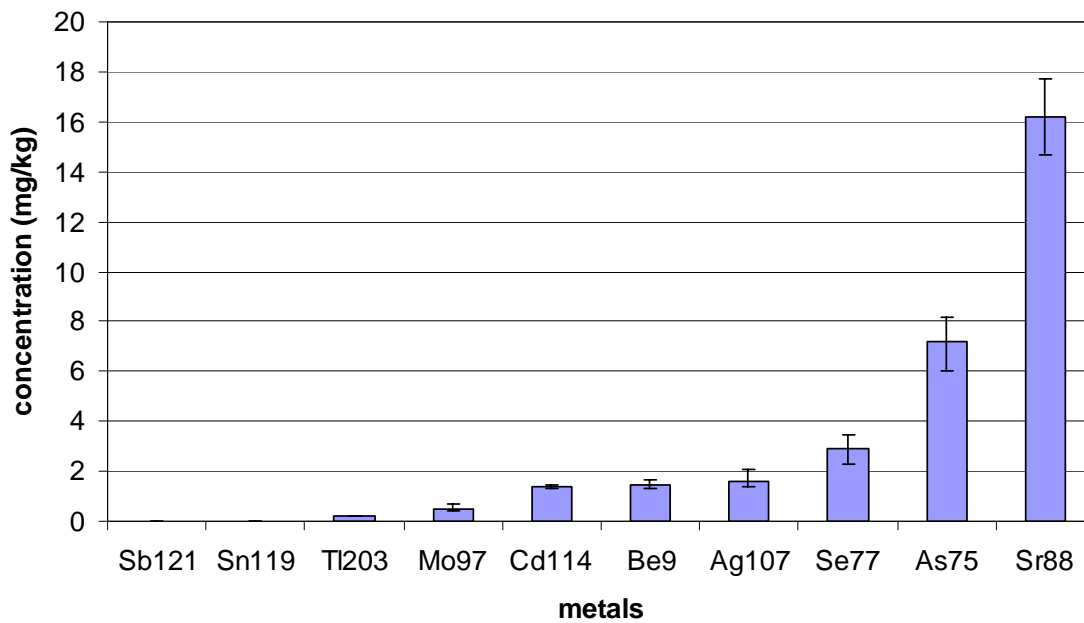


Figure 3.12 Concentrations of metals in the Anacostia River sediment (n=5, water=51.82%).

3.2.1.3 Metal Flux Measurement

The methodology described in 3.1.1.5 was used to measure the metal flux from capped and uncapped sediment. The experimental conditions are in Table 3.5. Metals in both water and sediment samples were measured with ICP-MS (Inductively Coupled Plasma Mass Spectrometry, PerkinElmer®). Water sample directly collected from the outlet of the diffusion chamber was split into two subsamples. One subsample was used to measure pH with pH meter (Model 214, Orion Research, Boston). The other was acidified by nitric acid to 3% for metal concentration measurement. The sediment samples were digested by nitric acid in the Multiwave 3000 oven (Anton Paar) according to the method MF100-T16 (EPA 3051) before ICP-MS analysis. The procedures are given in Appendix A.

Table 3.5 Conditions for the experiment with the Anacostia River sediment
Start of run: 11/06/2003 End of run: 02/06/2004

| Chamber | Cap material | Cap depth (mm) | Contaminated sediment depth (mm) | Average flow rate with stdev. (mL/hr) |
|---------|--------------|----------------|----------------------------------|---------------------------------------|
| A2 | No cap | 0 | 150 | 9.3±0.4 |
| B2 | No cap | 0 | 150 | 8.9±0.4 |
| C2 | Sand | 4 | 146 | 9.4±0.3 |
| D2 | Sand | 4 | 146 | 8.9±0.5 |
| E2 | Sand | 8 | 142 | 9.6±0.5 |
| F2 | Sand | 8 | 142 | 8.8±0.7 |

3.2.1.4 Sediment Oxygen Demand (SOD)

The SOD chamber (Figure 3.13) is a cylinder ($D \times H = 145 \times 1200$ mm²) of plexiglass (Shin, 1998). The top plate of the cylinder is equipped with a slow stirrer in order to keep uniform the oxygen concentration in the water layer. An oxygen probe (YSI Model 55) was used to monitor

the dissolved oxygen concentration with time. Then the slope of the linear best-fit part of the oxygen depletion vs. time line was used to calculate SOD (Nolan and Johnson, 1979; Rounds and Doyle, 1997) by the following equation:

$$SOD = \frac{s \cdot V}{A} \quad (3.14)$$

where s is the slope determined through linear regression, V is the volume of water, and A is the cross section area of the chamber.

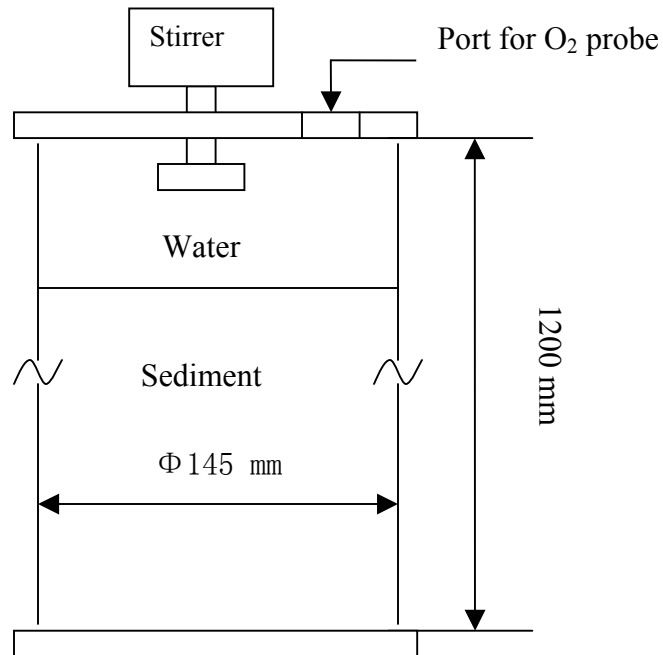


Figure 3.13 Schematic of SOD chamber.

3.2.1.5 Oxygen and Redox Potential in Sediment/Cap

Microelectrode (Diamond General, product #737 GC) was used to determine the oxygen concentration in water, sand and sediment. The absolute value of oxygen concentration (mg/L) in water was measured with an oxygen probe (YSI Model 55) at the same condition. Redox Potential was measured with platinum electrodes and calomel reference electrodes (Corning).

3.2.2 Results and Discussion

3.2.2.1 pH

pH values of aqueous samples were measured during the experiment. Figure 3.14 illustrates that pH of water increased slightly after it passed the chambers.

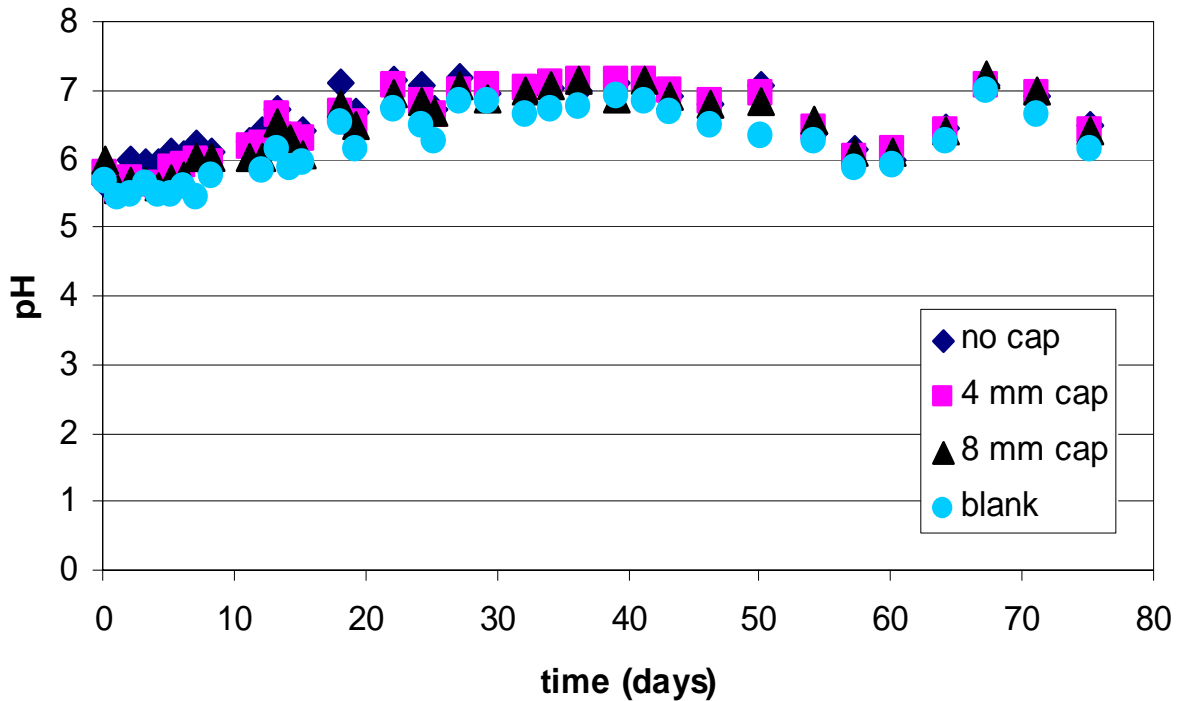


Figure 3.14 pH with time.

3.2.2.2 Metal Flux

Fluxes of eighteen metals from the Anacostia River sediment and two capped systems (sand thickness: 4 mm and 8 mm) were determined, and the data showed that cap decreased the metals flux. Penetration theory (P.T.) suggested by Thibodeaux (1996) (see Appendix B) was employed to fit the metal flux data. Figure 3.15 shows flux of Sr 88 for both capped and uncapped systems. Fluxes of other metals can be found in Appendix D.

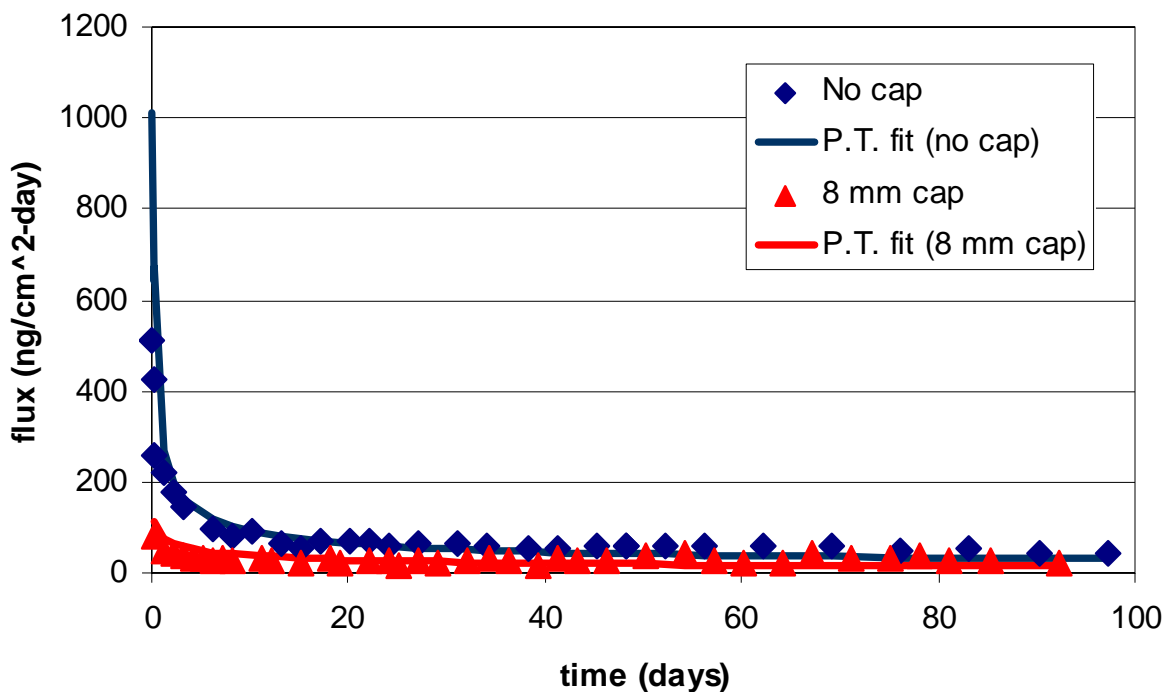


Figure 3.15 Flux of Sr 88 from the A.R. sediment with and without cap.

3.2.2.3 Metal Concentration Profiles in Sediment/Cap

For almost all the metals studied, there was no obvious decreasing trend of concentration at the top of sediment after 92 days of the experiment. This meant that three months was not long enough for metal depletion. The concentration profiles of metals can be found in Appendix D.

3.2.2.4 Oxygen Distribution in Sediment/Cap

SOD measured for the A.R. sediment was 290.7 mg/m²-day (n=3, Stedv=53.8) at 22.3 °C. Figures 3.16 to 3.18 show measured oxygen profiles, and Figure 3.19 is the redox potential meter reading (Ec, using a calomel reference electrode filled with a saturated KCl solution) with time at different depth. The Ec can be easily adjusted to Eh by adding 245 mV; Eh is the meter reading obtained by using a standard hydrogen electrode (SHE) (Patrick et al., 1996). By comparison, redox potentials match oxygen profiles very well.

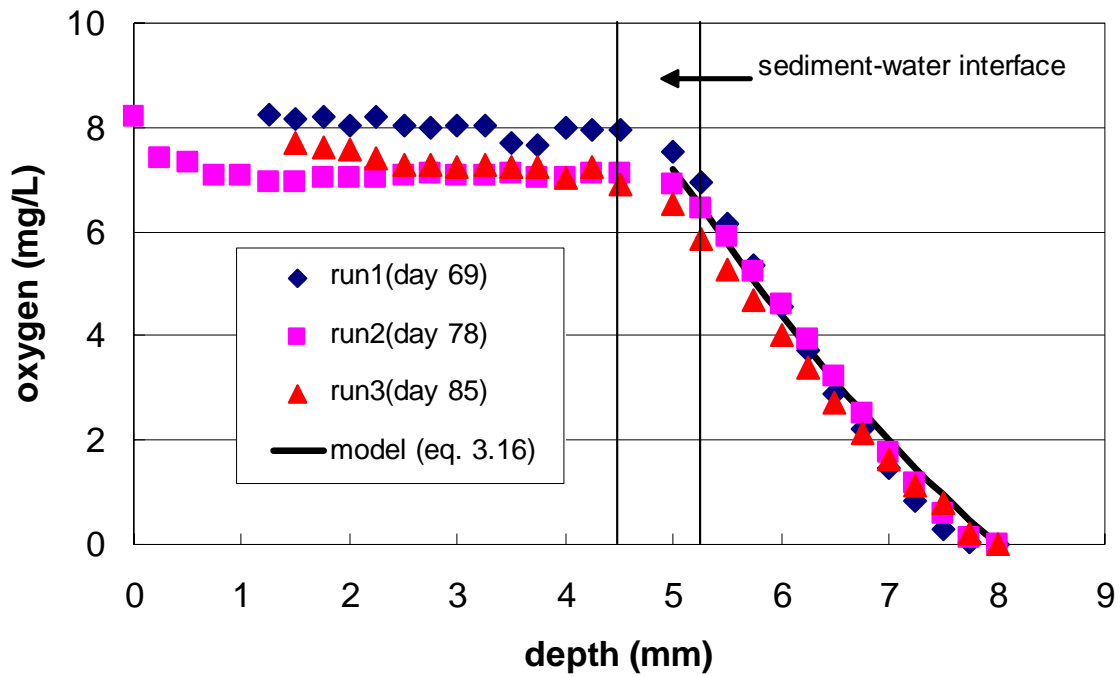


Figure 3.16 Oxygen profile in uncapped A.R. sediment (22.2 °C).

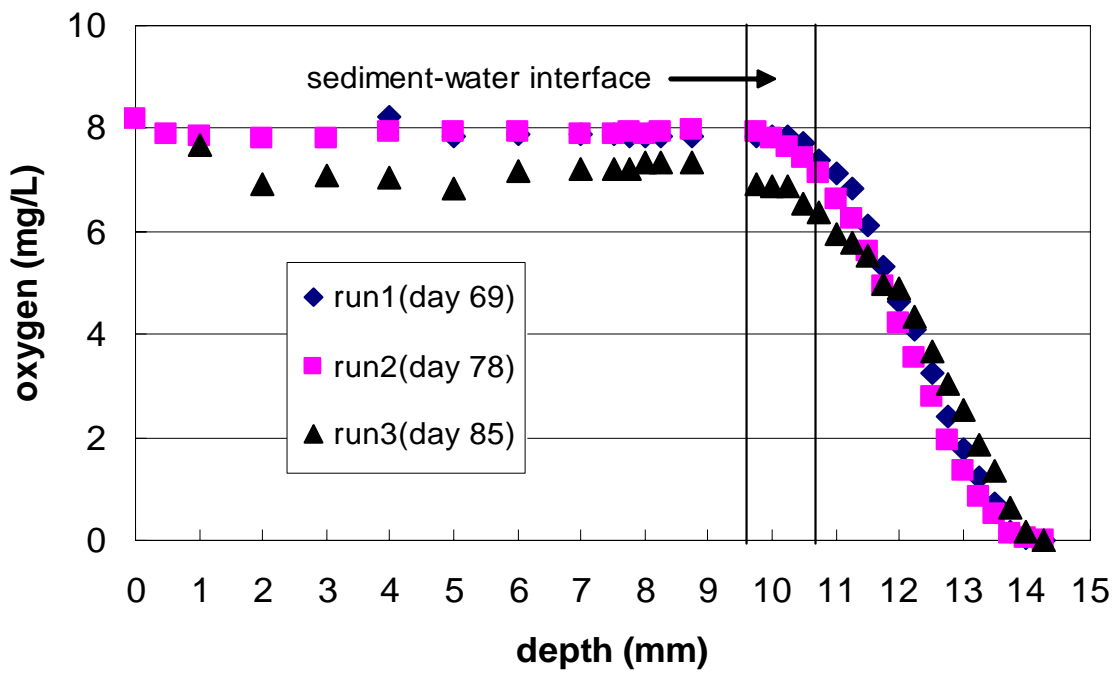


Figure 3.17 Oxygen profile in capped A.R. sediment (4 mm sand, 22.2 °C).

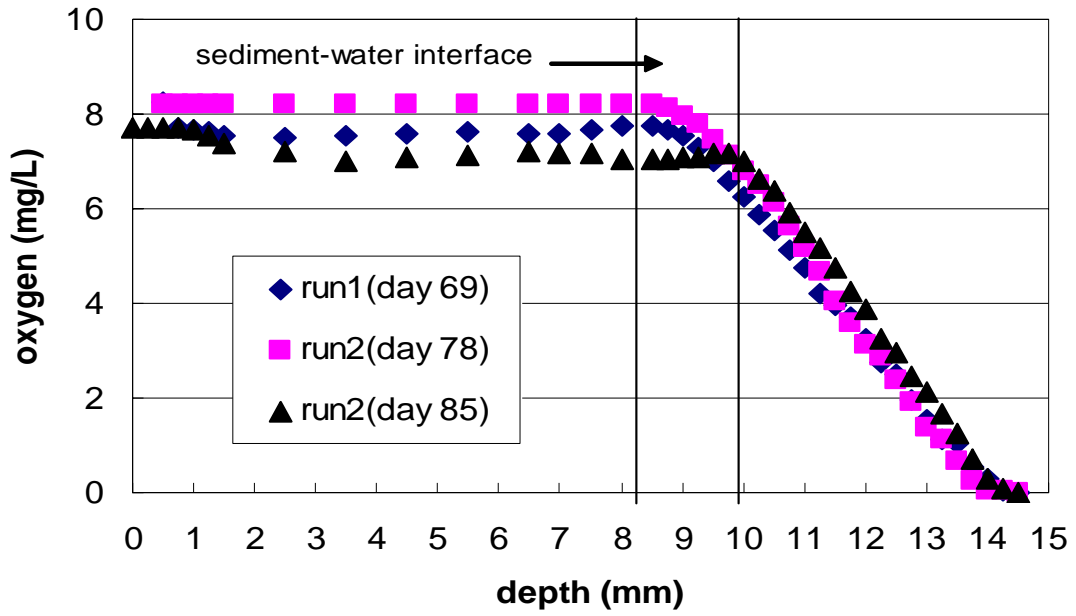


Figure 3.18 Oxygen profile in capped A.R. sediment (8 mm sand, 22.2 °C).

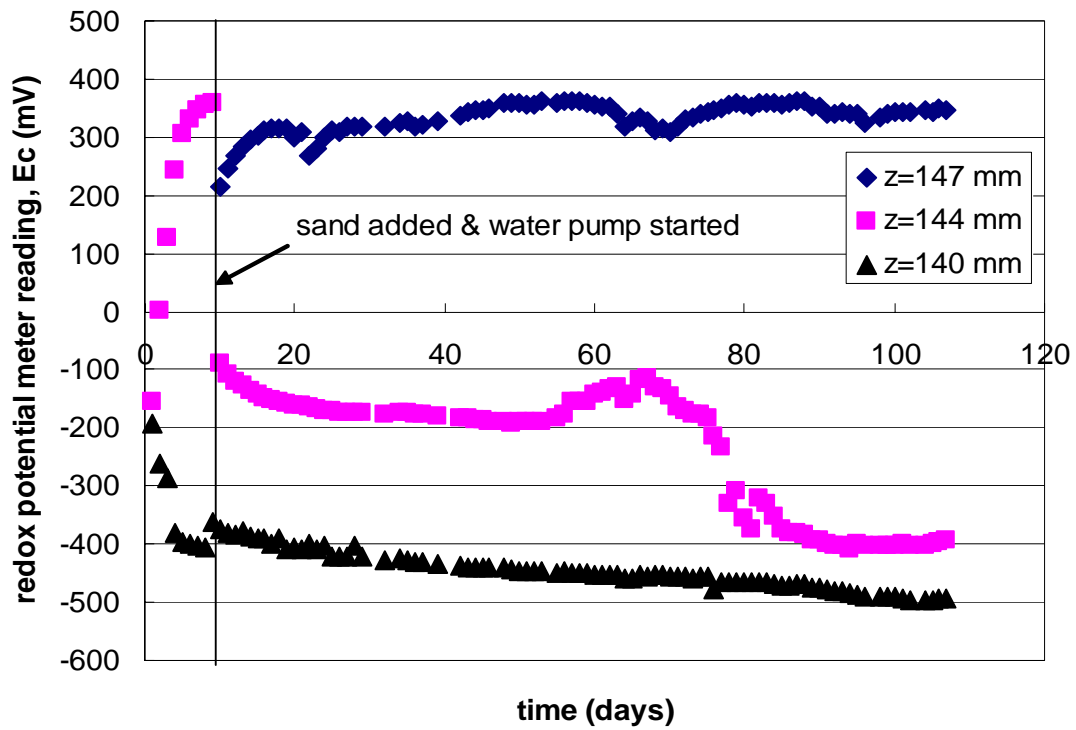


Figure 3.19 Redox potential with time at different depth (4 mm sand cap).

Oxygen profiles were measured after the experiment had been run for more than two months. The data from the three measurements (Figures 3.16 to 3.18) showed that oxygen diffusion reached steady state. Bouldin (1968) assumed that the consumption of oxygen is zero-order and constant in sediment (Di Toro, 2001). Considering our experimental results, we suggest the following model:

$$D_e \frac{d^2 C_{O_2}}{dx^2} - k = 0 \quad (3.15)$$

Boundary conditions: 1) $-D_e \frac{dC_{O_2}}{dx} \Big|_{x=0} = SOD$

$x=0$, at the interface between water and sediment

2) $C_{O_2} \Big|_{x=x_0=3mm} = 0$

where x is the depth below the sediment-water interface, D_e is the effective diffusivity of oxygen in pore water (m^2/s) that can be calculated by oxygen diffusivity in water (Ferrel and Himmelblau, 1967) and porosity, C_{O_2} is the oxygen concentration (kg/m^3), k is the zero-order consumption rate of oxygen ($kg/s-m^3$), and x_0 is the depth of the aerobic zone, below which the oxygen concentration is zero.

The solution to the above equation is

$$C(z, k) = \frac{k}{2D_e}(x^2 - x_0^2) + \frac{SOD}{D_e}(x_0 - x) \quad (3.16)$$

The optimal value of k (around $4.6 \times 10^{-7} \text{ kg/s-m}^3$) was obtained by minimizing the summation of the square residuals between model and experimental data. The model fits the experimental data well (Figure 3.16).

3.3 Summary

Both model and experimental results demonstrate that a sand cap can effectively reduce the maximum flux of contaminants (organics and metals) from sediments into overlying water.

Advection due to sediment consolidation can largely enhance contaminant flux during the initial stage after the cap placement. The diffusion-reaction model was used to simulate the effects of degradation on contaminant release in capped sediment. The simulation results showed that active capping materials could significantly decrease contaminant flux in the long run. Active capping offers good prospects and should be further investigated.

SOD and oxygen profiles in the A.R. sediment were measured. The diffusion and zero-order consumption model at steady state was used to fit the oxygen profile in uncapped A. R. sediment. The optical zero-order consumption rate of oxygen was around 4.6×10^{-7} kg/s-m³. Both redox potentials and oxygen profiles showed anaerobic conditions in capped sediment. As mentioned before, gas bubbles form in contaminated sediments under anaerobic circumstance. The impacts of gas bubble ebullition on contaminant transport and sediment/cap integrity are discussed in the next chapter.

CHAPTER 4. BUBBLE-FACILITATED CONTAMINANT TRANSPORT IN CAPPED SEDIMENT

In this chapter, experimental and modeling work on contaminant transport due to gas ebullition in capped and uncapped sediment is presented. A separate experiment was performed to measure methane-water Henry's law constants for three PAHs and their temperature dependence between 5 °C and 30 °C. The experimental results and some correlations are also included in this chapter.

4.1 Sediment and Contaminant Release during Gas Ebullition

A bubble column was used to investigate phenanthrene flux from sediment while injecting methane gas at the bottom of the column. A hexane layer was placed at the top to collect the material carried by the methane gas bubbles, a process known as solvent sublation (Smith et al., 1996; Smith and Valsaraj, 1997). Multiple samples from the water/slurry and hexane were taken during the experimental run. These samples provided contaminant distribution with time in the aqueous phase, hexane and suspended sediment particles. At the end of the experiment, the sediment in the column was cored. Several of the sediment cores were scanned with CT equipment in order to determine the void space distribution within the sediment and sand. Finally, all the cores were sliced and analyzed for phenanthrene. Contaminant mass balances were made to assure that the results are reasonable.

4.1.1 Experimental Materials and Methods

4.1.1.1 Materials

Tracer: Phenanthrene of 98% purity as a tracer in the experiment was purchased from Aldrich Chemicals, Milwaukee, WI.

Sand: The capping material was sand (QUIKRETE[®]) as used in the capping project.

Water Solution of Phenanthrene: About 0.03 grams of phenanthrene and 3.3 L of de-ionized water were added into a 3.5 L glass jar. The jar was capped and sealed. It was then rotated on the tumbler overnight. The solution was filtered through a glass filter (Whatman, Maidstone, England) to remove solid crystals of phenanthrene. The water solution was analyzed with HPLC for phenanthrene concentration before it was added into the column.

Sediment Slurry: A predetermined amount of sediment was added into the water solution of phenanthrene in a 3.5 L glass jar. Different amounts of sediment were used according to the desired water to dry sediment ratios. The jar was rotated on the tumbler overnight before use. The slurry samples were filtered through a 0.7 μ m glass fiber filter (Whatman) to remove the soil particles prior to HPLC analysis.

Sediment: The sediment used was from the Anacostia River (point 2, Washington, D. C.). The phenanthrene concentration in the original sediment was 0.68 mg/kg (n=5, Stdev.=0.06). The sediment was sieved using a grid with 10 \times 10mm² openings. The sieved sediment was inoculated with phenanthrene using a procedure described already in the literature (Thomas, 1994). Table 4.1 lists the initial phenanthrene concentrations in the sediment.

Table 4.1 Initial phenanthrene loading in sediment

| Jar # | Loading (mg/kg) | Measured (mg/kg) (n=5 each) | | Water (w %) (n=5 each) | |
|-------|-----------------|--------------------------------|--------|---------------------------|--------|
| | | Mean | Stdev. | Mean | Stdev. |
| 1 | 99.2 | 100.1 | 3.0 | 49.6 | 0.1 |
| 2 | 97.0 | 99.6 | 0.9 | 48.6 | 0.1 |
| 3 | 98.4 | 102.4 | 3.3 | 47.6 | 0.2 |

4.1.1.2 Setup

Figure 4.1 is a schematic of the basic experimental setup. The bubble column is a glass column with inside diameter of 8 cm and a total height 74 cm. The gas flow meter (65-mm PTFE

with valve) and volumetric flow controller (0.01 to 1 mL/min) were purchased from Cole-Parmer, Vernon Hills, Illinois.

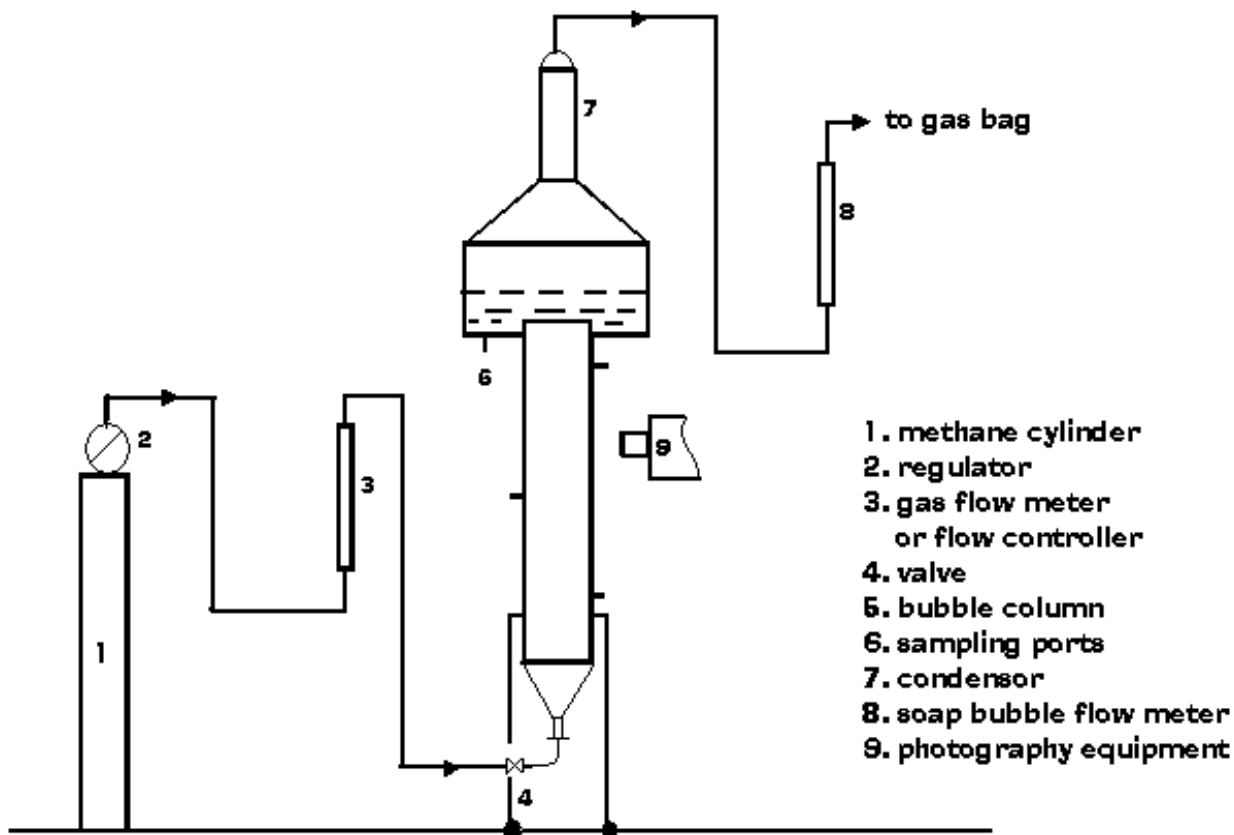


Figure 4.1 Setup for the bubble column experiment.

4.1.1.3 Experimental Operation and Conditions

Experiments with (i) water solution (ii) sediment slurry and (iii) sediment were conducted. Water solution or sediment slurry could be directly added into the column. Then hexane was gently added on the top of the water solution or sediment slurry. The purpose of the hexane was to capture the phenanthrene carried by methane gas bubbles exiting the water/slurry column. For the experiments with sediment, contaminated sediment was first added into the

bottom of the column. The thickness of the sediment was usually around 20 cm. Then sand (for the capping experiment) and water was slowly and carefully added into the column to minimize the mixing or sediment suspension. The height of the water was around 52 cm. Finally hexane was added on the top of the water. The thickness of the hexane was about 5 cm (about 380 grams) for a methane flow rate of 0.01 mL/min and capping experiments, and 10 cm (about 760 grams) for the other experiments. A cooling condenser was set up and the coolant water pump started to assure that no hexane evaporative loss occurred. Methane gas from a cylinder was then introduced at the base of the bubble column through a sparger with an estimated mean pore size of 1.7×10^{-6} m and a diameter 0.026 m. The gauge pressure of the gas was 100 Kpa for all the experiments. Tables 4.2 to 4.4 list the conditions of the experiments with water solution, sediment slurry and sediment respectively.

4.1.1.4 Sample Collection and Measurements

Multiple samples were collected from the water/slurry and hexane layers at several time intervals. The samples from hexane layer were collected into 2 mL flasks. The hexane was concentrated using a nitrogen blow-down and solvent-exchanged with acetonitrile (the procedure

Table 4.2 Conditions for the experiments with water solution

| Gas flow rate, mL/min (L/m ² -day) | | | Water solution | | Hexane (g) |
|---|--------|---|----------------|--------------------------------------|------------|
| Mean | Stdev. | N | Weight (g) | Initial concentration C_{w0} (ppb) | |
| 3.24 (929) | 0.48 | 5 | 3241.7 | 914.2 | 514.4 |
| 4.73 (1356) | 0.31 | 5 | 3250.6 | 865.7 | 487.0 |
| 6.26 (1794) | 0.03 | 6 | 3260.0 | 949.3 | 487.4 |
| 9.23 (2646) | 2.11 | 6 | 3261.0 | 903.8 | 500.6 |
| 11.81 (3385) | 2.85 | 6 | 3259.6 | 986.1 | 490.7 |

Table 4.3 Conditions for the experiments with sediment slurry

| Water to dry sediment ratios (w/w) (TSS, g/L) | | Gas flow rate, mL/min (L/m ² -day) | | | C _{w0} (ppb) | Slurry (g) | Hexane (g) |
|---|-------------------|---|--------|---|-----------------------|------------|------------|
| | | Mean | Stdev. | N | | | |
| 500:1 | 498.7:1(2 g/L) | 3.62 (1038) | 0.08 | 5 | 1009.5 | 3288.7 | 486 |
| | 498.6:1(2 g/L) | 6.59 (1889) | 0.15 | 5 | 1037.9 | 3264.3 | 481.8 |
| | 499.0:1(2 g/L) | 10.88 (3118) | 0.09 | 5 | 1001.6 | 3264.3 | 487.6 |
| 100:1 | 99.8:1(9.98 g/L) | 3.39 (972) | 0.05 | 5 | 962.0 | 3284.4 | 509.8 |
| | 99.7:1(9.99 g/L) | 6.52 (1869) | 0.31 | 6 | 1035.6 | 3290.5 | 480.1 |
| | 100.0:1(9.96 g/L) | 10.79 (3093) | 0.92 | 5 | 971.9 | 3240.8 | 503.3 |
| 50:1 | 50.0:1(19.85 g/L) | 3.41 (977) | 0.37 | 5 | 991.5 | 3321.7 | 466.6 |
| | 49.6:1(18.45 g/L) | 6.89 (1975) | 1.06 | 5 | 997.1 | 3318.3 | 496.2 |
| | 50.0:1(19.85 g/L) | 10.16 (2912) | 0.68 | 5 | 897.6 | 3304.1 | 485.1 |

Table 4.4 Condition for the experiments with sediment

| Cases | Gas flow rate, mL/min (L/m ² -day) | | | Sediment | | | DI water (g) | Hexane (g) |
|---|---|------------|----|------------|-------------|-------------------------------|--------------|------------|
| | Mean | Stdev. | N | Weight (g) | Height (cm) | Initial loading (mg/kg) (N=5) | | |
| Without cap and consolidation | 6.85 (1963) | 0.79 | 12 | 1140 | 20.2 | 100.1 | 2473.4 | 749.3 |
| | 1.07 (307) | 0.33 | 11 | 1188 | 20 | 99.6 | 2489.6 | 760.8 |
| | 0.01 (2.87) | Controller | | 1118 | 20 | 99.6 | 2511.1 | 382.6 |
| Without cap with 15 days' consolidation | 0.64 (183) | 0.12 | 13 | 1128 | 20 | 100.1 | 2489.6 | 761.2 |
| 2 cm sand cap | 0.77 (221) | 0.26 | 13 | 1159 | 20 | 102.4 | 2431.3 | 381.9 |

described in Appendix A), prior to HPLC analysis. HPLC analysis was conducted as set forth in the US EPA Standard Method 8270 (APHA/AWWA/WEF, 1991). The water samples were collected from the sampling ports in 2 mL vials and directly injected into the HPLC. Sediment slurry samples were collected using a syringe barrel and immediately filtered through a 0.7 μm glass fiber filter (Whatman) to remove the sediment particles. The experimental results showed that phenanthrene sorption to the filter was significant. Extensive tests were done to determine the phenanthrene fraction lost at different water to dry sediment ratios and phenanthrene aqueous concentrations. Analysis of these tests resulted in a factor to account for the fraction lost to the filter (Appendix E). The samples from three different heights of the column (bottom, middle and top) at the same time were analyzed. No significant difference was observed. This meant that the water/slurry was well mixed by the bubble movement. Total suspended soil (TSS) was measured by filtration of 4 mL sediment slurry. The data at several time intervals gave the variation of TSS with time.

After the experiment reached a steady state, the hexane and the slurry layers were drained from the column and sediment was cored with a transparent plastic tube ($D=30$ mm). One end of the plastic tube was machined to a thin edge. It was pushed through the sediment until it reached the sparger at the bottom. A soft tube was utilized to connect the top end of the tube to a self-made piston-cylinder vacuum system. The vacuum provided a suction pressure to keep the sediment sample in the tube. At this point the frit was unscrewed and removed; the tube was capped and sealed. A Dremel[®] tool was employed to remove the top part of the tube from the top end of the sediment core; and the top end of the core was also capped and sealed.

All CT scanning of the sediment and cap was performed at the High-Resolution X-ray CT Facility at the University of Texas at Austin (UTCT). The CT equipment used was a custom-

made CT unit manufactured by Bio-Imaging Research (BIR), Inc. (<http://www.bio-imaging.com/>). The X-ray source is a 200 kV FeinFocus model FXE 200.20, which is capable of a $<10\ \mu\text{m}$ focal spot size. The detector system is an image intensifier from which data are captured and digitized by a CCD 1024×1024 camera. All scans were done with X-ray peak energy at 150 kV and current between 0.21 and 0.25 mA. Each rotation consisted of 1000 angular positions (i.e., views), with an acquisition time of 0.133 s per view. Data for multiple slices was acquired during a single specimen rotation by utilizing data off the true horizontal plane used for standard tomography. A slice-based reconstruction algorithm is used to produce one 16-bit TIFF image for each slice. Each slice has an inter-pixel spacing of 0.03271 mm and the inter-slice spacing was 0.03675 mm.

The 16-bit TIFF images were loaded into BLOB3D, an IDL (Research Systems Inc., Boulder, Colorado) – based program which was designed for processing three-dimensional CT data sets and extracting information concerning features or objects within the data volume. It is designed for efficient and rigorous definition, separation, and measurement of hundreds to tens of thousands of distinct and irregular objects from a data volume comprising tens to hundreds of megabytes. In this work, BLOB3D was used to uniquely separate, identify, and characterize each individual ‘macro-void’ within the sediment or cap. Note that the resolution of the CT system is insufficient to uniquely identify the individual grains and void spaces that here we are using the word ‘void’ to identify a subregion with the system that has a significantly different density than the surrounding material. Output from BLOB3D included the size, and surface area of each individual void within the imaged subsection of the core. In order to make comparisons, a control sample was prepared. 20 cm sediment was placed into a glass cylinder and kept still for

20 days without methane going though. The sediment was cored using the same transparent plastic tube and scanned with CT equipment.

The sediment cores were then sliced to determine the concentration profiles. Sections were obtained by placing the core on a post. The plastic tube was scaled and lowered 2 mm each section. A section was cut from the top of the extruded core with knife and spatula (Thoma et al., 1993). Each section was split into two samples, one for moisture measurement and the other for contaminant analysis.

4.1.2 Results and Discussion

4.1.2.0 Determination of k_1 for Water Solution and Sediment Slurry

For the column experiment with water solution or sediment slurry, there are two compartments – water solution/slurry and hexane. Gas bubbles take contaminants from the water solution/slurry by partitioning process, and release them as they transit the hexane layer. The other major transport pathway is the water entrainment in hexane with the bubble (Valsaraj, 1995a; Smith, 1996). The contaminant flux associated with bubble-wake entrainment at the aqueous-organic solvent interface can be expressed as

$$F_{bw} = \pi r_c^2 k_1 \left(C_w - \frac{C_o}{K_{mw}} \right) \quad (4.1)$$

where F_{bw} is the solute (PHE) flux from the aqueous into organic phases (hexane) ($\text{kg}/\text{m}^2\text{-s}$), r_c is the radius of the column, k_1 is the mass transfer coefficient for solute transport between the organic and aqueous phases (m/s), C_w is the solute concentration in the aqueous phase (kg/m^3), C_o is the solute concentration in the organic solvent layer (kg/m^3), K_{mw} is the distribution coefficient for solute between the organic solvent and aqueous phases (dimensionless). Since the distribution coefficient of PHE between hexane and water is very large, the PHE flux caused by

methane bubble-wake entrainment in this experiment can be estimated by $\pi r_c^2 k_1 C_w$. The mass transfer coefficient k_1 is one of the key parameters in the modeling work (4.3.2.1). In order to determine the k_1 , the experiments with PHE water solution and sediment slurry were performed at several different methane gas flow rates and TSS's. The PHE concentrations with time in the aqueous phase or hexane can be used to estimate the mass transfer coefficient for PHE transport between the aqueous phases and hexane, i.e. k_1 . This was fully described in Appendix F.

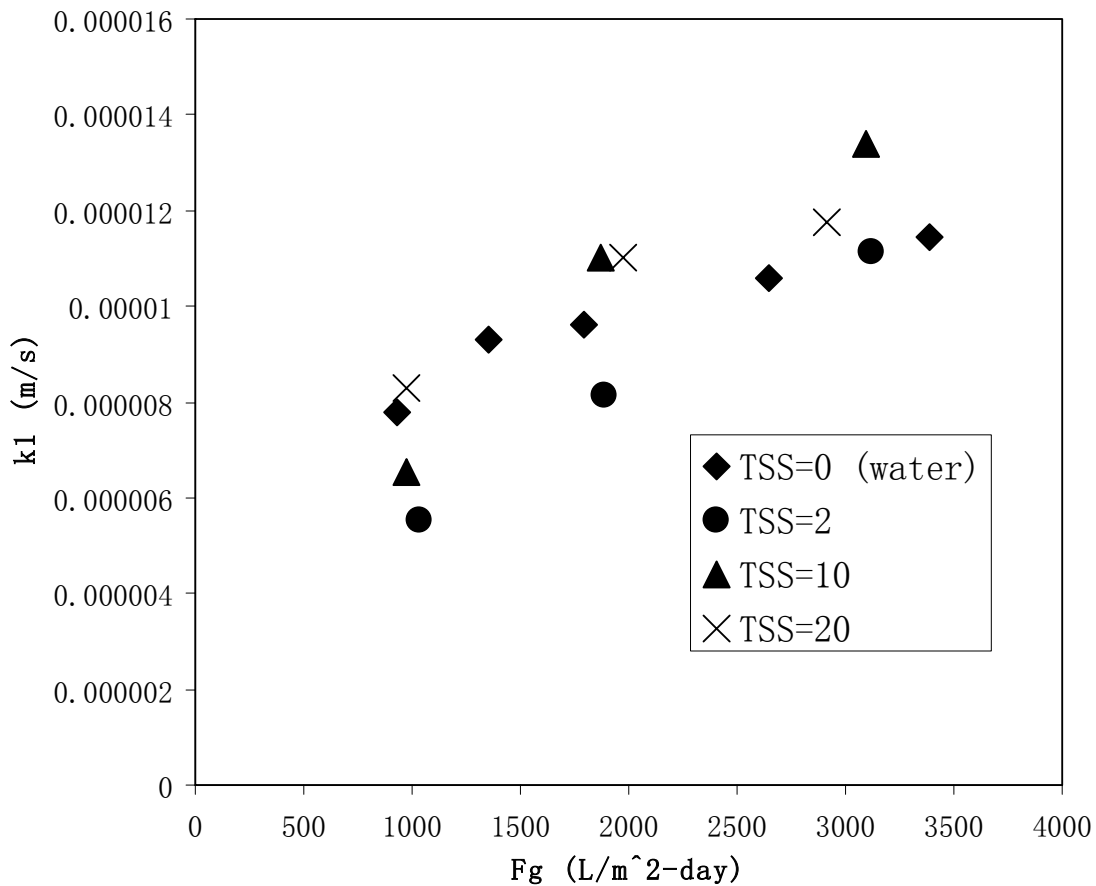


Figure 4.2 PHE mass transfer coefficients at the water/slurry-hexane interface with methane flux at different TSS's.

Figure 4.2 shows that the mass transfer coefficient k_1 increases with the gas flow rate. It seems that there is no obvious trend between k_1 and TSS. The data were then pooled together

and the following correlation (with $R^2=0.7166$) was obtained by the linear regression of the k_1 data and gas fluxes.

$$k_1 = 2 \times 10^{-9} F_g + 5 \times 10^{-6} \quad (4.2)$$

where k_1 is the MTC (m/s), and F_g is the gas flux (L/m^2 -day). The relationship (4.2) will be used in the modeling work (4.3.2.1).

4.1.2.1 Effects of Methane Flux on TSS or Sediment Flux

A video recording the bubble moving through the sediment-water interface was taken with a digital camera (Photron Motion Tools). The video showed that the bubbles brought sediment particles into the water column upon leaving the sediment. The larger, heavier particles fell back to the sediment bed, while the smaller, lighter particles remained suspended in the water column. The experimental results showed that TSS in the water column increased with time until it reached a constant value. Figure 4.3(a) shows the sediment fluxes with time at two different methane gas fluxes, derived from TSS data (Figure 4.16). It is clear that the sediment flux to the water column increased with time in the beginning, reached a maximum value and then gradually decreased to zero or a constant suspension-deposition equilibrium. The larger the methane flux, the higher the TSS or the sediment flux maximum value. This is understandable since the larger methane flux produces stronger forces on the particles resulting in larger final TSS.

4.1.2.2 Effects of Methane Flux and TSS on Contaminant Release

The experiments showed that the phenanthrene concentration in the aqueous phase increased with time, reached a maximum value and then decreased (Figure 4.17). This reflects the dynamics of the mass transfer processes occurring in the water column. Methane gas bubbles not only take up the contaminant from the pore water in the contaminated sediment but also

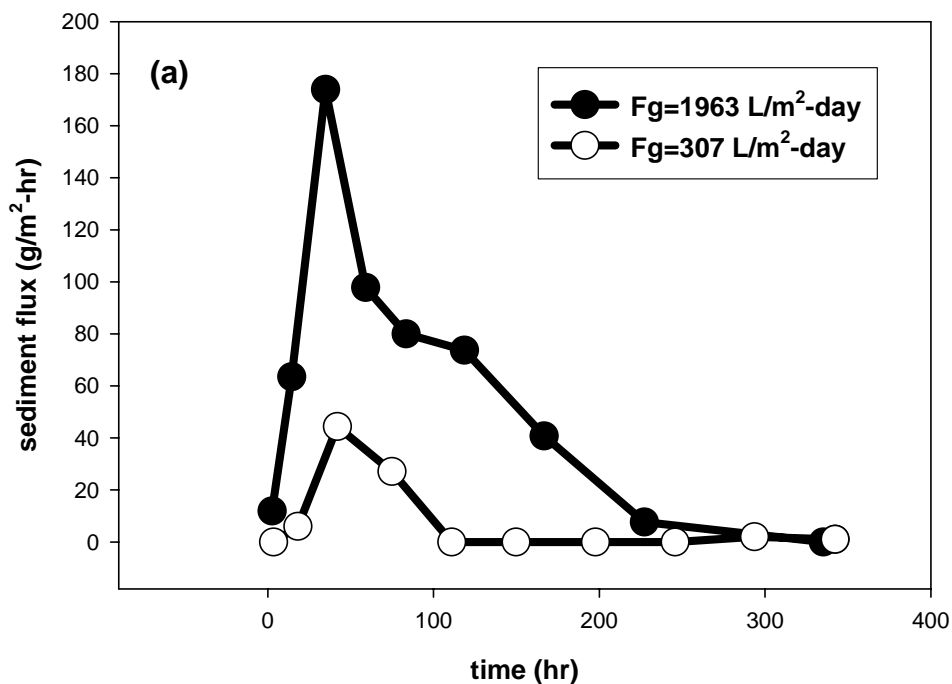


Figure 4.3 (a) Sediment flux with time at two different methane fluxes.

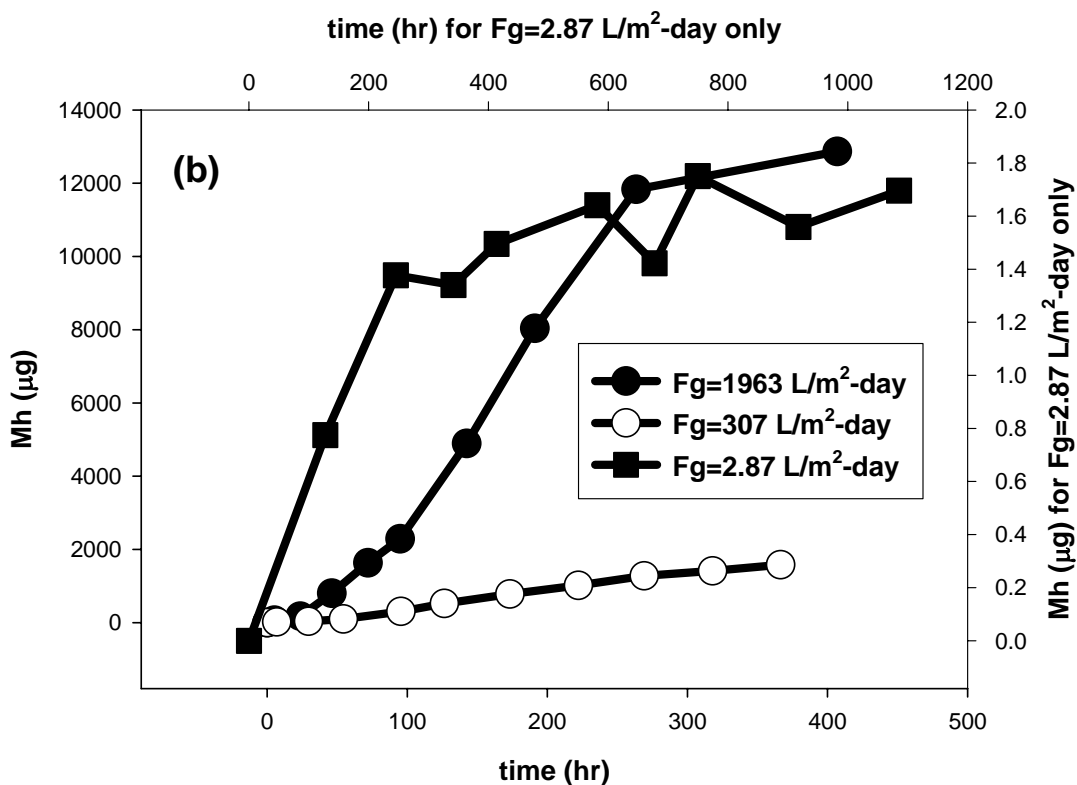


Figure 4.3 (b) PHE mass in hexane (Mh) with time at three different methane fluxes.

suspend fine particulates in the water column. Both contaminated sediment suspended particulates and methane gas bubbles release phenanthrene into the water. The driving force for mass transfer and phenanthrene desorption from gas bubbles and sediment particles is large in the beginning because phenanthrene concentration in the water is very small or near zero. This results in an increase in phenanthrene concentration in the water during the initial stages of the experiment. With time, the driving force decreases due to increasing aqueous phase concentration. As the methane gas bubbles transit the aqueous column they carry with it a certain fraction of phenanthrene to the overlying hexane layer. When phenanthrene mass gain by desorption from sediment particles to water and the loss by gas bubble transport are equal, the peak value of the phenanthrene concentration is reached in the water. Eventually the phenanthrene concentration in the aqueous phase will decrease with time because the rate of mass gain by desorption from sediment particles becomes smaller than the rate of mass lost by bubble transport. The mass increase in the hexane layer with time shows a characteristic S-shape (Figures 4.3 (b)). Initially in the hexane layer the phenanthrene mass increases slowly. Once the phenanthrene concentration in the aqueous phase reaches equilibrium with the sediment particles, the bubbles will transport phenanthrene from both sediment pore water and the aqueous phase. That causes the mass increase in hexane layer to be linear. As the aqueous phase concentration begins to decrease, the mass increase in the hexane layer becomes slow.

Methane flux influences the mass distribution of phenanthrene. A higher methane flux causes more sediment to be suspended in the water column and the peak value of phenanthrene concentration is reached earlier. It is obvious that the higher the flux of gas passing through the column, the more phenanthrene mass carried into the hexane. In fact, the total phenanthrene mass collected in the hexane layer is proportional to the methane gas flux.

Table 4.5 Contaminant fluxes and effective mass transfer coefficients at different methane fluxes

| Methane flux mL/min (L/m ² -day) | Phenanthrene flux (N_A) ^(a) ($\mu\text{g}/\text{m}^2\text{-hr}$) | Effective MTC ^(b) (cm/yr) |
|--|--|---|
| 6.85 (1963) | 7069 | 80.11 |
| 1.07 (307) | 877 | 9.94 |
| 0.01 (2.87) | 0.42 | 0.0047 |
| 0.0035 (1) | 0.15 ^(c) | 0.0017 |

(a) N_A is estimated by the slope of linear regression of the phenanthrene mass in hexane layer with time (Figure 4.3(b)) divided by the column cross-section area. (b) Effective MTC = $N_A / (\rho_b W_s)$, where ρ_b is the sediment bulk density (kg/m^3) and W_s is the sediment loading (mg/kg). (c) This value is estimated at expected rates of gas release under field conditions ($\sim 1 \text{ L}/\text{m}^2\text{-day}$, Himmelheber, et al. 2005) assuming that contaminant flux is linear function of gas flow at low gas release rates.

One experiment with low methane flux (0.01 mL/min or 2.87 L/m²-day) was conducted to simulate near field flux conditions. The phenanthrene concentration in the water column was very small and undetectable, but the dissolved organic compound (DOC) in water increased from 1.7 to 3.5 mg/L. The increase of phenanthrene mass in hexane layer with time was extremely slow (Figure 4.3 (b)). Phenanthrene fluxes and effective mass transfer coefficients (MTC) at various methane fluxes were estimated (Table 4.5). The effective mass transfer coefficient based on solid phase sediment concentration of 0.0017 cm/yr at the lowest gas release rate can be compared to a typical bioturbation sediment reworking coefficient of the order of 0.1 – 10 cm/yr or higher (Thibodeaux, 1996; Choi, et al., 2002). Thus contaminant release due to gas ebullition is not expected to be significant relative to contaminant release from bioturbation in exposed contaminated sediments unless gas migration occurs at much higher rates than that associated with the natural evolution of gas as a byproduct of anaerobic degradation of organic matter. As indicated previously, however, presence of contaminants in a liquid phase, either as a nonaqueous phase liquid or for soluble contaminants, the proportion moved by gas release could be much greater. The movement of contaminants by gas may also become the controlling release

rate in capped systems, in which bioturbation is displaced to the surface of a cap rather than within the contaminated sediments.

4.1.2.3 Effects of Consolidation on Contaminant Release

For this experiment, the sediment was consolidated for 15 days before the methane gas was introduced into the column. Note that the methane flux was slightly lower in the experiment with sediment consolidation. Figure 4.4(a) shows that the time needed for the sediment flux to reach zero (i. e., TSS to reach a constant value) is around 100 hours for the unconsolidated sediment system, but increases to about 350 hours for the consolidated sediment. The sediment consolidation can make the sediment more compact and harder to suspend. Since sediment suspension is a major phenanthrene release mechanism into the aqueous phase and transport into the hexane layer, the delay in the TSS reaching a maximum for consolidated sediment system leads to the delay in the peak aqueous concentration, and less phenanthrene mass in hexane layer (Figure 4.4(b)).

4.1.2.4 Effects of Cap on Contaminant Release

A 2 cm sand cap was used to cap the contaminated, consolidated sediment. The stable phenanthrene concentration in the aqueous phase is about 5 ppb, about 5 times less than those for uncapped systems. The mass in the hexane layer for the capped sediment is also much smaller than those for the uncapped systems (Figure 4.4 (b)). The reason is that the sand cap layer functions as a filter that effectively prevents sediment suspension. Although the water column became slightly turbid and the dissolved organic compound (DOC) in the aqueous phase increased from 1.3 to 5.7 mg/L, the TSS was too small to be measured using the filtration method. As stated earlier the phenanthrene transport from the contaminated sediment to the water column and hexane layer was facilitated by bubbles in the uncapped case. For the capped

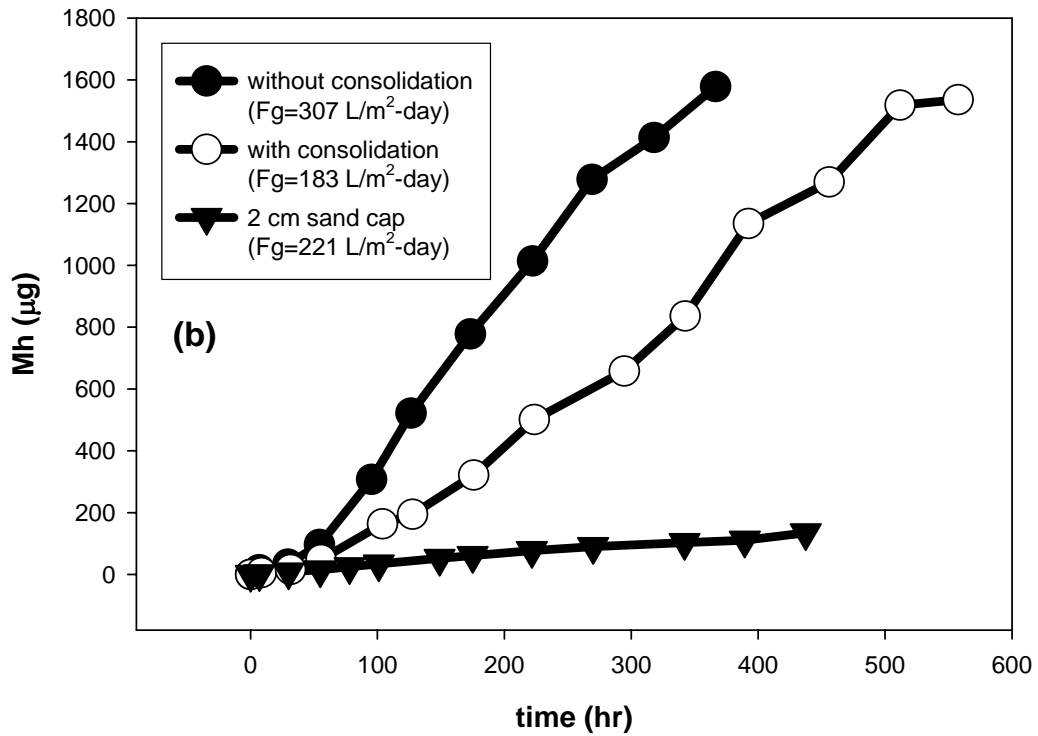
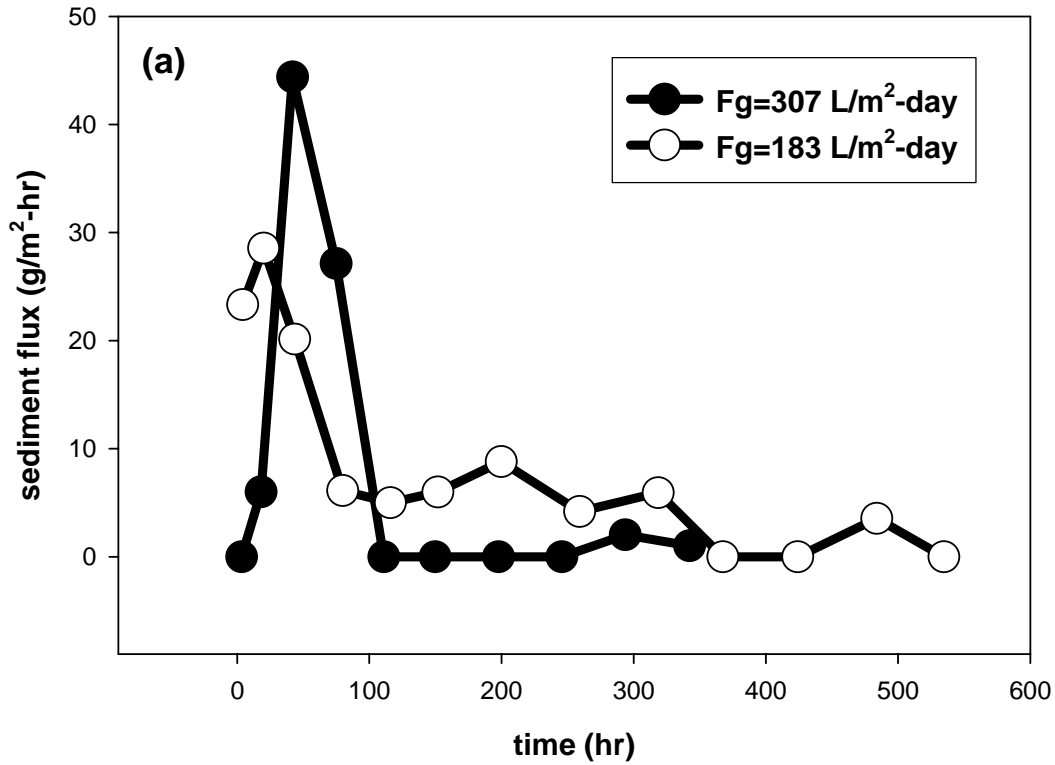


Figure 4.4 Sediment flux and phenanthrene mass in hexane (Mh) with time. (a) Sediment fluxes with and without consolidation; (b) Mh with and without cap.

system, although bubbles transported some phenanthrene there was much less sediment suspended in the water column. Hence, the water concentration of phenanthrene was very small.

4.1.2.5 Contaminant Concentration Profiles in Sediment Cores

The phenanthrene concentration profiles in all the sediment cores were measured. Figures 4.5(a) and 4.5(b) are two examples for capped and uncapped cores. The profiles demonstrate that there is a concentration decrease at either end of the sediment cores. At the top of the core, water, slurry and sediment mixing causes the concentration decrease. At the bottom of the core, phenanthrene transport from pore water into methane gas may be the reason for the concentration decrease. The concentration gradient between pore water and gas bubble should be larger at the column base due to the injection of clean methane. This can make PHE concentration in the sediment decrease faster. No obvious concentration difference was observed in the middle of the sediment core. This may mean that bubbles circulated the pore water in sediment. Pore water circulation in the sediment would make a uniform sediment loading possible. To confirm this hypothesis, further experiments should be performed using CT to quantify the void distributions during methane injection. For capped sediment cores, sediment and sand mixing at the sediment-sand interface was observed, which can be caused by the gas bubble movement and the density difference between sand and sediment.

4.1.2.6 Mass Balance

Total phenanthrene mass added with the sediment can be calculated by sediment loading and weight and water content that were measured when sediments were added to the column. During each experimental run, phenanthrene mass would redistribute in sediment, slurry and hexane layer. Phenanthrene mass in the hexane layer and in the aqueous phase are easily calculated using measured concentrations and volume. In order to estimate the phenanthrene

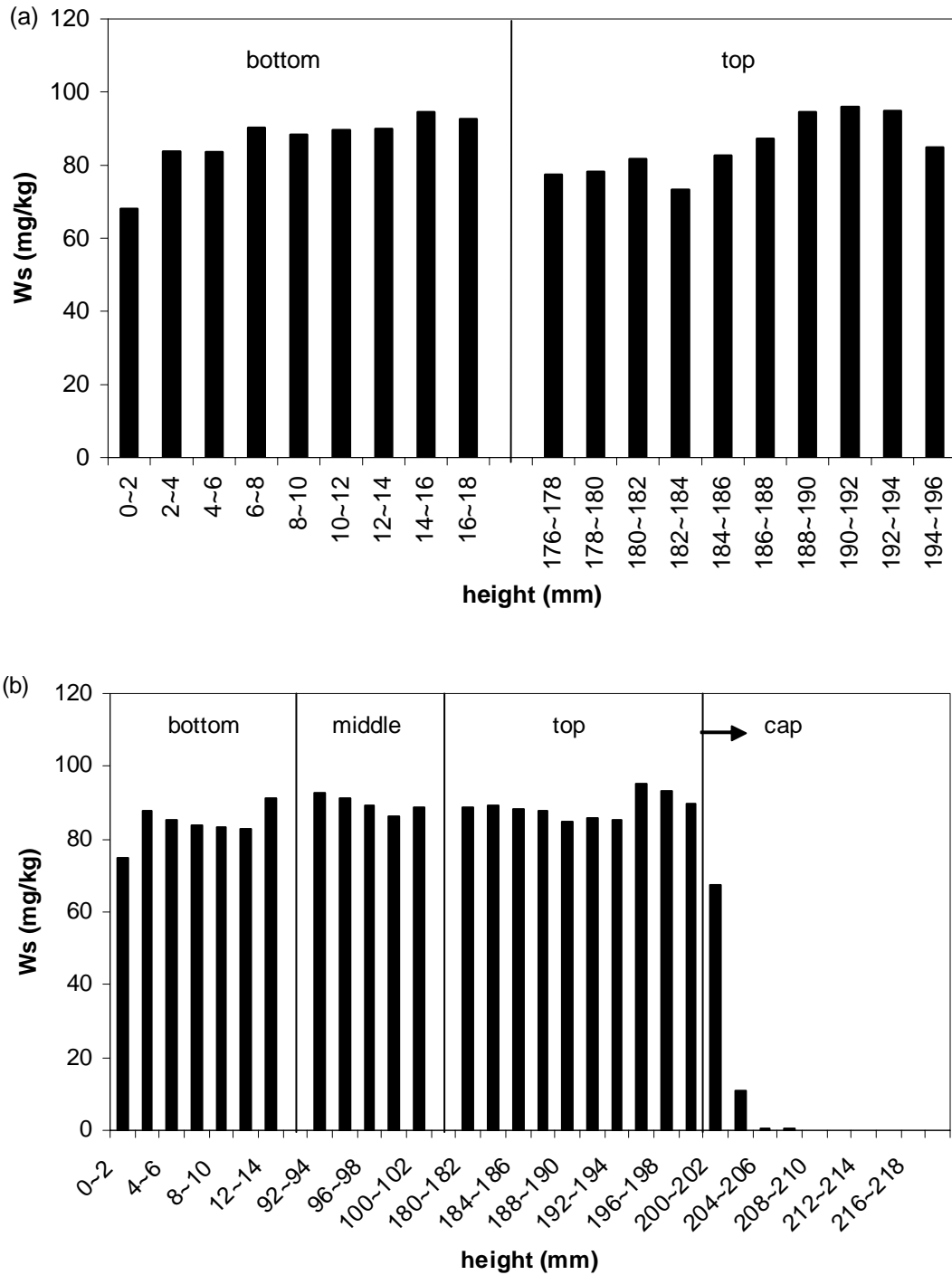


Figure 4.5 Phenanthrene concentration profiles. (a) in sediment core (Fg=307 L/m²-day); (b) in sediment and sand core (Fg=221 L/m²-day).

mass on the soil particles in the slurry, an equilibrium partition coefficient K_d was used to calculate the phenanthrene concentration on the soil particles. This should not cause a big difference even if they are not at equilibrium because the phenanthrene mass in the slurry is only a very small part of the total phenanthrene mass. However this practice can underestimate the phenanthrene mass on the sediment particles if no-equilibrium exists between aqueous phase and sediment. The particle weight can be estimated by TSS and slurry volume. The procedure to calculate the phenanthrene mass remained in the sediment is as follows.

The total phenanthrene remained in the sediment can be calculated by

$$m_s = \sum_{i=1}^n W_{si} V_{si} \rho_{bi} \quad (4.3)$$

where m_s is the phenanthrene mass (mg) in the sediment, W_{si} is the sediment loading in the i^{th} section (mg/kg), V_{si} is the volume of the i^{th} section, ρ_{bi} is the sediment bulk density (kg/m³) and n is the number of total sections, being equal to the total height of the sediment divided by the height of each section.

Usually sediment was sliced into several samples (2 mm each) from the top, middle and bottom of the sediment core. As mentioned before, both sediment loading and moisture were measured. Sediment moisture can be used to estimate the sediment bulk density since the volume of each section is known. The sediment loading can be directly used in the above equation. For the other part of the middle area where there are no experimental data, the average of the loading from the middle (or several inside data from both top and bottom) was used. Since each sediment section is a conical frustum (on the bottom side) or a cylinder (on the top side), the sediment volume each section can be estimated by

$$V_{si} = \frac{\pi \cdot h_i}{12} (Dh_{i1}^2 + Dh_{i1} \cdot Dh_{i2} + Dh_{i2}^2) \quad (4.4)$$

Table 4.6 Phenanthrene mass distribution in different phases and mass balance

| Cases | Total mass added with sediment (mg) | Mass distribution in different phases after the experimental run | | | | | Relative error (%) |
|--|-------------------------------------|--|--------------------------|--------------------|-------------------|-----------------|--------------------|
| | | Sediment (mg) | Slurry | | Hexane layer (mg) | Total mass (mg) | |
| | | | Suspended particles (mg) | Aqueous phase (mg) | | | |
| Fg=1963 L/m ² -day, t=406.9 hrs | 56.6 | 39.8 (72.8%) | 2.0 (3.6%) | 0.07 (0.1%) | 12.9 (23.5%) | 54.7 | 3.6 |
| Fg=307 L/m ² -day, t=366.5 hrs | 57.5 | 52.6 (96.4%) | 0.3 (0.6%) | 0.07 (0.1%) | 1.6 (2.9%) | 54.6 | 5.0 |
| 2 cm sand cap, Fg=221 L/m ² -day, t=473.5 hrs | 56.5 | 52.9 (98.5%) | 0.6 (1.2%) (In sand) | 0.02 (0.03%) | 0.1 (0.3%) | 53.7 | 4.9 |
| Fg=183 L/m ² -day, 15 days' sediment consolidation, t=557.5 hrs | 56.0 | 49.5 (96%) | 0.454 (0.9%) | 0.07 (0.1%) | 1.5 (3.0%) | 51.5 | 8.0 |

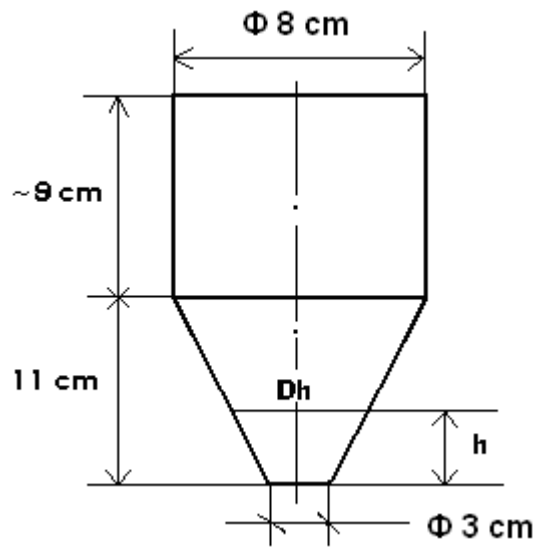


Figure 4.6 Schematic of sediment in the column.

where V_{si} is the volume of the section (m^3), h_i is the height of the section (m), Dh_{i1} is the top diameter (m), and Dh_{i2} is the bottom diameter (m), which can be calculated by $Dh = 5h/11 + 0.03$ (m) for this specific column (Figure 4.6).

Table 4.6 lists the phenanthrene mass distributions for different cases. Each case gives a reasonably good mass balance. The data also indicate that methane flux is one major factor for phenanthrene mass distribution. Higher methane fluxes result in more contaminant mass release from the sediment. The sand cap can be another major factor for phenanthrene mass distribution if the cap maintains its integrity.

4.1.2.7 Void Size Distribution in Sand and Sediment

Four separate sediment cores were imaged using CT. The first core was from the experiment at the high gas flow rate (6.85 mL/min or 1963 L/m²-day) and the second one from the experiment with a lower gas flow rate (1.07 mL/min or 307 L/m²-day). These two sediment cores were scanned in three regions each 3 mm thick. The “top” region begins 5 mm below top; “middle” starts from the center of the sediment; and “bottom” starts 8 mm above bottom. For the capped sediment core, four regions (6 mm each) were scanned, located at the middle of the sand layer and the top, the middle and the bottom of the sediment. Only the middle part (6 mm) of the control sediment core was scanned. Figure 4.7(a) and (b) are the examples of the original CT images. Qualitatively (see Figure 4.8(a), 4.8(b), 4.8(c) and 4.8(d)) it appears that there are a large number and better spatial distribution of void spaces in the experiments with methane injection compared to the control column. Quantitative analysis shows that the number of voids in the column sediments is larger than in the control sediment (Table 4.7). This helps support our hypothesis that bubble migration enhances the pore water circulation within the sediment column and may help redistribute the void spaces. Analyses of the size distributions indicate that void

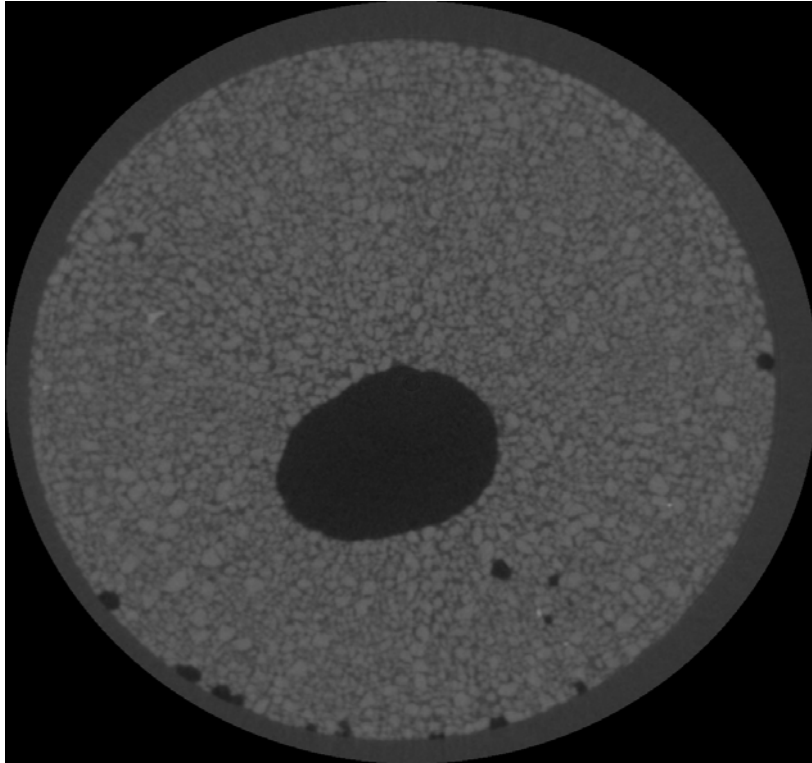


Figure 4.7(a) Original CT image of one slice in sand layer.

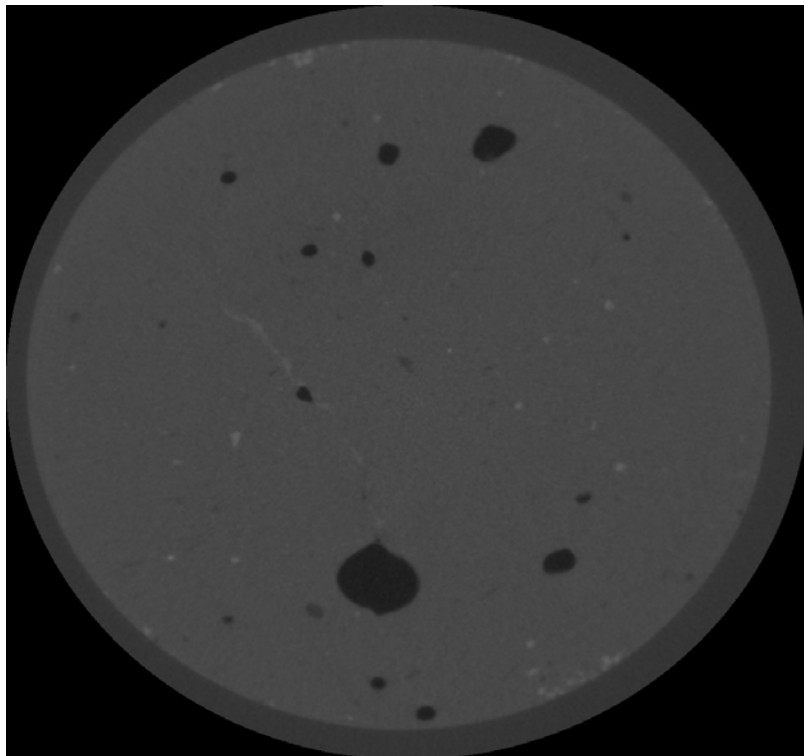


Figure 4.7(b) Original CT image of one slice in sediment.

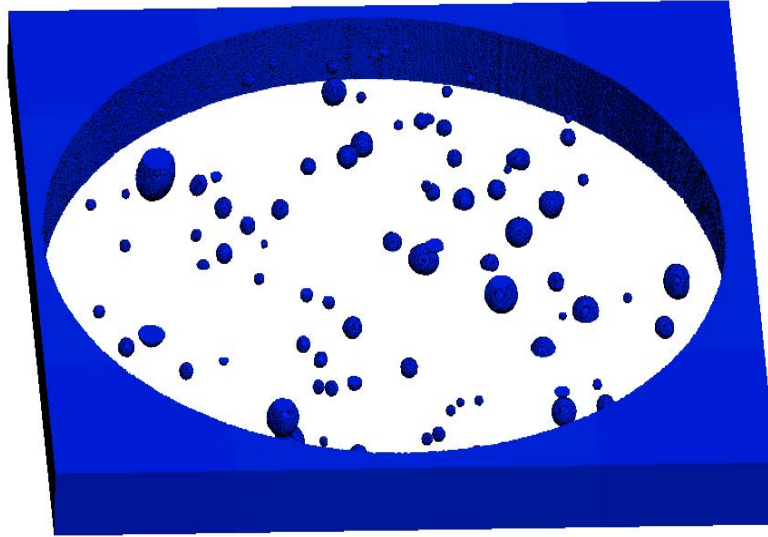


Figure 4.8 (a) Image of void distribution in the middle of sediment core without cap ($F_g=307$ L/m^2 -day).

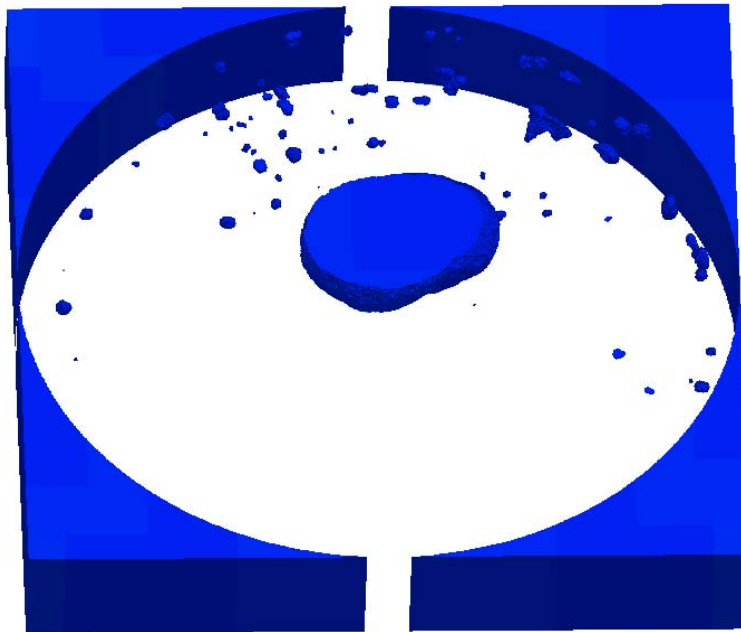


Figure 4.8 (b) Images of void distribution in the middle of sand cap ($F_g=221$ L/m^2 -day).

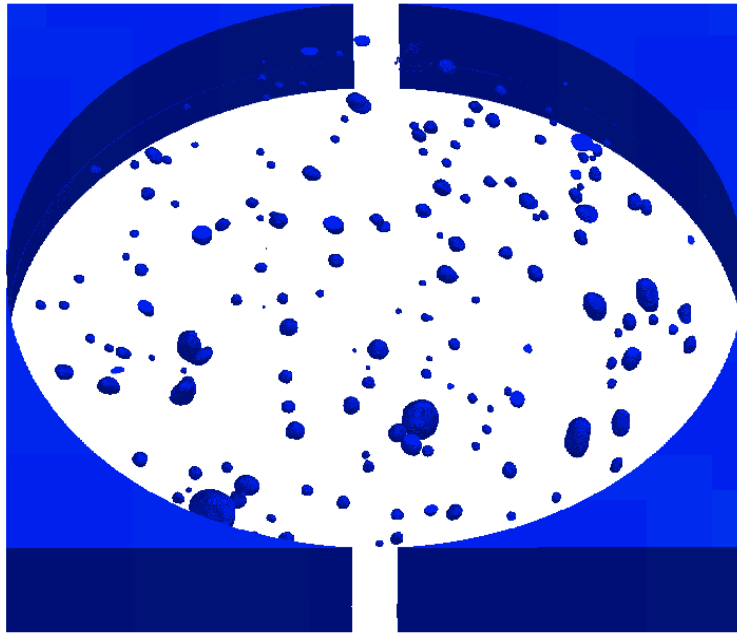


Figure 4.8 (c) Images of void distribution in the middle of sediment core with cap ($F_g=221$ L/m^2 -day).

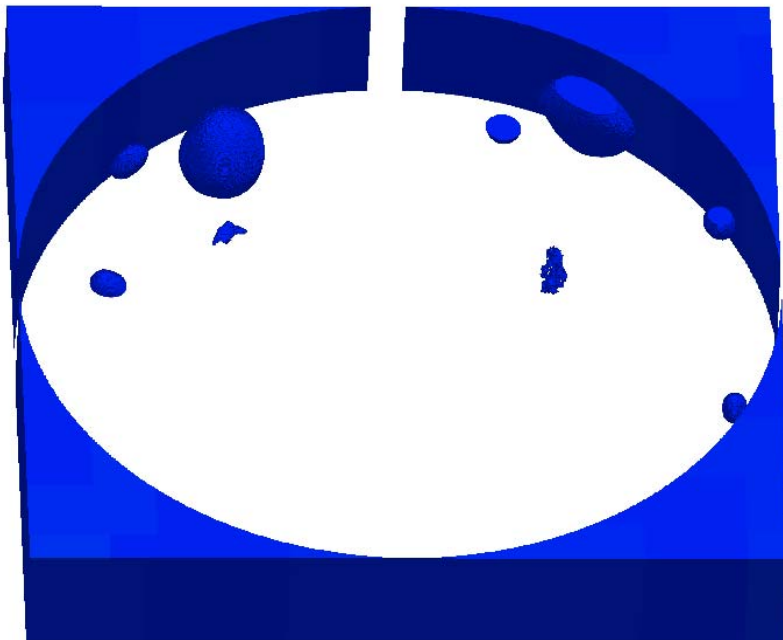


Figure 4.8 (d) Images of void distribution in the middle of the control sediment core (without methane gas flow).

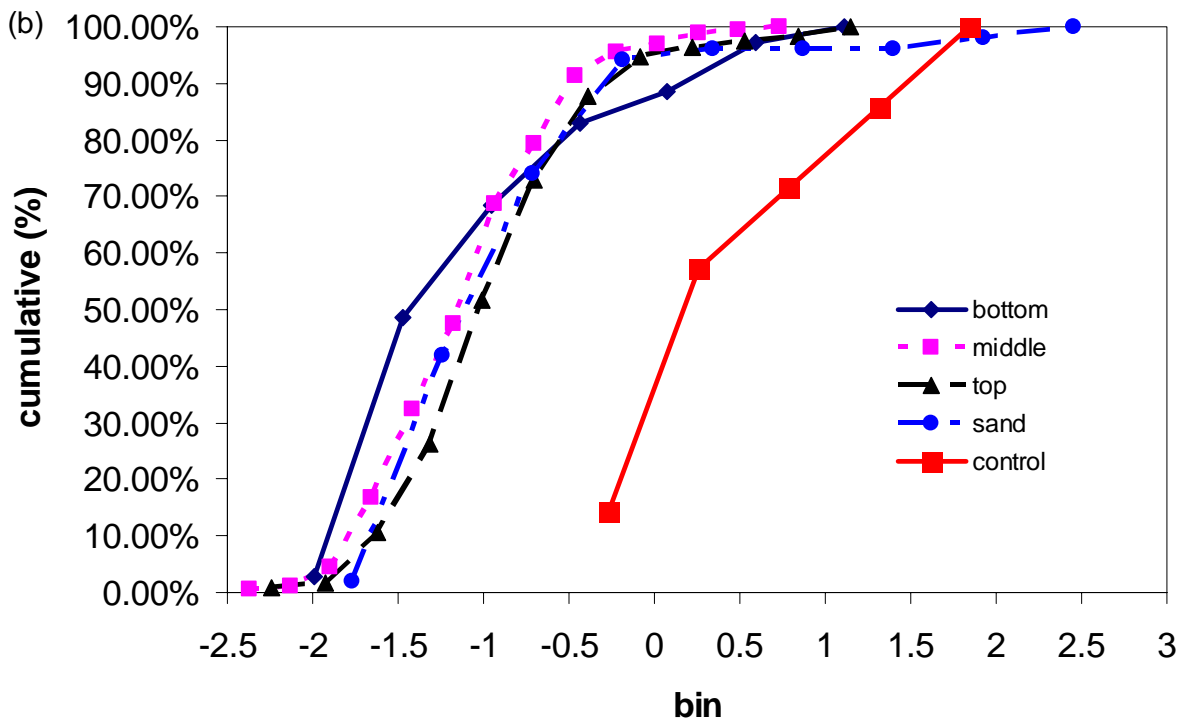
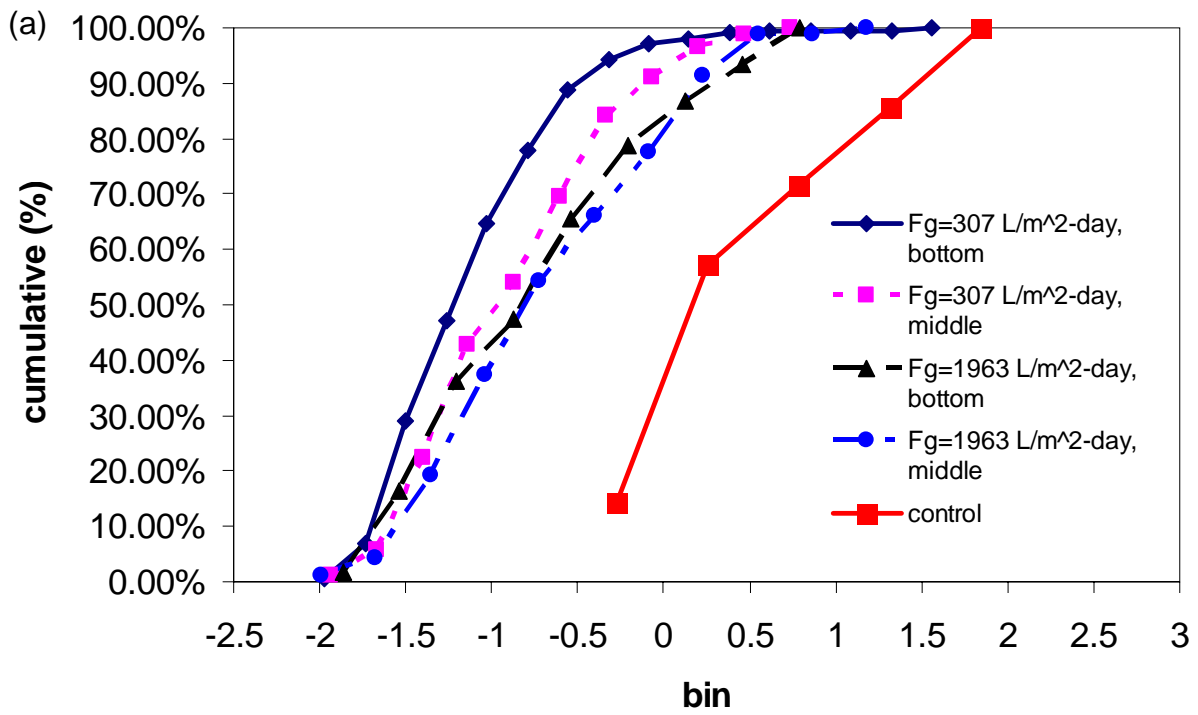


Figure 4.9 Void volume distributions (on a log scale). (a) in uncapped sediment cores; (b) in capped sediment/sand core ($F_g=221 \text{ L/m}^2\text{-day}$).

Table 4.7 Void count and total volume for the different experimental conditions

| Sediment specimens | Scanning parts | Scanning thickness (mm) | Number of voids | Total void volume (mm ³) |
|---|----------------|-------------------------|-----------------|--------------------------------------|
| The first core F _g =1963 L/m ² -day | Middle | 3 | 94 | 59.0 |
| | Bottom | 3 | 61 | 35.2 |
| The second core F _g =307 L/m ² -day | Middle | 3 | 89 | 25.3 |
| | Bottom | 3 | 204 | 54.8 |
| Capping sediment F _g =221 L/m ² -day | Sand layer | 6 | 50 | 123.9 |
| | Top | 6 | 114 | 44.6 |
| | Middle | 6 | 160 | 28.5 |
| | Bottom | 6 | 35 | 20.5 |
| Control sediment | Middle | 6 | 7 | 54.6 |

spaces are smaller and more uniform at lower flow rates (Figures 4.9(a) and 4.9(b), and Table 4.7). Finally, a large ‘bubble’ or void space in the sand layer was observed (Figures 4.8(b) and 4.9(b)), suggesting the coalescence of the methane bubbles in the sand layer.

4.1.2.8 Contaminant Transport Pathway

Based on the above experimental observations, we postulate a pathway of gas bubble facilitated sediment contaminant transport through sediment systems. For an uncapped system (see Figure 4.15), organics in the contaminated sediment can be converted into methane, CO₂ and N₂ by biological and microbial activities under anaerobic condition. Bubbles form with increasing gas vapor pressure. The bubbles take up contaminants from pore water in the contaminated sediment via gas/water partitioning and would move up into the water column when the pressure inside is larger than atmospheric plus hydrostatic pressure. We visually observed that the oblate bubbles (or ellipsoid) with the major (long) axis in the horizontal direction bring soil particles in their wakes as they move through the sediment-water interface.

The large/heavy particles would sink to the sediment and the small/light ones remain in the water column and form a slurry. The contaminated particles in the slurry will desorb contaminants into the aqueous phase and so will the bubbles initially. This increases the contaminant concentration in the aqueous phase. As the bubbles traverse the aqueous phase and break the surface, contaminants are released into the air. The experimental results clearly show that the sediment suspension is the major contaminant transport mechanism.

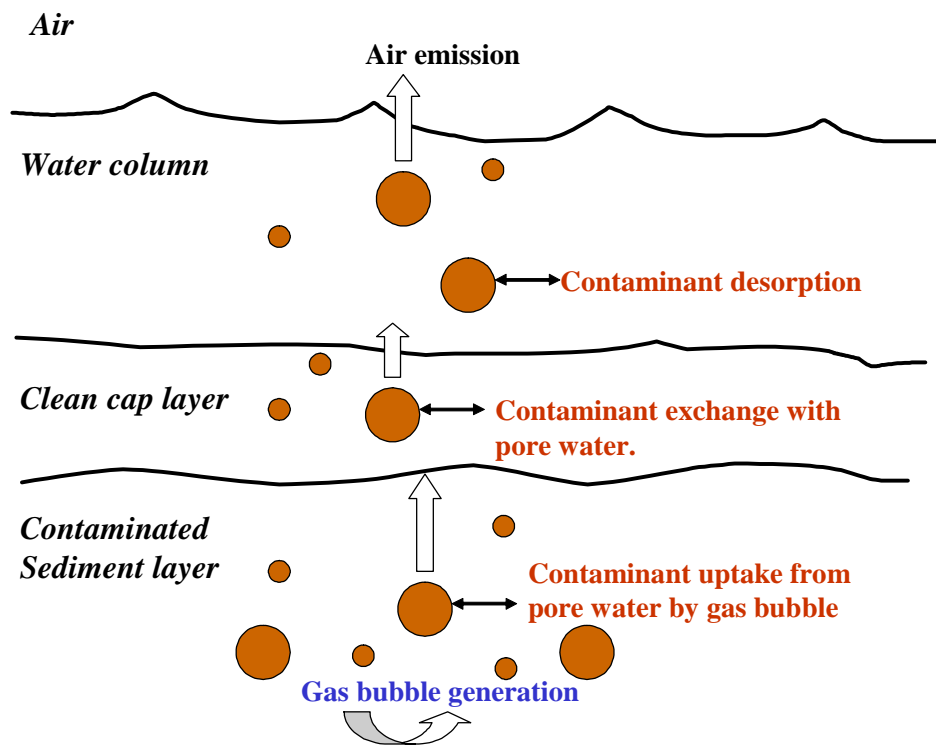


Figure 4.10 Depictions of Gas Bubble Generation and Migration through a Cap.

In the capped system (Figure 4.10), the bubbles generated in the contaminated sediment will move through the clean cap material. The gas bubbles release the contaminants into the pore water in the sand cap and water column. Although gas bubble movement may lead to some

mixing of the sediment and sand at the sediment-sand interface, no significant sediment suspension is observed if the sand cap is not breached by the gas bubbles. In fact, the cap functions as a filter inhibiting sediment suspension, which eliminates or reduces the source of contaminant into the water column.

4.2 Measurement of Methane-Water Henry's Law Constants of PAHs and Their Temperature Dependence between 5 and 30 °C

The vapor-water equilibrium partition constant or Henry's law constant (H) is a parameter that facilitates the estimation of vapor phase concentrations of chemicals, if estimates of the pore water concentration are available. In the modeling of volatile losses from exposed dredged materials, the ratio K_d/H represents the parameter $K_{SA} (w_A / C_{Ag})$ or the sediment-air equilibrium partition constant defined as a ratio of sediment contaminant loading to contaminant concentration in the gaseous phase. This quantity represents the thermodynamic limit of the vapor concentration of a chemical, when the concentration in the solid is known. The determination of H will allow for the estimation of pore vapor concentrations. The majority of the reported values of H are for exchange between air and water (Staudinger and Roberts, 2001; Sander, 1999). However, methane is a common gas in contaminated sediments, formed by biological and microbial processes (Di Toro, 2001; Klaucke et al., 2005; Hovland and Judd, 1992). To model the contaminant transport caused by methane gas ebullition in sediment, methane-water H is necessary (Yuan et al., 2005 and 2006).

Estimates of H in literature vary widely mainly due to the different methods of estimation. The primary obstacle in the measurement of H for semi-volatile hydrocarbons such as PAHs is the low vapor pressures of some of these chemicals. Direct measurement of the chemical concentrations in the water and vapor phases in contact after equilibration is the preferred method for the estimation of H, but the low vapor pressures and water solubilities of

some of these compounds lead to uncertainties in the estimation. Several methods such as WWC (the wetted-wall column) and fog chamber (Fendinger et al., 1989 and 1990) have been used to measure Henry's law constant (H) for a variety of organic compounds by direct ratio of chemical concentrations in the aqueous and vapor phases in equilibrium. Jayasinghe et al. (1992) used a flow-through gas-liquid equilibration method to measure the Henry's law constants of organic compounds of low volatility. When the chemical is volatile ($H > 0.1$), bulk equilibration technique or static methods is sensitive enough since this method can yield significant concentration differences to resolve H (Gossett, 1987). However, for semi-volatile chemicals such PAHs and PCBs, static methods may not yield sufficient concentrations in the vapor phase. Large volumes of vapor space are necessary to conduct static experiments for these types of chemicals. Alternatively, a gas stripping method has been used for the measurement of H for PAHs (Mackay et al., 1979; Bamford et al., 1999; DeMaagd et al., 1998). In this method, humidified air is bubbled through an aqueous solution to strip the PAHs from the liquid phase into the vapor phase. The volume of the vapor phase is proportional to the flow rate and the time interval of the collection. The vapor phase PAH concentration is measured by trapping the chemicals in the vapor stream over a period of time. The Henry's law constant is estimated by the ratio of the vapor phase concentration and the average aqueous phase concentration over the interval of vapor phase collection. The prerequisite for the experiment is that the residence time of the vapor phase in the liquid is sufficient for it to be in equilibrium with the aqueous phase. This can be tested by the experiments with different water heights.

4.2.1 Theoretical Background

4.2.1.1 Henry's Law

It has been observed that the solubility of a gas in a liquid is proportional to its partial pressure in the gas phase, provided that the partial pressure is not large and no chemical reaction

takes place between the liquid and the gas (Valsaraj, 2000; Prausnitz et al., 1999). The law is named after William Henry (1774-1836), the English chemist who first reported the relationship. Henry's law always provides a good approximation when the solubility and partial pressure of the solute are small and when the temperature is below the critical point of the solvent. Henry's law assumes that the gas-phase fugacity is equal to the partial pressure and liquid-phase activity is equal to the concentration. The proportionality constant is called the Henry's law constant and is denoted by H . If the liquid and gaseous concentrations are expressed on a molar basis (mol/m^3) a dimensionless Henry's law constant is expressed as:

$$H_{cc} = \frac{C_g}{C_w} \quad (4.5)$$

Henry's law constant also has other expressions due to the different concentration units chosen. If both the liquid and gas phase concentrations are expressed as mole fractions, another dimensionless value is obtained for Henry's law constant ($H_{yx} = y/x$). If the gas phase concentration is in pressure and liquid phase concentration is in mole fraction, the Henry's law constant has a unit ($H_{pz} = p/x$, Pa). If the gas phase concentration is denoted in pressure units (Pa) and liquid phase concentration is in molarity ($\text{mol}\cdot\text{m}^3$), a different unit for Henry's constant ($H_{ipc} = p_i / C_{wi}$, $\text{Pa}\cdot\text{m}^3/\text{mol}$) can be obtained. Usually, the ideal gas law can be employed to convert from one unit to another. For example, $H_{pc} = H_{cc} \cdot RT$ where R is the ideal gas constant ($8.314 \text{ Pa}\cdot\text{m}^3/\text{mol}\cdot\text{K}$) and T is the absolute temperature (K).

4.2.1.2 van't Hoff Equation

Henry's law constant depends on both temperature and pressure. However, for most environmental systems, pressure rarely increases beyond atmospheric pressure, and usually the dependence of H on pressure does not need to be considered. The effect of temperature on H is

more dramatic. Equating the Gibbs equations $\Delta G = -RT \ln H$ and $\Delta G = \Delta H - T\Delta S$ (Prausnitz et al., 1999) yields

$$\ln H = \left(\frac{-\Delta H}{R} \right) \cdot \frac{1}{T} + \left(\frac{\Delta S}{R} \right) \quad (4.6)$$

where ΔG is the standard Gibbs free energy change (J/mol) between gas and aqueous phases, ΔH is the enthalpy of phase change (J/mol), ΔS is the entropy of phase change (J/mol-K), R is the ideal gas constant and T is the absolute temperature (K). Over a narrow range of temperature, it is reasonable to assume that ΔH and ΔS are independent of temperature. The above equation shows a linear relationship between $\ln H$ and $1/T$. With measured H values at different temperatures, ΔH and ΔS can be determined by the linear regression.

Writing Equation (4.6) twice for two temperatures and subtracting one from the other give the van't Hoff equation

$$\ln \frac{H(T_2)}{H(T_1)} = \frac{-\Delta H}{R} \left(\frac{1}{T_2} - \frac{1}{T_1} \right) \quad (4.7)$$

Knowing $H(T_1)$ at a given temperature (T_1) and ΔH for a given compound, Equation (4.7) can be used to estimate $H(T_2)$ at any other temperature.

4.2.2 Materials and Methods

4.2.2.1 Chemicals

Naphthalene (NAPH) of 99+% purity, and phenanthrene (PHE) and pyrene (PYR) of 98% purity were purchased from Aldrich Chemicals, Milwaukee, WI.

4.2.2.2 Experimental Setup and Operations

Figure 4.11 illustrates the experimental apparatus for this study. The main part of the apparatus is a glass bubble column (5 cm in diameter and 120 cm long), fitted with a coarse glass

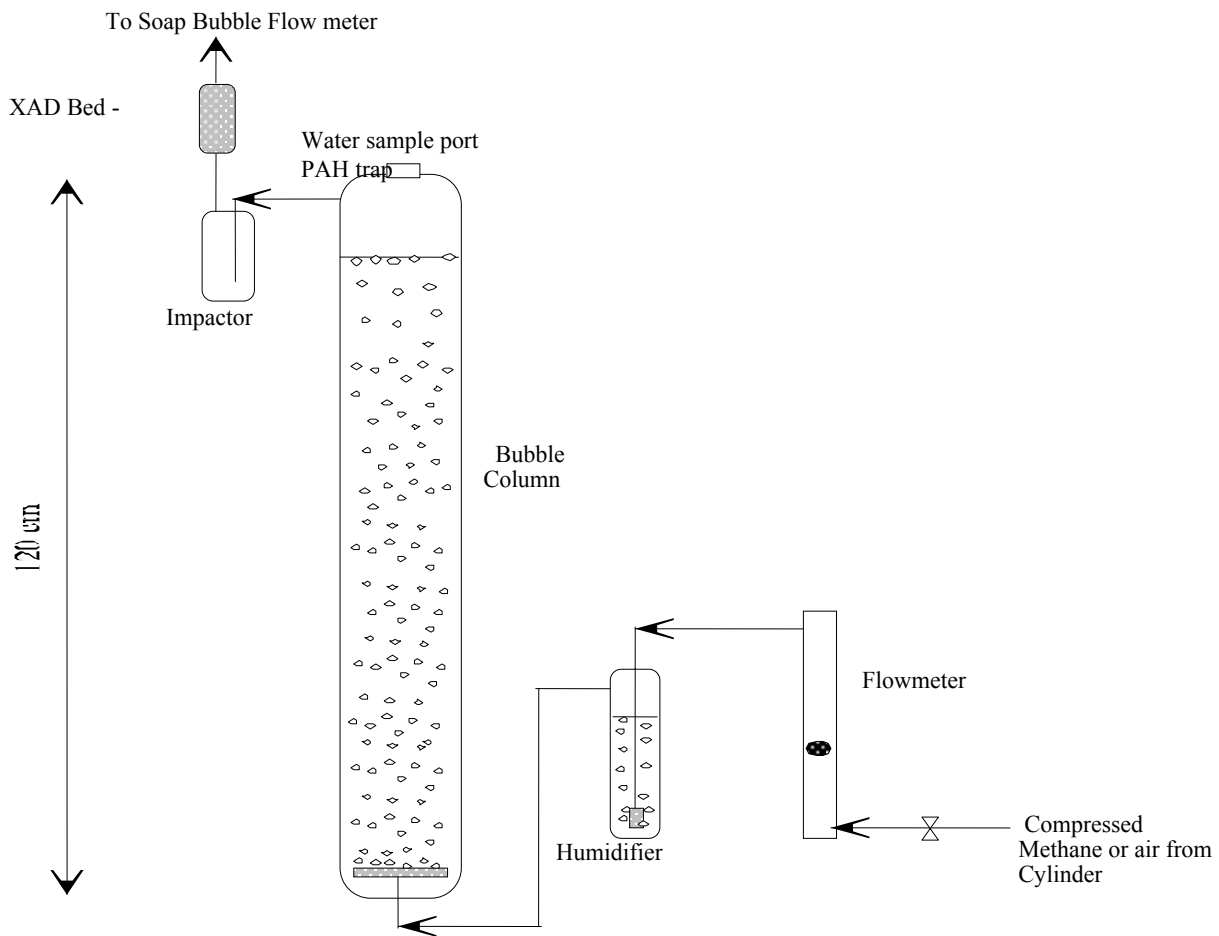


Figure 4.11 Experimental setup for the measurement of Henry's law constant.

sparger near the base of the column. The temperature was controlled by a water bath (RM20, LAUDA, Brinkmann). All the parts of the apparatus (including the humidifier, the bubble column, the impactor and the soap bubble flow meter) and gas tubing were wrapped with coolant (water) tubing (Tygon[®] R-3603). In fact, the coolant tubing accompanied the gas tubing all the way from its entrance into the humidifier to its exit from the soap bubble flow meter. One thermometer was attached to the wall of the bubble column and the other to the wall of the soap bubble flow meter to monitor the temperature (± 0.1 °C). The whole setup was wrapped with insulation materials (Duct Insulation, Foil and Fiberglass, Frost King[®] All Season).

Saturated aqueous solution was prepared by dissolving pure crystals of these chemicals in de-ionized water for several days followed by filtration through a 0.7 μm glass fiber filter (Whatman). The solution was diluted with de-ionized water to the concentrations around 10% of their aqueous solubility. With this solution, the column was filled to a depth of 80 – 82.5 cm (solution weight around 1710 g). Methane or air from the cylinder was passed through a regulator, a flowmeter and a humidifier to prevent water loss from the glass column, and then introduced into the bubble column through the sparger. The gas flow rate was maintained between 60 to 80 mL/min. The gas exiting the bubble column passed through an impactor to remove aerosols created by bubbles, then through an XAD trap (ORBO-43, SUPELCO, Bellefonte, PA) to collect the PAHs in the gas stream. The XAD trap has been successfully used to capture vapor phase PAHs in several studies in our group (Ravikrishna et al. 2000, 2005). The flowrate of exit gas was measured with a soap bubble flowmeter.

4.2.2.3 Sample Collection and Analysis

To allow the chemicals to become well mixed and equilibrated with the apparatus, the gas was bubbled through the bubble column for more than 24 hours prior to sampling. At the

same time, the coolant water was supplied in order that the bubble column reached the expected temperature. Aqueous samples were taken from the top of the bubble column simultaneously when XAD trap was assembled into and disassembled from the system. The time interval of the sampling was 10 to 12 hours for the experiments conducted at 10, 18, 25, and 30°C and 18 to 24 hours for those experiments conducted at 5 °C. The aqueous samples were directly injected into HPLC. HPLC analysis was conducted as set forth in the US EPA Standard Method 8270 (APHA/AWWA/WEF, 1991). The XAD traps were extracted overnight with 20 mL of HPLC grade acetonitrile. The extracts were analyzed with HPLC using the same methods as that for aqueous samples.

4.2.2.4 Calculations of Henry's Law Constants

The gas phase PAH concentration was calculated by the gas flow rate, the time interval of sampling and the PAH mass trapped by the XAD trap. The aqueous phase PAH concentration was the average of two aqueous concentrations measured at the start and end of each gas sample over that time interval. The value of H was calculated as the ratio of the gas phase concentration to the aqueous phase concentration:

$$H = \frac{2m_g}{Q_g \cdot t \cdot (C_{wi} - C_{wf})} \quad (4.8)$$

where m_g is the PAH mass trapped by XAD trap (μg), Q_g is the gas flow rate (L/min), t is the time interval of gas sampling (min), C_{wi} and C_{wf} are the initial and final aqueous phase PAH concentrations over that time interval ($\mu\text{g/L}$).

4.2.3 Results and Discussion

4.2.3.1 Method Verification

It is critical to ensure that the system reaches equilibrium. Experiments with different water heights can be used to test the extent to which the gas and liquid at the top of the bubble

column are in equilibrium (Mackay et al., 1979). Bamford et al. (1999) measured air-water H of PAHs at several different water heights with air flow rate 130 mL/min to 200 mL/min. They concluded that equilibrium between the gaseous and aqueous phases is established at purge height levels above 53 cm. Experiments with different PHE water solution heights were conducted with methane gas flow rate from 16 to 80 mL/min at 25°C in this work. The values of H measured at water heights of 41, 61, 80, and 81 cm are similar (relative standard deviation or RSD < 11.7%). The values of H were also measured at methane flow rates of 16, 25, 75, and 79 mL/min with water height 80 to 81 cm. No significant difference was found (RSD < 5.5%).

To check the possible chemical interactions among chemicals, the values of H for NAPH alone and PHE alone were measured at 25°C. T-test shows that the Henry's law constants obtained by using single chemical do not significantly differ from those by using a mixture of three chemicals (p-value > 50% for NAPH and p-value > 20% for PHE).

Table 4.8 Air-water Henry's law constants (H_{cc} , dimensionless) at 25°C

| Chemicals | This work Mean \pm stdev. (n=6) | Literature |
|-----------|--------------------------------------|---|
| NAPH | $0.0197 \pm 1.73 \times 10^{-3}$ | 0.0197 (Mackay, et al., 1997) 0.0182 (20°C) (De Maagd, et al., 1998) |
| PHE | $0.00148 \pm 6.69 \times 10^{-5}$ | 0.00161 (Mackay and Shiu, (1981) 0.0016 (Mackay, et al., 1997) |
| PYR | $0.000516 \pm 7.44 \times 10^{-5}$ | 0.00069 (Bamford, et al., 1999) 0.000484 (Mackay and Shiu, 1981) |

Table 4.8 lists values of air-water H from literature and this work. Air-water Henry's law constants of three compounds from this study are almost the same as the data from literature. This demonstrates the accuracy of the apparatus.

The values of methane-water H for three PAHs were measured at five different temperatures (Table 4.9). A t-test was performed and no statistic difference was found between

air-water H and methane-water H of the three compounds at 25 °C (p-value > 15% for NAPH, p-value > 10% for PHE and p-value > 25% for PYR).

Table 4.9 Methane-water Henry's law constants measured at different temperatures (H_{cc} , dimensionless)

| Chemicals | 5.0 °C | 10.0 °C | 18.0 °C | 25 °C | 30.2°C |
|-----------|---|--|--|---|--|
| NAPH | 56×10 ⁻⁴ ±2.8×10 ⁻⁴ n=6 (53×10 ⁻⁴ , 59×10 ⁻⁴) | 78.4×10 ⁻⁴ ±7.6×10 ⁻⁴ n=8 (72×10 ⁻⁴ , 85×10 ⁻⁴) | 136×10 ⁻⁴ ±7.4×10 ⁻⁴ n=6 (128×10 ⁻⁴ , 144×10 ⁻⁴) | 201×10 ⁻⁴ ±10.2×10 ⁻⁴ n=16 (195×10 ⁻⁴ , 207×10 ⁻⁴) | 298×10 ⁻⁴ ±34.3×10 ⁻⁴ n=6 (262×10 ⁻⁴ , 334×10 ⁻⁴) |
| PHE | 3.09×10 ⁻⁴ ±0.37×10 ⁻⁴ n=6 (2.6×10 ⁻⁴ , 3.5×10 ⁻⁴) | 4.92×10 ⁻⁴ ±0.82×10 ⁻⁴ n=8 (4.2×10 ⁻⁴ , 5.7×10 ⁻⁴) | 7.99×10 ⁻⁴ ±0.76×10 ⁻⁴ n=6 (7.1×10 ⁻⁴ , 8.8×10 ⁻⁴) | 16×10 ⁻⁴ ±0.17×10 ⁻⁴ n=16 (15×10 ⁻⁴ , 17×10 ⁻⁴) | 22.6×10 ⁻⁴ ±3.9×10 ⁻⁴ n=6 (18.5×10 ⁻⁴ , 26.7×10 ⁻⁴) |
| PYR | 0.654×10 ⁻⁴ ±0.124×10 ⁻⁴ n=6 (0.52×10 ⁻⁴ , 0.79×10 ⁻⁴) | 1.18×10 ⁻⁴ ±0.38×10 ⁻⁴ n=8 (0.86×10 ⁻⁴ , 1.5×10 ⁻⁴) | 2.41×10 ⁻⁴ ±1.36×10 ⁻⁴ n=6 (0.98×10 ⁻⁴ , 3.9×10 ⁻⁴) | 4.75×10 ⁻⁴ ±1.51×10 ⁻⁴ n=4 (2.3×10 ⁻⁴ , 7.2×10 ⁻⁴) | 8.46×10 ⁻⁴ ±0.63×10 ⁻⁴ n=6 (7.7×10 ⁻⁴ , 9.1×10 ⁻⁴) |

Mean ± standard deviation and 95% confidence intervals in parentheses

4.2.3.2 Correlation between log H and Molar Volume at 25 °C

Several researchers suggested that the relationship between log H for PAHs and molar volume (MV) be described by a linear fit (DeMaagd et al., 1998; Mackay et al., 1981; Bamford

et al., 1999, 2000, and 2002). However, Mackay et al. (1992) did not predict a simple linear relationship between $\log H$ and molar volume for a wide range of PAHs. Anyway, it is a common trend that the values of H decrease with molar volume. Figure 4.12 is the plot of $\log H$ (methane-water) and molar volume (cm^3/mol) of three PAHs at 25 °C. It seems that there is a good linear relationship between $\log H$ and molar volume in the MV range of 148 to 214 (cm^3/mol). The linear regression gave a slope and standard error of the slope to be -0.02279 ± 0.00051 , intercept and standard error of the intercept 5.08197 ± 0.09094 and r^2 0.9836.

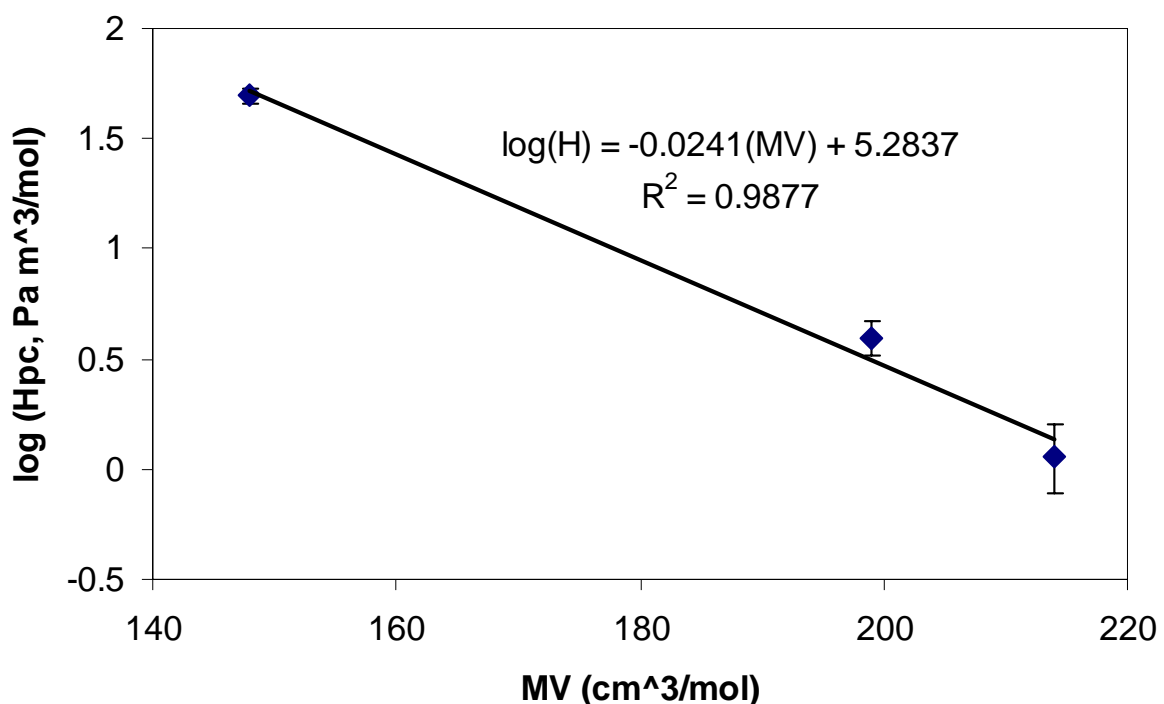


Figure 4.12 \log Henry's law constant (methane-water, $\text{Pa m}^3/\text{mol}$) with molar volume (MV, cm^3/mol) for the three PAHs at 25 °C.

4.2.3.3 Determination of Enthalpy and Entropy of Phase Change

As discussed before, the slope and the intercept from the plot of $\ln H$ versus reciprocal temperature yield the enthalpy and entropy of phase change respectively (Figure 4.13), or $-\Delta H$

is equal to the slope multiplied by R and ΔS is equal to the intercept multiplied by R . Table 4.10 lists the results for the three chemicals and the linear regression analysis with SAS (Statistic Analysis System). The $r^2 > 0.888$ for all the three compounds indicates reasonably good linear relationship between $\ln H$ and $1/T$. It also validates the assumption that ΔH and ΔS are independent of temperature in the experimental temperature range.

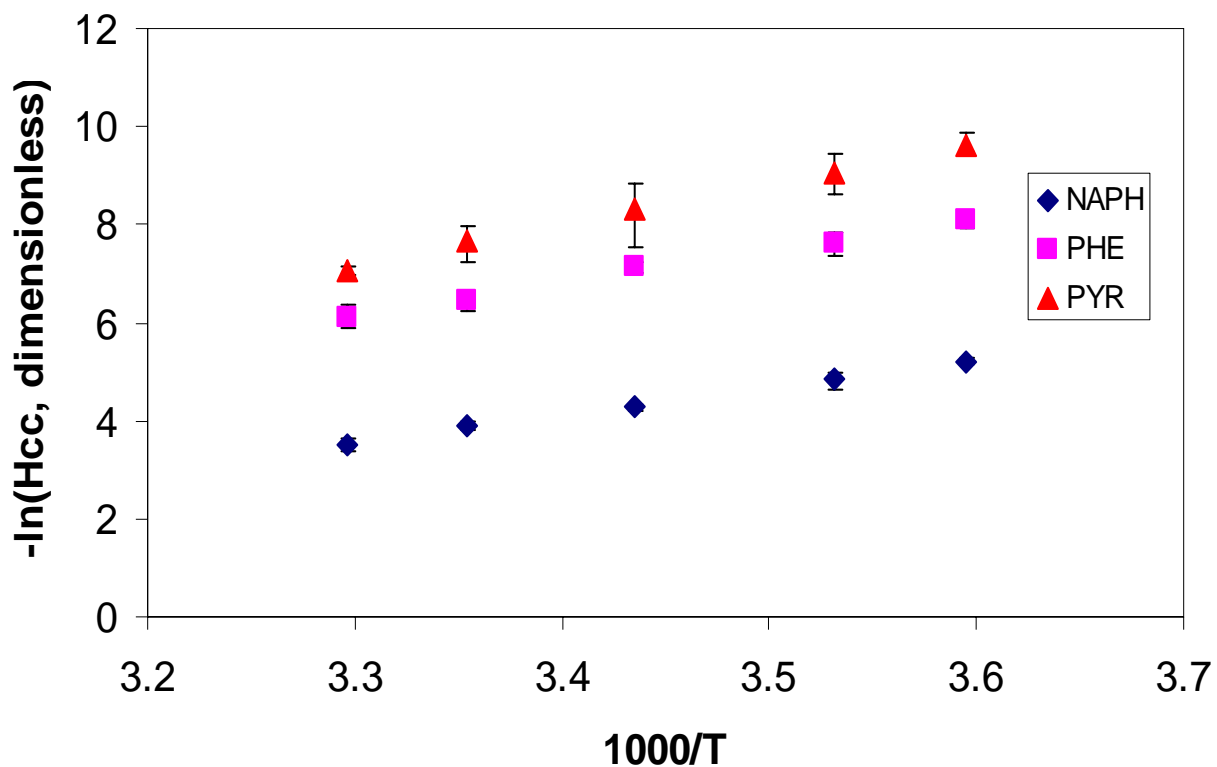


Figure 4.13 Influence of temperature on the methane-water Henry's law constant for the three PAHs in this work.

Table 4.10 Enthalpy and entropy of phase change (methane-water)

| Chemicals | ΔH (kJ/mol) | ΔS (kJ/mol-K) | R^2 | n |
|-----------|---------------------|-----------------------|--------|----|
| NAPH | 45.34 ± 0.94 | 0.1198 ± 0.0032 | 0.9831 | 42 |
| PHE | 55.64 ± 1.65 | 0.1328 ± 0.0057 | 0.9659 | 42 |
| PYR | 69.71 ± 4.66 | 0.1702 ± 0.0161 | 0.8886 | 30 |

Mean \pm standard error (se)

4.2.3.4 The Enthalpy-Entropy Compensation Analysis

Plots of ΔH versus ΔS often form straight lines (Leffler et al., 1963, and Hammett, L. P., 1970). This relationship is called the enthalpy-entropy compensation effect or the isokinetic effect. Krug et al. (1996 a, b c) demonstrated that many reported linear relationships between enthalpy and entropy were due to statistical propagation of errors, and they also noted that linear compensation might be a local linearity of a nonlinear function. However, chemical compensation analysis may serve to identify common behavior mechanisms (Tomlinson, E., 1983; Bustamante, 1996). Bamford et al. (1999) once employed the relationship to check whether the system was in equilibrium. Figure 4.14 illustrates a good linear relationship between ΔH and ΔS for the three compounds in this work ($r^2=0.9665$), suggesting the system to achieve equilibrium. This is consistent with the experimental results in the method verification section. The linear regression analysis of the plot ΔH versus ΔS yielded the slope \pm standard error 0.0021 ± 0.0004 and the intercept \pm standard error 0.0213 ± 0.0226 .

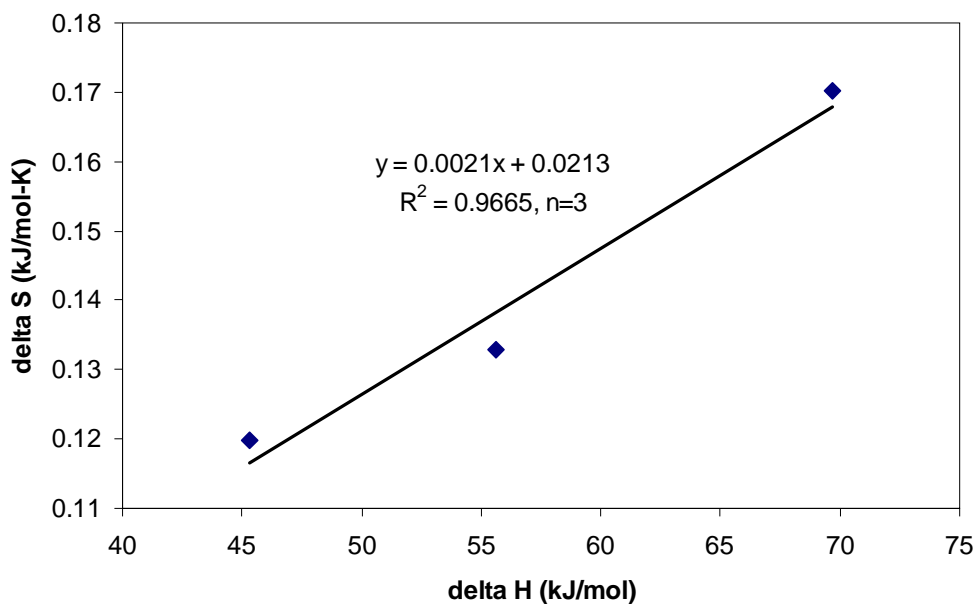


Figure 4.14 Relationship between enthalpy and entropy of phase change for the three PAHs in this work (methane-water).

4.2.4 Summary

A t-test was performed and no statistical difference was found between air-water H and methane-water H of the three compounds at 25 °C. van't Hoff equation (4.6) or (4.7) can be used to model the temperature-dependence H data. The relationships established in this work can be used to estimate the values of H (methane-water) at any temperature for the three chemicals in the experimental temperature range. They are useful for predicting the values of H (methane-water) of other PAHs; however, further investigation is necessary.

4.3 Mathematical Modeling

In this section, a model for contaminant transport associated with bubble ebullition is constructed for both capped and uncapped sediment systems. The model is verified with the data from the bubble column experiments, and used to investigate the effects of several factors (gas flux, total suspended soil and sand cap) on the contaminant flux under field conditions. Model sensitivity is also analyzed with the cap thickness and fractional organic carbon for capped sediment.

4.3.1 Model Development

4.3.1.1 Assumptions

In our bubble column experiments, no obvious PHE concentration variation was observed in the sediment, and the PHE concentrations at the different positions in the slurry/water were similar. The bubble movement could make pore water circulate in sediment, and slurry be well mixed. This leads to an assumption that contaminant concentration is uniform in each compartment.

Experiments were conducted to test how long it takes for the equilibrium to be established between water and methane bubbles by changing the water height in a bubble column

(section 4.2). The experimental results show that the bubble residence time in the column for the equilibrium is less than an hour. However, it takes days of time for bubble growth (Boudreau et al., 2001a; Boudreau et al., 2001b). Therefore, the time for gas bubbles to grow and move out of sediment is long enough for contaminants to reach the equilibrium between the gas and aqueous phase. Chanton et al. (1989) measured the methane composition in the bubbles and its concentration in the sediment pore waters, and concluded that the equilibrium existed between gas bubble and bulk pore water. So we assume that local equilibrium exists among soil particle, aqueous phase and gas.

Field observations show that bubbles form in organic-rich sediments on annual time scales (Strayer and Tiedje, 1978; Martens and Klump, 1980; Chanton et al., 1989). But methane fluxes vary seasonally (Kipphut and Martens, 1982) primarily due to variations in temperature (Huls and Costello, 2005). In principle, methane flux is time dependent. Inclusion of such time independence can be easily done if the functionality is known, without adding fundamentally important new chemistry or physics to the model. To simplify, we chose to treat it as a constant.

4.3.1.2 Uncapped Sediment

Figure 4.15 is a schematic of sediment and contaminant movement during bubble ebullition in uncapped contaminated sediment. The whole system (Figure 4.15) consists of three compartments – sediment, slurry (suspended sediment plus overlying water) and the air, which are like tanks in series. Mass balances for each compartment are as follows.

For the sediment layer, the gases generated in the sediment will bring contaminant from porewater by partitioning into the overlying water. The mass balances can be described by the following equation.

$$\frac{d(A_s L_s \rho_b W_{s1})}{dt} = -F_g A_s H C_{w1}(t) \quad (4.9)$$

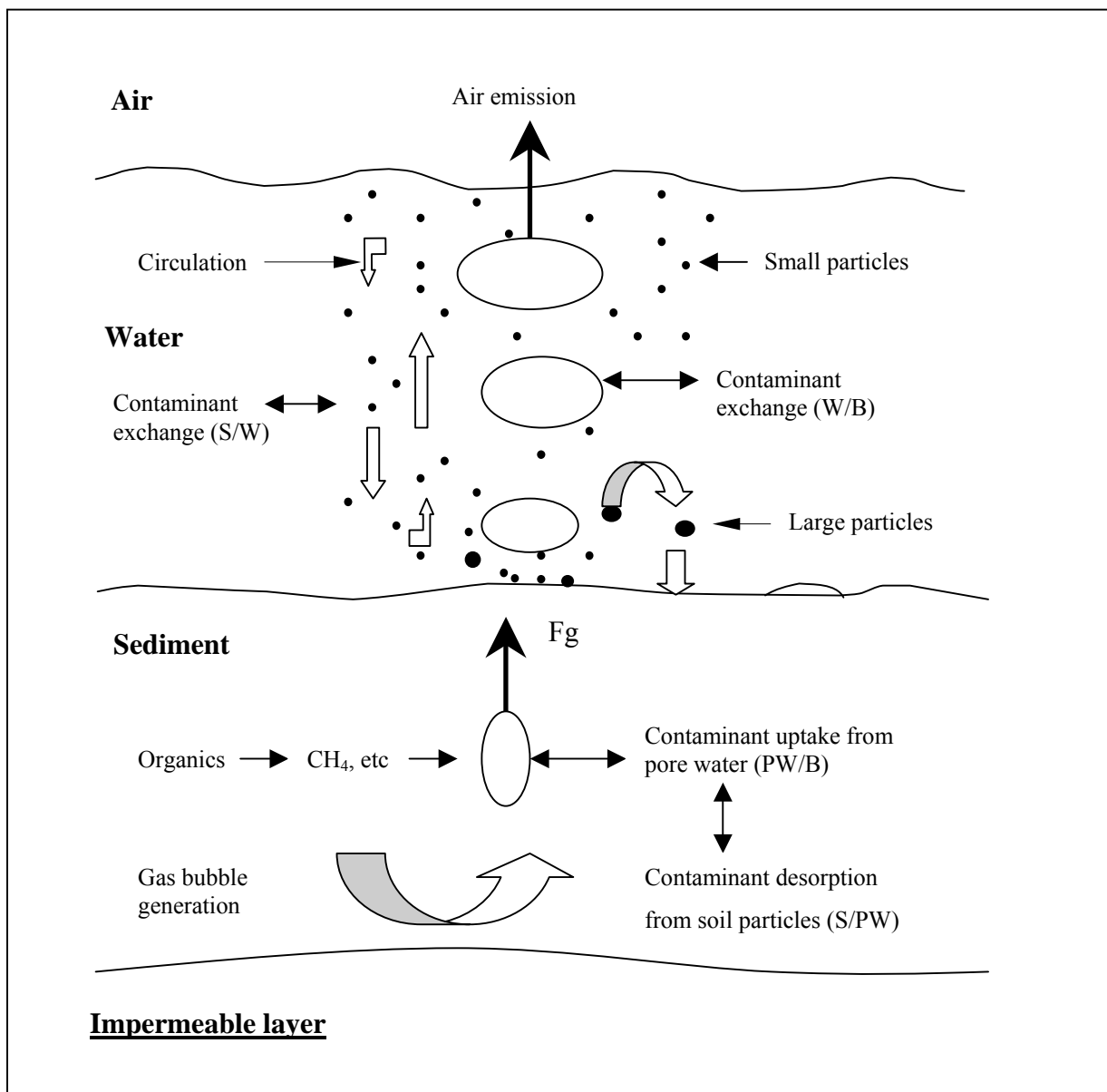


Figure 4.15 A schematic of sediment and contaminant movement in uncapped contaminated sediment during gas bubble ebullition (S = soil particles, PW = pore water, W = water, and B = bubbles).

where A_s is the cross section area of the sediment (m^2), L_s is the depth of the contaminated sediment (m), ρ_b is the sediment bulk density (kg/m^3), W_{s1} is the sediment loading (kg/kg), F_g is the methane gas flux (m^3/m^2-s), H is the Henry's law constant (methane-water, dimensionless), $C_{w1}(t)$ is the contaminant concentration in the porewater.

At equilibrium, the relationship between the sediment loading and contaminant concentration in the porewater is from the mass balance considerations

$$W_{s1}(t) = \frac{\varepsilon + K_d \rho_b}{\rho_b} C_{w1}(t) \quad (4.10)$$

where ε is the sediment porosity, K_d is the partition coefficient between water and sediment (m^3/kg), which can be estimated by the equation $K_d = K_{oc} f_{oc}$, K_{oc} is the organic carbon-water partition coefficient, f_{oc} is the fractional organic carbon.

Substituting equation (4.10) into (4.9) gives

$$\frac{dC_{w1}}{dt} = -\frac{F_g H}{L_s (\varepsilon + K_d \rho_b)} \cdot C_{w1}(t) \quad (4.11)$$

The slurry compartment gains contaminant mass from the gas bubbles and suspended sediment out of the sediment layer, and loses contaminant mass to gas bubbles out of the slurry.

Mass balance in this layer results in

$$\frac{d(\rho_{ss} V_w W_{s2})}{dt} = \frac{d(\rho_{ss} V_w W_{s1})}{dt} + F_g A_s H (C_{w1}(t) - C_{w2}(t)) \quad (4.12)$$

where ρ_{ss} is the total suspended soil (kg/m^3), V_w is the slurry volume (m^3), W_{s2} is the sediment loading in the slurry (kg/kg), and C_{w2} is the contaminant concentration in the aqueous phase of the slurry (kg/m^3).

The relationship between the sediment loading and aqueous contaminant concentration in the slurry can also be obtained from the mass balance

$$W_{s2}(t) = \frac{1 + K_d \rho_{ss}(t)}{\rho_{ss}(t)} C_{w2}(t) \quad (4.13)$$

Combining equations (4.10) through (4.13) and considering V_w a constant

($V_w \approx V_{w0} = A_s L_w$ since $\frac{\rho_{ss}(t)}{\rho_{sb}} \ll 1$, where L_w is the overlying water depth) yield:

$$\frac{dC_{w2}}{dt} = \left[\frac{\frac{\varepsilon + K_d \rho_b}{\rho_b} \frac{d\rho_{ss}}{dt} - \frac{F_g H \rho_{ss}(t)}{\rho_b L_s} + \frac{F_g H}{L_w}}{(1 + K_d \rho_{ss}(t)))} \right] \cdot C_{w1}(t) - \left[\frac{\frac{F_g H}{L_w} + K_d \frac{d\rho_{ss}}{dt}}{(1 + K_d \rho_{ss}(t)))} \right] \cdot C_{w2}(t) \quad (4.14)$$

The flux of contaminant ($\text{kg/m}^2\text{-s}$) into the air compartment can be calculated by

$$f_{ca}(t) = F_g H C_{w2}(t) \quad (4.15)$$

To normalize the system in the contaminant concentrations and flux, the following nondimensional parameters are defined,

$$C_1 = \frac{C_{w1}}{C_{w10}}, \quad C_2 = \frac{C_{w2}}{C_{w10}}, \quad W_1 = \frac{W_{s1}}{W_{s10}}, \quad F_{ca} = \frac{f_{ca}}{f_{cw0}} = \frac{F_g H C_{w2}}{F_g H C_{w10}} = C_2$$

where C_{w10} is the initial contaminant concentration in sediment pore water (kg/m^3), W_{s10} is the initial sediment loading (kg/kg), and f_{cw0} is the initial contaminant flux from sediment into slurry by water/gas partitioning process ($\text{kg/m}^2\text{-s}$).

The model for uncapped sediment from equations (4.11), (4.14) and (4.15) can be expressed as in the above normalized parameters

$$\frac{dC_1}{dt} = - \frac{F_g H}{L_s (\varepsilon + K_d \rho_b)} \cdot C_1(t) \quad (\text{Sediment layer}) \quad (4.11')$$

$$\frac{dC_2}{dt} = \left[\frac{\varepsilon + K_d \rho_b}{\rho_b} \frac{d\rho_{ss}}{dt} - \frac{F_g H \rho_{ss}(t)}{\rho_b L_s} + \frac{F_g H}{L_w} \right] \cdot C_1(t) - \left[\frac{F_g H}{L_w} + K_d \frac{d\rho_{ss}}{dt} \right] \cdot C_2(t) \quad (\text{Slurry layer}) \quad (4.12')$$

$$F_{ca}(t) = C_2(t) \quad (\text{Normalized contaminant flux into the air}) \quad (4.15')$$

with initial conditions $C_1(t=0) = 1$, $C_2(t=0) = 0$

4.3.1.3 Capped Sediment

A sand cap can effectively prevent or at least decrease sediment suspension. For capped sediment without sediment suspension ($\rho_{ss} = 0$), we have four compartments – sediment, sand cap, overlying water and the air. Let C_{sd} ($= C_{wsd} / C_{w10}$) and L_{sd} represent the normalized contaminant concentration in the sand and sand depth (m) respectively. Following the procedure for uncapped sediment, we can obtain the model for capped system

$$\frac{dC_1}{dt} = -\frac{F_g H}{L_s (\varepsilon + K_d \rho_b)} \cdot C_1(t) \quad (\text{Sediment layer}) \quad (4.16)$$

$$\frac{dC_{sd}}{dt} = \frac{F_g H}{L_{sd} (\varepsilon_s + K_{ds} \rho_{sb})} \cdot C_1(t) - \frac{F_g H}{L_{sd} (\varepsilon_s + K_{ds} \rho_{sb})} \cdot C_{sd}(t) \quad (\text{Sand layer}) \quad (4.17)$$

$$\frac{dC_2}{dt} = \frac{F_g H}{L_w} \cdot C_{sd}(t) - \frac{F_g H}{L_w} \cdot C_2(t) \quad (\text{Overlying water layer}) \quad (4.18)$$

with initial conditions: $C_1(t=0) = 1$, $C_{sd}(t=0) = 0$, $C_2(t=0) = 0$.

The above ordinary differential equations (4.16 through 4.18) have an analytical solution.

The normalized contaminant flux into the air can be calculated by

$$F_{ca}(t) = \frac{a_2 a_3}{a_2 - a_1} \cdot \left[\frac{\exp(-a_1 t)}{a_3 - a_1} - \frac{\exp(-a_2 t)}{a_3 - a_2} - \frac{(a_1 - a_2) \exp(-a_3 t)}{(a_3 - a_1)(a_3 - a_2)} \right] \quad (4.19)$$

where $a_1 = F_g H / [L_s (\varepsilon + K_d \rho_b)]$, $a_2 = F_g H / [L_{sd} (\varepsilon_s + K_{ds} \rho_{sb})]$, $a_3 = F_g H / L_w$, ε_s is the sand porosity, ρ_{sb} is the sand bulk density (kg/m³), K_{ds} is the partition coefficient between pore water and sand (m³/kg).

4.3.2 Results and Discussion

4.3.2.1 Model Verification

The experiment with a bubble column has been described in section 4.1 and Yuan et al. (2006). The data from the experiment will compare with the model results in this section. As mentioned in 4.1.2.0 (also see Appendix F), the contaminant flux associated with bubble-wake entrainment at the aqueous-organic solvent interface is significant, and can be estimated by $\pi r_c^2 k_1 C_w$. Therefore, the model for uncapped sediment in the column experiment is given by the following equations, after the bubble-wake entrainment term is added.

$$\frac{dC_{w1}}{dt} = -\frac{Q_g H}{V_{sf} (\varepsilon_0 + K_d \rho_b)} \cdot C_{w1}(t) \quad (\text{Sediment layer}) \quad (4.20)$$

$$\frac{dC_{w2}}{dt} = \left[\frac{\varepsilon_0 + K_d \rho_b}{\rho_b} \frac{d\rho_{ss}}{dt} - \frac{Q_g H \rho_{ss}(t)}{\rho_b V_{sf}} + \frac{Q_g H}{V_w} \right] \cdot C_{w1}(t) - \left[\frac{Q_g H}{V_w} + \frac{\pi r_c^2 k_1}{V_w} + K_d \frac{d\rho_{ss}}{dt} \right] \cdot C_{w2}(t) \quad (\text{Slurry layer}) \quad (4.21)$$

$$\frac{dC_h}{dt} = \left(\frac{Q_g H}{V_h} + \frac{\pi r_c^2 k_1}{V_h} \right) C_{w2}(t) \quad (\text{Hexane layer}) \quad (4.22)$$

with initial conditions: $C_{w1}(t=0) = \rho_b W_{s1}(t=0) / (\varepsilon + K_d \rho_b)$, $C_{w2}(t=0) = 0$, $C_h(t=0) = 0$.

Here V_{sf} is the immobile (or final) sediment volume (m³) and V_w is the water or slurry volume in the column (m³), Q_g is the methane volumetric flow rate (m³/s), and V_h is the hexane volume (m³).

Equation (4.2) was used to estimate the mass transfer coefficients k_1 at two experimental gas flow rates (1.07 and 6.85 mL/min), which are necessary for the model application to the bubble column experiments. Total suspended soil (TSS, ρ_{ss}) was measured at two different methane flow rates for the uncapped sediment system. A Langmuir-like expression was used to fit the data (Figure 4.16). The operational parameters (such as V_{sf} , Q_g , V_w and V_h) in the model were measured for each specific experiment. Table 4.11 lists the general parameters used in the simulation. Please note that the measured k_1 and the best fit k_1 have the same order of magnitude for the experiment with gas flux $Q_g=1.07$ mL/min.

Table 4.11 Parameters used in the simulation

| | | | |
|--|---------------------------------------|-------------------|----------------------|
| Bubble column | Diameter (cm) | | 80 |
| | Length (cm) | | 740 |
| Sediment | Bulk density (kg/m ³) | | 789 |
| | Particle density (kg/m ³) | | 2600 |
| | Initial loading (mg/kg) | | 100 |
| | Porosity (ϵ) | | 0.69 |
| | foc (measured) | | 0.041 |
| Sand | Bulk density (kg/m ³) | | 1541 |
| | Porosity (ϵ) | | 0.5 |
| | foc | | 0.0001 |
| Phenanthrene | Log K_{oc} (m ³ /kg) | | 1.4 |
| | k_1 (m/s) | $Q_g=1.07$ mL/min | 5.6×10^{-6} |
| | | $Q_g=6.85$ mL/min | 8.9×10^{-6} |
| | $k_{1(opt.)}$ (m/s) | $Q_g=1.07$ mL/min | 2.9×10^{-6} |
| | | $Q_g=6.85$ mL/min | 20×10^{-6} |
| Henry's law constant (methane –water) (Hcc, dimensionless) | | 0.0016 | |

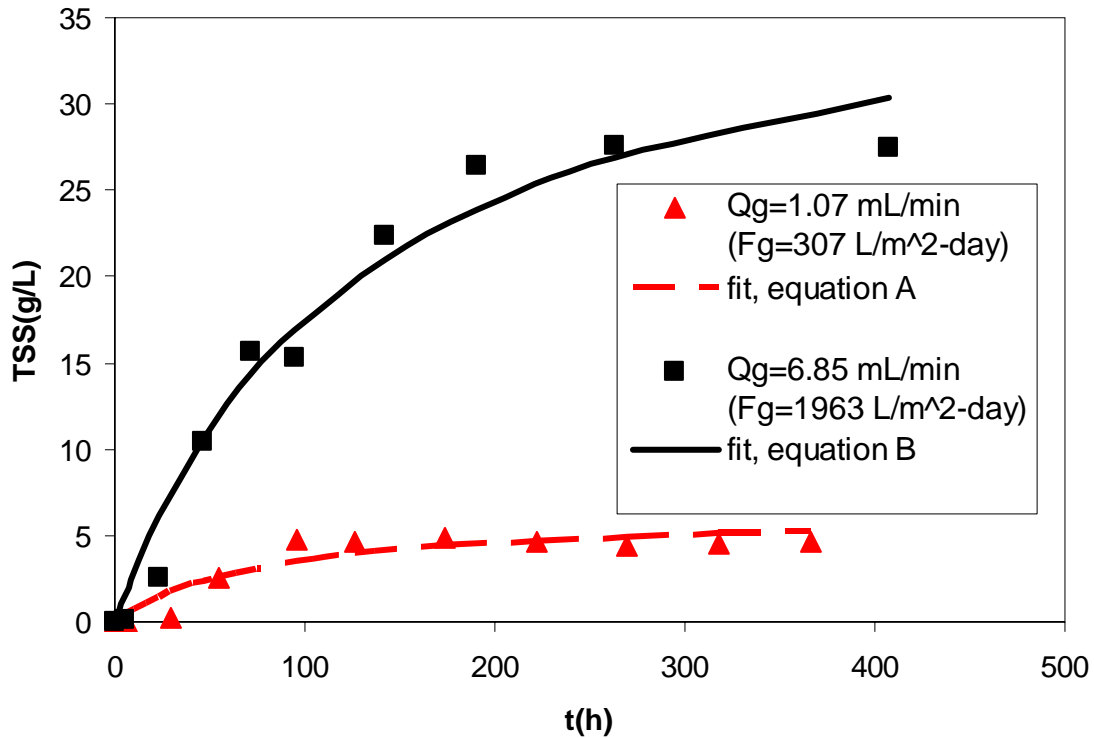


Figure 4.16 Total suspended soil (TSS, ρ_{ss}) with time at two different methane flow rates – fit equation A: $\rho_{ss}(t) = 6.4t/(81+t)$ and fit equation B: $\rho_{ss}(t) = 40t/(129+t)$ where ρ_{ss} (g/L) and t (hr).

Owing to TSS time dependence, an analytical solution to the model for uncapped sediment is impossible. Runge-Kutta Method and Adams-Moulton Method (Carnahan, et al., 1969) were used to numerically integrate these ordinary differential equations for uncapped sediment systems. In order to obtain an accurate calculation, the Runge-Kutta method was used only to calculate initial values. After enough initial values, the Adams-Moulton method was employed to continue the calculation (see Appendix B for mathematical formulas and Appendix C for MATLAB codes). The comparisons between the model and experimental results show that the model satisfactorily describes the experimental data (Figure 4.17). The parity plots (Figure 4.18 and Figure 4.19) also demonstrate a reasonable agreement between the model and the experimental data.

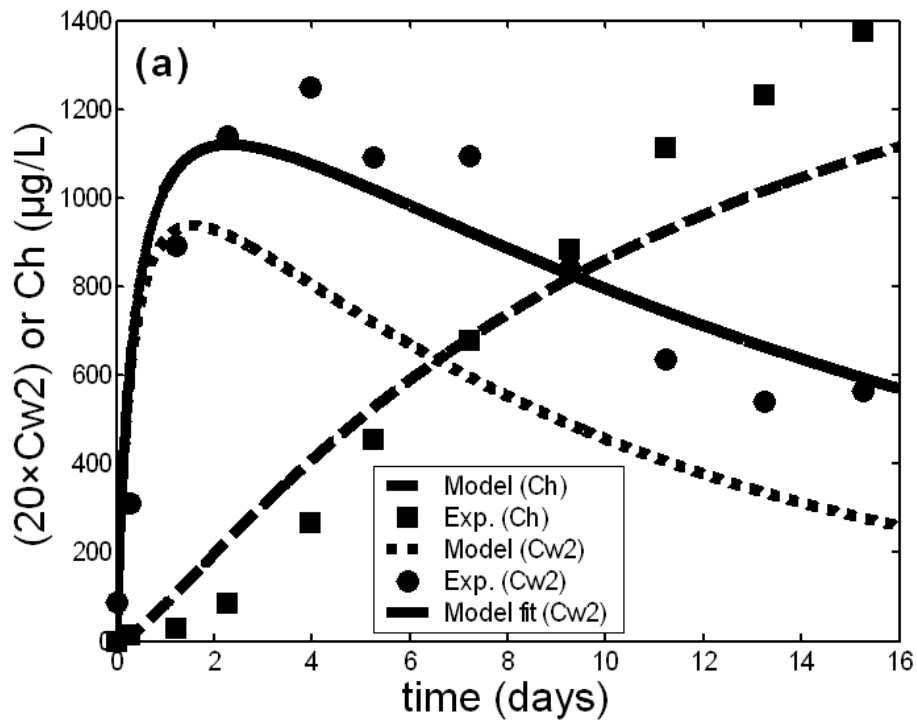
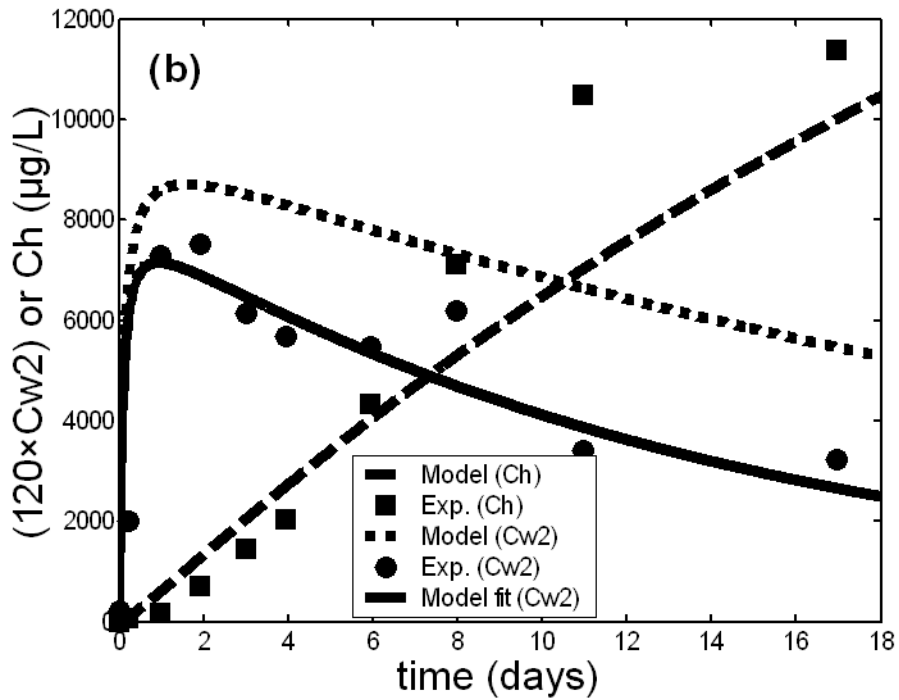


Figure 4.17 (a) Comparisons between the model and experimental results for methane flow rate $Q_g=1.07$ mL/min (307 L/m²-day), measured $k_1=5.6 \times 10^{-6}$ m/s, model fit $k_1=2.9 \times 10^{-6}$ m/s.



(b) Comparisons between the model and experimental results for methane flow rate $Q_g=6.85$ mL/min (1963 L/m²-day), measured $k_1=8.9 \times 10^{-6}$ m/s, model fit $k_1=2 \times 10^{-5}$ m/s.

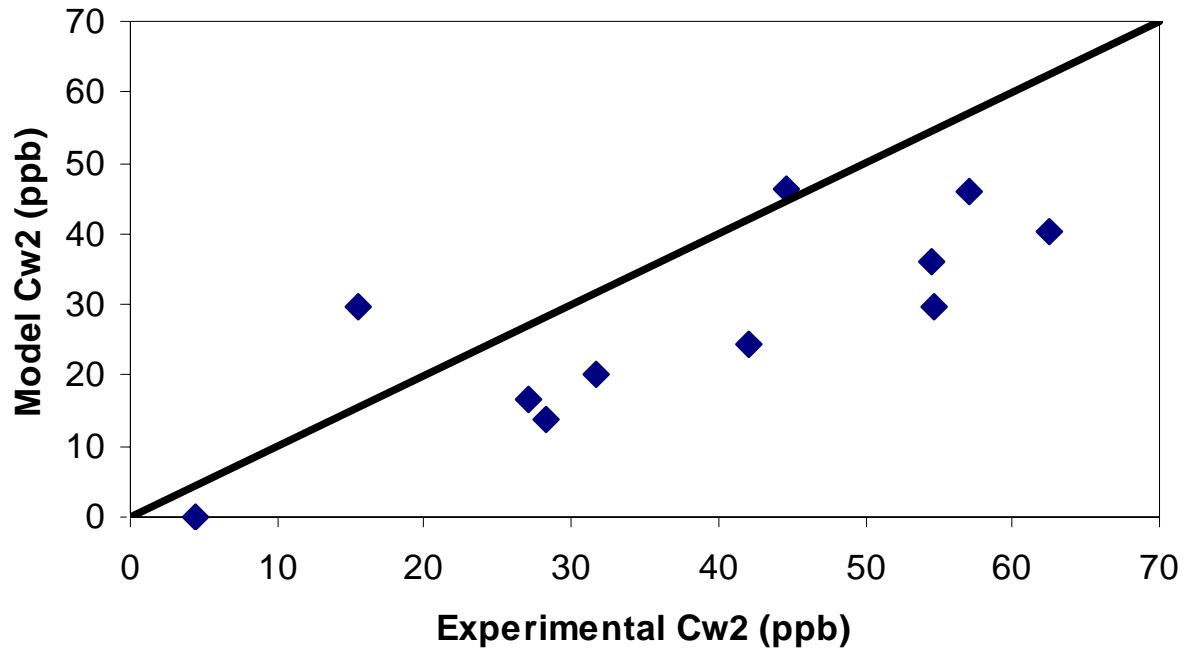
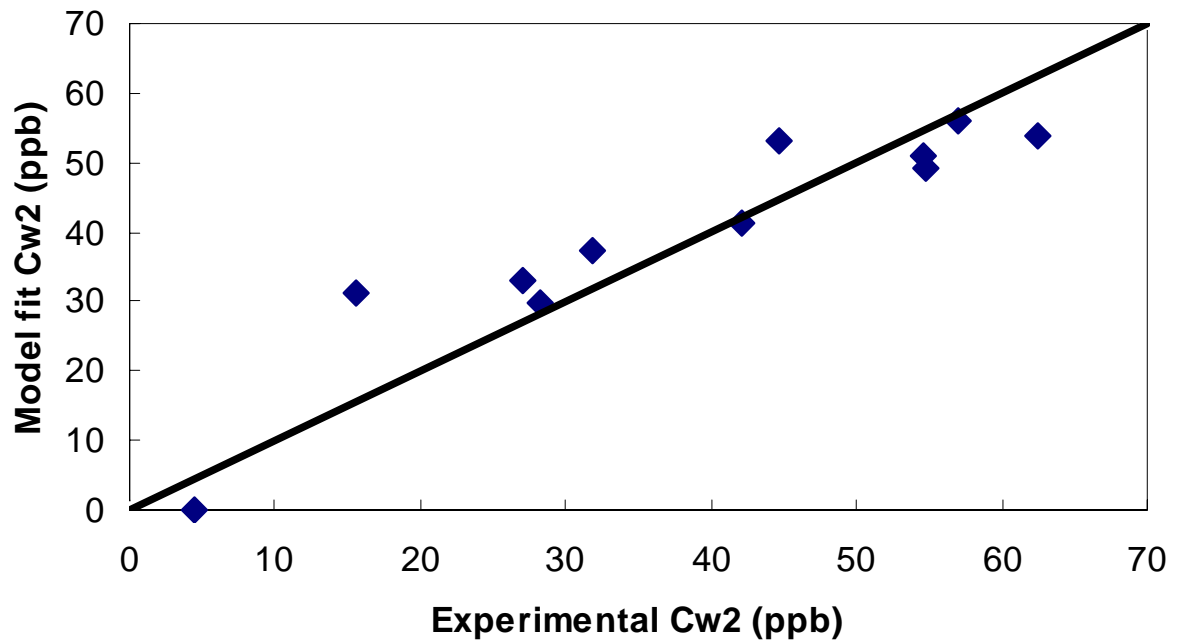
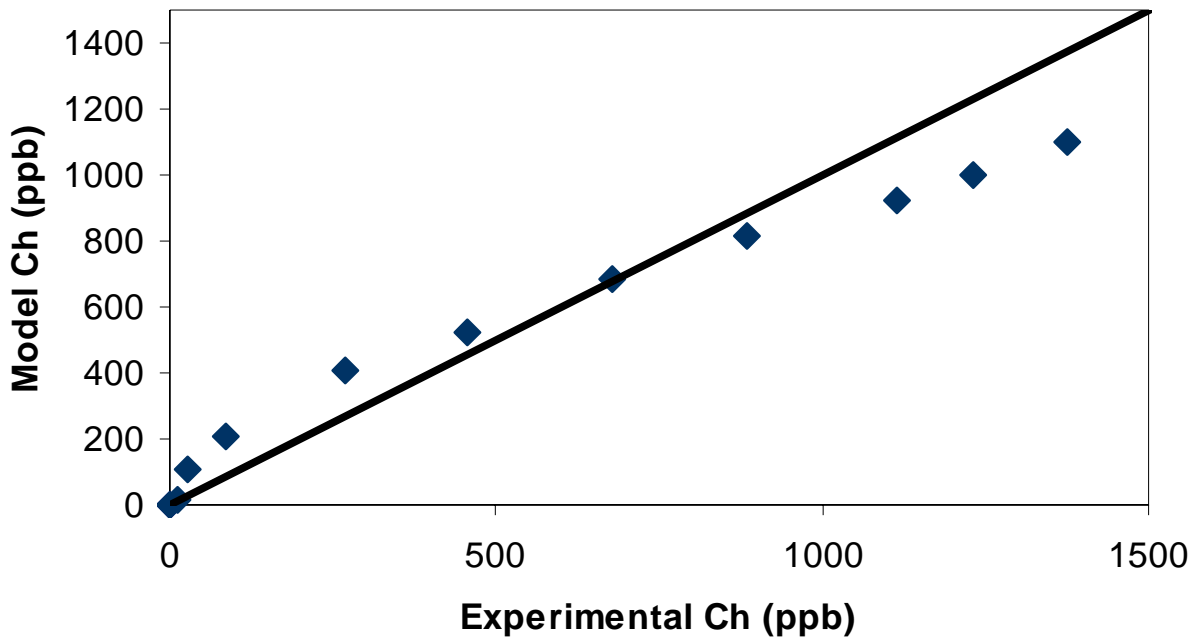


Figure 4.18 (a) Parity plots for $Q_g=1.07$ mL/min, C_{w2} (model, RMSE=12.5)
 RMSE= Square Root of the Mean Square Error.



(b) Parity plots for $Q_g=1.07$ mL/min, C_{w2} (model fit, RMSE=7.0). (Fig. con'd.)



(c) Parity plots for $Q_g=1.07$ mL/min, Ch (model, RMSE=140).

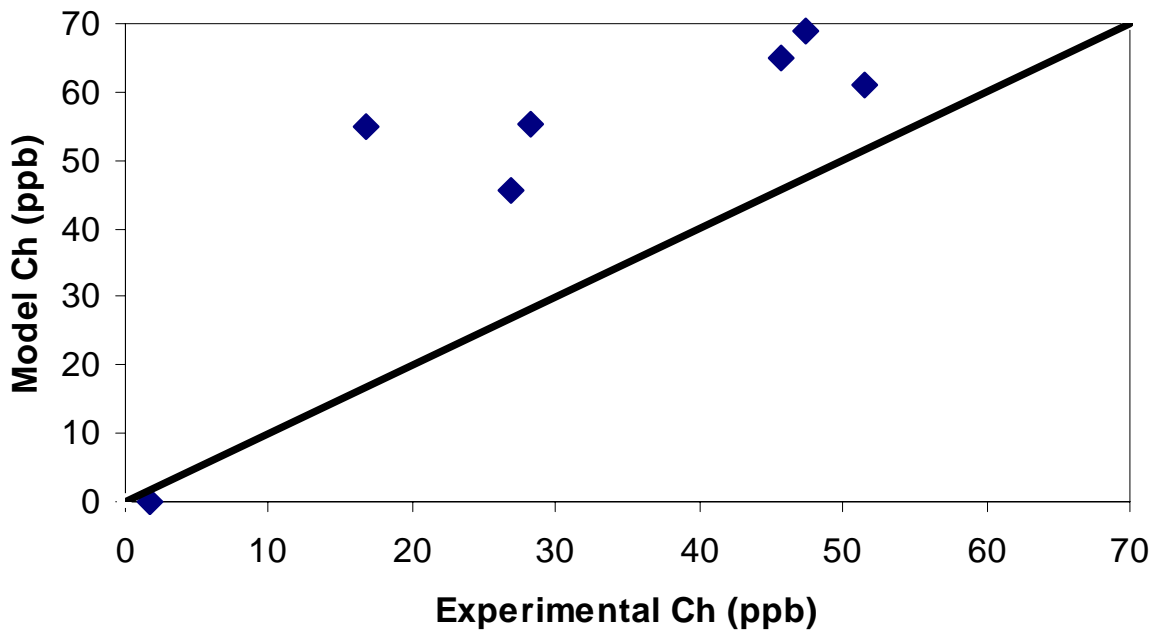
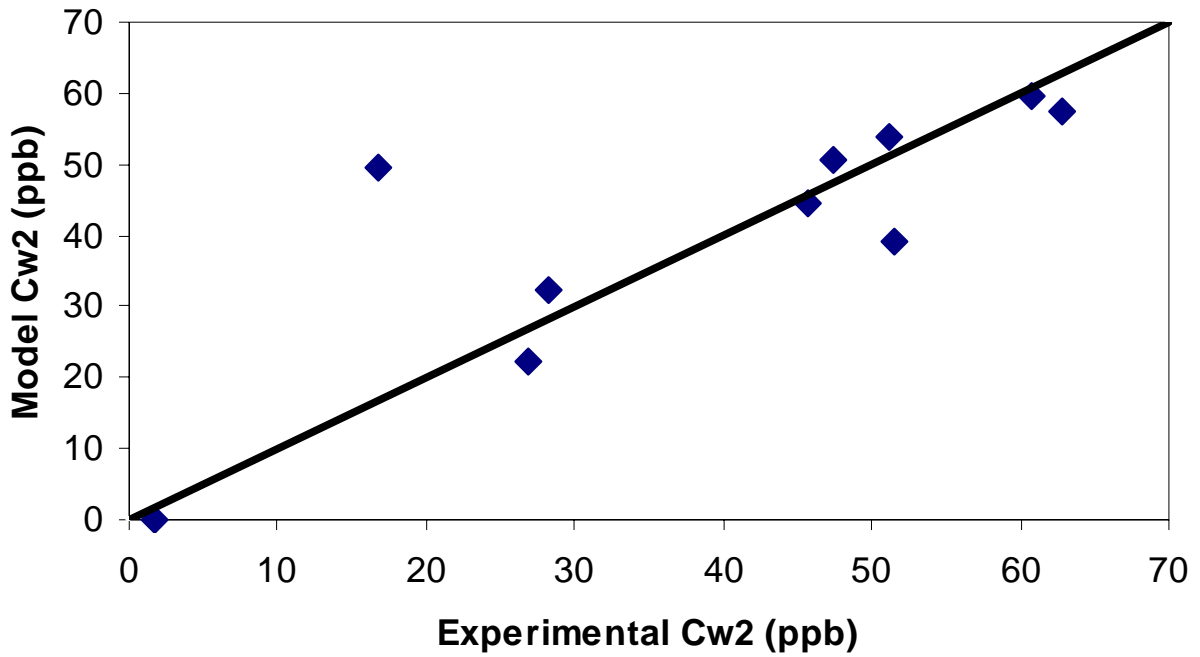
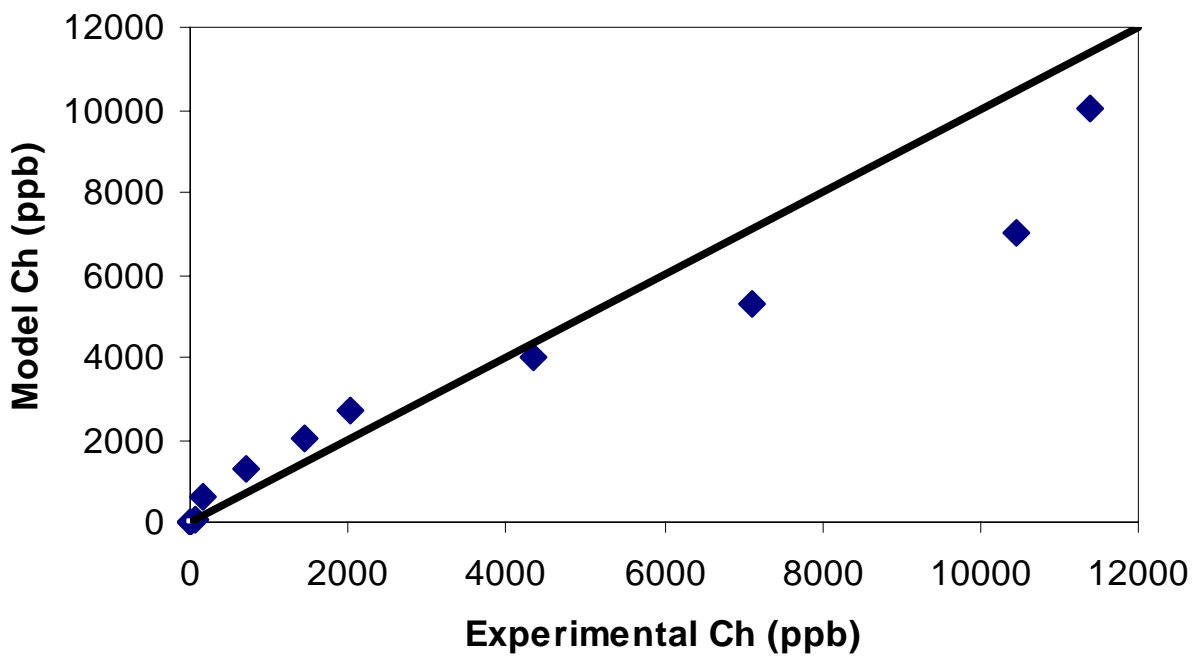


Figure 4.19 (a) Parity plots for $Q_g=6.85$ mL/min, C_{w2} (model, RMSE=21.7). (Fig. con'd)



(b) Parity plots for $Q_g=6.85$ mL/min, C_{w2} (model fit, RMSE=11.5).



(c) Parity plots for $Q_g=6.85$ mL/min, Ch (model, RMSE=1363).

4.3.2.2 Model Performance under Field Conditions

Let us assume that the depth of the contaminated sediment is 2 meters, the sand cap 0.3 meter and overlying water 3 meters. Field methane gas flux measured from the Anacostia River sediment is around 1 L/m²-day at 22 °C (Himmelheber and Hughes, 2005). The PHE loading measured in the Anacostia River sediment (4.1.1.1) is around 0.68 mg/kg. The steady state TSS measured in the column experiment shows a good linear relationship with methane gas flux ($TSS(g/L, at \text{ steady state}) = 4.05Q_g (mL/min)$, $r^2 > 0.99$, methane gas flow rate from 0.66 mL/min (189 L/m²-day) to 6.85 mL/min (1963 L/m²-day)). This linear relationship and measured $\rho_{ss}(t)$ at methane flow rate of 1.07 mL/min (307 L/m²-day) were used to estimate $\rho_{ss}(t)$ at the field methane flow rate (1 L/m²-day). The other parameters are from Table 4.11.

Figure 20 (a) shows that the PHE flux into the air increases with time dramatically at the beginning and finally reaches a plateau for uncapped sediment. The aqueous phase PHE concentration in the slurry follows the same trend (Figure 20(b)). This is because TSS increases quickly at the beginning and finally reaches a constant value; TSS is a main contributor for aqueous phase PHE concentration that determines the PHE flux into the air (Equation (4.15)). For capped sediment, the only contributor to the PHE flux into the air and PHE concentration in water phase is gas bubbles by the partitioning process. So it is increasing along the time, but much (six orders of magnitude in the simulation time scale) smaller than that for uncapped sediment. Since the gas bubbles release PHE into the sand porewater when going through the sand layer, the PHE concentration in the sand keeps increasing with time (Figure 20(c)). The sediment loadings for both uncapped and capped sediments should decrease with time because of PHE partitioning into the gas bubbles from sediment pore water. The trend of sediment loadings with time can only be seen in a large time scale.

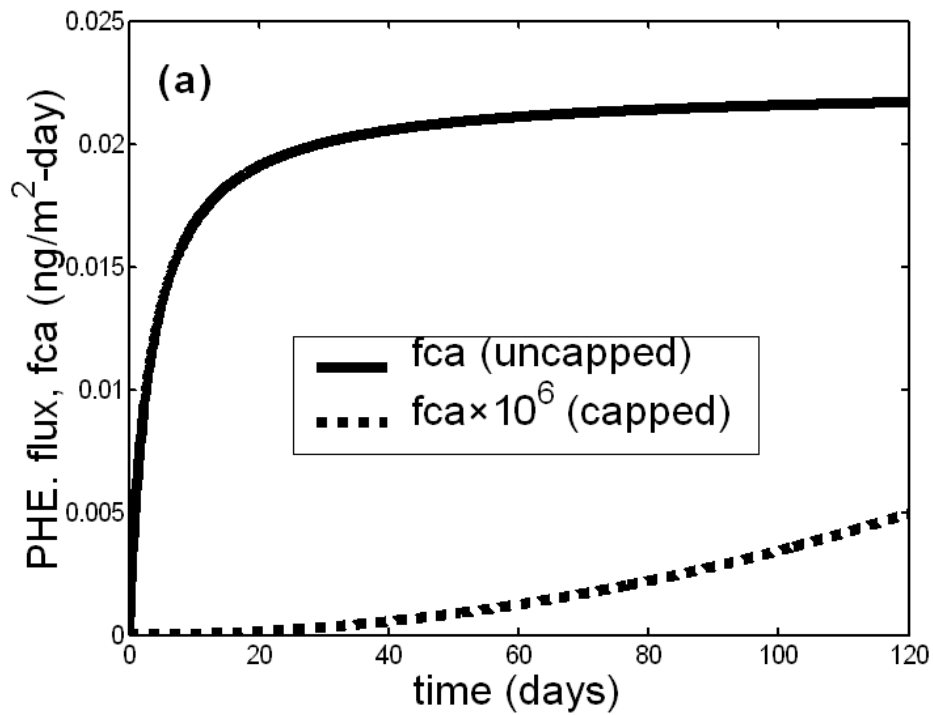
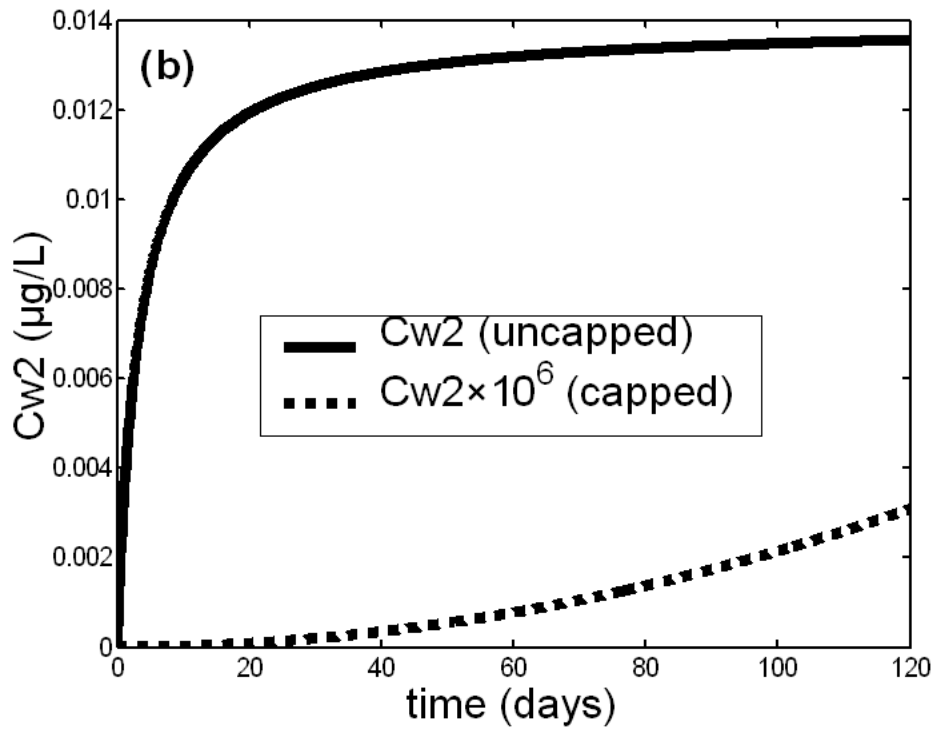
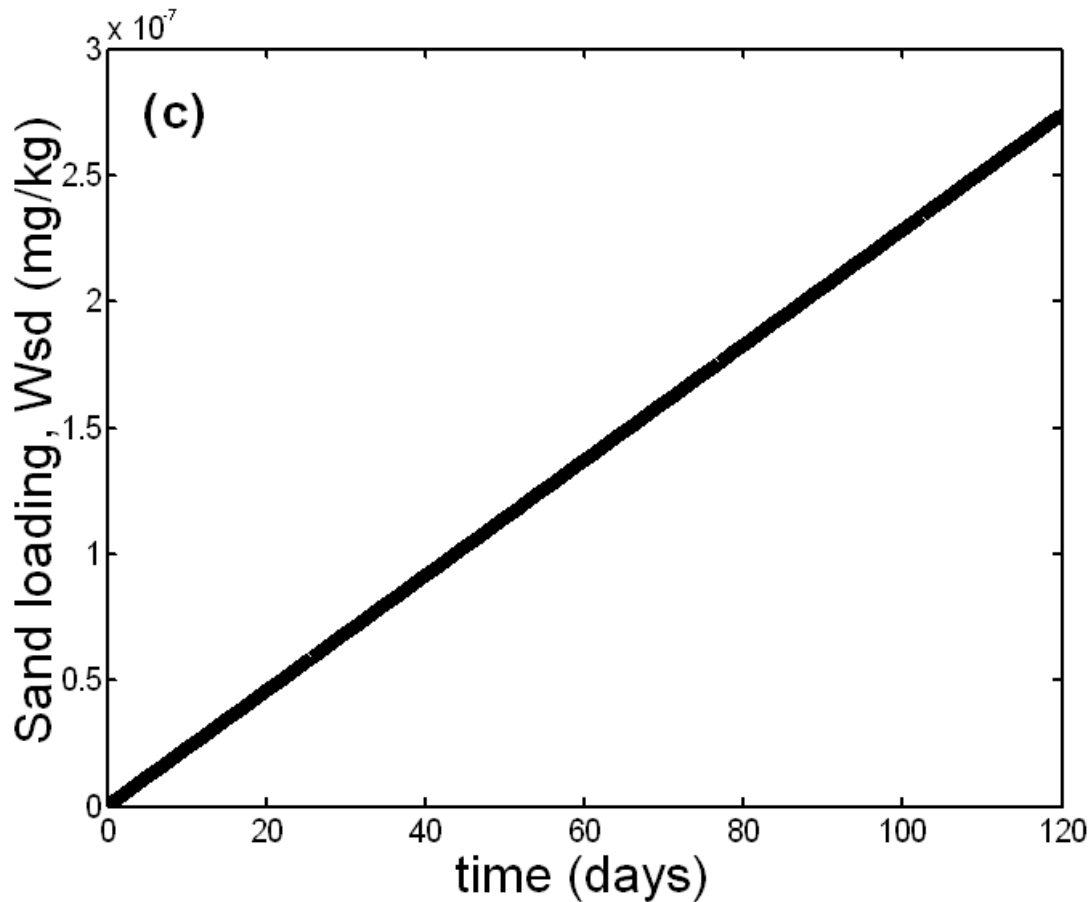


Figure 4.20(a) Comparison of PHE flux into the air between uncapped and capped sediment.



(b) Comparison of aqueous phase PHE concentration in slurry between uncapped and capped sediment. (Fig. con'd)



(c) PHE loading in sand.

4.3.2.3 Effects of Gas Flux, TSS and Cap on Contaminant Flux

Gas flux, TSS and sand cap are three main factors for contaminant transport associated with bubble ebullition in contaminated sediment. Figure 4.21 demonstrates their effects on the contaminant flux into the air. For both uncapped and capped sediments, the contaminant fluxes into the air increase with methane gas flux (Figure 4.21(a) and (b)). As expected, the contaminant flux into the air for uncapped sediment (with sediment suspension) is much larger than the contaminant flux for capped sediment (without sediment suspension). Figure 4.21(c) demonstrates the influence of the gas flux on the contaminant flux for uncapped sediment (without sediment suspension). It rarely exists in the real world that there is no sediment

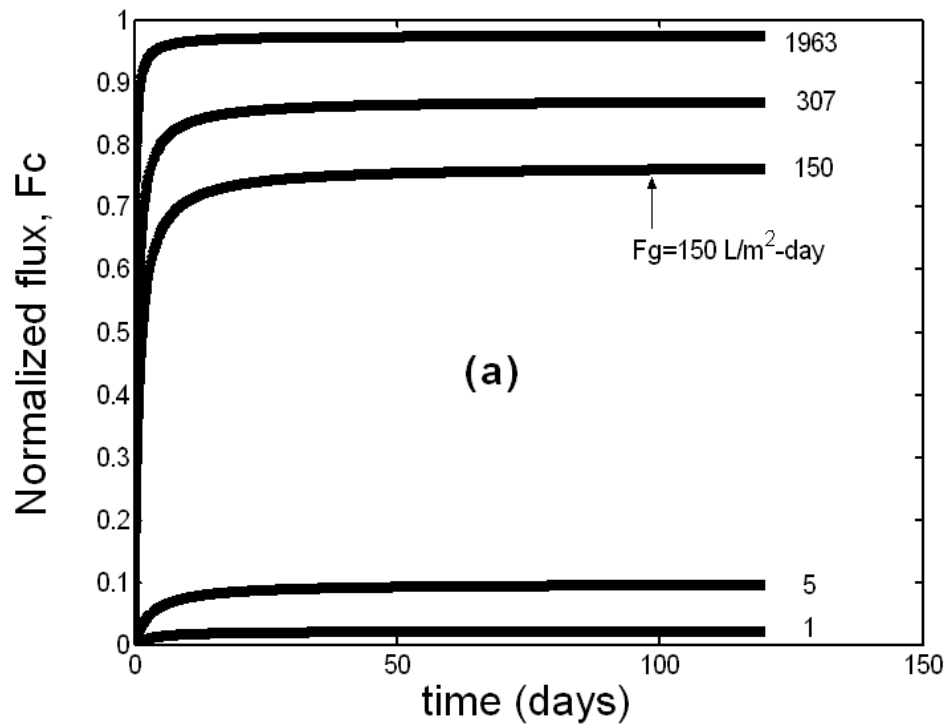
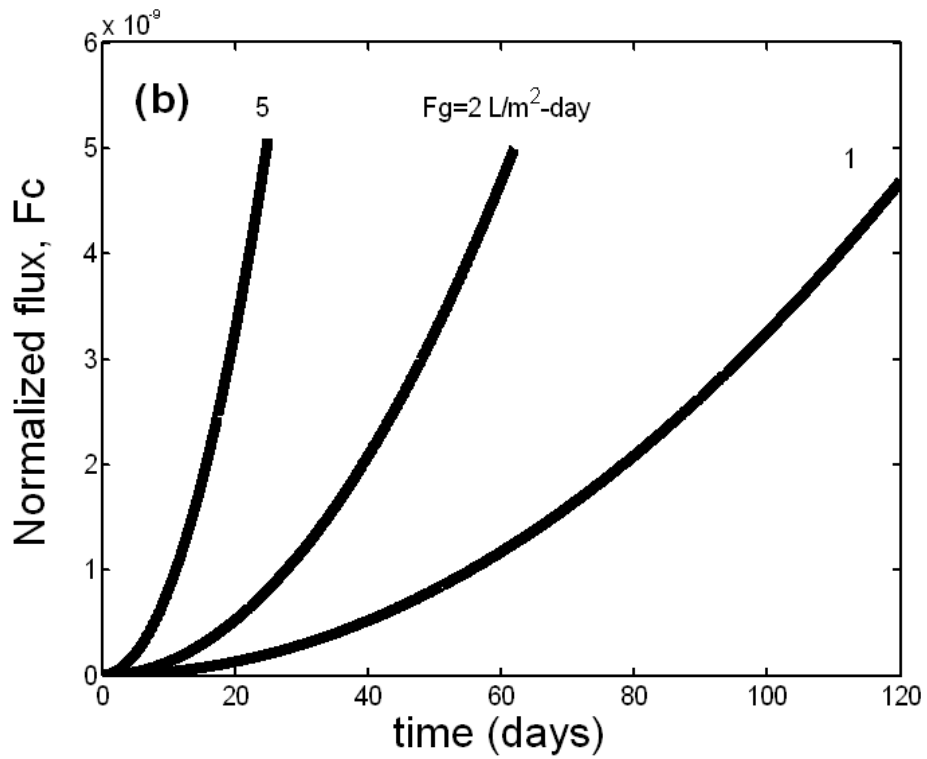
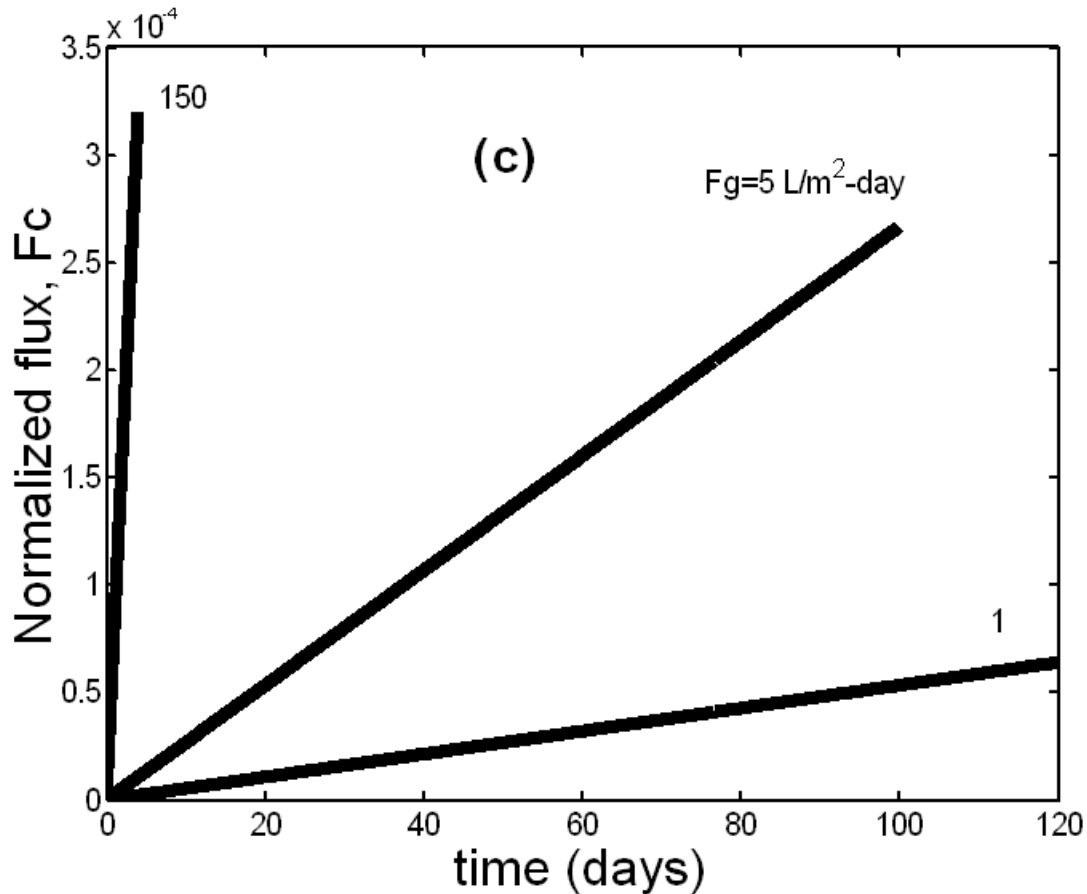


Figure 4.21(a) PHE flux into the air with time during bubble ebullition at different methane fluxes for uncapped sediment (with sediment suspension).



(b) PHE flux into the air with time during bubble ebullition for capped sediment. (Fig. con'd)



(c) PHE flux into the air with time during bubble ebullition for uncapped sediment (without sediment suspension).

suspension during the bubble ebullition for uncapped sediment. Yet, it can serve as a base to see how large the contribution of sediment suspension is for contaminant transport; also to see another function of the cap, i.e., retardation of the contaminant transport. Figure 4.21(a) and (c) show that the sediment suspension largely enhances the contaminant flux. Similarly, comparing Figure 4.21(b) and (c), we can see the cap retardation - the contaminant flux for capped sediment is much smaller than that for uncapped sediment even though there is no sediment suspension.

4.3.2.4 Sensitivity Analysis

There are two operational or adjustable parameters in the model for capped sediment, i.e., cap thickness and cap fractional organic carbon (f_{oc}). Figures 4.22(a) and (b) show the

normalized contaminant flux as a function of the cap thickness and cap fractional organic carbon under field gas flux. As expected, increasing either parameter decreases the contaminant flux. In order to see the trend that the contaminant flux can reach a maximum, the contaminant fluxes with time at the different organic carbon contents were calculated at a high gas flux ($F_g=50 \text{ L/m}^2\text{-day}$). Figure 4.22(c) demonstrates that high cap organic carbon can increase the time required to reach the maximum contaminant flux. This is also true for the cap thickness. These results can be used in the cap design, e.g., artificially increasing the organic carbon content of the cap by adding some organic carbon-rich materials such as fly ash or active materials to decrease the contaminant flux.

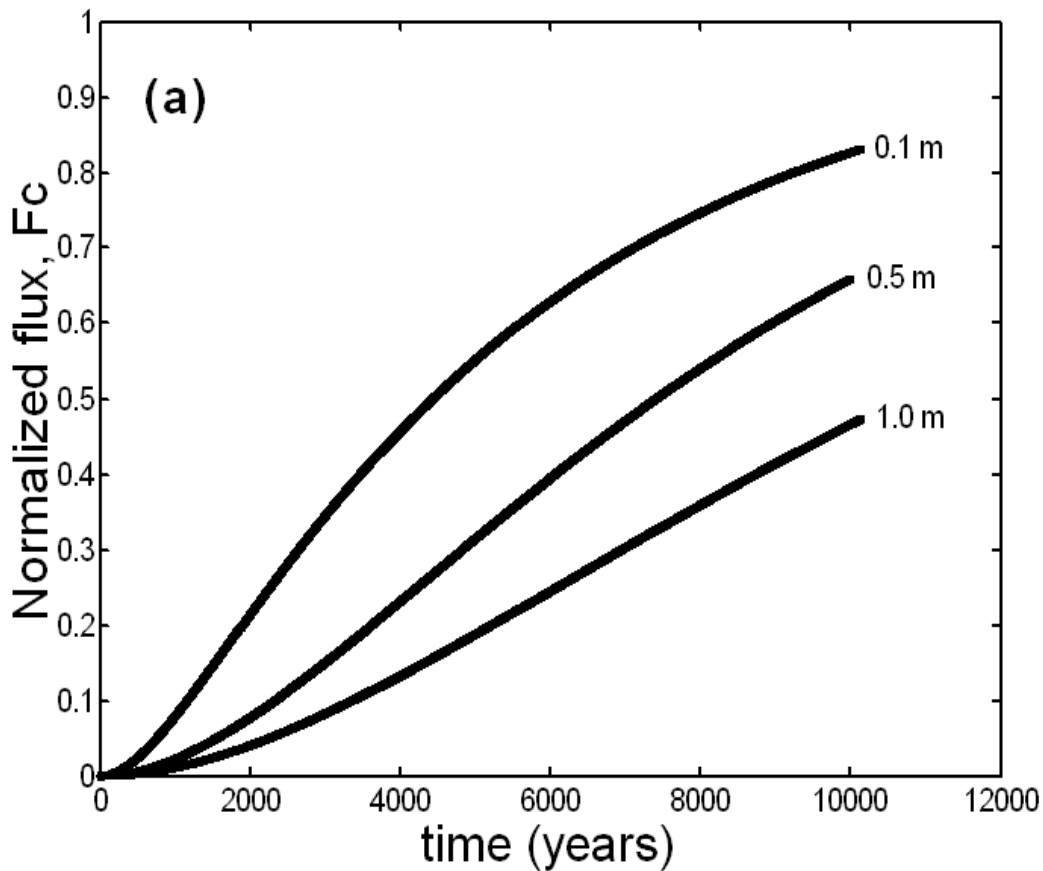
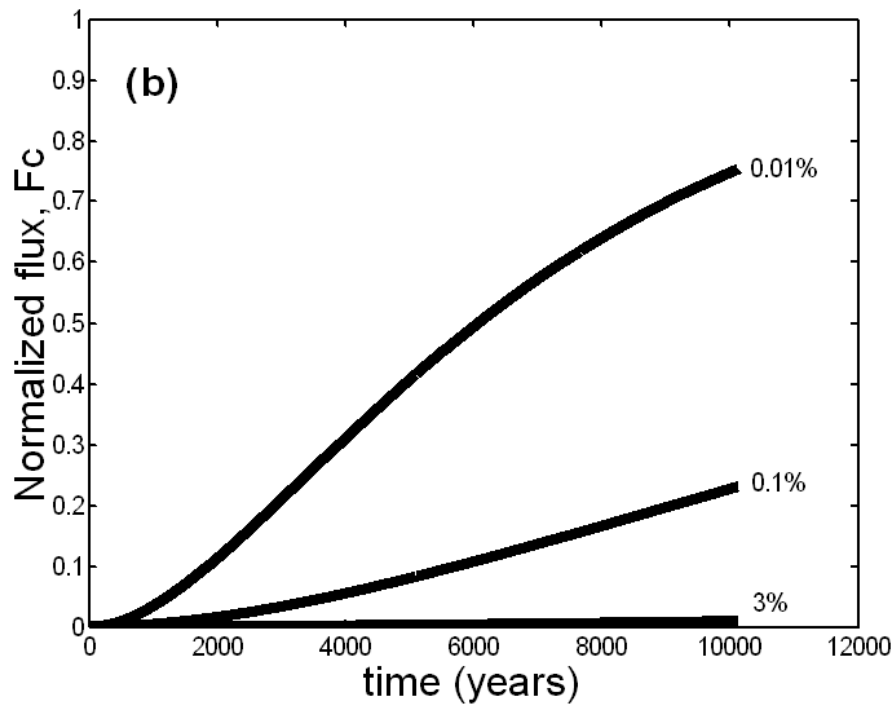
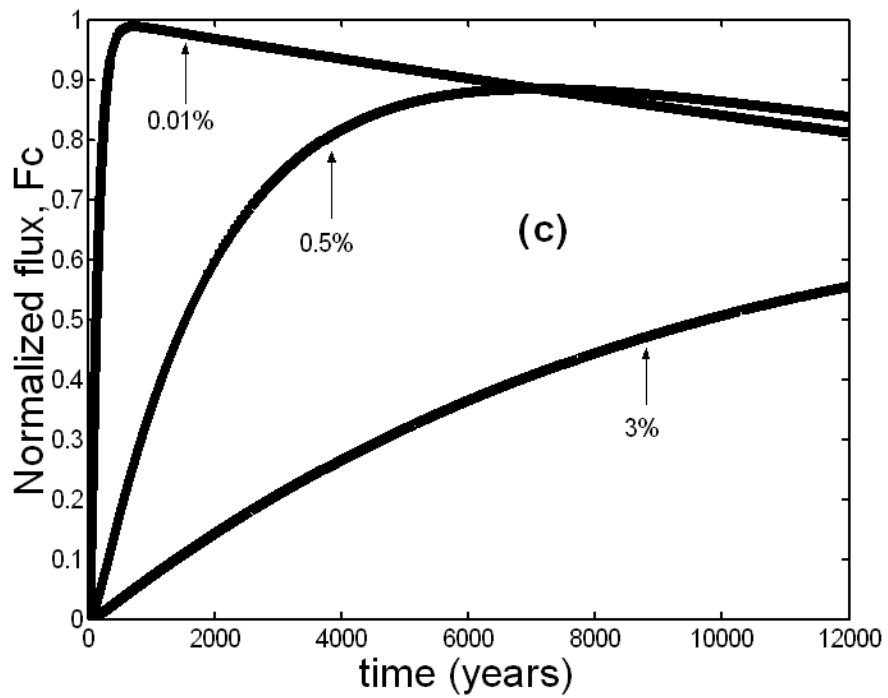


Figure 4.22(a) Normalized PHE flux into the air with time during bubble ebullition at different cap thickness. (Fig. con'd)



(b) Normalized PHE flux into the air with time during bubble ebullition at different cap frictional organic carbon (f_{oc}).



(c) Normalized PHE flux into the air with time during bubble ebullition at different cap f_{oc} with a high gas flux ($F_g = 50 \text{ L/m}^2\text{-day}$).

4.4 Summary

Sediment suspension and partition are main factors responsible for the bubble-associated contaminant transport in sediments. Since the contaminant (i.e., PHE) partition coefficient between water and methane is relatively very small, sediment suspension is the primary factor for the bubble-facilitated contaminant release from sediment. A sand cap can substantially reduce the contaminant flux for it can effectively prevent sediment release. Under field conditions or at low gas rates, the magnitude of contaminant release caused by gas ebullition is expected to be less than that by bioturbation in uncapped sediments. CT images from sediment cores show that the bubble movement has influence on the sediment/cap structures.

A model was developed and verified for gas bubble-facilitated contaminant transport in both uncapped and capped sediment systems. The simulation supports the experimental observations. The model sensitivity analysis shows that contaminant flux into the air increases with gas flux, and decreases with cap thickness and fractional organic carbon.

CHAPTER 5. CONCLUSIONS AND RECOMMENDATIONS

5.1 Conclusions

5.1.1 Capping Contaminated Sediments

Diffusion chambers were used to simulate the capping process with sediment consolidation. Fluxes of three organic chemicals were measured for both capped and uncapped systems. The experimental data showed that a sand cap was effective in retarding the transport of chemicals from contaminated sediment to water. An advection term was added to the diffusion model to account for sediment consolidation. The mass transfer coefficient at the sediment-water interface, and porosity were considered as functions of time. The model results agreed satisfactorily with the experimental data. Simulation results under typical field conditions showed that sediment consolidation shortened the breakthrough time and enhanced the initial contaminant flux. The flux enhancement disappeared as consolidation reached zero. The results also showed that a sand cap was effective in retarding chemical transport even under sediment consolidation. Active capping has potential. Simulation demonstrated that contaminant degradation in the cap and/or sediment could substantially reduce the contaminant flux. Due to the anaerobic environment in capped sediments and long-term containment, the microbial and biological degradation of chemicals can occur, thus further enhancing the cap effectiveness.

A sand cap is also an effective barrier for the transport of metals from contaminated sediment to water, especially in the early stages of the experimental run. Penetration theory fits the metal flux data well. The oxygen distribution in the cap/sediment was investigated by measuring the oxygen and redox potential. Both oxygen and redox potential data showed that it was aerobic in the upper cap (sand) layer (4-6 mm). For uncapped sediment, oxygen was only

observed in the depth of no more than 3 mm. Below 3 mm, the sediment was in the reduced form and anaerobic. Diffusion and zero-order degradation model at steady state could satisfactorily describe the oxygen distribution in sediment. According to the experimental results, the optimal zero-order rate constant of oxygen consumption is around 4.6×10^{-7} kg/s-m³.

5.1.2 Bubble-Facilitated Contaminant Transport

Partitioning and sediment suspension are responsible for contaminant transport associated with bubble ebullition in contaminated sediment. Experimental results showed that sediment suspension was an important factor as a contaminant release mechanism. A sand cap can prevent or at least decrease the sediment suspension, making it a good barrier to bubble-facilitated contaminant release from sediments. At natural rates of gas generation and evolution in sediments (≤ 1 L/m²·day), particle resuspension rates and facilitated release rates of solid associated contaminants are relatively small. For example, bioturbation would be expected to give rise to far more rapid contaminant transport in stable uncapped sediments. CT images showed that the bubble movement could redistribute the void spaces and increase pore water circulation in the sediment, thus changing the sediment structure and integrity. Bubbles can also coalesce in the sand layer and large bubbles are more likely to break the sand cap. These factors should be considered in the design of caps over contaminated sediments in the field.

A model was developed to describe the gas bubble-facilitated contaminant transport in capped sediment. The simulation showed that contaminant flux from uncapped sediment increases with gas generation rate due to the sediment suspension and the partitioning process. Without sediment suspension, the contaminant flux into the air would be much smaller than that with sediment suspension which prevails in uncapped sediment when gas bubbles move through the sediment. The cap can prevent sediment suspension during bubble ebullition if it maintains

its integrity. It can also retard the contaminant transport by increasing the contaminant transport path and due to its absorption capacity. Therefore a sand cap is an effective barrier for contaminant transport during gas bubble ebullition. All the simulation results compare favorably with those observed from our experiments.

5.2 Recommendations

5.2.1 Capping Contaminated Sediments

Simulation has shown that active capping materials can significantly decrease the contaminant flux. Experiments should be designed to test some potential reactive capping materials with good prospects to be used under field conditions. The contaminant flux data can be measured with the diffusion chambers. This kind of data gives a trend that can be used to roughly evaluate the capping effectiveness of the materials. However, the investigation of degradation rate and mechanism will be difficult since many factors or processes (such as bioavailability, intraphase diffusion and soil characteristics) can affect the degradation rate of hazardous materials in sediment. The study of degradation mechanism should begin with very simple experiments with pure substances, and then gradually move into more complicated experiments.

The model in this dissertation has included partition, diffusion, advection and reaction components. Some other processes (such as bioturbation, water seepage, current, etc.) should be incorporated into the model. The work to collect all the information and couple them together to form a more realistic model should be done in the future.

For metal transport in sediment, fundamental data such as isotherms and transport mechanism are needed. Environmental factors such as groundwater pH, redox conditions, and groundwater flow rate have influence on metal mobility through its partitioning/solubility

characteristics. The experiments should be conducted to investigate how these factors affect the metal movement in sediment. Based on a good understanding of the mechanisms, more complex models can be developed for metal transport in capped sediments.

5.2.2 Bubble-Facilitated Contaminant Transport

Bubble growth under natural conditions is not well understood. Images and video records demonstrating the active process of bubble growth will be interesting and helpful to better understand chemical, mechanical and transport mechanisms. This experiment can be performed by on-line X-ray imaging techniques. The experiment should also be designed to measure the contaminant mass change within a growing bubble. With this kind of information, a transient model can be constructed to describe the contaminant transport during the bubble growth.

At the higher gas flux, sediment suspension is the main factor for contaminant transport. At very low gas flux under field conditions, the amount of the sediment suspension and gas becomes extremely small. Under such conditions, long-time scale experiments should be conducted to observe contaminant migration in each compartment. This may give a different scenario compared to the experiment with a high gas flux. The experimental findings are more realistic, and useful for a better understanding and model improvement.

A key parameter in describing contaminant transport by bubble is the bubble-water partition coefficient, K_{bw} , which tends to significantly exceed the conventional air-water Henry's law constant due to the accumulation of hydrophobics at the interface. This interface is highly conducive to the adsorption and uptake of dissolved hydrophobic contaminants (such as PAHs) (Raja et al, 2002; Smith and Valsaraj, 1997; Sojitra et al, 1996). The partition coefficient may also be different in the sediment pore water from that in the bulk aqueous phase. Experiments should be designed and carried out to measure this coefficient in sediment or sediment slurry.

The model for bubble-facilitated contaminant transport developed in this work has several assumptions. These assumptions may be invalid in some situations. For example, non-equilibrium between the sediment particles, aqueous phase and gas may sometimes exist, especially when gas generation rate is very high. For this case, the two-resistance model can be used to formulate the interphase transport of contaminants, and the relevant mass transfer coefficients should be studied experimentally and mathematically. In field conditions, contaminant concentration in sediment may not be uniform and gas flux usually is a function of time. These factors should also be included in the model.

BIBLIOGRAPHY

- Abegg, F., and Anderson A. L. (1997) The acoustic turbid layer in muddy sediments of Eckernförde Bay, western Baltic: methane concentration, saturation and bubble characteristics, *Marine Geology*, 137(1/2), 137-147.
- Adams, D. D., and Naguib, M. (1999) Carbon gas cycling in the sediments of Plussee, a northern German eutrophic lake, and 16 nearby water bodies of Schleswig-Holstein, *Advances in Limnology*, 54, 91-104.
- Adams, D. D., Naguib, M., and Brown, D. H. (1987) Cycling of methane in acidified freshwater environments, *Acid Rain*, 451-6.
- Agency for Toxic Substances and Disease Registry (ATSDR) (1995) Toxicological Profile for polycyclic aromatic hydrocarbons (PAHs), Atlanta, GA: U.S. Department of Health and Human Services, Public Health Service.
- Akita, K., and Yishida, F. (1973) Gas holdup and volumetric mass transfer coefficient in bubble columns, *Ind. Eng. Chem. Proc. Des. Dev.*, 12, 76.
- Akita, K., and Yishida, F. (1974) Bubble size, interfacial area, and liquid phase mass transfer coefficients in bubble columns, *Ind. Eng. Chem. Proc. Des. Dev.*, 13, 84.
- Allen-King, R. M., Grathwohl, P., and Ball, W. P. (2002) New modeling paradigms for the sorption of hydrophobic organic chemicals to heterogeneous carbonaceous matter in soils, sediments, and rocks, *Adv. Water Resour*, 25, 985-1016.
- Alshawabkeh, A. N., Rahbar, N., and Sheahan, T. (2005) A model for contaminant mass flux in capped sediment under consolidation, *Journal of Contaminant Hydrology*, 78(3), 147-165.
- Andersen, O., Rasmussen, A. D., Timmermann, K., Christensen, M., and Banta, G. (2001) Effect of polychaete bioturbation on sediment-water fluxes of pyrene or cadmium, *Progress in Water Resources*, 3 (Water Pollution VI), 357-366.
- Andersson, K., Eyans, S., and Albinsson, Y. (1992) Diffusion of radionuclides in sediments-in-situ studies, *Radiochimica Acta*, 58-59(Pt.2), 321-7.
- Anderson, S. H., Gantzer, C. J., Boone, J. M., and Tully, R. J. (1988) Rapid nondestructive bulk density and soil-water content determination by computed tomography, *Soil Sci. Soc. Am. J.*, 52, 35-40.
- APHA/AWWA/WEF. (1991) Standard Methods for the Examination of Water and Wastewater, 18th Edition, American Public Health Association, Washington D.C.

Bamford, H. A., Poster, D. L., and Baker, J. E. (1999) Temperature dependence of Henry's law constants of thirteen polycyclic aromatic hydrocarbons between 4°C and 31°C, *Environ. Toxicol. Chem.*, 18(9), 1905-1912.

Bamford, H. A., Poster, D. L., and Baker, J. E. (2000) Henry's law constants of polychlorinated biphenyl congeners and their variation with temperature, *J. Chem. Eng. Data*, 45(6), 1069-1074.

Bamford, H. A., Poster, D. L., and Baker, J. E. (2002) Using Extrathermodynamic relationships to model the temperature dependence of Henry's law constants of 209 PCB congeners, *Environ. Sci. Technol.*, 36(20), 4395-4402.

Baron, J. A., Thibodeaux, L. J., Reible, D. D., Templet, P. H., and Heney, C. B. Jr. (1990) Laboratory simulation of diffusion in contaminated marine sediments, *Estuaries*, 13, No.1, 81-88.

Baudo, R., Giesy, J., and Muntau, H. (1990) Sediments: chemistry and toxicity of in-place pollutants, Chapter 7, Lewis publisher.

Beyer, W. N., Day, D., Mark, J., and Sileo, L. (2000) Toxicity of Anacostia River, Washington, D. C. USA, sediment fed to mute swans (*Cygnus olor*), *Environmental Toxicology and Chemistry*, 19(3), 731-735.

Bosworth, W. S., and Thibodeaux, L. J. (1990) Bioturbation: a facilitator of contaminant transport in bed sediment, *Environmental Progress*, 9(4), 211-17.

Boudreau, B. P., Algar, C., Johnson, B. D., Croudace, I., Reed, A., Furukawa, Y., Dorgan, K. M., Jumars, P. A., Grader, A. S., and Gardiner, B. S. (2005) Bubble growth and rise in soft sediments, *Geology*, 33(6), 517-520.

Boudreau, B. P., Gardiner, B. S., and Johnson, B. D. (2001a) Rate of growth of isolated bubbles in sediments with a diagenetic source of methane, *Limnology and Oceanography*, 46(3), 616-622.

Boudreau, B. P., Gardiner, B. S., and Johnson, B. D. (2001b) Rate of growth of isolated bubbles in sediments with a diagenetic source of methane, [Erratum to document cited in CA135:81463], *Limnology and Oceanography*, 46(6), 1578.

Boudreau, B. P. (2001c) Benthic Boundary Layer: transport processes and biogeochemistry, Oxford University Press, Oxford, England.

Boudreau, B. P., Choi, J., and Francois-Carcaillet, F. (2001d) Diffusion in a lattice-automation model of bioturbation by small deposit feeders, *Journal of Marine Research*, 59, 749-768.

Boudreau, B. P. (2000) The mathematics of early diagenesis: from worms to waves, *Reviews of Geophysics*, 38(3), 389-416.

Boudreau, B. P. (1996) Diagenetic Models and their Implementation: Modeling Transport and Reactions in Aquatic Sediments, Springer, NY.

Boudreau, B.P. (1989). The diffusion and telegraph equations in diagenetic modeling, *Geochimica et Cosmochimica Acta*, 53(8), 1857-66.

Brannon, J., Hoeppe, R. E., and Gunnison, D. (1987) Capping contaminated dredged material, *Marine Pollution Bulletin*, 18(4), 175-179.

Burke, C. M. (1999) Molecular diffusive fluxes of oxygen in sediments of Port Phillip Bay in south-eastern Australia, *Mar. Freshwater Res.*, 50, 557-66.

Bustamante, C., and Bustamante, P. (1996) Nonlinear enthalpy-entropy compensation for the solubility of phenacetin in dioxane-water solvent mixtures, *J. Pharm. Sci.*, 85(10), 1109-1111.

Callebaut, F., Gabriels, D., Minjauw, W., and Boodt, M. D. (1982) Redox potential, oxygen diffusion rate, and soil gas composition in relation to water table level in two soils, *Soil Science*, 134(3), 149-156.

Cargill, K. W. (1985) Mathematical model of the consolidation/desiccation process in dredged material, *Technical Report D-85-4*, U. S. Army Engineer Waterways Experiment Station, Vicksburg, MS.

Carnahan, B., Luther, H. A., and Wilkes, J. O. (1969) Applied numerical methods, John Wiley & Sons, New York.

Chandra, P. K., and Singh, R. P. (1994) Applied Numerical Methods for Food and Agricultural Engineers, CRC Press, Boca Raton.

Chanton, J. P., Martens, C. S., and Kelley, C. A. (1989) Gas transport from methane-saturated tidal freshwater and wetland sediments, *Limnology and Oceanography*, 34(5), 809-19.

Chapra, S. C. (2002) Numerical methods for engineers: with software and programming applications, 4th ed., McGraw-Hill.

Choi, J., Francois-Carcaillet, F., and Boudreau, B. P. (2002) Lattice-automaton bioturbation simulator (LABS): implementation for small deposit feeders, *Computers and Geosciences*, 28, 213-222.

Choy, B., and Reible, D. D. (1999) Diffusion Models of Environmental Transport, Boca Raton, Fla, Lewis Publishers.

Ciarcia, D., Jeris, J. S., and Toro, D. M. D. (1985) Diffusion and partitioning of hexachlorobiphenyl in sediments, *Environ. Sci. Technol.*, 19, 1169-1176.

Ciutat, A., and Boudou, A. (2003) Bioturbation effects on cadmium and zinc transfers from a contaminated sediment and on metal bioavailability to benthic bivalves, *Environmental Toxicology and Chemistry*, 22(7), 1574-1581.

Cornelissen, G. and Gustafsson, O. (2005) Importance of unburned coal carbon, black carbon, and amorphous organic carbon to phenanthrene sorption in sediments, *Environ. Sci. Technol.*, 39(3), 764-769.

Cummingham, P. B., Reible, D. D., Fleeger, J. F., Valsaraj, K. T. and Thibodeaux, L. J. (1999) Assessment of the effects of bioturbation in contaminated sediments, Proceedings of the Conference on Hazardous Waste Research: Gateways to Environmental Solutions, St. Louis, MO, United States, May 24-27, 1999, 276-285.

Curtis, G. P., Reinhard, M., and Roberts, P. V. (1986) Sorption of hydrophobic organic compounds by sediments, *Geochemical Processes at Mineral Surfaces ACS Symp. Series*, Vol. 323, 191-216.

De Maagd, P.G-J., TEN Hulscher, D. TH. E. M., and DEN Heuvel, H. V. (1998) Physicochemical properties of polycyclic aromatic hydrocarbons: aqueous solubilities, n-octanol/water partition coefficients, and Henry's law constants, *Environmental Toxicology and Chemistry*, 17(2), 251-257.

Di Toro, D. M. (2001) Sediment flux modeling, Wiley-Interscience, New York.

Dutch Ministry of Public Works (1995-1998) Gas production in sediment storage-depots, (<http://www.wldelft.nl/cons/appl/soilwati/gp-sedlay.html>).

EPA (Environmental Protection Agency, US) (1997) The incidence and severity of contamination in surface waters of the United States, Vol. 1, National sediment quality survey, *EPA 823-R-97-006*, Office of water.

Fendinger, N. J., Adams, D. D., and Glotfelty, D. E. (1992) The role of gas ebullition in the transport of organic contaminants from sediments, *Science of the Total Environment*, 112(2-3), 189-201.

Fendinger, N. J., and Glotfelty, D. E. (1990) Henry's law constants for selected pesticides, PAHs and PCBs, *Environmental Toxicology and Chemistry*, 9(6), 731-5.

Fendinger, N. J., Glotfelty, D. E., and Freeman, H. P. (1989) Comparison of two experimental techniques for determining air/water Henry's law constants, *Environmental Science and Technology*, 23(12), 1528-31.

Fendinger, N. J. and Glotfelty, D. E. (1988) A laboratory method for the experimental determination of air-water Henry's law constants for several pesticides, *Environmental Science and Technology*, 22(11), 1289-93.

- Fendinger, N. J. and Adams, D. D. (1986) A headspace equilibrium technique for measurement of dissolved gases in sediment pore water, *International Journal of Environmental Analytical Chemistry*, 23(4), 253-65.
- Ferrell, R. T. and Himmelblau, D. M. (1967) Diffusion coefficients of nitrogen and oxygen in water, *J. Chem. Eng. Data*, 12, 111-115.
- Formica, S. J., Baron, J. A., Thibodeaux, L. J., and Valsaraj, K. T. (1988) PCB transport into lake sediments - Conceptual model and laboratory simulation, *Environ. Sci. Technol.*, 22, 1435-1440.
- Fox, P. F. (2003) Numerical model for contaminant transport in consolidating sediments, *Contaminated Sediments*, 266-281.
- Galyin, K. P. (1996) Measurement of particle velocity during sediment consolidation, *Chemical Engineering Science*, 51(21), 3241-3246.
- Gambrell, R. P. (1984) Fate of selected toxic compounds under controlled redox potential and pH conditions in soil and sediment-water systems, chapter 7: Redox measurement of soil, Athens, GA: U.S. Environmental Protection Agency, Environmental Research Laboratory, Cincinnati, OH: Center for Environmental Research Information (distributor).
- Gardiner, B. S., Boudreau, B. P., and Johnson, B. D. (2003) Growth of disk-shaped bubbles in sediments, *Geochimica et Cosmochimica Acta*, 67(8), 1485-14494.
- Gibson, R. E., Schiffman, R. L., and Cargill, K. W. (1981) The theory of one-dimensional consolidation of saturated clay, II. Finite, non-linear consolidation of thick homogeneous layers, *Canadian Geotechnical Journal*, 8, 280-293.
- Glanze, W. D. (1996) Mosby medical encyclopedia, Revised Edition, St. Louis, MO, C.V. Mosby.
- Goldhaber, M. B., Aller, R. C., Cochran, J. K., Rosenfeld, J. K., Martens, C. S., and Berner, R. A. (1997) Sulfate reduction, diffusion, and bioturbation in Long Island Sound sediments: report of the FOAM group, *American Journal of Science*, 277(3), 193-237.
- Gossett, J. M. (1987) Measurements of Henry's law constants for C1 and C2 chlorinated hydrocarbons, *Environ. Sci. Technol.*, 19, 202-208.
- Grimberg, S. J., Nagel, J., and Aitken, M. D. (1995) Kinetics of phenanthrene dissolution into water in the presence of nonionic surfactants, *Environ. Sci. Technol.*, 29, 1480-1487.
- Hagerty, P. A. and Trotman, T. D. (2001) In situ contaminated sediment management: Unique case studies, *Contaminated Soils*, 6, 403-410.
- Hammett, L. P. (1970) Physical organic chemistry, 2nd Ed, McGraw-Hill, New York.

Henry, P., Thomas, M., and Clennell, M. B. (1999) Formation of natural gas hydrates in marine sediments 2. Thermodynamic calculations of stability conditions in porous sediments, *Journal of Geophysical Research*, 104(B10), 23005-230022.

Hikita, J., Asai, K., Tanigawa, K., Segawa, K., and Kitao, M. (1980) Gas holdup in bubble column, *J. Chem. Eng.*, 20, 59.

Himmelheber, D. and Hughes, J. (2005) Complete tetrachloroethene dechlorination in Anacostia River Sediment, SETAC 26th Annual Meeting in North America, Baltimore, Maryland, USA, November 13-17, 2005.

Holler, P. and Kogler, F. C. (1990) Computer tomography: A nondestructive, high-resolution technique for investigation of sedimentary structures, *Marine Geology*, 91, 263-266.

Hovland, M. and Judd, A. G. (1992) The global production of methane from shallow submarine sources, *Cont. Shelf Res.*, 12, 1231-1238.

Huang, W., Schlautman, M. A., and Weber, W. J. Jr. (1996) A distributed reactivity model for sorption by soils and sediment. 5. the influence of near-surface characteristics in mineral domains, *Environ. Sci. Technol.*, 30(10), 2993-3000.

Hughes, J. B., Valsaraj, K. T., and Willson, C. S. (2005) In-situ containment and treatment: Engineering cap integrity and reactivity, Presentation at the 10th Annual Meeting of the Hazardous Substance Research Center/South & Southwest, Houston, Texas, December 2004.

Huls, H., Costello, M., and Sheets, R. (2003) Bench test design evaluation of a remedial wetland cap (with regard to ebullition and its control), In-situ contaminated sediment capping workshop, Cincinnati, OH, May 12-14, 2003.

Huls, H., Costello, M., and Sheets, R. (2005) Gas, NAPL and PAH flux assessment in sediments, (<http://www.serviceenv.com/Web2005/Docs/Paper55byHuls.pdf>).

Huls, H. and Costello, M. (2005) Designing assessments for decision making for remediation of contaminated sediments, Third International Conference on Remediation of Contaminated Sediments, New Orleans, LA, USA, January 24-27.

International Occupational Safety and Health Information Center (1999) Metals. In basics of chemical safety, Chapter 7, Geneva, International Labor Organization.

Jacobs, P. H., and Waite, T. D. (2004) The role of aqueous iron(II) and manganese(II) in subaqueous active barrier systems containing natural clinoptilolite, *Chemosphere*, 54(3), 313-24.

Jacobs, P. H. and Forstner, U. (1999) Concept of subaqueous capping of contaminated sediments with active barrier systems (ABS) using natural and modified zeolites, *Water Research*, 33(9), 2083-2087.

- Jacobs, P. H. (2003) Monitoring of subaqueous depots with active barrier systems for contaminated dredged material using dialysis samplers and DGT probes, *Journal of Soils and Sediments*, 3(2), 100-107.
- Jayasinghe, D. S., Brownawell, B. J., Chen, H., and Westall, J. C. (1992) Determination of Henry's constants of organic compounds of low volatility: methylanillnes in methanol-water, *Environ. Sci. Technol.*, 26(11), 2275-2281.
- Jepsen, R., McNeil, J., and Lick, W. (2000) Effects of gas generation on the density and erosion of sediments from the Grand River, *J. Great Lakes Res.*, 26(2), 209-219.
- Johnson, B. D., Boudreau, B. P., Gardiner, B. S., and Maass, R. (2002) Mechanical response of sediments to bubble growth, *Marine Geology*, 187, 347-363.
- Kamp-Nielsen, L., Mejer, H., and Joergensen, S. E. (1982) Modeling the influence of bioturbation on the vertical distribution of sedimentary phosphorus in Lake Esrom, *Hydrobiologia*, 91-92, 197-206.
- Kaplan, D. I. and Knox, A. S. (2004) Enhanced contaminant desorption induced by phosphate mineral additions to sediment, *Environ. Sci. Technol.*, 38, 3153-3160.
- Kenter, J. A. M. (1989) Application of computerized tomography in sedimentology, *Marine Geotechnology*, 8, 201-211.
- Ketcham, R. A. and Carlson, W. D. (2001) Acquisition, optimization and interpretation of X-ray computed tomographic imagery: applications to the geosciences, *Computers & Geosciences*, 27, 381-400.
- Kipphut, G. W. and Martens, C. S. (1982) Biogeochemical cycling in an organic-rich coastal marine basin, 3. Dissolved gas transport in methane-saturated sediments, *Geochimica et Cosmochimica Acta*, 46(11), 2049-60.
- Klaucke, I., Sahling, H., Bürk, D., Weinrebe, W., and Bohrmann, G. (2005) Mapping deep-water gas emissions with sidescan sonar, *EOS, Transactions, American Geophysical Union*, 86(38), 341-346.
- Krug, R. R., Hunter, W. G., and Grieger, R. A. (1976a) Enthalpy-entropy compensation. 1. Some fundamental statistical problems associated with the analysis of van't Hoff and Arrhenius data, *J. Phys. Chem.*, 80(21), 1335-2341.
- Krug, R. R., Hunter, W. G., and Grieger, R. A. (1976b) Enthalpy-entropy compensation. 2. Separation of the chemical from the statistical effect, *J. Phys. Chem.*, 80(21), 2341-2351.
- Krug, R. R., Hunter, W. G., and Grieger, R. A. (1976c) Statistical interpretation of enthalpy compensation, *Nature (London, United Kingdom)*, 261(5561), 566-7.

Kuivila, K. M., Murray, J. W., Devol, A. H., and Novelli, P. C. (1989) Methane production, sulfate reduction and competition for substrates in the sediments of Lake Washington, *Geochim. Cosmochim. Acta*, 53, 409-416.

Lee, E. B., Birkham, T. K., Wassenaar, L. I., and Hendry, M. J. (2003) Microbial respiration and diffusive transport of O₂, ¹⁶O₂, and ¹⁸O¹⁶O in unsaturated soils and geologic sediments, *Environ. Sci. Technol.*, 37, 2913-2919.

Lee, H. and Schwartz, R. C. (1980) Biological processes affecting the distribution of pollutants in marine sediments, Part II. Biodeposition and bioturbation. In Baker, R. A. (Ed.), Contaminants and sediments, Volume 2, Science Publisher, Ann Arbor, MI.

Lei, L., Khodadous, A. P., Suidan, M. T., and Tabak, H. H. (2005) Biodegradation of sediment-bound PAHs in field-contaminated sediment, *Water Research*, 39(2-3), 349-361.

Leffler, J. E. and Grunwald, E. (1963) Rates and equilibria of organic reactions, Wiley, New York.

Levitt Jeffrey S., N'Guessan, A. L., Rapp, K. L., and Nyman M. C. (2003) Remediation of alpha-methylnaphthalene-contaminated sediments using peroxy acid, *Water Research*, 37(12), 3016-22.

Lide, D. (1992) CRC handbook of chemistry and physics, 73rd Edition, CRC Press, Boca Raton, FL.

Liu, C., Jay, J. A., Ika, R., Shine, J. P., and Ford, T. E. (2001) Capping efficiency for metal-contaminated marine sediment under conditions of submarine groundwater discharge, *Environmental science & Technology*, 35(11), 2334-40.

Lohmann, R., Macfarlane, J. K., and Gschwend, P. M. (2005) Importance of black carbon to sorption of native PAHs, PCBs, and PCDDs in Boston and New York harbor sediments, *Environ. Sci. Technol.*, 39(1), 141-148.

Lu, X. (1992) Solvent sublation and bubble fractionation for wastewater treatment, thesis (Master), Louisiana State University, Baton Rouge, LA.

Mackay, D. and Shiu, W. Y. (1981) A critical review of Henry's law constants for chemicals of environmental interest, *J. Phys. Chem. Ref. Data*, 10, 1175-1199.

Mackay D., Shiu, Y. W., and Ma, C. K. (1992) Illustrated handbook of physical-chemical properties and environmental fate for organic chemicals, Lewis, Chelsea, MI, USA.

Mackay, D., Shiu, W. Y., and Sutherland, R. P. (1979) Determination of air-water Henry's law constants for Hydrophobic Pollutants, *Environmental Science & Technology*, 13(3), 333-337.

- Malicki, M. (1990) Measurement of redox potential and oxygen diffusion rate (ODR) in the soil, *Zeszyty problemowe postepow nauk rolniczych*, 388.
- Marinelli, B. L. and Boudreau, B. P. (1996) An experimental and modeling study of pH and related solutes in an irrigated anoxic coastal sediment, *Journal of Marine Research*, 54(5), 939-966.
- Marshall, W. L. and Slusher, R. (1966) Thermodynamics of calcium sulfate dehydrate in aqueous sodium chloride solutions, 0 – 110 °C, *J. Phys. Chem.*, 70(12), 4015-4027.
- Martens, C. S. and Klump, J. V. (1980) Biogeochemical cycling in an organic rich coastal marine basin – I. Methane sediment-water exchange processes, *Geochim. Cosmochim. Acta*, 44, 471-490.
- Martens, C. S. (1976) Control of methane sediment-water bubble transport by macroinfaunal irrigation in Cape Lookout Bight, North Carolina, *Science*, 192, 998-999
- Mason, R. P. and Sullivan, K. A. (1998) Mercury and methylmercury transport through an urban watershed, *Water Research*, 32(2), 321-330.
- Matis, K. A. (1995) Flotation science and engineering, Marcel Dekker, Inc.
- Maus, L. D., Rose, V. C., and Nacci, V. A. (1973) Gamma-ray monitoring of sediment consolidation test, *Ocean Engineering*, 2(4), 195-205.
- McDuff, R. E. and Ellis, R. A. (1979) Determining diffusion coefficients in marine sediments: a laboratory study of the validity of resistivity techniques, *American Journal of Science*, 279(6), 666-75.
- Meier, H., Zimmerhackl, E., Zeitler, G., Menge, P., and Albrecht, W. (1992) Experimental investigations of radionuclide diffusion in site-specific sediment/groundwater systems, *Radiochimica Acta*, 58-59(Pt.2), 341-6.
- Moo-Young, H., Myers, T., Tardy, B., Ledbetter, R., Vanadit-Ellis, W., and Kim, T. H. (2002) Modeling contaminant transport through capped dredged sediment using a centrifuge, *Journal of Soils and Sediments*, 2(3), 117-128.
- Moo-Young, H., Myers, T., Tardy, B., Ledbetter, R., Vanadit-Ellis, W., and Sellasie, K. (2001) Determination of the environmental impact of consolidation induced convective transport through capped sediment, *Journal of Hazardous Materials*, 85(1-2), 53-72.
- Munz, C. and Roberts, P. V. (1984) The ratio of gas-phase to liquid-phase mass transfer coefficient in gas-liquid contacting processes, in Gas transfer at water surface, edited by Brutsaert, W. and Jirka, G. H., D. Reidel publishing company.

- Mulder, H., Breure, A. M., Van Andel, J. G., Grotenhuis, J. T. C., and Rulkens, W. H. (1997) Influence of hydrodynamics conditions on naphthalene dissolution and subsequent biodegradation, *Biotechnol. Bioeng.*, 57, 145-154.
- Nguyen, T. H., Goss, K. U., and Ball, W. P. (2005) Polyparameter linear free energy relationships for estimating the equilibrium partition of organic compounds between water and the natural organic matter in soils and sediments, *Environ. Sci. Technol.*, 39(4), 913-924.
- Nolan, P. M. and Johnson, A. F. (1979) A method for measuring sediment oxygen demand using a bench model benthic respirometer, US EPA region I library JFK federal Bldg., Boston, MA.
- Nomura, Y., Nakai, S., and Hosomi, M. (2005) Elucidation of degradation mechanism of dioxins during mechanochemical treatment, *Environ. Sci. Technol.*, 39(10), 3799-3804.
- O'Connor, J. M. and O'Connor, S. G. (1983) Evaluation of the 1980 Capping Operations at the Experimental Mud Dumpsite, New York Bight Apex, *Technical Report, D-83-3*. US Army Engineer Waterways Experimental Station, Vicksburg, MS.
- Oelkers, E. H. (1991) Calculation of diffusion coefficients for aqueous organic species at temperatures from 0 to 350 °C, *Geochimica et Cosmochimica Acta*, 55(12), 3515-29.
- Palermo, M. R., etc. (2003) Palos Verdes capping pilot study successful: Breaks record for capping in deep water, *Dredging Research*, 6 (1), 3-7. (www.wes.army.mil/el/elpubs/pdf/tr02-5.pdf).
- Palermo, M. R., Clausner, J. E., Rollings, M. P., Williams, G. L., Myers, T. E., Fredette, T. J., and Randall, R. E. (1998) Guidance for subaqueous dredged material capping, *Technical Report DOER-1*, U. S. Army Engineer Waterways Experiment Station, Vicksburg, MS.
- Palermo, M. R. (1998 a) Design considerations for in-situ capping of contaminated sediments, *Water Science and Technology*, 37(6-7), 315-321.
- Palermo, M., Maynard, S., Miller, J., and Reible, D. (1998 b) Guidance for in-situ subaqueous capping of contaminated sediments, *EPA 905-B96-004*. Great Lakes National Program Office, Chicago, IL.
- Patrick, W. H., Gambrell, R. P., and Faulkner, S. P. (1996) Chapter 42, Redox measurement of soils, 1255-1273, in Sparks, D. L. et al., eds. *Methods of soil analysis Part 3*. Soil Science Society of America, Madison, Wisconsin.
- Purwaningsih, I. S., Hill, G. B., and Headley, J. V. (2002) Air stripping and dissolution rates of aromatic hydrocarbon particles in a bioreactor, *Chem. Eng. Comm.*, 189(2), 268-283.
- Phelps, H. L. (1993) Sediment toxicity of the Anacostia river estuary, Washington, D. C., *Bulletin of Environmental Contamination and Toxicology*, 51(4), 582-7.

Poindexter-Rollings, M. E. (1990) Methodology for analysis of subaqueous sediment mounds, *Technical Report D-90-2*, U. S. Army Engineer Waterways Experiment Station, Vicksburg, MS.

Prausnitz, J. M., Lichtenthaler, R. N. and Azevedo, E. G. (1999) Molecular Thermodynamics of Fluid-Phase Equilibria, third edition, Prentice Hall PTR.

Rahbar, N. (2003) Numerical modeling of coupled consolidation and contaminant transport in a deformable porous medium, thesis (Master of Science), Northeastern University, Boston, Massachusetts, USA.

Raja, S., Yacone, F. S., Ravikrishna, R., and Valsaraj, K. T. (2002) Thermodynamic parameters for the adsorption of aromatic hydrocarbon vapors at the gas-water environmental interface, *Journal of Chemical and Engineering Data*, 47, 1213-1219.

Rathbun, R. E. and Tai, D. Y. (1984) Volatilization of chlorinated hydrocarbons from water, in Gas transfer at water surface, edited by Brutsaert, W. and Jirka, G. H., D. Reidel publishing company.

Ravikrishna, R. (2000) Evaporative mass transfer of hydrophobic organic compounds from exposed contaminated sediment and dredged materials, Ph. D. dissertation, Louisiana State University, Baton Rouge, LA.

Ravikrishna, R. (2002) Volatilization of contaminants from suspended sediment in a water column during dredging, *Journal of the Air & Waste Management Association*, 52, 1214-1229.

Ravikrishna, R., Valsaraj, K. T., and Thibodeaux, L. J. (2005) Measurement of air-water partition constants (Henry's law constants) for chemicals of concern in the Indiana Harbor Canal dredged material, Report submitted to Engineering Research and Development Center, US Army Engineer Waterways Experimental Station, 3909 Halls Ferry Road, Vicksburg, MS 39180-6199.

Reible D. D. and Lowry, G. V. (2005) Active capping of contaminated sediments, Presented at AIChE Annual Meeting (Cincinnati, OH).

Reible D. D. and Constant, W. D. (2004) Active capping demonstration project Anacostia DC, on the site www.hsrc-ssw.org/anacostia/.

Reible, D. D., Constant, W. D., Roberts, K., and Zhu, Y. W. (2003) Active capping demonstration project in Anacostia DC, Battelle Sediments Conference Proceeding Paper, October 2003.

Reibel, D. D., Constant, W. D., and Zhu, Y. (2004) Update on reactive capping project in the Anacostia River, RTDF Workshop, Baltimore, MD, February 19, 2004.

Reible, D. D. (2002) Update on Anacostia River comparative validation of innovative capping technologies, presented to Remediation Technology Development Forum, Seattle, WA. October 29, 2002.

Reible, D. D., Valsaraj, K. T., and Thibodeaux, L. J. (1991) Chemodynamic models for transport of contaminants from sediment beds, Volume 2, Part F, Reactions and Processes, in the Handbook of Environmental Chemistry, Edited by O. Hutzinger, Springer-Verlag Berlin Heidelberg, Germany.

Revsbech, N. P., Jorgensen, B. B., and Blackburn, T. H. (1980 a) Oxygen in the sea bottom measured with a microelectrode, *Science*, 207, 1353-1354.

Revsbech, N. P., Sorensen, J., Blackburn, T. H., and Lomholt, J. P. (1980 b) Distribution of oxygen in marine sediments measured with microelectrodes, *Limnol. Oceanogr.*, 25(3), 403-411.

Rounds, S. A. and Doyle, M. C. (1997) Sediment oxygen demand in the Tualatin river basin, Oregon, 1992-96, U. S. Geological survey, water-resources investigations report 97-4103.

Rothfuss, F. and Conrad, R. (1998) Effect of gas bubbles on the diffusive flux of methane in anoxic paddy soil, *Limnology and Oceanography*, 43(7), 1511-1518.

Sanchez, F. F., Thibodeaux, L., Valsaraj, K. T., and Reible, D. D. (2002) Multimedia chemical fate model for environmental dredging, *Practice Periodical of Hazardous, Toxic, and Radioactive Water Management*, 6(2), 120-128.

Sander R. (1999) Compilation of Henry's law constants for inorganic and organic species of potential importance in environmental chemistry (version 3), (<http://www.mpch-mainz.mpg.de/~sander/res/henry.html>).

Santschi, P. H., Anderson, R., and Fleishier, M. Q. (1991) Measurement of diffusive sublayer thicknesses in the ocean by Alabaster dissolution, and their implications for the measurements of benthic fluxes, *Journal of Geophysical Research*, 96(C6), 10,641-10,657.

Santschi, P. H., Bower, P., Nyffeler, URS P., Azevedq, A. and Broecker, W. (1983) Estimation of the resistance to chemical transport posed by the deep-sea boundary layer, *Limnol. Oceanogr.*, 28(5), 899-912.

Schlekat, C. E., McGee, B. L., Boward, D. M., Reinharz, E., Velinsky, D. J., and Wade, T. L. (1994) Tidal river sediments in the Washington, D. C. area. III. Biological effects associated with sediment contamination, *Estuaries*, 17(2), 334-44.

Selomulya, C., Jia, X., and Williams, R. A. (2005) Direct prediction of structure and permeability of flocculated structures and sediments using 3D tomographic imaging, *Chemical Engineering Research and Design*, 83(A7), 844-852.

Shah, Y. T., Kelkar, B. G., Godbole, S. P., and Deckwer, W. D. (1982) Design parameters estimations for bubble column reactors, *AIChE Journal*, 28(3), 353-379.

Shaikh, A. U., Hawk, R. M., Sims, R. A., and Scott, H. D. (1985) Redox potential and oxygen diffusion rate as parameters for monitoring biodegradation of some organic wastes in soil, *Nuclear and Chemical Waste Management*, 5, 337-343.

Shin, W. S. (1998) Bioremediation of petroleum hydrocarbons in Louisiana's salt water marshes: sediment oxygen demand model, Ph. D. Dissertation, Louisiana State University, Baton Rouge, LA.

Simpson, S. L., Pryor, I. D., Mewburn, B. R., Batley, G. E., and Jolley, D. (2002) Considerations for Capping Metal-Contaminated Sediments in dynamic estuarine environments, *Environmental Science and Technology*, 36(17), 3772-3778.

Silva, A. J., Brandes, H. G., Uchytel, C. J., Fredette, T. J., and Carey, D. (1994) Geotechnical analysis of capped dredged material mounds, Proceedings of Dredging '94, ASCE, New York, 410-419.

Slauenwhite, D. E. and Johson, B. D. (1999) Bubble shattering: differences in bubble formation in fresh water and seawater, *Journal of Geophysical Research*, [Oceans], 104(C2), 3265-3275.

Smith, J. S. (1996) Pilot-scale solvent sublation for the removal of hydrophobic compounds from wastewaters, Ph. D. dissertation, Louisiana State University, Baton Rouge, LA.

Smith, J. S., Valsaraj, K. T., and Thibodeaux, L. J. (1996) Bubble column reactor for wastewater treatment. 1. Theory and modeling of continuous countercurrent solvent sublation, *Ind. Eng. Chem. Res.*, 35, 1688-1699.

Smith, J. S., Burns, L. F., Valsaraj, K. T., and Thibodeaux, L. J. (1996) Bubble column reactors for wastewater treatment. 2. the effect of sparger design on sublation column hydrodynamics in the homogeneous flow regime, *Ind. Eng. Chem. Res.*, 35, 1700-1710.

Smith, J. S. and Valsaraj, K. T. (1997). Bubble column reactors for wastewater treatment. 3. Pilot-scale solvent sublation of pyrene and pentachlorophenol from simulated wastewater, *Ind. Eng. Chem. Res.*, 36, 903-914.

Sojitra, I., Valsaraj, K. T., Reible, D. D., and Thibodeaux, L. J. (1996) Transport of hydrophobic organics by colloids through porous media 2. Commercial humic acid macromolecules and polyaromatic hydrocarbons, *Colloids and Surfaces*, 110:141-157.

Staudinger, J. and Roberts, P. V. (2001) A critical compilation of Henry's law constant temperature dependence relations for organic compounds in dilute aqueous solutions, *Chemosphere*, 44, 561-576.

Tang, Y. J., Carpenter, S., Deming, J., and Krieger-Brockett, B. (2005) Controlled release of nitrate and sulfate to enhance anaerobic bioremediation of phenanthrene in marine sediment, *Environ. Sci. Technol.*, 39(9), 3368-3373.

Tanner, C. C., Adams, D. D., and Downes, M. T. (1997) Methane emissions from constructed wetlands treating agricultural wastewaters, *Journal of Environmental Quality*, 26(4), 1056-1062.

Tarabara, V. V. and Wiesner, M. R. (2000) Bench-scale investigation of the performance of subaqueous reactive barriers (caps), 2nd International Symposium on Contaminated Sediments.

Taylor, R. and Krishna, R. (1993) Multicomponent Mass Transfer, J. Wiley & Sons.

TechData Sheet, (2002) Naval facilities engineering command, Washington DC 20374-5065, December 2002 (TDS-2092-ENV).

Thibodeaux, L. J. (1996) Environmental chemodynamics: movement of chemicals in air, water, and soil, J. Wiley & Sons.

Thibodeaux, L. J. and Boyle, J. D. (1978) Bedform-generated convective transport in bottom sediment, *Nature*, 325, 341-343.

Thoma, G. J. (1994) Studies on the diffusive transport of hydrophobic organic chemicals in bed sediments, Ph. D. Dissertation, Louisiana State University, Baton Rouge, LA.

Thoma, G. J., Reible, D. D., Valsaraj, K. T., and Thibodeaux, L. J. (1993) Efficiency of capping contaminated sediments in Situ. 2. Mathematics of diffusion-adsorption in the capping layer, *Environ. Sci. Technol.*, 27, 2412-2419.

Tomlinson, E. (1983) Enthalpy-entropy compensation analysis of pharmaceutical, biochemical and biological systems, *International Journal of Pharmaceutics*, 13(2), 115-44.

Tungittiplakorn, W., Cohen, C., and Lion, L. W. (2005) Engineered polymeric nanoparticles for bioremediation of hydrophobic contaminants, *Environ. Sci. Technol.*, 37(5), 1354-1358.

Urban, N. R., Brezonik, P. L., Baker, L. A., and Sherman, L. A. (1994) Sulfate reduction and diffusion in sediments of Little Rock Lake, Wisconsin, *Limnology and Oceanography*, 39(4), 797-815.

U. S. EPA (2004) Index to the ARCS (Assessment and Remediation of Contaminated Sediments) in-situ capping guidance, Great lakes contaminated sediments, (www.epa.gov/glnpo/sediment/iscmain/).

Valsaraj, K. T. and Yuan, Q. Z. (2004) Transport and fate of hazardous substances in capped contaminated sediment system, platform presentation in the 4th SETAC World Congress, Portland, Oregon, USA, November 14-18, 2004, p147.

Valsaraj, K. T. and Sojitra, I. (1997) Transport of hydrophobic organic compounds by colloids through porous media. 3. Diffusion from sediment porewater to overlying water in laboratory microcosms, *Colloids and Surfaces, A: Physicochemical and Engineering Aspects*, 121(2-3), 125-133.

Valsaraj, K. T. (1995a) Removal of organics from water by nonfoaming flotation, Chapter 13 in Matis' book titled Flotation science and engineering, Marcel Dekker, Inc.

Valsaraj, K. T. (1995b). Elements of environmental engineering, Thermodynamics and Kinetics, Lewis Publishers.

Valsaraj, K. T., Choy, B., Ravikrishna, R., Reible, D.D., Thibodeaux, L. J., Price, C. B., Brannon, J. M., and Myers, T. E. (1997) Air emissions from exposed, contaminated sediments and dredged materials 1. Experimental data in laboratory microcosms and mathematical modeling, *Journal of Hazardous Materials*, 54, 65-87.

Valsaraj, K. T., Porter, J. L., Liljenfeldt, E. K., and Springer, C. (1986) Solvent sublation for the removal of hydrophobic chlorinated compounds from aqueous solutions, *Wat. Res.*, 20(9), 1161-1175.

Van Kessel, T. and van Kesteren, W. G. M. (2002) Gas production and transport in artificial sludge depots, *Waste Management* (Oxford, United Kingdom), 22(1), 19-28.

Velinsky, D. J., Wade, T. L., Schlekat, C. E., McGee, B. L., and Presley, B. J. (1994) Tidal river sediments in the Washington, D. C. area. I. Distribution and sources of trace metals, *Estuaries*, 17(2), 305-20.

Wade, T. L., Velinsky, D. J., Reinharz, E., and Schlekat, C. E. (1994) Tidal river sediments in the Washington, D.C. area. II. Distribution and sources of organic contaminants, *Estuaries*, 17(2), 321-33.

Walters, R. W. and Luthy, R. G. (1984) Equilibrium adsorption of polycyclic aromatic hydrocarbons from water onto activated carbon, *Environ. Sci. Technol.*, 18(6), 395-403.

Wammer, K. H. and Peters, C. A. (2005) Polycyclic aromatic hydrocarbon biodegradation rates: a structure-based study, *Environ. Sci. Technol.*, 39(8), 2571-2578.

Wang, X. Q., Thibodeaux, L. J., Valsaraj, K. T., and Reible, D. D. (1991) Efficiency of capping contaminated bed sediments in situ. 1. Laboratory-scale experiments on diffusion-adsorption in the capping layer, *Environ. Sci. Technol.*, 25, 1578-1584.

Wassmann, R., Thein, U. G., Whiticar, M. J., Rennenberg, H., Seiler, W., and Junk, W. J. (1992) Methane emissions from the Amazon floodplain: characterization of production and transport, *Global Biogeochemical Cycles*, 6(1), 3-13.

Weber, W. J. Jr., LeBoeuf, E. J., Young, T. M., and Huang, W. (2001) Contaminant interactions with geosorbent organic matter: Insights drawn from polymer sciences, *Water Res.*, 35, 853-868.

Wever, T. F., Fiedler, H. M., Fechner, G., Abegg, F., and Stender, Ingo H. (1997) Side-scan and acoustic subbottom characterization of the sea floor near the Dry Tortugas, Florida, *Geo-Marine Letters*, 17(4), 246-252.

Wilkinson, P. M. and Dierendonck, L. L. V. (1994) A theoretical model for the influence of gas properties and pressure on single-bubble formation at an orifice, *Chemical Engineering Science*, 49, 1429-1438.

Wilson, S. C. and Jones, K. C. (1993) Bioremediation of soil contaminated with polycyclic aromatic hydrocarbons (PAHs): A Review, *Environ. Pollut.*, 81, 229-249.

Wilson, T. R. S. (1986) Vertical porewater advection in deep-ocean sediments, investigated by means of a general diagenetic model, *Science of the Total Environment*, 49, 163-73.

Wong, K. S. and Duncan, J. M. (1984) CONSOL: a computer program for 1-D consolidation analysis of layered soil masses, Report No. UCB/GT/84-06, Department of Civil Engineering, University of California, Berkeley, CA.

Yuan, Q. Z., Valsaraj, K. T., Willson, C. S., and Reible, D. D. (2005) Sediment and contaminant release during gas ebullition, Presentation at the 2005 AIChE Annual Meeting, Cincinnati, OH, October 30-November 4.

Yuan, Q. Z., Valsaraj, K. T., Reible, D. D., and Willson C. S. (2006) Sediment and contaminant release during gas ebullition, *Journal of the Air and Waste Management Association*, submitted.

APPENDIX A: ANALYTICAL PROCEDURES FOR SEDIMENT AND AQUEOUS SAMPLES

A1 PAH Analysis (US EPA Method 8270 and 8310)

A1.1 Sediment Samples

1. The sediment sample is split for moisture determination and QA/AC and, then about 5 g of wet sediment subsample is placed in a 50 mL glass jar.
2. About 20 g of anhydrous sodium sulfate is added, and mixed with the sediment thoroughly with a spatula.
3. 60 ml of solvent (1:1 hexane/acetone, v/v) is added to the jar, and the jar is capped immediately. Vibrate the jar in the sonicator for about 20 minutes. Stay still overnight.
4. 2 ml of extract solution is removed with Pasteur pipette to a 2 ml volumetric flask.
5. The extract solution is evaporated to approximately 0.2 ml with Blowdone system, and acetonitrile is added to make the final volume of 2 ml. HAAKEBUCHLER shaker is used to mix the solution and acetonitrile thoroughly.
6. The sample is transferred to a 2 ml vial and analyzed with HPLC.
7. Sediment loading is calculated by

$$W_s (mg / kg) = \frac{0.06f \cdot A}{W_{ws} \cdot (1 - w)} \quad (A1)$$

where f is the factor (ppb/area) which is obtained by the calibration, A is the area of the peak, W_{ws} is the weight of the wet sediment (g), and w is the content of water in the sediment samples (%).

A1.2 Aqueous Samples

1. 10 ml of hexane is added into a subsample from the sample directly obtained from the outlet of the diffusion chamber.

2. The sample is vigorously shaken for about 3 minutes and followed by sonication in a Cole-Parmer ultrasonic water bath for about 20 minutes.
3. 2 ml of the hexane is taken with Pasteur pipette to a 2 ml volumetric flask.
4. The hexane is exchanged to acetonitrile by a procedure as described in A1.1, and then analyzed with HPLC.

A2 Metal Analysis (US EPA Method 6020 and 200-8)

A2.1 Sediment Samples

1. The sediment sample is split for moisture determination and QA/AC and then about 0.25 g of wet sediment (less than 0.25 g for 16 samples and 0.25-0.5 g for 8 samples) is placed in the plastic tubes.
2. 10 ml of nitric acid (68.0 – 71.0% w/w, Trace Metal Grade, Fisher) is added to each sample. The samples are shaken several times in about 15 minutes.
3. The samples are put into ‘Microwave sample preparation system’ (Anton Paar, PerkinElmer, Multiwave 3000) for the digestion. After the digestion, the samples are allowed to get cold for about 1 hour.
4. The samples are filtrated and washed 2 – 3 times using 3% nitric acid. The final volume is 50 ml.
5. 1 ml of the above solution is diluted to 10 ml using 3% nitric acid. Then 20 µL of each standard solution (single-element internal standard and multi-element internal standard, SPEX CertiPrep, Inc. METUCHEN, NJ) is added to the samples.
6. Each sample is shaken for 3 minutes and ready for ICP-MS analysis.
7. The calibration is obtained using Instrument Calibration Standard (SPEX CertiPrep, Inc. NJ).

8. Metal concentration in sediment can be calculated by

$$W_s (mg / kg) = \frac{0.5C_m}{W_{ws} \cdot (1 - w)} \quad (A2)$$

where C_m is the metal concentration (ppb) measured with ICP-MS, W_{ws} is the weight of the wet sediment (g), and w is the content of water in the sediment sample (%).

A2.2 Aqueous Sample

1. 0.45 ml of nitric acid (68.0 – 71.0% w/w) and 20 μ L of each internal standard (single-element and multi-element) are added to a 15 ml plastic tube (Corning 430290) with volumetric pipettes.
2. The sample collected directly from the diffusion chamber is added to the above plastic tube to make the final volume 10 ml.
3. The sample is shaken for 3 minutes and ready to be analyzed with ICP-MS.

APPENDIX B: MATHEMATICAL METHODS AND DERIVATIONS

B1 Diffusion, Advection and Reaction in a Two-layer Finite System

B1.1 Coordinates

Figure B1 shows the coordinate system on the diffusion chamber.

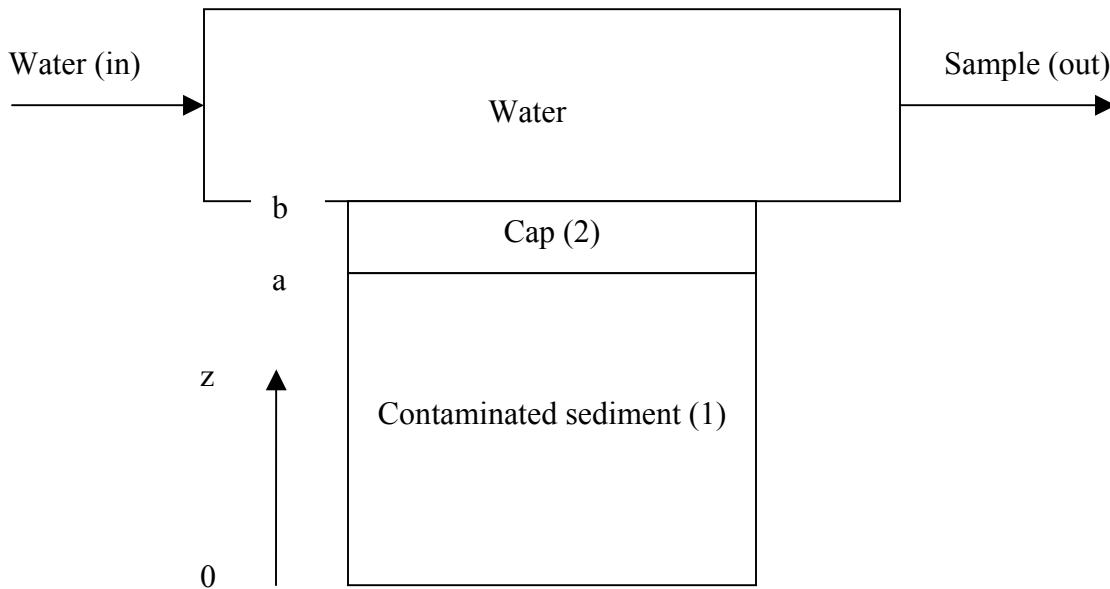


Figure B1 Schematic of the two layer capped system.

B1.2 Model

The general equations governing the fate and transport of contaminants in the sediment and the cap are developed by mass balance (Choy and Reible, 2000).

$$R_{f2} \frac{\partial C_{A2}}{\partial t} = D_{A(eff)2} \frac{\partial^2 C_{A2}}{\partial z^2} - v \frac{\partial C_{A2}}{\partial z} - k_2 C_{A2} \quad (\text{Cap layer}) \quad (\text{B1})$$

$$R_{f1} \frac{\partial C_{A1}}{\partial t} = D_{A(eff)1} \frac{\partial^2 C_{A1}}{\partial z^2} - v \frac{\partial C_{A1}}{\partial z} - k_1 C_{A1} \quad (\text{Sediment layer}) \quad (\text{B2})$$

Initial conditions:

$$1. C_{A1}(z, t)|_{t=0} = C_{A0}$$

$$2. C_{A2}(z, t)|_{t=0} = 0$$

Boundary conditions:

$$1. \left. \frac{\partial C_{A1}}{\partial z} \right|_{z=0} = 0 \quad (z=0, \text{ at the bottom of the chamber})$$

$$2. C_{A1}(z, t)|_{z=a} = C_{A2}(z, t)|_{z=a}$$

(z=a, at the sediment-cap interface)

$$3. D_{A(eff)1} \left. \frac{\partial C_{A1}}{\partial z} \right|_{z=a} = D_{A(eff)2} \left. \frac{\partial C_{A2}}{\partial z} \right|_{z=a}$$

$$4. D_{A(eff)2} \left. \frac{\partial C_{A2}}{\partial z} \right|_{z=b} + (k_a - v)C_{A2}|_{z=b} = 0$$

(z=b, at the water-sediment/cap interface)

Boundary condition 4 is from the mass balance in overlying water layer or

$$-AD_{A(eff)2} \left. \frac{\partial C_{A2}}{\partial z} \right|_{z=b} + AvC_{A2}|_{z=b} = qC_{Aw} = Ak_m(C_{A2}|_{z=b} - C_{Aw}) + AvC_{A2}|_{z=b}, \quad \text{where } C_A \text{ is the}$$

concentration of species A in water (kg/m^3), $D_{A(eff)}$ is the effective diffusivity of species A

(m^2/s), calculated by $D_{A(eff)} = D_{Aw} \varepsilon^{\frac{4}{3}}$, D_{Aw} is the diffusivity of species A in water (m^2/s), ε is

porosity, $R_f = \varepsilon + \rho_b K_d$ is the retardation factor, ρ_b is the sediment bulk density (kg/m^3), K_d is

the partition coefficient of species A between water and sediment (m^3/kg), $K_d = K_{oc} f_c$, K_{oc} is

the organic carbon-water partition coefficient, f_c is the fractional organic

carbon, $k_a = \frac{q(k_m + v)}{q + k_m A}$, q is the water flow rate (m^3/s), k_m is the mass transfer coefficient at the

interface between water and sediment (m/s), and A is the mass transfer area (m^2).

B1.3 A Numerical Algorithm-----Fully Implicit Method

From Taylor series, we obtain finite difference formulas for differentiation as follows

$$f'(z_i) = \frac{f(z_{i+1}) - f(z_{i-1}))}{2\Delta z} + o(\Delta z^2) \quad (\text{B3})$$

$$f''(z_i) = \frac{f(z_{i+1}) - 2f(z_i) + f(z_{i-1}))}{(\Delta z)^2} + o(\Delta z^2) \quad (\text{B4})$$

So, the governing equations (B1) and (B2) in finite difference can be expressed as

$$R_{f2} \frac{C_{i,j+1} - C_{i,j}}{\Delta t} = D_{A(\text{eff})2} \left[\frac{C_{i+1,j+1} - 2C_{i,j+1} + C_{i-1,j+1}}{(\Delta z)^2} \right] - v_{j+1} \frac{C_{i+1,j+1} - C_{i-1,j+1}}{2\Delta z} - k_2 C_{i,j+1} \quad (\text{B1-1})$$

$$R_{f1} \frac{C_{i,j+1} - C_{i,j}}{\Delta t} = D_{A(\text{eff})1} \left[\frac{C_{i+1,j+1} - 2C_{i,j+1} + C_{i-1,j+1}}{(\Delta z)^2} \right] - v_{j+1} \frac{C_{i+1,j+1} - C_{i-1,j+1}}{2\Delta z} - k_1 C_{i,j+1} \quad (\text{B2-1})$$

where the subscript i is used for a step in space and j for a step in time.

Collecting terms gives

$$\lambda_{21} C_{i-1,j+1} + \lambda_{22} C_{i,j+1} + \lambda_{21} C_{i+1,j+1} = C_{i,j} \quad (\text{B1-2})$$

$$\lambda_{11} C_{i-1,j+1} + \lambda_{12} C_{i,j+1} + \lambda_{11} C_{i+1,j+1} = C_{i,j} \quad (\text{B2-2})$$

where $\lambda_{21} = -\frac{\Delta t}{R_{f2}\Delta z} \left(\frac{D_{e2}}{\Delta z} + \frac{v_{j+1}}{2} \right)$, $\lambda_{22} = 1 + \frac{2D_{e2}\Delta t}{R_{f2}(\Delta z)^2} + \frac{k_2\Delta t}{R_{f2}}$, $\lambda_{23} = \frac{\Delta t}{R_{f2}\Delta z} \left(\frac{v_{j+1}}{2} - \frac{D_{e2}}{\Delta z} \right)$,

$$v_{j+1} = \frac{1.1}{[1 + 0.11(j+1)\Delta t]^2} \quad (\text{see Equation (3.11)}), \quad \lambda_{11} = -\frac{\Delta t}{R_{f1}\Delta z} \left(\frac{D_{e1}}{\Delta z} + \frac{v_{j+1}}{2} \right),$$

$$\lambda_{12} = 1 + \frac{2D_{e1}\Delta t}{R_{f1}(\Delta z)^2} + \frac{k_1\Delta t}{R_{f1}}, \lambda_{13} = \frac{\Delta t}{R_{f1}\Delta z} \left(\frac{v_{j+1}}{2} - \frac{D_{e1}}{\Delta z} \right), \varepsilon = \varepsilon_0 - \frac{1.1(j+1)\Delta t}{150[1+0.11(j+1)\Delta t]} \text{ (see$$

Equation (3.12)), $D_{A(eff)} = D_w \varepsilon^{\frac{4}{3}}$, $R_f = R_{f0} + K_d \rho_b$, and $K_d = K_{oc} f_c$.

For $i=1$, equation (B2-2) can be written as

$$\lambda_{11}C_{0,j+1} + \lambda_{12}C_{1,j+1} + \lambda_{13}C_{2,j+1} = C_{1,j}$$

The $C_{0,j+1}$ can be removed by employing the boundary condition 1, which can be rewritten as in finite difference

$$\frac{C_{2,j+1} - C_{0,j+1}}{2\Delta z} = 0 \quad \text{or} \quad C_{0,j+1} = C_{2,j+1}$$

Substituting the above into the equation for $i=1$ yields

$$\lambda_{12}C_{1,j+1} + (\lambda_{11} + \lambda_{13})C_{2,j+1} = C_{1,j}$$

For $i=2$,

$$\lambda_{11}C_{1,j+1} + \lambda_{12}C_{2,j+1} + \lambda_{13}C_{3,j+1} = C_{2,j}$$

For $i=3$,

$$\lambda_{11}C_{2,j+1} + \lambda_{12}C_{3,j+1} + \lambda_{13}C_{4,j+1} = C_{3,j}$$

.....

For $i=m_1-1$,

$$\lambda_{11}C_{m_1-2,j+1} + \lambda_{12}C_{m_1-1,j+1} + \lambda_{13}C_{m_1,j+1} = C_{m_1-1,j}$$

For $i=m_1$ (at the interface between sediment and cap), boundary condition 3 is used:

$$D_{A(eff)1} \frac{C_{m_1,j+1} - C_{m_1-1,j+1}}{\Delta z} = D_{A(eff)2} \frac{C_{m_1+1,j+1} - C_{m_1,j+1}}{\Delta z}$$

$$\text{or} \quad -D_{A(eff)1}C_{m_1-1,j+1} + DC_{m_1} - D_{A(eff)2}C_{m_1+1} = 0$$

where $D = D_{A(eff)1} + D_{A(eff)2}$

For $i=m_1+1$, equation (B1-2) can be used:

$$\lambda_{21}C_{m_1,j+1} + \lambda_{22}C_{m_1+1,j+1} + \lambda_{23}C_{m_1+2,j+1} = C_{m_1+1,j}$$

In fact, equations for $i=m_1-1$, m_1 and m_1+1 ensure boundary condition 2 to hold.

For $i=m_1+2$,

$$\lambda_{21}C_{m_1+1,j+1} + \lambda_{22}C_{m_1+2,j+1} + \lambda_{23}C_{m_1+3,j+1} = C_{m_1+2,j}$$

.....

For $i=m_2$ (at the interface between cap and water),

$$\lambda_{21}C_{m_2-1,j+1} + \lambda_{22}C_{m_2,j+1} + \lambda_{23}C_{m_2+1,j+1} = C_{m_2,j}$$

Boundary condition 4 can be rewritten as in finite difference

$$D_{A(eff)2} \frac{C_{m_2+1,j+1} - C_{m_2-1,j+1}}{2\Delta z} + (k_{a,j+1} - v_{j+1})C_{m_2,j+1} = 0$$

$$\text{or } C_{m_2+1,j+1} = C_{m_2-1,j+1} - \frac{2(\Delta z)(k_{a,j+1} - v_{j+1})}{D_{A(eff)2}} C_{m_2,j+1}$$

Substituting the above into equation for $i=m_2$ gives

$$(\lambda_{21} + \lambda_{23})C_{m_2-1,j+1} + \lambda_{22}C_{m_2,j+1} = C_{m_2,j}$$

where $\lambda = \lambda_{22} - \lambda_{23} \frac{2\Delta z(k_{a,j+1} - v_{j+1})}{D_{A(eff)2}}$ and

$$k_{a,j+1} = \frac{8 \cdot 10^{-8} q \cdot \exp\left[\frac{-0.3633 \cdot 1.1 \cdot (j+1)\Delta t}{1 + 0.11(j+1)\Delta t}\right]}{q + 8 \cdot 10^{-8} A \cdot \exp\left[\frac{-0.3633 \cdot 1.1 \cdot (j+1)\Delta t}{1 + 0.11(j+1)\Delta t}\right]} \quad (\text{see Equation (3.13)}).$$

Now we have m_2 equations and m_2 unknowns. The system in the form of matrix can be expressed as:

$$X_{i,n+1} = X_{i,n} + \frac{K_{1,i} + 2K_{2,i} + 2K_{3,i} + K_{4,i}}{6} \quad (\text{B7})$$

where $K_{1,i} = hf_i(t_n, X_{1,n}, X_{2,n})$, $K_{2,i} = hf_i\left(t_n + \frac{h}{2}, X_{1,n} + \frac{K_{11}}{2}, X_{2,n} + \frac{K_{12}}{2}\right)$,

$K_{3,i} = hf_i\left(t_n + \frac{h}{2}, X_{1,n} + \frac{K_{21}}{2}, X_{2,n} + \frac{K_{22}}{2}\right)$, $K_{4,i} = hf_i(t_n + h, X_{1,n} + K_{31}, X_{2,n} + K_{32})$, and h is

the step size for integration across the i^{th} step.

Adams-Moulton Method: The following two equations are used in this method.

Prediction equation:

$$X_{i,n+1}^p = X_{i,n} + \frac{h}{12}(23f_{i,n} - 16f_{i,n-1} + 5f_{i,n-2}) \quad (\text{B8})$$

Check equation:

$$X_{i,n+1} = X_{i,n} + \frac{h}{12}(5f_{i,n+1} + 8f_{i,n} - f_{i,n-1}) \quad (\text{B9})$$

B3 Penetration Theory

For uncapped sediment, contaminant flux can be estimated by

$$N_m = \sqrt{\frac{D_{eff}}{\pi t}} \cdot \frac{w_A}{K_d} \quad (\text{B10})$$

where D_{eff} is the effective diffusivity (m^2/s), w_A is the sediment loading (kg/kg), t is the time,

K_d is the partition coefficient of contaminant between water and sediment (m^3/kg). So K_d or the

parameter $\frac{w_A}{K_d} \sqrt{\frac{D_{eff}}{\pi}}$ can be determined by the slope of linear regression of the experimental

data (N_m vs $1/\sqrt{t}$).

For capped sediment, the following equation is used to calculate contaminant flux

$$N_m = \frac{\frac{w_A}{K_d}}{\frac{h}{D_{eff}} + \sqrt{\frac{\pi t}{D_{eff}}}} \quad (\text{B11})$$

where h is the cap thickness (m). Similarly, K_d or the parameter $\frac{w_A}{K_d}$ can be determined by the

slope of linear regression of the experimental data (N_m vs $1/\left(\frac{h}{D_{eff}} + \sqrt{\frac{\pi t}{D_{eff}}}\right)$).

APPENDIX C: COMPUTER (MATLAB) CODES

C1 Fully Implicit Method to Solve Partial Differential Equations (PDEs)

%PDEs includes diffusion, advection and reaction in a sediment-cap two layer finite domain, solved by finite difference---fully implicit method

```
clear all
close all
%I Assign physical parameters:
%1.Diffusion chamber dimensions and water flow rate
l=0.1;           %length of mass transfer region---m
w=0.05;         %width of mass transfer---m
h=0.008;       %height of water---m
q=9.3/(1000000*3600); %water flow rate -m3/s
L1=0.138;      %thickness of sediment (m)
L2=0.012;      %thickness of cap (m)

%2. Sediment properties  1-Dibenzofuran, 2-phenanthrene, 3-pyrene
Koc1=101; Koc2=101.4; Koc3=101.8; %organic carbon-water partition constant-m3/kg.
foc=0.05; %fractional organic carbon.
Kd1=Koc1*foc; Kd2=Koc2*foc; Kd3=Koc3*foc; %sediment -water partition constant-m3/kg.
ew0=0.69; %initial water filled porosity.
bd=725.2; %sediment bulk density-kg/m3.
Rf10=ew0+Kd1*bd; Rf20=ew0+Kd2*bd; Rf30=ew0+Kd3*bd; %initial retardation factor.
k1=1*10(-6); %First-order reaction constant in the sediment(1/s)

%3. sand properties
ews0=0.5; %porosity
bds=1541; %bulk density -kg/m3
focs=0.00001; %fractional organic carbon
Kds1=Koc1*focs;Kds2=Koc2*focs;Kds3=Koc3*focs; %sand-water partition constant
Rfs10=ews0+Kds1*bds;Rfs20=ews0+Kds2*bds; Rfs30=ews0+Kds3*bds; %initial retardation
factor of sand
k2=2*10(-6); %first-order reaction constant in the cap (1/s)

%4 Tracer properties
Dw1=6*10(-10); Dw2=5.8*10(-10); Dw3=5.5*10(-10); %diffusivity in water of tracers-
m2/s.
Dwg=8.12*10(-10); %diffusivity in water of gypsum.
De10=Dw1*(ew0)(4/3); De20=Dw2*(ew0)(4/3); De30=Dw3*(ew0)(4/3); %effective
diffusivity of tracers in porewater.
Ws01=118/1000000; Ws02=118/1000000; Ws03=111/1000000; %initial sediment
concentrations of tracers.-kg/kg
```

```

Ca01=Ws01*bd/Rf10; Ca02=Ws02*bd/Rf20; Ca03=Ws03*bd/Rf30;    %initial concentrations
of tracers in porewater-kg/m3
km1=((Dw1/Dwg)^0.5)*6.26*10(-8); km2=((Dw2/Dwg)^0.5)*6.26*10(-8);
km3=((Dw3/Dwg)^0.5)*6.26*10(-8);    %sediment-water mass transfer
coefficients, m/s
ka1=q*km1/(q+km1*w); ka2=q*km2/(q+km2*w); ka3=q*km3/(q+km3*w);

%II Numerical solution
%Assign computational parameters
tfinal=30;    %Final time for unsteady state solution (day)
nnt=2000;    %number of time steps
nnz=1501;    %number of spatial nodes (including ends)

%Prompt the user to choose what wanted
fprintf('Choose from the followings:\n');
fprintf('1. contaminant flux with time for capped system\n');
fprintf('2. concentration profile for capped system\n');
fprintf('3. contaminant flux with time for uncapped system\n');
fprintf('4. concentration profile for uncapped system\n');
itype=input(' ');

%1.contaminant flux with time for capped system

if itype==1
dt=tfinal*3600*24/(nnt);
dz=(L1+L2)/(nnz-1);
m1=1+(nnz-1)*L1/(L1+L2);
z=0:dz:(0.15);
t=0:dt:tfinal*3600*24;

%Initialize C vector and variable vectors
C=zeros(nnz,1);
for p=1:m1;
    C(p)=1;
end

ew=zeros(nnt+1,1);
De12=zeros(nnt+1,1);
Rf12=zeros(nnt+1,1);
F=zeros(nnt+1,1);
vj=zeros(nnt+1,1);
lam11=zeros(nnt+1,1);
lam12=zeros(nnt+1,1);
lam13=zeros(nnt+1,1);
lam21=zeros(nnt+1,1);
lam22=zeros(nnt+1,1);

```

```

lam23=zeros(nnt+1,1);
lam=zeros(nnt+1,1);
D=zeros(nnt+1,1);
ka2j=zeros(nnt+1,1);
kmgj=zeros(nnt+1,1);

time=0;
F(1,1)=ka2*Ca01*(C(nnz))*36*24*10^10;

plot(t/(3600*24),F,'-o','markersize',4,'linewidth',2,'markeredgecolor','k',...
      'markerfacecolor','k')
      xlabel('time (day)')
      ylabel('flux (ng/cm^2-day)')
      title(['Flux of tracer with time at interface between sediment and water'])
%hold on %pause

%Iterate through the time steps
for j=1:nnt;
    ew(j,1)=ew0-1.1*((j+1)*dt/(24*3600))/(150*(1+0.11*(j+1)*dt/(24*3600)));
    De12(j,1)=Dw2*(ew(j,1)^(4/3));
    Rf12(j,1)=ew(j,1)+Kd2*bd;
    De22=Dw2*(ews0^(4/3));
    Rfs22=Rfs20;
    vj(j,1)=1.1/((24*36*10^(5))*(1+0.11*(j+1)*dt/(24*3600))^2);
    lam11(j,1)=-dt*(De12(j,1)/dz+vj(j,1)/2)/(Rf12(j,1)*dz);
    lam12(j,1)=1+2*De12(j,1)*dt/(Rf12(j,1)*dz^2)+k1*dt/Rf12(j,1);
    lam13(j,1)=dt*(vj(j,1)/2-De12(j,1)/dz)/(Rf12(j,1)*dz);
    lam21(j,1)=-dt*(De22/dz+vj(j,1)/2)/(Rfs22*dz);
    lam22(j,1)=1+2*De22*dt/(Rfs22*dz^2)+k2*dt/Rfs22;
    lam23(j,1)=dt*(vj(j,1)/2-De22/dz)/(Rfs22*dz);
    ka2j(j,1)=(j+1)*dt/(24*3600);
    kmgj(j,1)=(8*10^(-8))*exp(-0.3622*1.1*ka2j(j,1)/(1+0.11*ka2j(j,1)));
    ka2j(j,1)=((Dw2/Dwg)^0.5)*kmgj(j,1);
    ka2j(j,1)=q*(ka2j(j,1)+vj(j,1))/(q+1*w*ka2j(j,1));
    lam(j,1)=lam22(j,1)-lam23(j,1)*2*dz*(ka2j(j,1)-vj(j,1))/De22;
    D(j,1)=De12(j,1)+De22;

%Assemble the matrix at each time step.
    A=zeros(nnz,nnz);
    A(1,1)=lam12(j,1);
    b(1,1)=C(1);
    A(1,2)=lam11(j,1)+lam13(j,1);

    for i=2:m1-1;
        A(i,i-1)=lam11(j,1);
        A(i,i)=lam12(j,1);

```

```

        A(i,i+1)=lam13(j,1);
        b(i,1)=C(i);
    end
    A(m1,m1-1)=-De12(j,1);
    A(m1,m1)=D(j,1);
    A(m1,m1+1)=-De22;
    b(m1,1)=0;

    for q=(m1+1):(nnz-1);
        A(q,q-1)=lam21(j,1);
        A(q,q)=lam22(j,1);
        A(q,q+1)=lam23(j,1);
        b(q,1)=C(q);
    end

    A(nnz,nnz-1)=lam21(j,1)+lam23(j,1);
    A(nnz,nnz)=lam(j,1);
    b(nnz,1)=C(nnz);

    %Solve for new values of C.
    C=A\b;

    F(j+1,1)=ka2j(j,1)*Ca02*(C(nnz))*36*24*10^10;
    time=dt*(j);

    plot(t/(3600*24),F,'-o','markersize',4,'linewidth',2,'markeredgecolor','k',...
        'markerfacecolor','k')
    xlabel('time (day)')
    ylabel('Flux (ng/cm^2-day)')
    title(['Flux of PHEN. with time (12 mm sand cap)'])
end
hold on
%experimental data for capped system
texp=[0.83,1.39,3.08,8.37,10.36,12.25,14.19,16.21,19.21,21.21,26.21,28.21,30.19];
Fexp=[6,3.79,7.32,7,4.085,2.96,2.285,1,2.405,2.12,1.555,1.43,1.66];
plot(texp,Fexp, '-s','markersize',12, 'LineStyle','none','markeredgecolor','k','markerfacecolor','k')
legend('model', 'exp',2)
hold off

end

%2.concentration profile for capped system
if itype==2
dt=tfinal*3600*24/(nnt);
dz=(L1+L2)/(nnz-1);
m1=1+(nnz-1)*L1/(L1+L2);

```

```

z=0:dz:(0.15);
t=0:dt:tfinal*3600*24;

%Initialize C vector and variable vectors
C=zeros(nnz,1);
for p=1:m1;
    C(p)=1;
end

Ws1=zeros(nnz,1);
Ws2=zeros(nnz,1);
ew=zeros(nnt+1,1);
De12=zeros(nnt+1,1);
Rf12=zeros(nnt+1,1);
F=zeros(nnt+1,1);
vj=zeros(nnt+1,1);
lam11=zeros(nnt+1,1);
lam12=zeros(nnt+1,1);
lam13=zeros(nnt+1,1);
lam21=zeros(nnt+1,1);
lam22=zeros(nnt+1,1);
lam23=zeros(nnt+1,1);
lam=zeros(nnt+1,1);
D=zeros(nnt+1,1);
ka2j=zeros(nnt+1,1);
kmgj=zeros(nnt+1,1);

time=0;
Ws(1,1)=Ca02*C(1,1)*Rf20*10^6/bd;

plot(z,Ws,'-o','markersize',4,'linewidth',2,'markeredgecolor','k',...
      'markerfacecolor','k')
xlabel('Length (m)')
ylabel('Concentration (Ws)')
title(['Concentration profile of Phen. in sediment, time(day)=' num2str(time/(3600*24))])

%Iterate through the time steps
for j=1:nnt;

ew(j,1)=ew0-1.1*((j+1)*dt/(24*3600))/(150*(1+0.11*(j+1)*dt/(24*3600)));
De12(j,1)=Dw2*(ew(j,1)^(4/3));
Rf12(j,1)=ew(j,1)+Kd2*bd;
De22=Dw2*(ews0^(4/3));
Rfs22=Rfs20;
vj(j,1)=1.1/((24*36*10^5)*(1+0.11*(j+1)*dt/(24*3600))^2);
lam11(j,1)=-dt*(De12(j,1)/dz+vj(j,1)/2)/(Rf12(j,1)*dz);

```

```

lam12(j,1)=1+2*De12(j,1)*dt/(Rf12(j,1)*dz^2)+k1*dt/Rf12(j,1);
lam13(j,1)=dt*(vj(j,1)/2-De12(j,1)/dz)/(Rf12(j,1)*dz);
lam21(j,1)=-dt*(De22/dz+vj(j,1)/2)/(Rfs22*dz);
lam22(j,1)=1+2*De22*dt/(Rfs22*dz^2)+k2*dt/Rfs22;
lam23(j,1)=dt*(vj(j,1)/2-De22/dz)/(Rfs22*dz);
ka2j(j,1)=(j+1)*dt/(24*3600);
kmgj(j,1)=(8*10^(-8))*exp(-0.3622*1.1*ka2j(j,1)/(1+0.11*ka2j(j,1)));
ka2j(j,1)=((Dw2/Dwg)^0.5)*kmgj(j,1);
ka2j(j,1)=q*ka2j(j,1)/(q+1*w*ka2j(j,1));
lam(j,1)=lam22(j,1)-lam23(j,1)*2*dz*(ka2j(j,1)-vj(j,1))/De22;
D(j,1)=De12(j,1)+De22;

```

```

%Assemble the matrix at each time step.

```

```

A=zeros(nnz,nnz);
A(1,1)=lam12(j,1);
b(1,1)=C(1);
A(1,2)=lam11(j,1)+lam13(j,1);

```

```

for i=2:m1-1;
A(i,i-1)=lam11(j,1);
A(i,i)=lam12(j,1);
A(i,i+1)=lam13(j,1);
b(i,1)=C(i);
end

```

```

A(m1,m1-1)=-De12(j,1);
A(m1,m1)=D(j,1);
A(m1,m1+1)=-De22;
b(m1,1)=0;

```

```

for q=(m1+1):(nnz-1);
A(q,q-1)=lam21(j,1);
A(q,q)=lam22(j,1);
A(q,q+1)=lam23(j,1);
b(q,1)=C(q);
end

```

```

A(nnz,nnz-1)=lam21(j,1)+lam23(j,1);
A(nnz,nnz)=lam(j,1);
b(nnz,1)=C(nnz);

```

```

%Solve for new values of C.

```

```

C=A\b;

```

```

Ws1=Ca02*C*Rf12(j,1)*10^6/bd;
Ws2=Ca02*C*Rfs22*10^6/bds;

```

```

for u=1:m1;
    Ws(u,1)=Ws1(u,1);
end

for v=m1+1:nnz;
    Ws(v,1)=Ws2(v,1);
end

    time=dt*(j);

plot(z, Ws, '-o', 'markersize', 4, 'linewidth', 2, 'markeredgecolor', 'k', ...
     'markerfacecolor', 'k')
    xlabel('Length (m)')
    ylabel('Concentration (Ws)')
    title(['Concentration profile of PHEN. in sediment and (12 mm) cap,
time(day)=' num2str(time/(3600*24))])
end
end

%3.contaminent flux with time for uncapped system
if itype==3
dt=tfinal*3600*24/(nnt);
dz=(0.15)/(nnz-1);
z=0:dz:(0.15);
t=0:dt:tfinal*3600*24;

    %Initialize C vector
    C=zeros(nnz,1);
    for p=1:(nnz);
        C(p)=1;
    end
ew=zeros(nnt+1,1);
De2=zeros(nnt+1,1);
Rf2=zeros(nnt+1,1);
F=zeros(nnt+1,1);
vj=zeros(nnt+1,1);
lam1=zeros(nnt+1,1);
lam2=zeros(nnt+1,1);
lam3=zeros(nnt+1,1);
ka2j=zeros(nnt+1,1);
kmgj=zeros(nnt+1,1);

    time=0;
F(1,1)=ka2*Ca02*C(nnz)*36*24*10^10;

plot(t/(3600*24),F, '-o', 'markersize', 4, 'linewidth', 2, 'markeredgecolor', 'k', ...

```

```

'markerfacecolor','k')
    xlabel('time (day)')
    ylabel('flux (ng/cm^2-day)')
    title(['Flux of tracer with time at interface between sediment and water'])
%hold on %pause

%Iterate through the time steps
for j=1:nnt;

ew(j,1)=ew0-1.1*((j+1)*dt/(24*3600))/(150*(1+0.11*(j+1)*dt/(24*3600)));
De2(j,1)=Dw2*(ew(j,1)^(4/3));
Rf2(j,1)=ew(j,1)+Kd2*bd;
vj(j,1)=1.1/((24*36*10^(5))*(1+0.11*(j+1)*dt/(24*3600))^2);
lam1(j,1)=-dt*(De2(j,1)/dz+vj(j,1)/2)/(Rf2(j,1)*dz);
lam2(j,1)=1+2*De2(j,1)*dt/(Rf2(j,1)*dz^2)+k1*dt/Rf2(j,1);
lam3(j,1)=dt*(vj(j,1)/2-De2(j,1)/dz)/(Rf2(j,1)*dz);
ka2j(j,1)=(j+1)*dt/(24*3600);
kmgj(j,1)=(8*10^(-8))*exp(-0.3633*1.1*ka2j(j,1)/(1+0.11*ka2j(j,1)));
ka2j(j,1)=((Dw2/Dwg)^0.5)*kmgj(j,1);
ka2j(j,1)=q*(ka2j(j,1)+vj(j,1))/(q+1*w*ka2j(j,1));
lam(j,1)=lam2(j,1)-lam3(j,1)*2*dz*(ka2j(j,1)-vj(j,1))/De2(j,1);

%Assemble the matrix at each time step.
A=zeros(nnz,nnz);
A(1,1)=lam2(j,1);
b(1,1)=C(1);
A(1,2)=lam1(j,1)+lam3(j,1);

for i=2:nnz-1;
A(i,i-1)=lam1(j,1);
A(i,i)=lam2(j,1);
A(i,i+1)=lam3(j,1);
b(i,1)=C(i);
end

A(nnz,nnz-1)=lam1(j,1)+lam3(j,1);
A(nnz,nnz)=lam(j,1);
b(nnz,1)=C(nnz);

%Solve for new values of C.
C=A\b;
F(j+1,1)=ka2j(j,1)*Ca02*(C(nnz))*36*24*10^10;
time=dt*(j);

plot(t/(3600*24),F,'-o','markersize',4,'linewidth',2,'markeredgecolor','k',...
'markerfacecolor','k')

```

```

        xlabel('time (day)')
        ylabel('Flux (ng/cm^2-day)')
        title(['Flux of Phenanthrene with time (no cap)'])
end
hold on

% experimental data for uncapped system
texp=[0.83,1.39,3.08,4.72,6.3,8.37,10.36,12.25,14.19,16.21,19.21,21.21,26.21,28.21,30.19];
Fexp=[32.14,6.43,17.22,4.34,10.25,7.25,4.71,3.72,2.73,0.19,0.91,1.08,1.02,0.94,1.06];
plot(texp,Fexp, '-o','markersize',12, 'LineStyle','none','markeredgecolor','r','markerfacecolor','r')
legend('model', 'exp',2)
hold off

end

%4.concentration profile for uncapped system
if itype==4
dt=tfinal*3600*24/(nnt);
dz=(0.15)/(nnt-1);
z=0:dz:(0.15);
t=0:dt:tfinal*3600*24;

        %Initialize C vector
        C=zeros(nnt,1);
        for p=1:(nnt);
            C(p)=1;
        end
Ws=zeros(nnt,1);
eb=zeros(nnt+1,1);
De2=zeros(nnt+1,1);
Rf2=zeros(nnt+1,1);
F=zeros(nnt+1,1);
vj=zeros(nnt+1,1);
lam1=zeros(nnt+1,1);
lam2=zeros(nnt+1,1);
lam3=zeros(nnt+1,1);
ka2j=zeros(nnt+1,1);
kmgj=zeros(nnt+1,1);

        time=0;
Ws(1,1)=Ca02*C(1,1)*Rf20*10^6/bd;

plot(z,Ws,'-o','markersize',4,'linewidth',2,'markeredgecolor','k',...
     'markerfacecolor','k')
    xlabel('Length (m)')
    ylabel('Concentration (Ws)')

```

```

title(['Concentration profile in sediment, time(day)=' ,num2str(time/(3600*24))])

%Iterate through the time steps
for j=1:nnt;

ew(j,1)=ew0-1.1*((j+1)*dt/(24*3600))/(150*(1+0.11*(j+1)*dt/(24*3600)));
De2(j,1)=Dw2*(ew(j,1)^(4/3));
Rf2(j,1)=Rf20-1.1*((j+1)*dt/(24*3600))/(150*(1+0.11*(j+1)*dt/(24*3600)));
vj(j,1)=1.1/(((24*36*10^(5))*(1+0.11*(j+1)*dt/(24*3600))^2);
lam1(j,1)=-dt*(De2(j,1)/dz+vj(j,1)/2)/(Rf2(j,1)*dz);
lam2(j,1)=1+2*De2(j,1)*dt/(Rf2(j,1)*dz^2)+k1*dt/Rf2(j,1);
lam3(j,1)=dt*(vj(j,1)/2-De2(j,1)/dz)/(Rf2(j,1)*dz);
ka2j(j,1)=(j+1)*dt/(24*3600);
kmgj(j,1)=(8*10^(-8))*exp(-0.3633*1.1*ka2j(j,1)/(1+0.11*ka2j(j,1)));
ka2j(j,1)=((Dw2/Dwg)^0.5)*kmgj(j,1);
ka2j(j,1)=q*(ka2j(j,1)+vj(j,1))/(q+1*w*ka2j(j,1));
lam(j,1)=lam2(j,1)-lam3(j,1)*2*dz*(ka2j(j,1)-vj(j,1))/De2(j,1);

%Assemble the matrix at each time step.
A=zeros(nnz,nnz);
A(1,1)=lam2(j,1);
b(1,1)=C(1);
A(1,2)=lam1(j,1)+lam3(j,1);

for i=2:nnz-1;
A(i,i-1)=lam1(j,1);
A(i,i)=lam2(j,1);
A(i,i+1)=lam3(j,1);
b(i,1)=C(i);
end

A(nnz,nnz-1)=lam1(j,1)+lam3(j,1);
A(nnz,nnz)=lam(j,1);
b(nnz,1)=C(nnz);

%Solve for new values of C.
C=A\b;

Ws=Ca02*C*Rf2(j,1)*10^6/bd;
time=dt*(j);

plot(z,Ws,'-o','markersize',4,'linewidth',2,'markeredgecolor','k',...
'markerfacecolor','k')
xlabel('Length (m)')
ylabel('Concentration (Ws)')
title(['Concentration profile in sediment (no cap), time(day)=' ,num2str(time/(3600*24))])

```

```

    %hold on %pause
end
end

```

C2 Runge-Kutta and Adams-Moulton Methods to Solve Ordinary Differential Equations (ODEs)

% Runge-Kutta and Adams-Moulton method to solve ODE for bubble associated contaminant transport from capped/uncapped sediment under field conditions- comparison between capped and uncapped systems.

```

%I uncapped
%Parameters
%1.sediment
bd=789.1; pd=2600;ew0=1-bd/pd;      %sediment bulk density (kg/m^3), particle density
(kg/m^3) and porosity
Ls=2;          %sediment depth(m)
Koc=10^1.4; fc=0.041; Kd=Koc*fc;    %partition coefficient (m^3/kg)
Rfs=ew0+Kd*bd;
%2. water and gas
Lw=3;          %water depth (m),
Fg=1/(1000*24*3600); H=0.0016; % methane flux 1L/m^2-day, Henry's constant(0);
%3. constants in equations
a1=Fg*H/(Ls*(ew0+Kd*bd));
a2=(ew0+Kd*bd)/bd;b2=Fg*H/(bd*Ls);c2=Fg*H/Lw;
%4. initial conditions
Ws10=0.68*10^(-6);tss0=0;Cw10=Ws10*bd/Rfs;Cw20=0;t0=0;

tfinal=120*24*3600; %s
nnt=1000;
h=tfinal/(nnt);
t=0:h:tfinal;
%f1 for dCw1/dt
f1=inline('Cw1*(-a1)', 'a1', 'Cw1');
%f2 for dCw2/dt
f2=inline('Cw1*(a2*(6.4*2.9*10^5/(2.9*10^5+t)^2-
b2*6.4*t/(2.9*10^5+t)+c2*307)/(307+1.027*6.4*t/(2.9*10^5+t)))-
Cw2*((307*c2+1.027*6.4*2.9*10^5/(2.9*10^5+t)^2)/(307+1.027*6.4*t/(2.9*10^5+t)))', 'a2', 'b2', 'c2', 't', 'Cw1', 'Cw2');

Cw1=zeros(nnt+1,1);Cw2=zeros(nnt+1,1);t=zeros(nnt+1,1);
Cw1p=zeros(nnt+1,1);Cw2p=zeros(nnt+1,1);
Fc=zeros(nnt+1,1);
Cw1(1)=Cw10;Cw2(1)=Cw20;t(1)=t0;Fc(1)=Fg*H*Cw20;

K11=zeros(3,1);K12=zeros(3,1);
K21=zeros(3,1);K22=zeros(3,1);

```

```

K31=zeros(3,1);K32=zeros(3,1);
K41=zeros(3,1);K42=zeros(3,1);

K11(1)=h*f1(a1,Cw1(1));
K12(1)=h*f2(a2,b2,c2,t(1),Cw1(1),Cw2(1));

K21(1)=h*f1(a1,Cw1(1)+K11(1)/2);
K22(1)=h*f2(a2,b2,c2,t(1)+h/2,Cw1(1)+K11(1)/2,Cw2(1)+K12(1)/2);

K31(1)=h*f1(a1,Cw1(1)+K21(1)/2);
K32(1)=h*f2(a2,b2,c2,t(1)+h/2,Cw1(1)+K21(1)/2,Cw2(1)+K22(1)/2);

K41(1)=h*f1(a1,Cw1(1)+K31(1));
K42(1)=h*f2(a2,b2,c2,t(1)+h,Cw1(1)+K31(1),Cw2(1)+K32(1));

for i=2:3;
    Cw1(i)=Cw1(i-1)+(K11(i-1)+2*K21(i-1)+2*K31(i-1)+K41(i-1))/6;
    Cw2(i)=Cw2(i-1)+(K12(i-1)+2*K22(i-1)+2*K32(i-1)+K42(i-1))/6;
    Fc(i)=Fg*H*Cw2(i);
    t(i)=t(1)+(i-1)*h;

    K11(i)=h*f1(a1,Cw1(i));
    K12(i)=h*f2(a2,b2,c2,t(i),Cw1(i),Cw2(i));

    K21(i)=h*f1(a1,Cw1(i)+K11(i)/2);
    K22(i)=h*f2(a2,b2,c2,t(i)+h/2,Cw1(i)+K11(i)/2,Cw2(i)+K12(i)/2);

    K31(i)=h*f1(a1,Cw1(i)+K21(i)/2);
    K32(i)=h*f2(a2,b2,c2,t(i)+h/2,Cw1(i)+K21(i)/2,Cw2(i)+K22(i)/2);

    K41(i)=h*f1(a1,Cw1(i)+K31(i));
    K42(i)=h*f2(a2,b2,c2,t(i)+h,Cw1(i)+K31(i),Cw2(i)+K32(i));
end

for i=3:nnt;

    t(i)=t(1)+(i-1)*h;t(i+1)=t(1)+(i)*h;
    Cw1p(i+1)=Cw1(i)+(23*f1(a1,Cw1(i))-16*f1(a1,Cw1(i-1))+5*f1(a1,Cw1(i-2)))*h/12;
    Cw2p(i+1)=Cw2(i)+(23*f2(a2,b2,c2,t(i),Cw1(i),Cw2(i))-16*f2(a2,b2,c2,t(i-1),Cw1(i-1),Cw2(i-1))+5*f2(a2,b2,c2,t(i-2),Cw1(i-2),Cw2(i-2)))*h/12;

    Cw1(i+1)=Cw1(i)+(5*f1(a1,Cw1p(i+1))+8*f1(a1,Cw1(i))-f1(a1,Cw1(i-1)))*h/12;

    Cw2(i+1)=Cw2(i)+(5*f2(a2,b2,c2,t(i+1),Cw1p(i+1),Cw2p(i+1))+8*f2(a2,b2,c2,t(i),Cw1(i),Cw2(i))-f2(a2,b2,c2,t(i-1),Cw1(i-1),Cw2(i-1)))*h/12;
    Fc(i+1)=Fg*H*Cw2(i+1);

```

```

t(i+1)=t(1)+(i)*h;t(nnt+1)=t(1)+(nnt)*h;
end

%II capped
%Parameters
%1. sediment
bd=789.1; pd=2600;ew0=1-bd/pd;      %sediment bulk density (kg/m^3), particle density
(kg/m^3) and porosity
Ls=2;          %sediment depth(m)
Koc=10^1.4; fc=0.041; Kd=Koc*fc;      %partition coefficient (m^3/kg)
Rfs=ew0+Kd*bd;
%2. water and gas
Lw=3;          %water depth (m),
Fg=1/(1000*24*3600); H=0.0016; % methane flux 1L/m^2-day, Henry's constant(0);
%3. sand
bds=1541;ews0=0.5;Lsd=0.3;      %sand bulk density (kg/m^3), porosity and sand height(m)
Koc=10^1.4; focs=0.0001; Kds=Koc*focs;      %partition coefficient (m^3/kg)
Rfsd=ews0+Kds*bds;
%4. constants in equations
a1=Fg*H/(Ls*(ew0+Kd*bd));
a2=Fg*H/(Lsd*(ews0+Kds*bds));
a3=Fg*H/Lw;
%5. initial conditions
CWs10=0.68*10^(-6);CCw10=CWs10*bd/Rfs;CCws0=0;CCw20=0;t0=0;

tfinal=120*24*3600; %s
nnt=1000;
h=tfinal/(nnt);
t=0:h:tfinal;

%f1 for dCw1/dt
f1=inline('CCw1*(-a1)', 'a1', 'CCw1');
%f2 for dCws/dt
f2=inline('CCw1*a2-CCws*a2', 'a2', 'CCw1', 'CCws');
%f2 for dCw2/dt
f3=inline('CCws*a3-CCw2*a3', 'a3', 'CCws', 'CCw2');

CCw1=zeros(nnt+1,1);CCws=zeros(nnt+1,1);CCw2=zeros(nnt+1,1);t=zeros(nnt+1,1);
CCw1p=zeros(nnt+1,1);CCs2p=zeros(nnt+1,1);CCw2p=zeros(nnt+1,1);CFc=zeros(nnt+1,1);
CCw1(1)=CCw10;CCws(1)=CCws0;CCw2(1)=CCw20;t(1)=t0;CFc(1)=Fg*H*CCw2(1);

K11=zeros(3,1);K12=zeros(3,1);K13=zeros(3,1);
K21=zeros(3,1);K22=zeros(3,1);K23=zeros(3,1);
K31=zeros(3,1);K32=zeros(3,1);K33=zeros(3,1);
K41=zeros(3,1);K42=zeros(3,1);K43=zeros(3,1);

```

```

K11(1)=h*f1(a1,CCw1(1));
K12(1)=h*f2(a2,CCw1(1),CCws(1));
K13(1)=h*f3(a3,CCws(1),CCw2(1));

K21(1)=h*f1(a1,CCw1(1)+K11(1)/2);
K22(1)=h*f2(a2,CCw1(1)+K11(1)/2,CCws(1)+K12(1)/2);
K23(1)=h*f3(a3,CCws(1)+K12(1)/2,CCw2(1)+K13(1)/2);

K31(1)=h*f1(a1,CCw1(1)+K21(1)/2);
K32(1)=h*f2(a2,CCw1(1)+K21(1)/2,CCws(1)+K22(1)/2);
K33(1)=h*f3(a3,CCws(1)+K22(1)/2,CCw2(1)+K23(1)/2);

K41(1)=h*f1(a1,CCw1(1)+K31(1));
K42(1)=h*f2(a2,CCw1(1)+K31(1),CCws(1)+K32(1));
K43(1)=h*f3(a3,CCws(1)+K32(1),CCw2(1)+K33(1));
for i=2:3;
    CCw1(i)=CCw1(i-1)+(K11(i-1)+2*K21(i-1)+2*K31(i-1)+K41(i-1))/6;
    CCws(i)=CCws(i-1)+(K12(i-1)+2*K22(i-1)+2*K32(i-1)+K42(i-1))/6;
    CCw2(i)=CCw2(i-1)+(K13(i-1)+2*K23(i-1)+2*K33(i-1)+K43(i-1))/6;
    CFc=Fg*H*CCw2(i);
    t(i)=t(1)+(i-1)*h;

    K11(i)=h*f1(a1,CCw1(i));
    K12(i)=h*f2(a2,CCw1(i),CCws(i));
    K13(i)=h*f3(a3,CCws(i),CCw2(i));

    K21(i)=h*f1(a1,CCw1(i)+K11(i)/2);
    K22(i)=h*f2(a2,CCw1(i)+K11(i)/2,CCws(i)+K12(i)/2);
    K23(i)=h*f3(a3,CCws(i)+K12(i)/2,CCw2(i)+K13(i)/2);

    K31(i)=h*f1(a1,CCw1(i)+K21(i)/2);
    K32(i)=h*f2(a2,CCw1(i)+K21(i)/2,CCws(i)+K22(i)/2);
    K33(i)=h*f3(a3,CCws(i)+K22(i)/2,CCw2(i)+K23(i)/2);

    K41(i)=h*f1(a1,CCw1(i)+K31(i));
    K42(i)=h*f2(a2,CCw1(i)+K31(i),CCws(i)+K32(i));
    K43(i)=h*f3(a3,CCws(i)+K32(i),CCw2(i)+K33(i));
end

for i=3:nnt;

    t(i)=t(1)+(i-1)*h;t(i+1)=t(1)+(i)*h;
    CCw1p(i+1)=CCw1(i)+(23*f1(a1,CCw1(i))-16*f1(a1,CCw1(i-1))+5*f1(a1,CCw1(i-2)))*h/12;
    CCwsp(i+1)=CCws(i)+(23*f2(a2,CCw1(i),CCws(i))-16*f2(a2,CCw1(i-1),CCws(i-1))+5*f2(a2,CCw1(i-2),CCws(i-2)))*h/12;

```

```

CCw2p(i+1)=CCw2(i)+(23*f3(a3,CCws(i),CCw2(i))-16*f3(a3,CCws(i-1),CCw2(i-1))+5*f2(a2,CCws(i-2),CCw2(i-2)))*h/12;

CCw1(i+1)=CCw1(i)+(5*f1(a1,CCw1p(i+1))+8*f1(a1,CCw1(i))-f1(a1,CCw1(i-1)))*h/12;
CCws(i+1)=CCws(i)+(5*f2(a2,CCw1p(i+1),CCwsp(i+1))+8*f2(a2,CCw1(i),CCws(i))-f2(a2,CCw1(i-1),CCws(i-1)))*h/12;
CCw2(i+1)=CCw2(i)+(5*f3(a3,CCwsp(i+1),CCw2p(i+1))+8*f3(a3,CCws(i),CCw2(i))-f3(a3,CCws(i-1),CCw2(i-1)))*h/12;
CFc(i+1)=Fg*H*CCw2(i+1);
t(i+1)=t(i)+h;t(nnt+1)=t(nnt)+h;
end

```

```

%Comparison of contaminant fluxes between uncapped and capped sediment
plot(t/(24*3600),Fc*24*3600*10^12,'o','markersize',4,'linewidth',2,'markeredgecolor','k','markerfacecolor','k')
xlabel('time (days)')
ylabel('fca (ng/m^2-day)')
title('Figure: PHE. flux with time')
hold on
plot(t/(24*3600),10^6*CFc*24*3600*10^12,'o','markersize',4,'linewidth',2,'markeredgecolor','k','markerfacecolor','k')
xlabel('time (days)')
ylabel('PHE. flux, fca (ng/m^2-day)')
title('Figure: PHE. flux with time')
legend('fca (uncapped)','fca×10^6 (capped)');

```

```

%Comparison of aqueous phase concentrations between uncapped and capped sediment
plot(t/(24*3600),Cw2*10^6,'o','markersize',4,'linewidth',2,'markeredgecolor','k','markerfacecolor','k')
xlabel('time (days)')
ylabel('Cw2')
hold on
plot(t/(24*3600),10^6*CCw2*10^6,'o','markersize',4,'linewidth',2,'markeredgecolor','k','markerfacecolor','k')
xlabel('time (days)')
ylabel('Cw2 (µg/L)')
legend('Cw2 (uncapped)','Cw2×10^6 (capped)');

```

```

%loading in sand layer
plot(t/(24*3600),CCws*10^6,'o','markersize',4,'linewidth',2,'markeredgecolor','k','markerfacecolor','k')
xlabel('time (days)')
ylabel('CCws(µg/L)')
hold on
plot(t/(24*3600),Rfsd*CCws*10^6/bds,'o','markersize',4,'linewidth',2,'markeredgecolor','k','markerfacecolor','k')

```

```
xlabel('time (days)')
ylabel('Sand loading, Wsd (mg/kg)')
```

```
%loading in sediment
```

```
plot(t/(24*3600),Cw1*10^6,'o','markersize',4,'linewidth',2,'markeredgecolor','k','markerfacecolor',
'k')
```

```
xlabel('time (days)')
```

```
ylabel('Cw1')
```

```
hold on
```

```
plot(t/(24*3600),10^6*CCw1*10^6,'o','markersize',4,'linewidth',2,'markeredgecolor','k','markerfa
cecolor','k')
```

```
xlabel('time (days)')
```

```
ylabel('10^6*CCw1')
```

```
hold on
```

```
plot(t/(24*3600),Cw1*Rfs*10^6/bd,'o','markersize',4,'linewidth',2,'markeredgecolor','k','markerfa
cecolor','k')
```

```
xlabel('time (days)')
```

```
ylabel('Ws1')
```

```
hold on
```

```
plot(t/(24*3600),Rfs*CCw1*10^6/bd,'o','markersize',4,'linewidth',2,'markeredgecolor','k','marker
facecolor','k')
```

```
xlabel('time (days)')
```

```
ylabel('Sediment loading, Ws (mg/kg)')
```

```
legend('Ws (uncapped)','Ws (capped)');
```

APPENDIX D: CONCENTRATION PROFILES IN SEDIMENTS AND METAL FLUXES

D1 Tracer Concentration Profiles in the U.L. Sediment

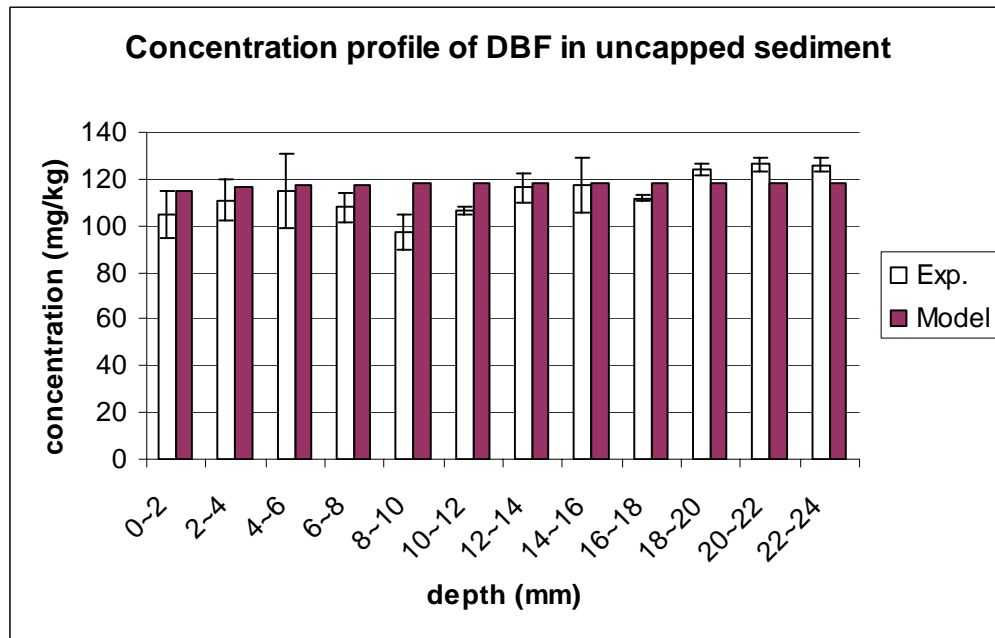


Figure D1.1 Concentration profile of DBF in uncapped sediment.

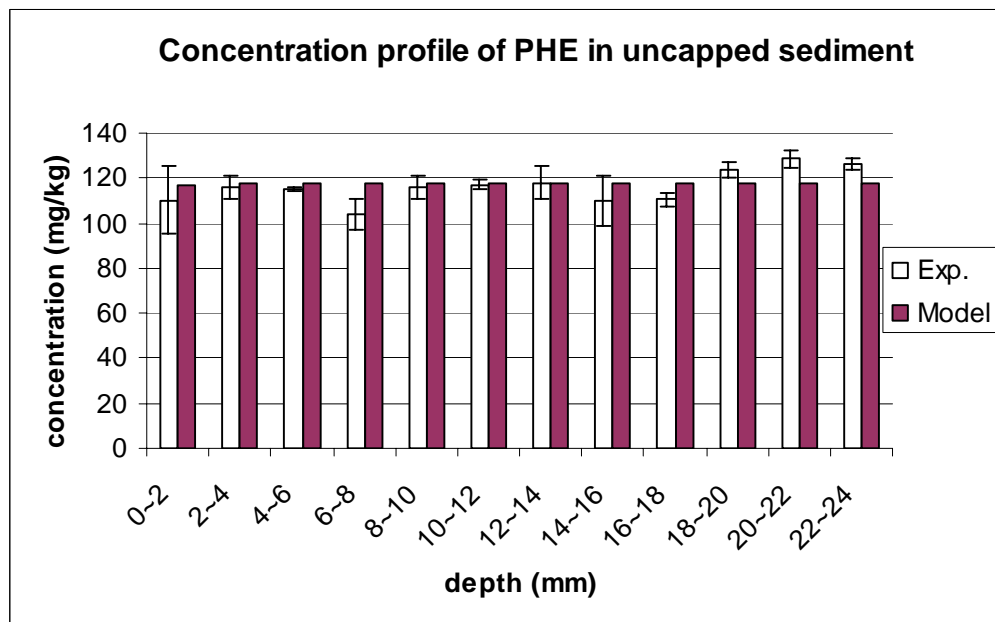


Figure D1.2 Concentration profile of PHE in uncapped sediment.

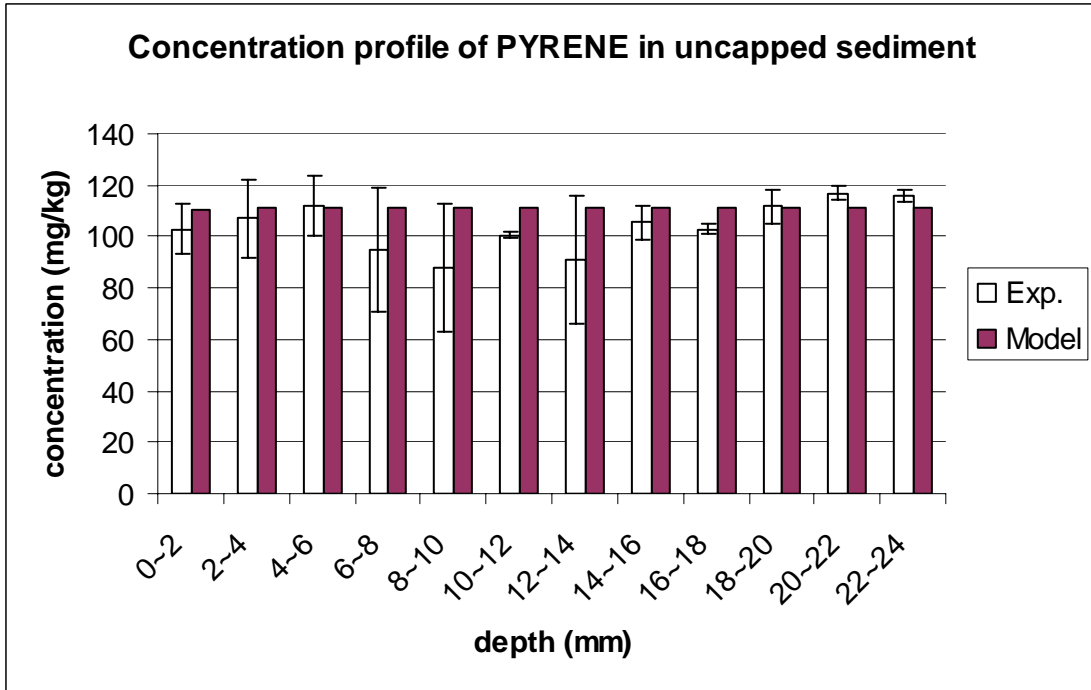


Figure D1.3 Concentration profile of pyrene in uncapped sediment.

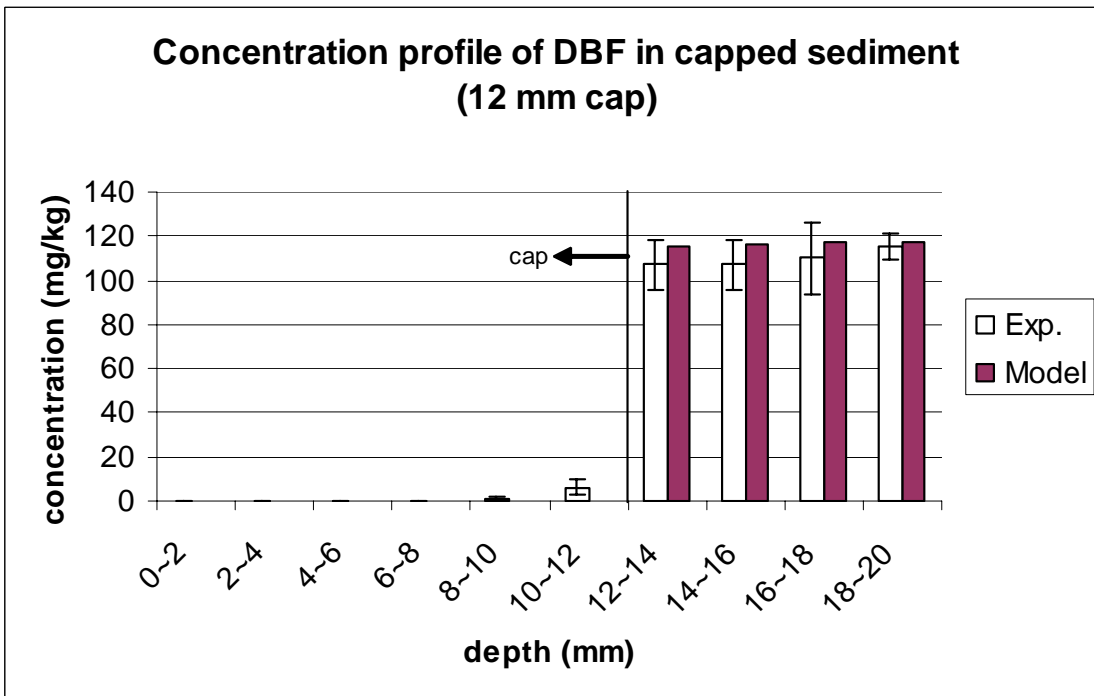


Figure D1.4 Concentration profile of DBF in capped sediment (12 mm sand cap).

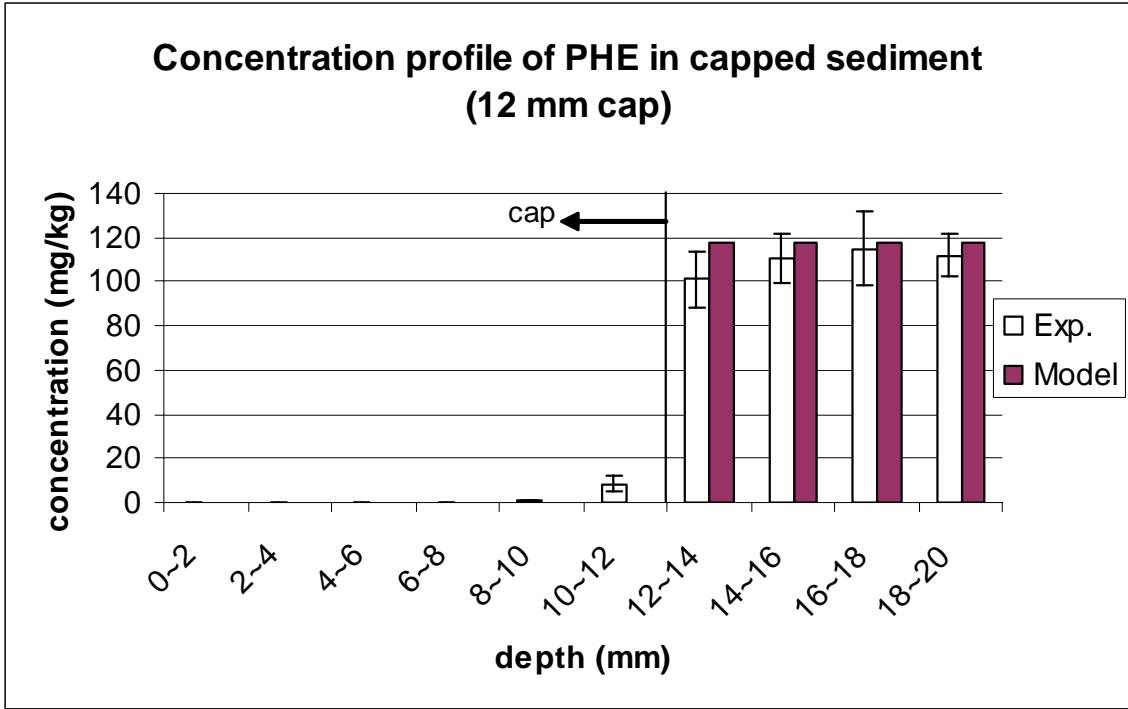


Figure D1.5 Concentration profile of PHE in capped sediment (12 mm sand cap).

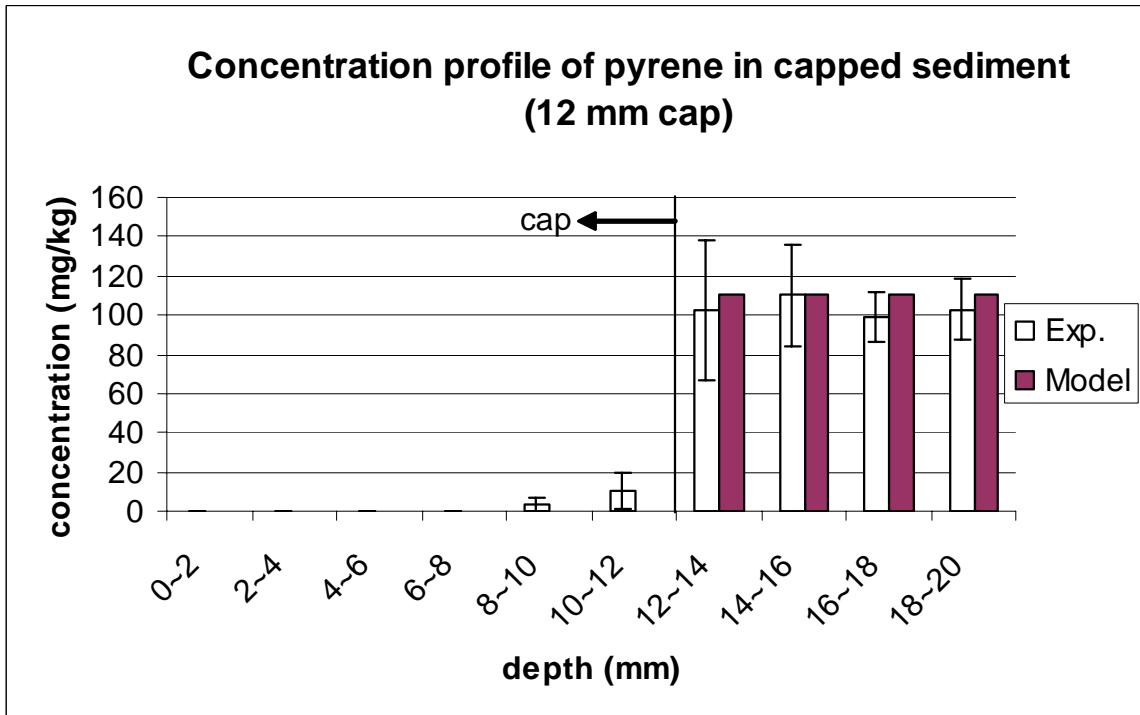


Figure D1.6 Concentration profile of pyrene in capped sediment (12 mm sand cap).

D2 Metal Flux from the A.R. Sediment with and without Sand Cap

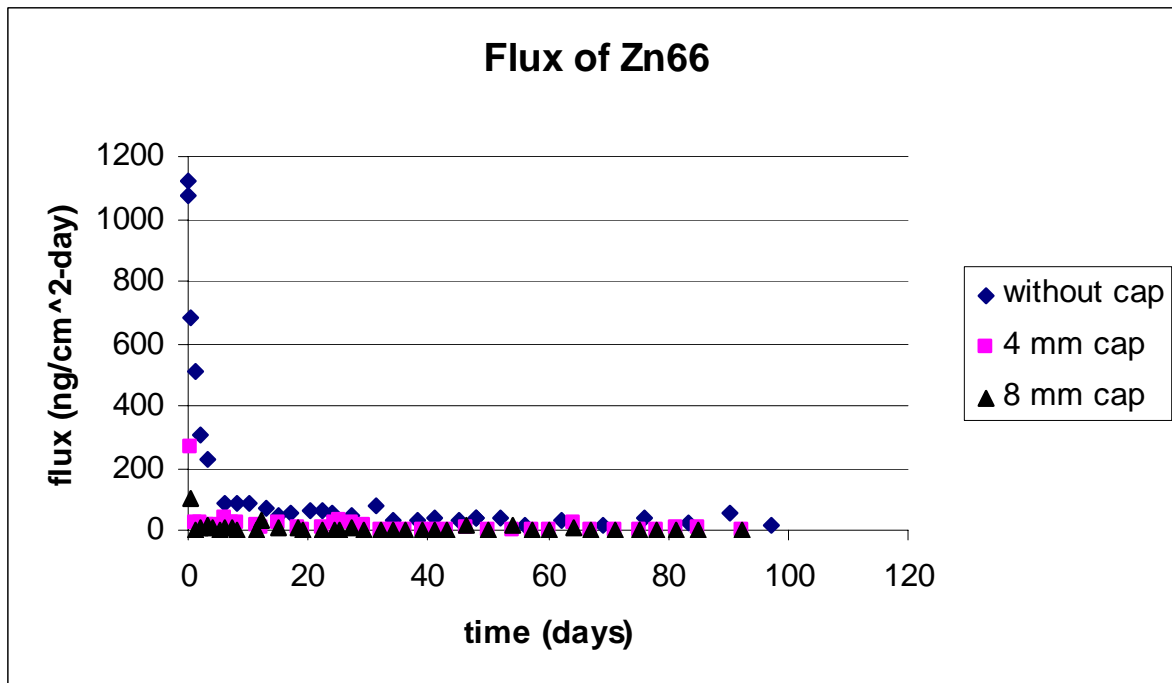
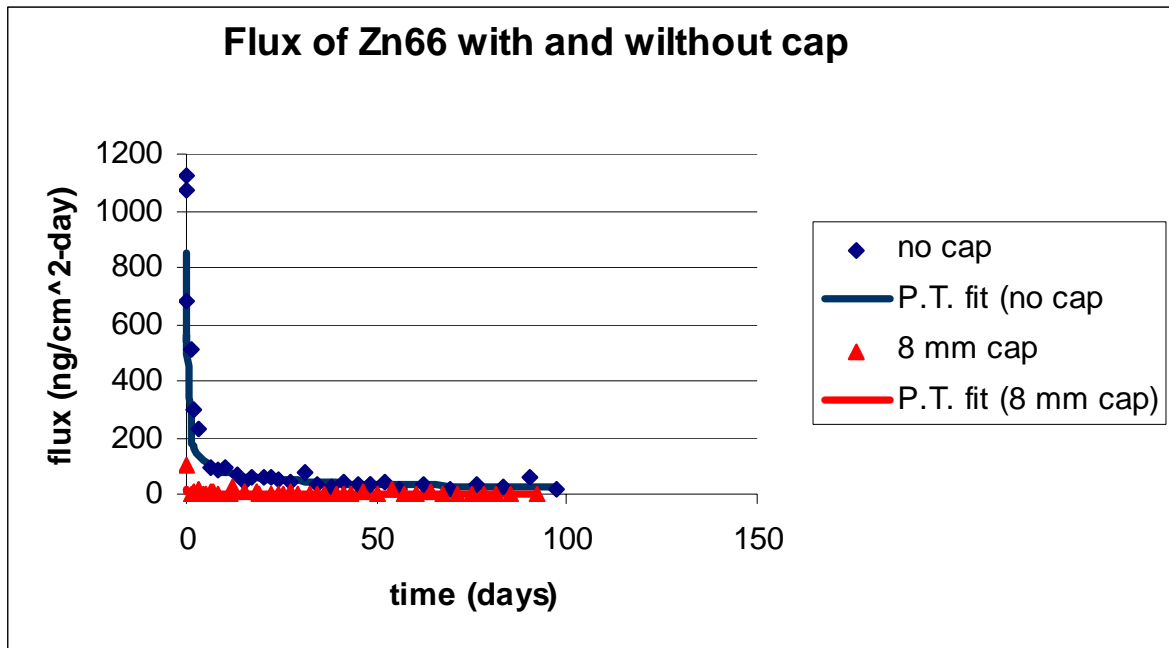


Figure D2.1 Flux of Zn66.

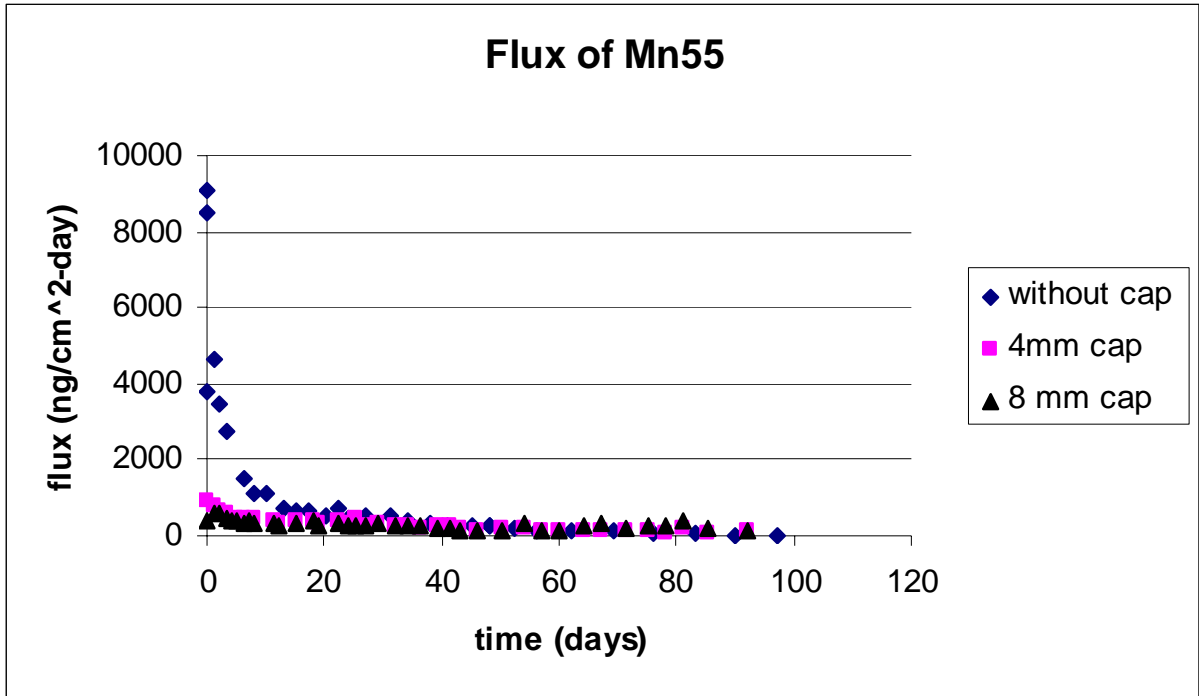


Figure D2.2 Flux of Mn55.

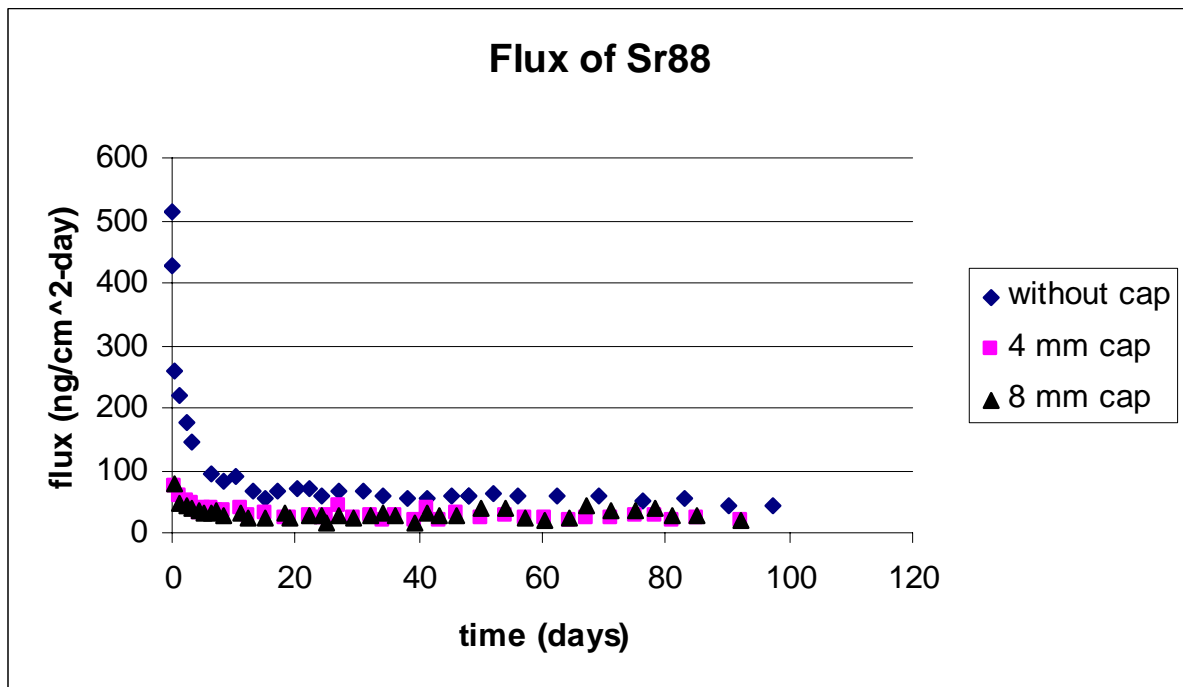


Figure D2.3 Flux of Sr88.

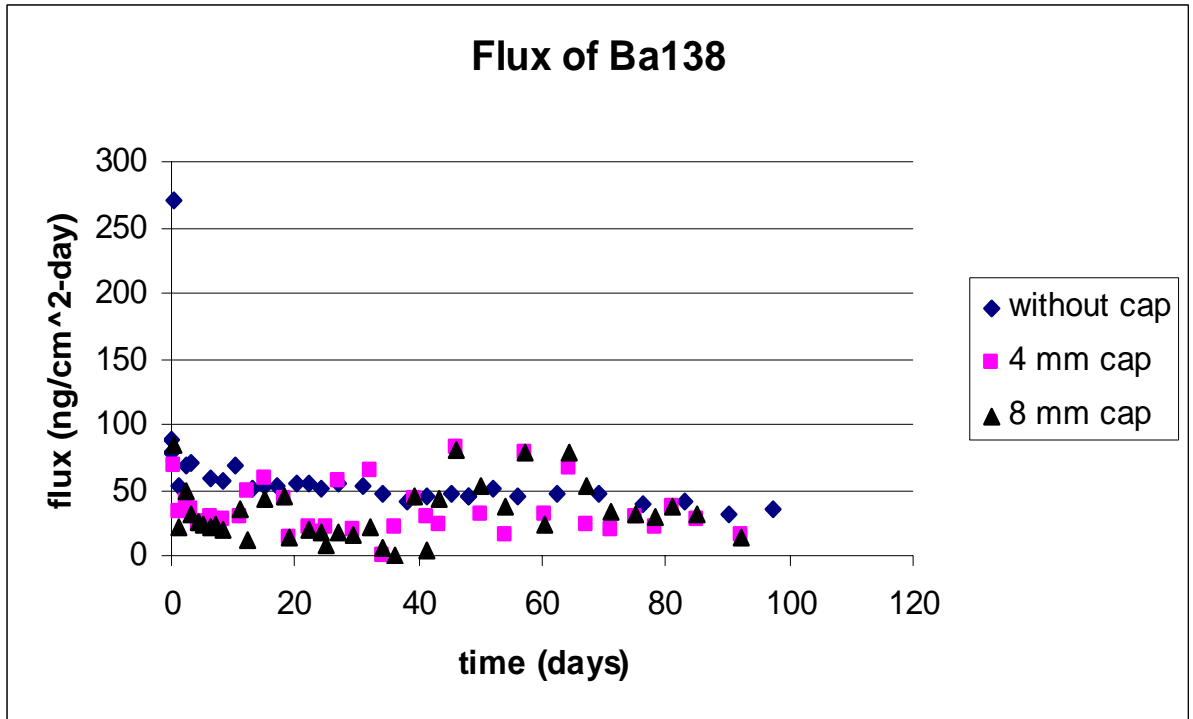


Figure D2.4 Flux of Ba138.

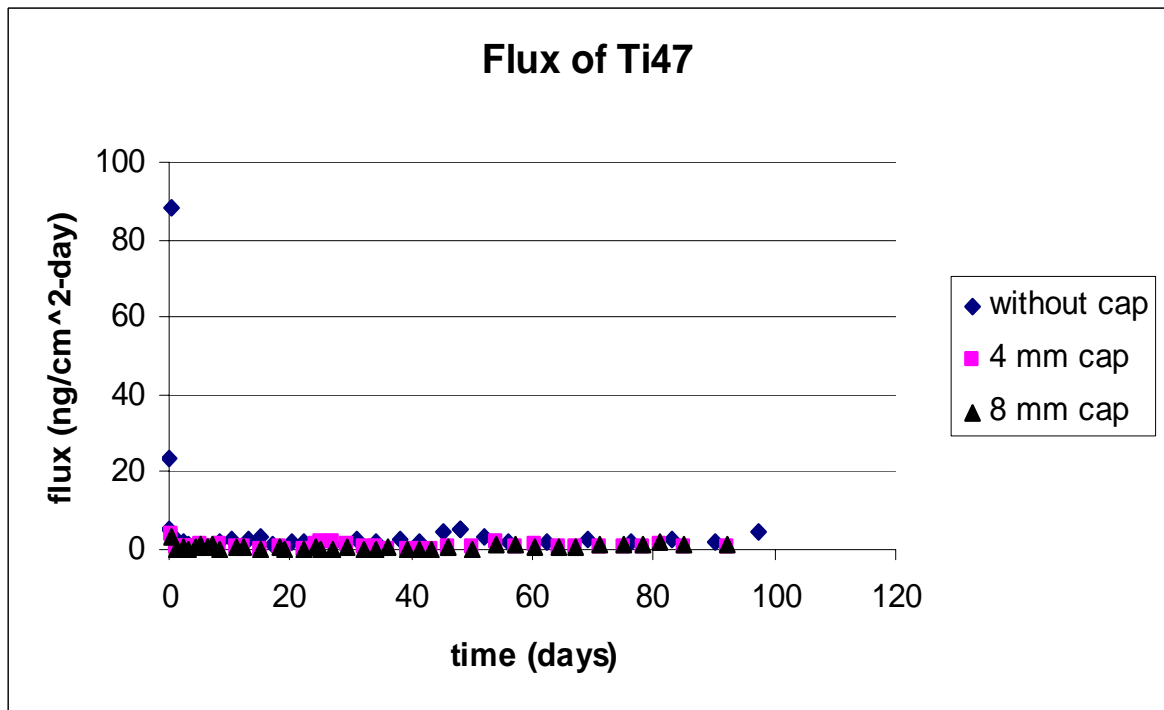


Figure D2.5 Flux of Ti47.

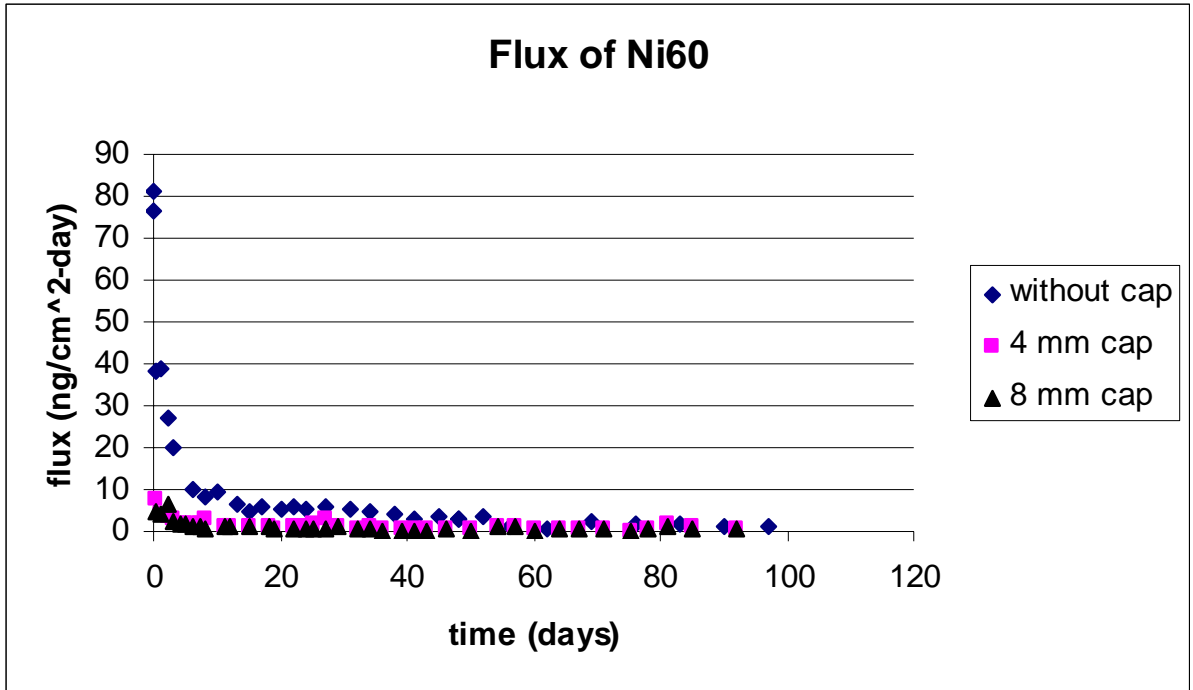


Figure D2.6 Flux of Ni60.

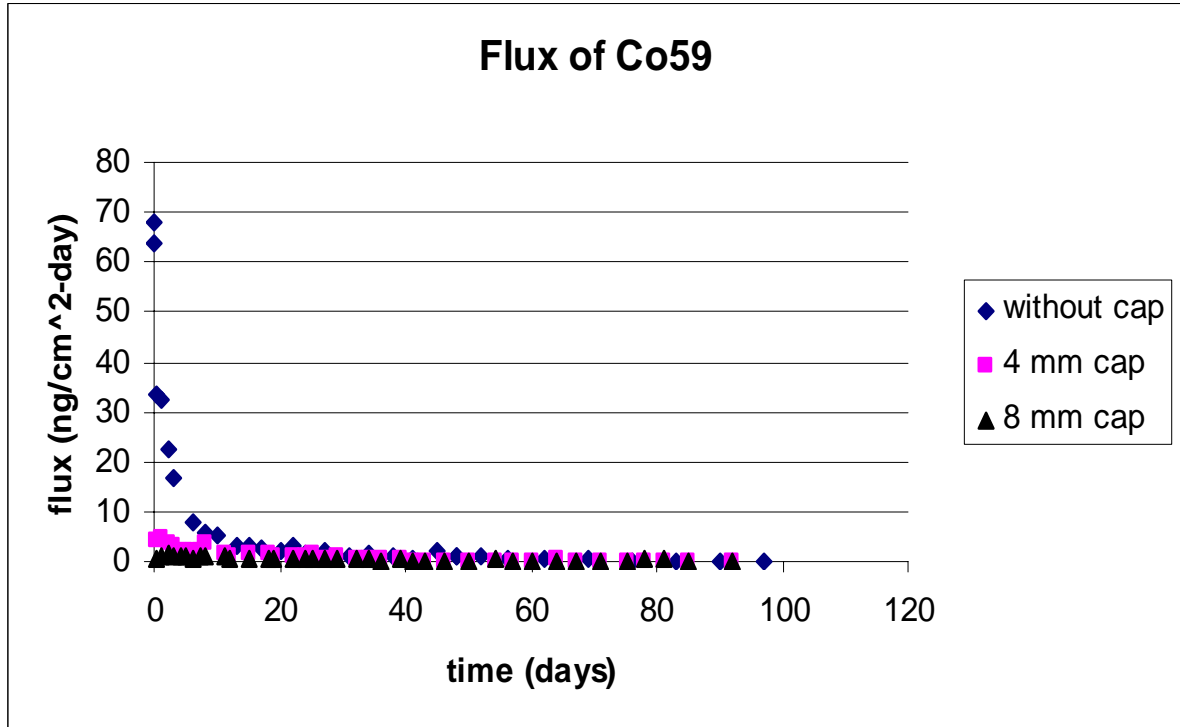


Figure D2.7 Flux of Co59.

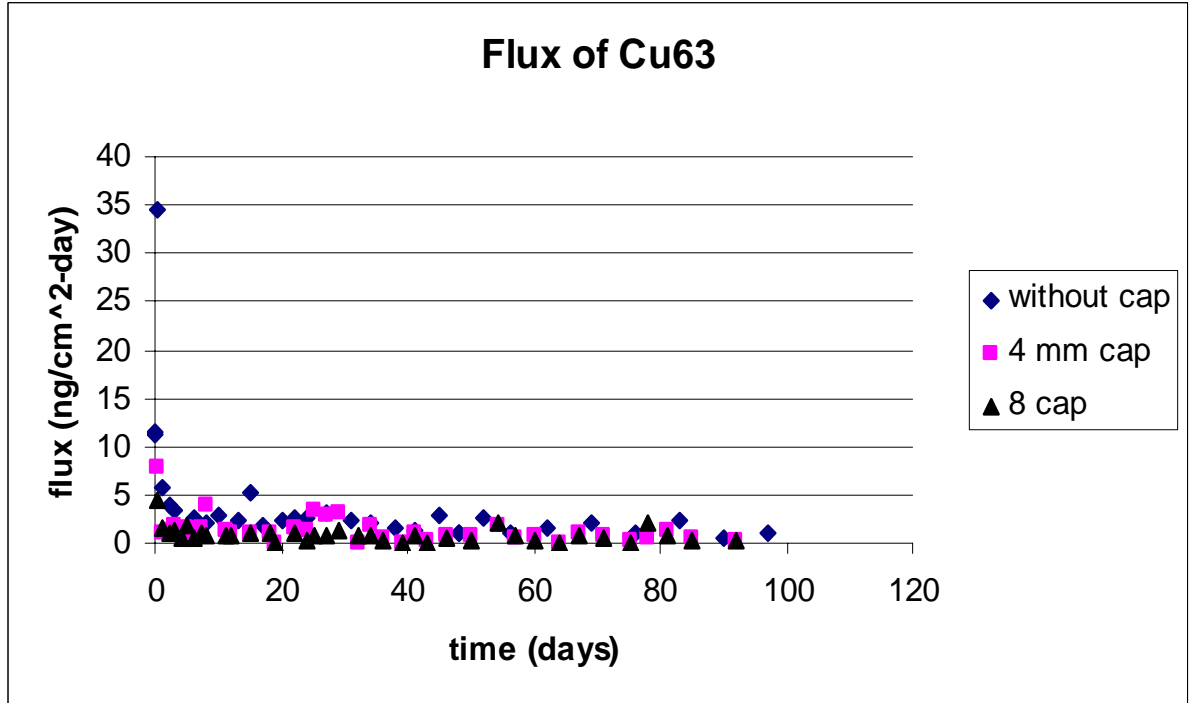
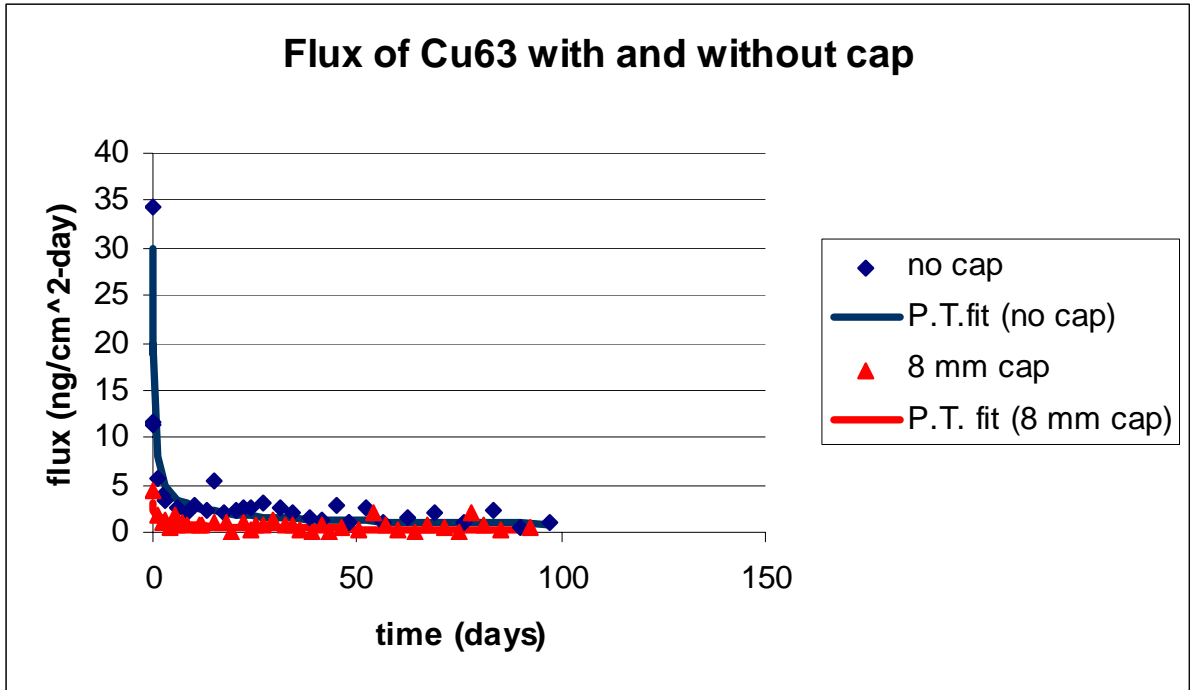


Figure D2.8 Flux of Cu63.

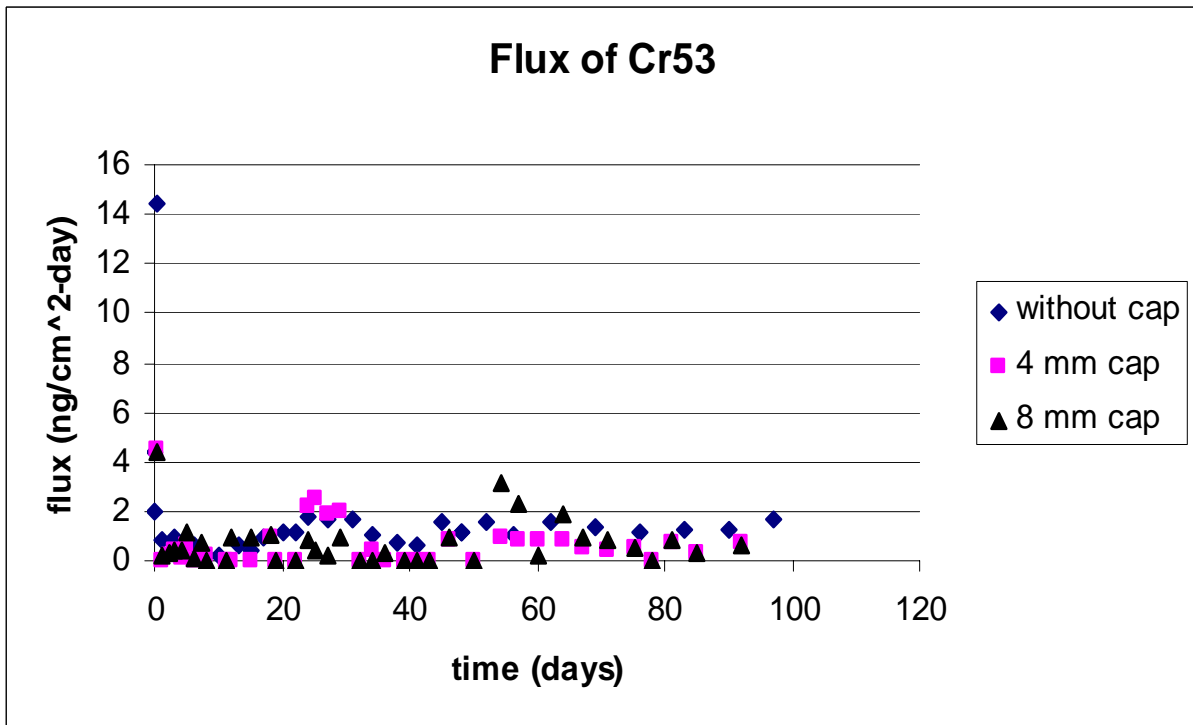
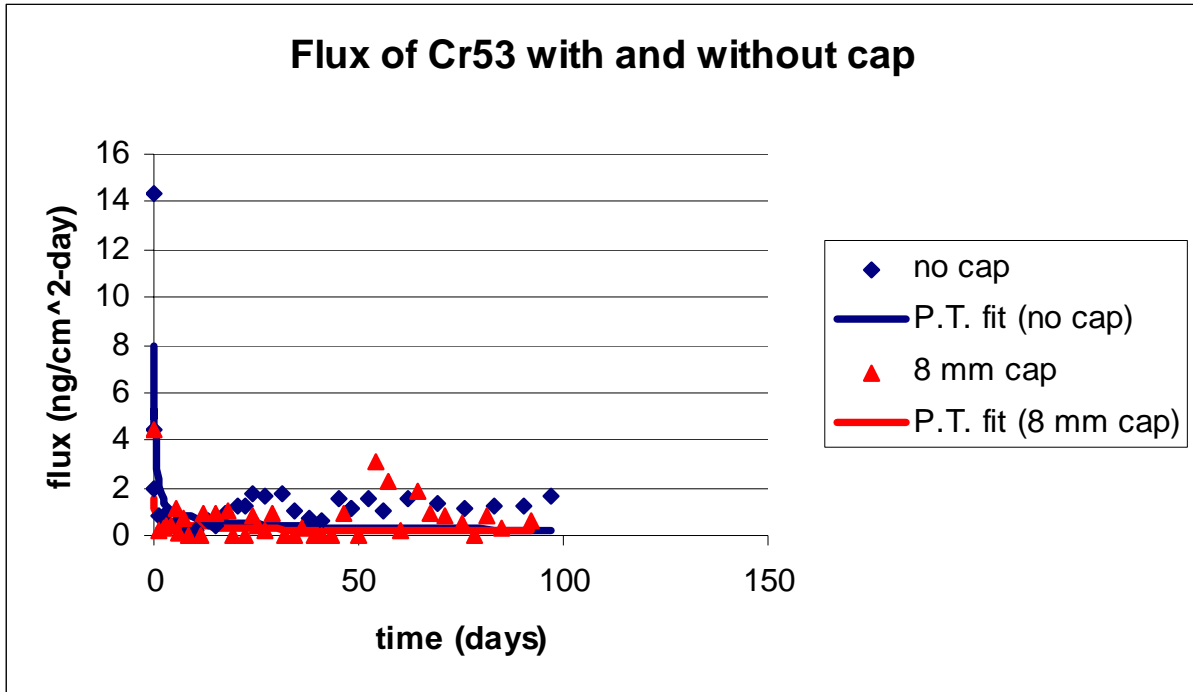


Figure D2.9 Flux of Cr53.

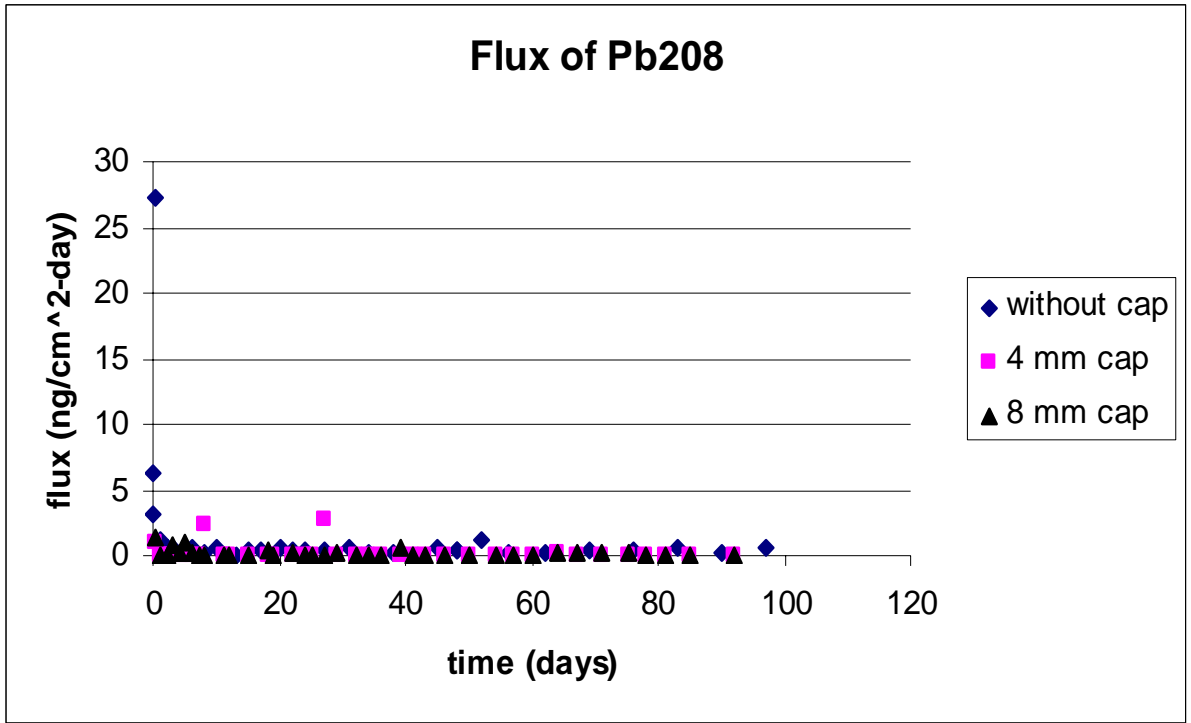


Figure D2.10 Flux of Pb208.

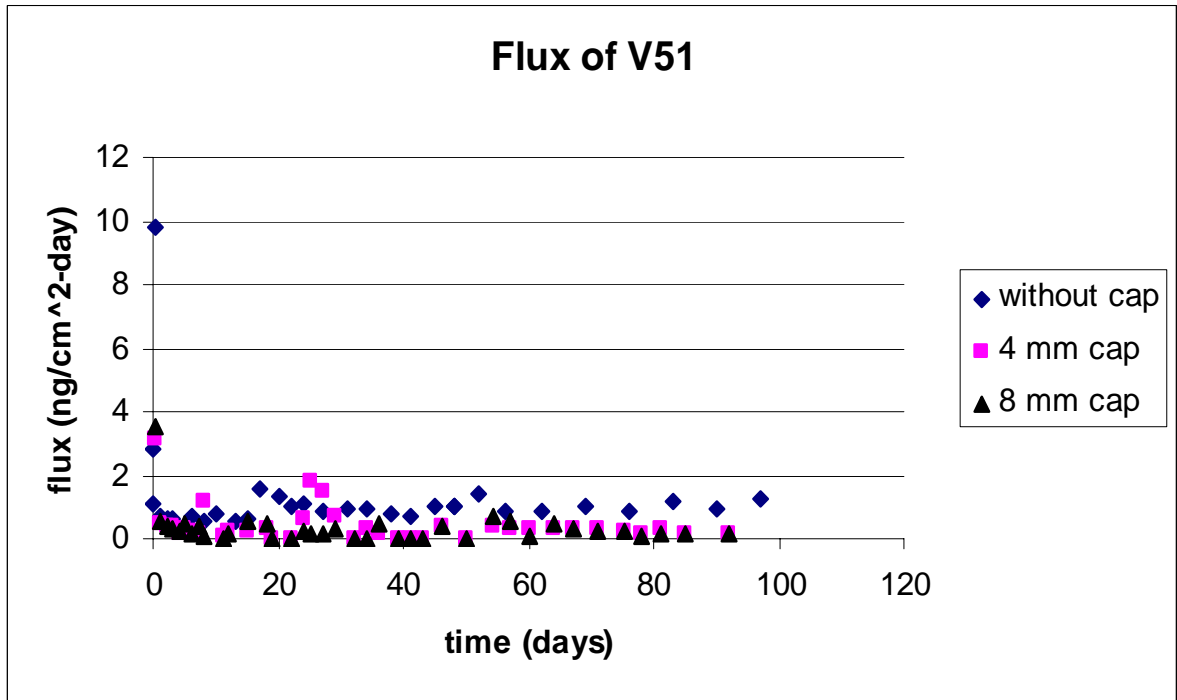


Figure D2.11 Flux of V51.

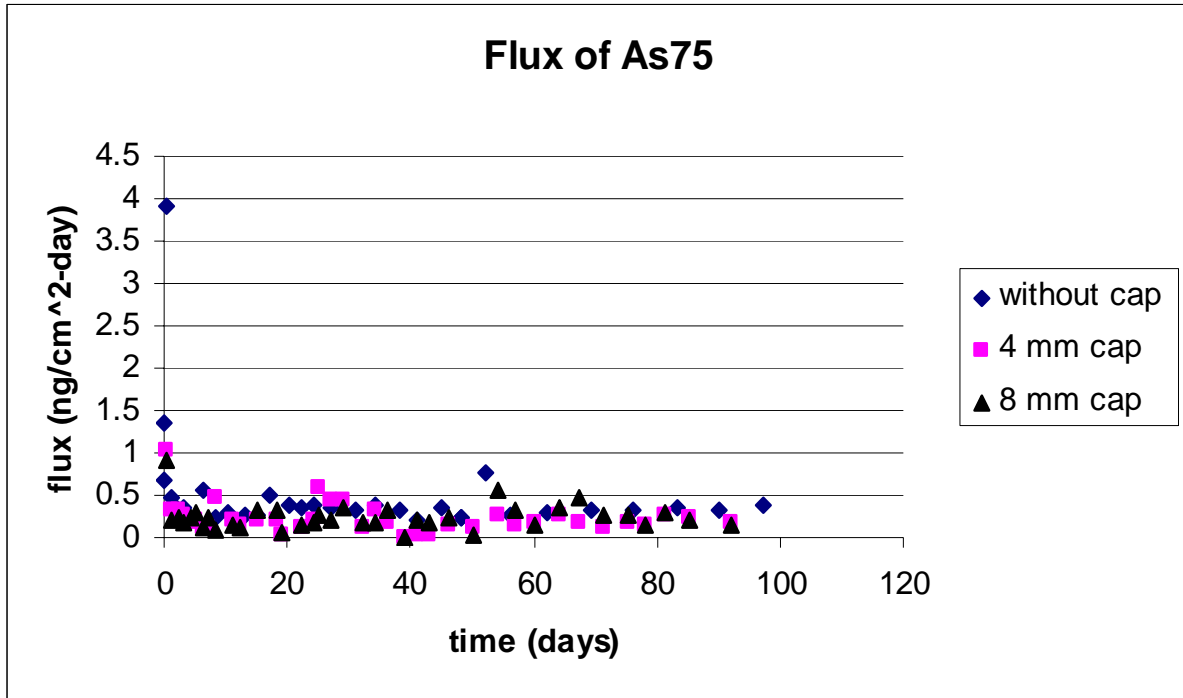


Figure D2.12 Flux of As75.

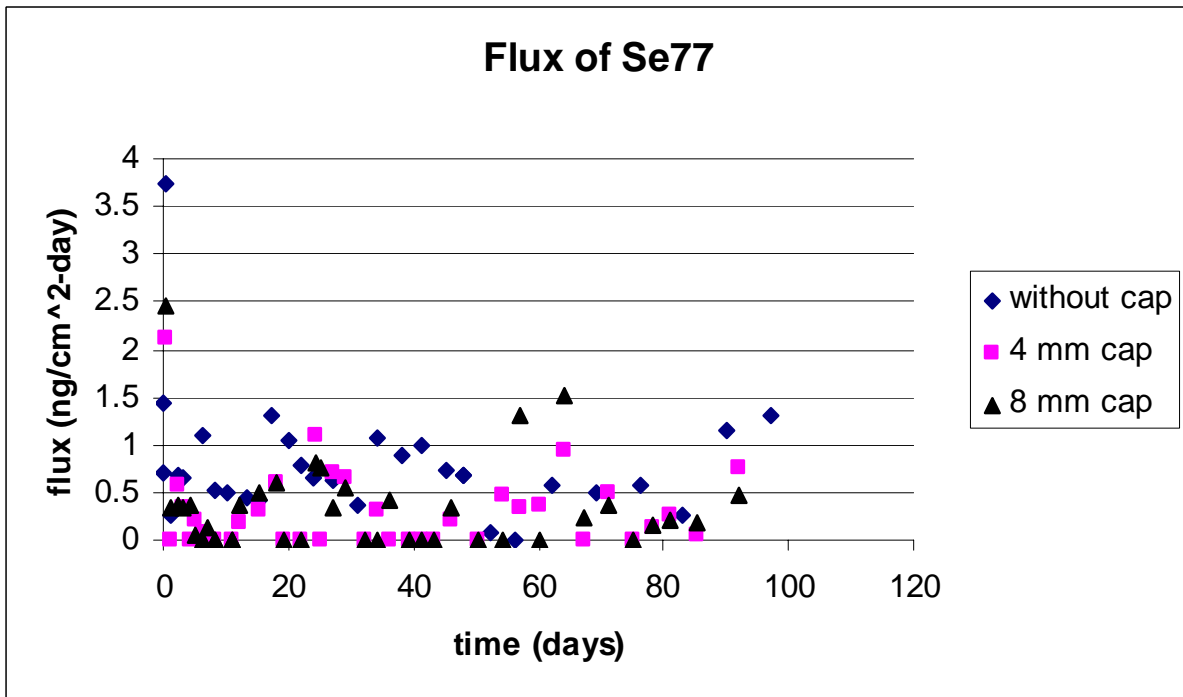


Figure D2.13 Flux of Se77.

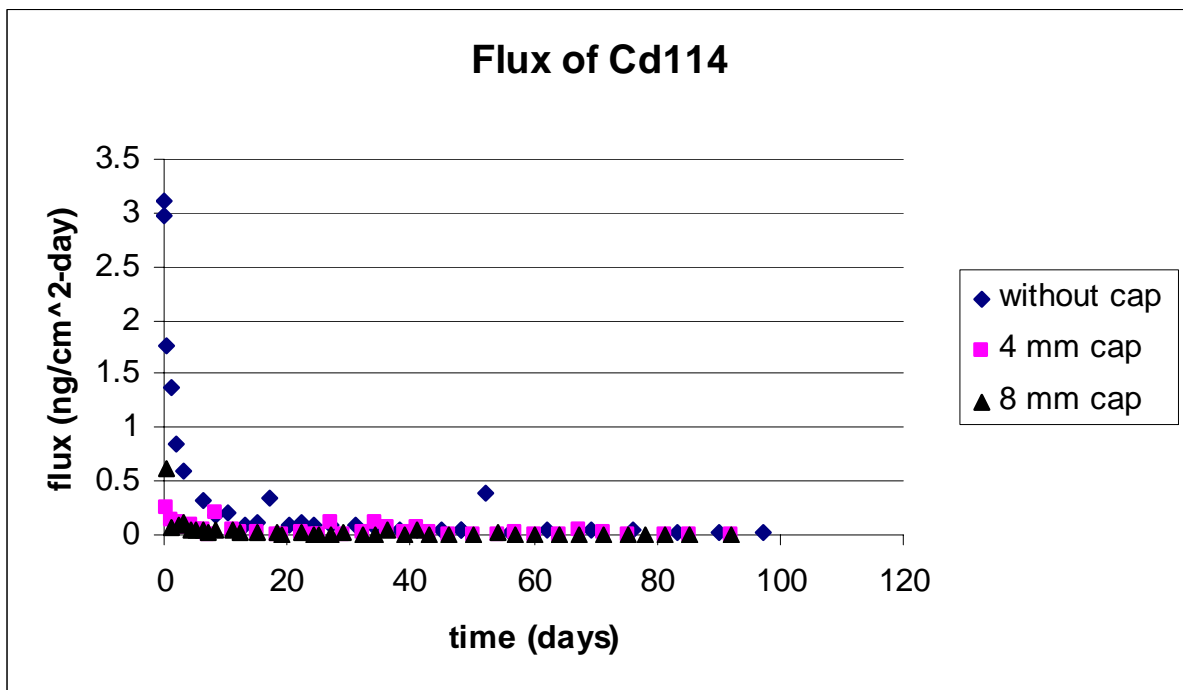
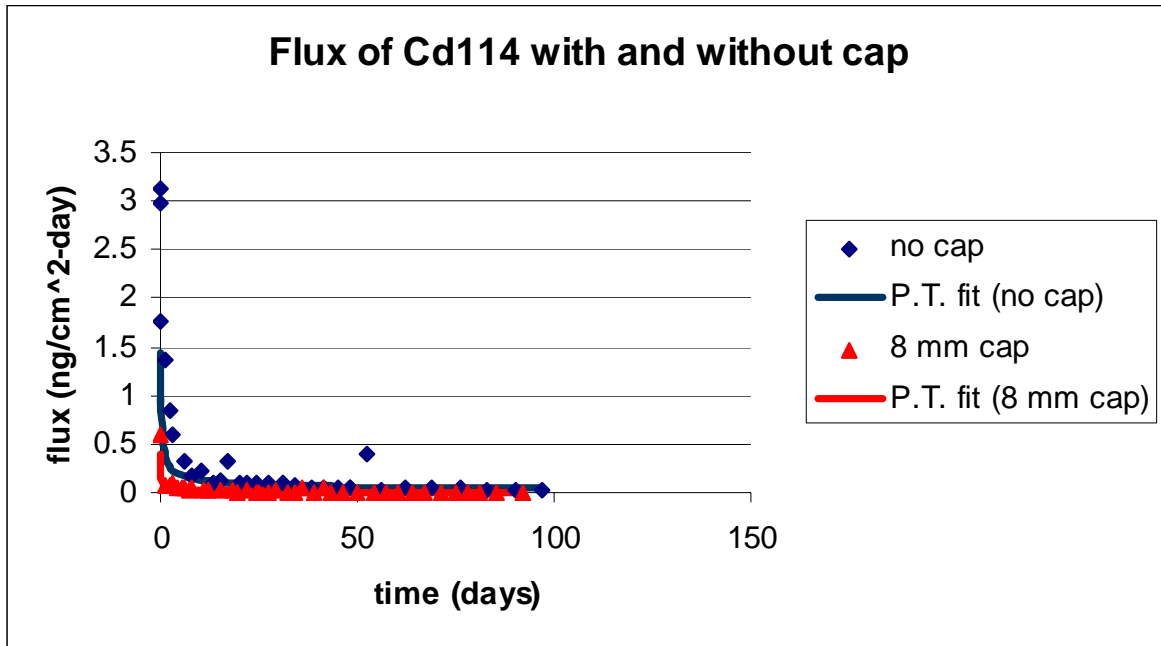


Figure D2.14 Flux of Cd114.

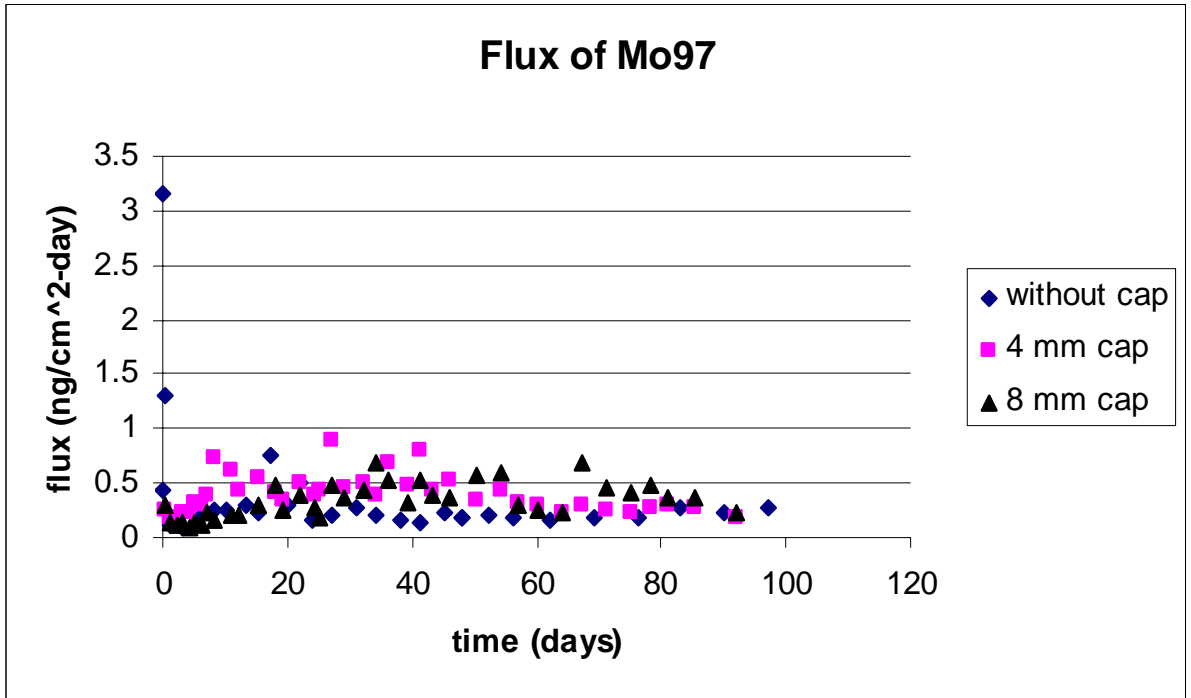


Figure D2.15 Flux of Mo97.

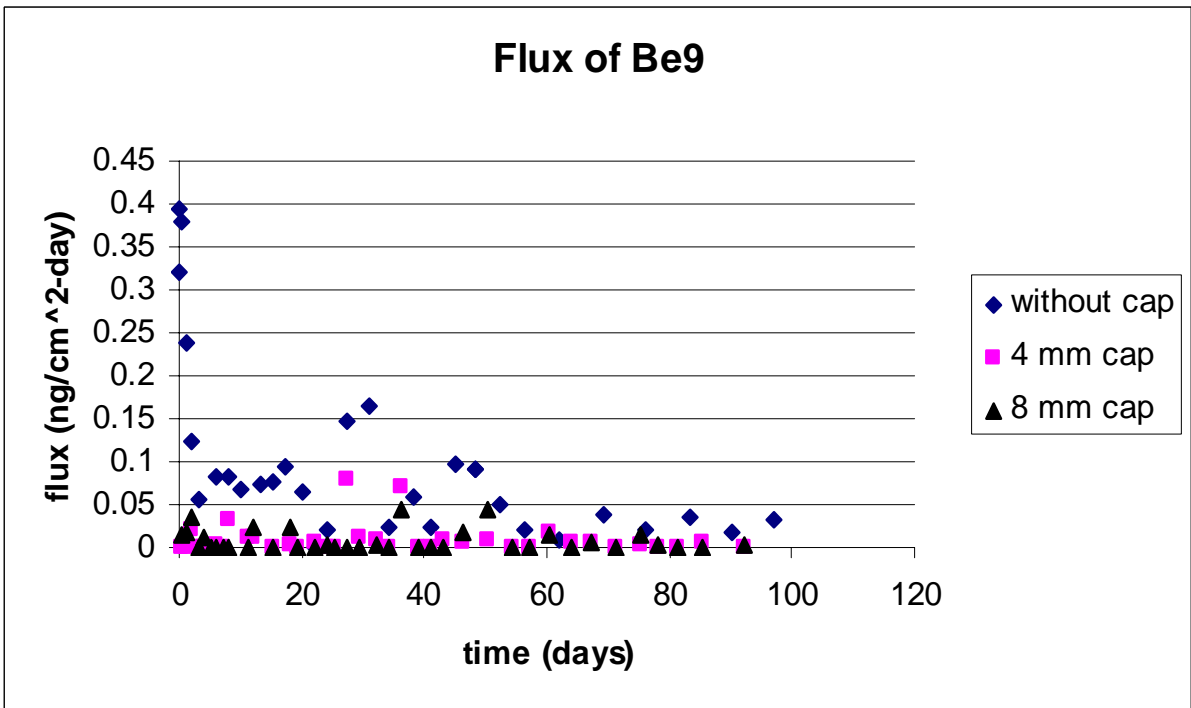


Figure D2.16 Flux of Be9.

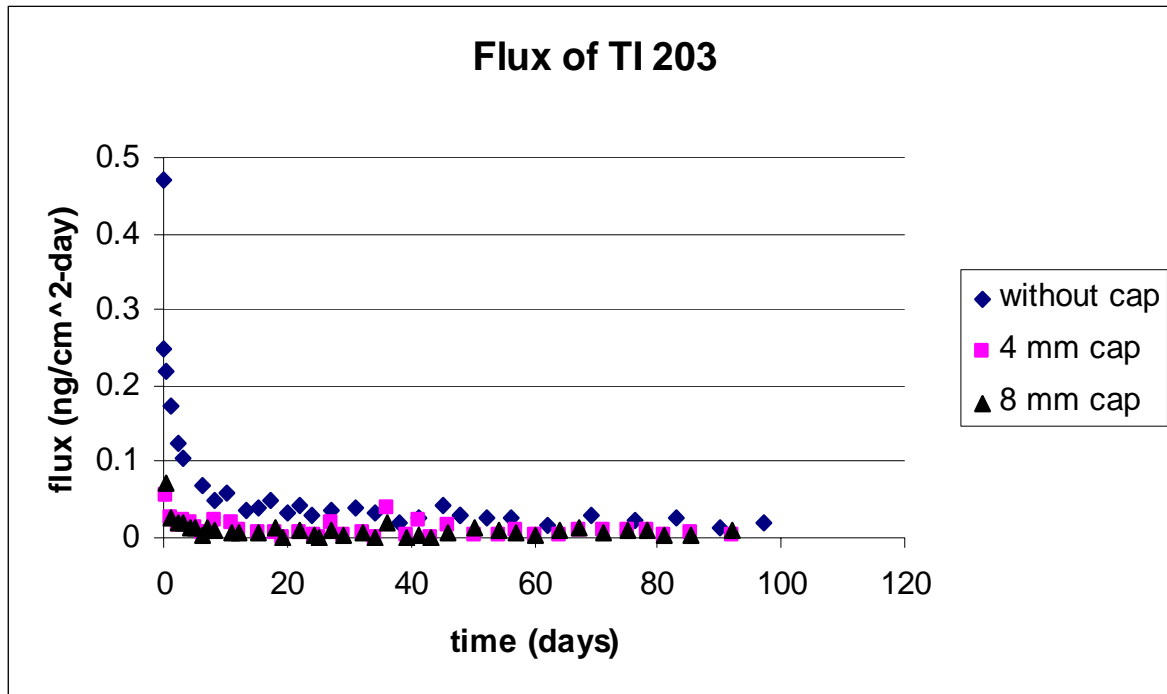


Figure D2.17 Flux of TI 203.

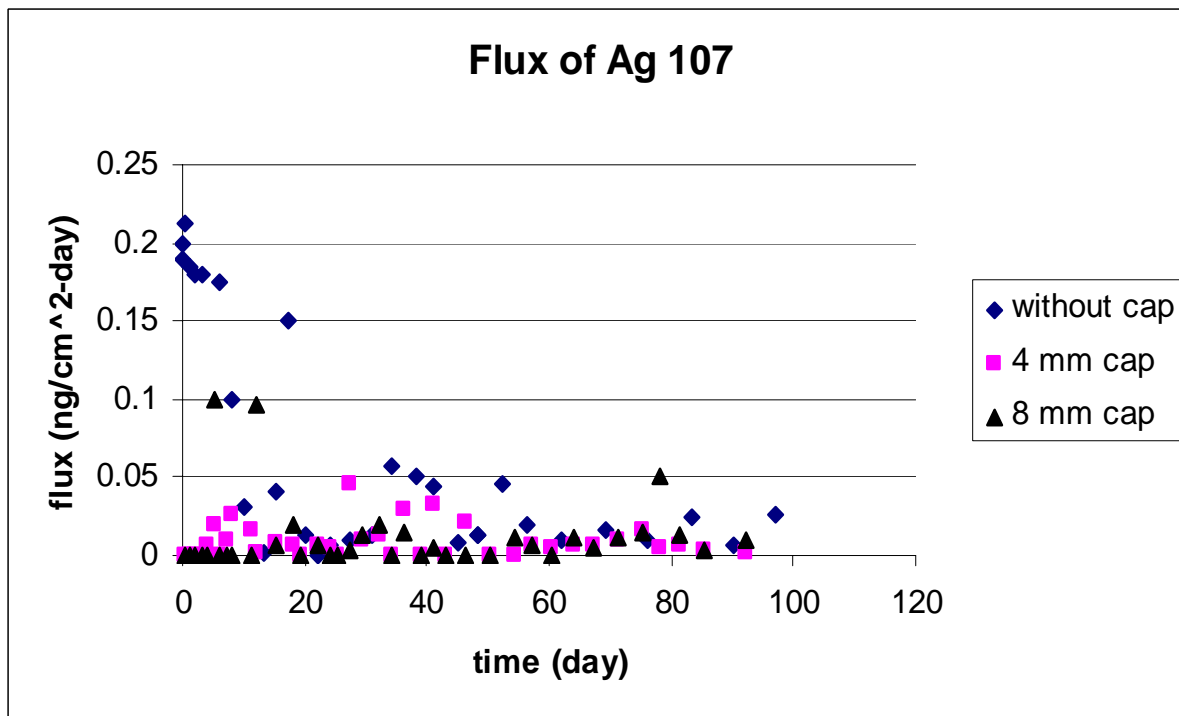


Figure D2.18 Flux of Ag107.

D3 Metal Concentration Profiles in the A.R. Sediment

D3.1 Uncapped Sediment

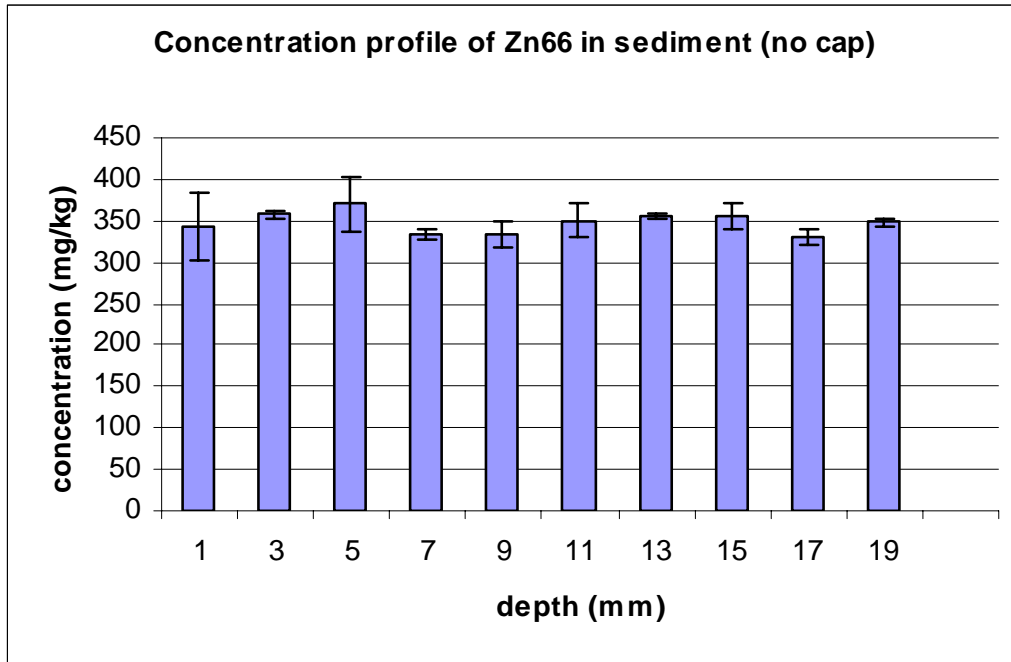


Figure D3.1.1 Concentration profile of Zn 66.

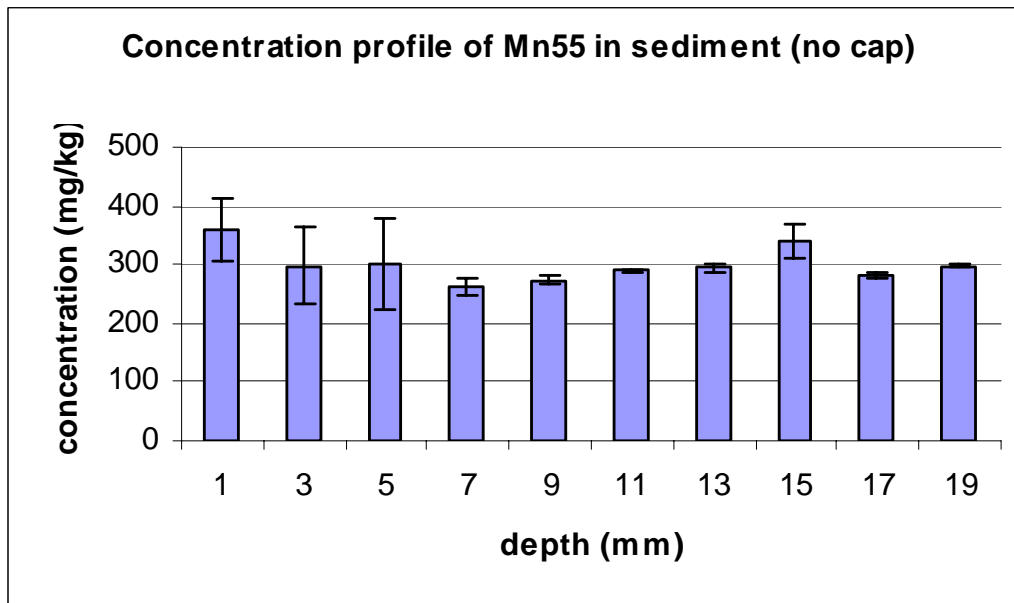


Figure D3.1.2 Concentration profile of Mn55.

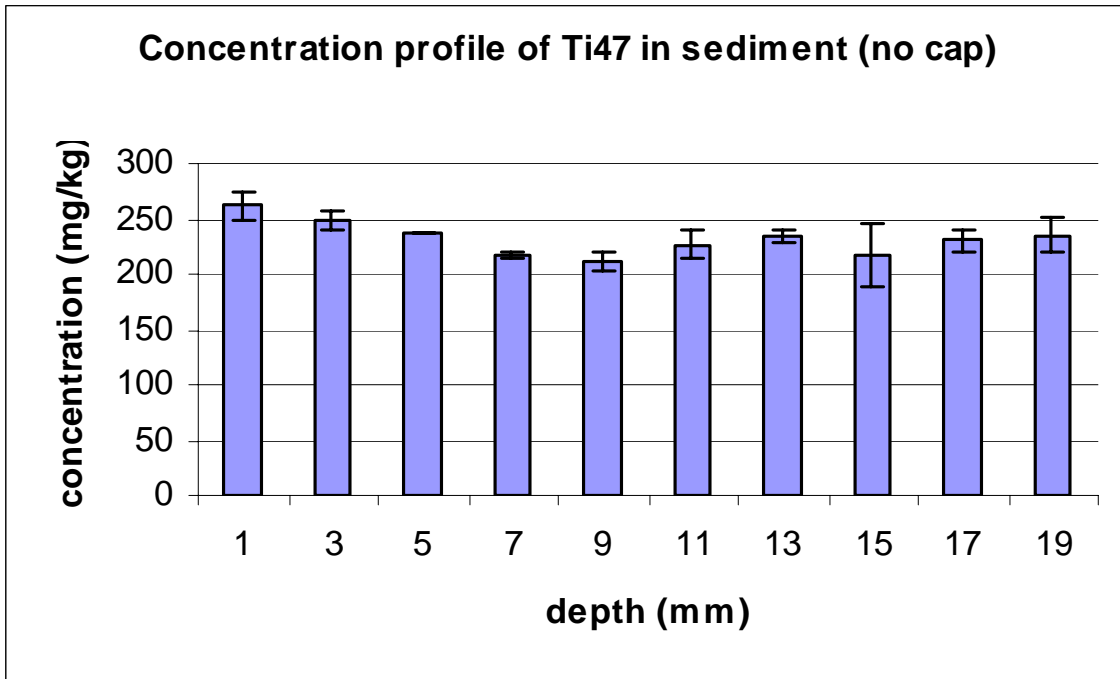


Figure D3.1.3 Concentration profile of Ti47.

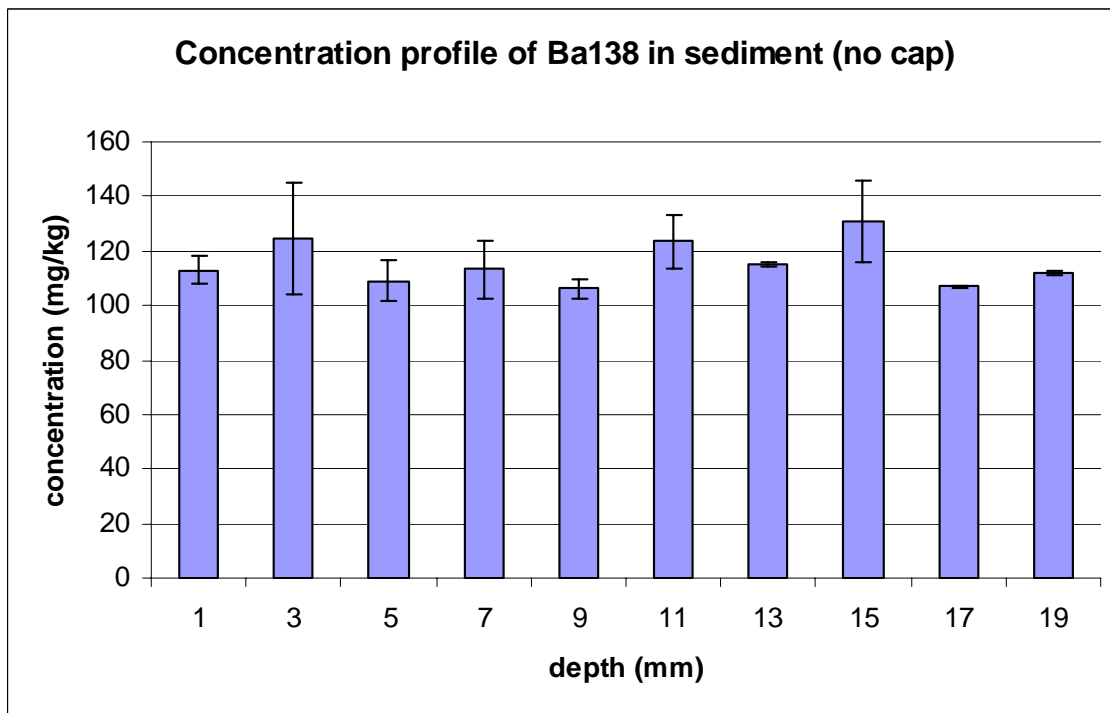


Figure D3.1.4 Concentration profile of Ba138.

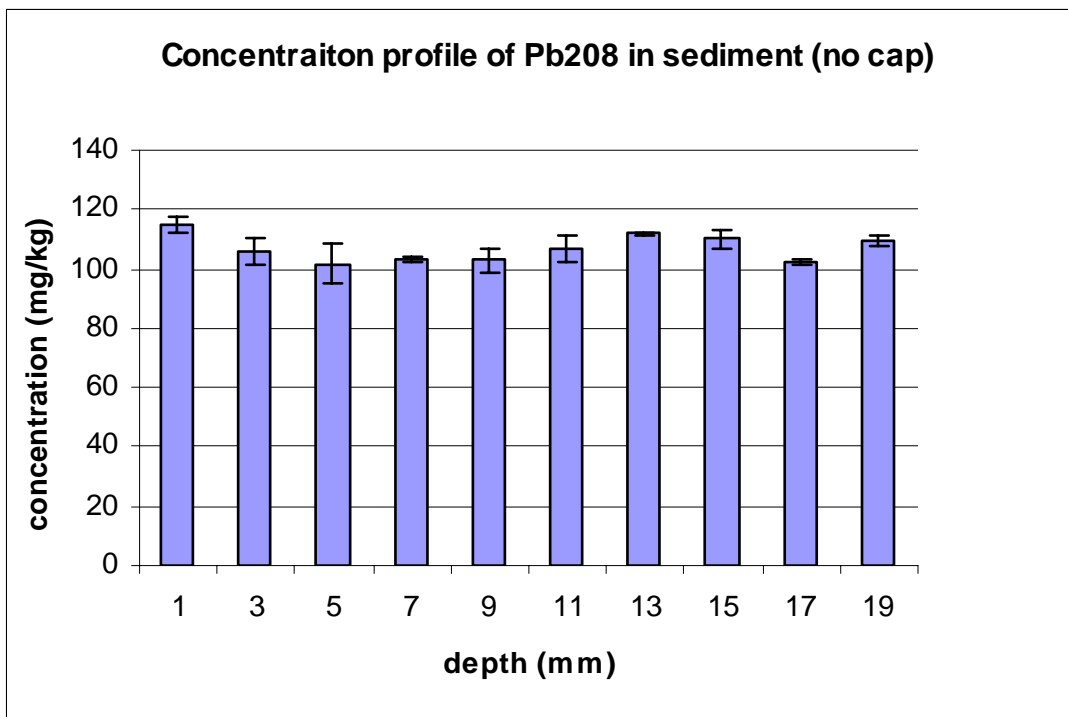


Figure D3.1.5 Concentration profile of Pb208.

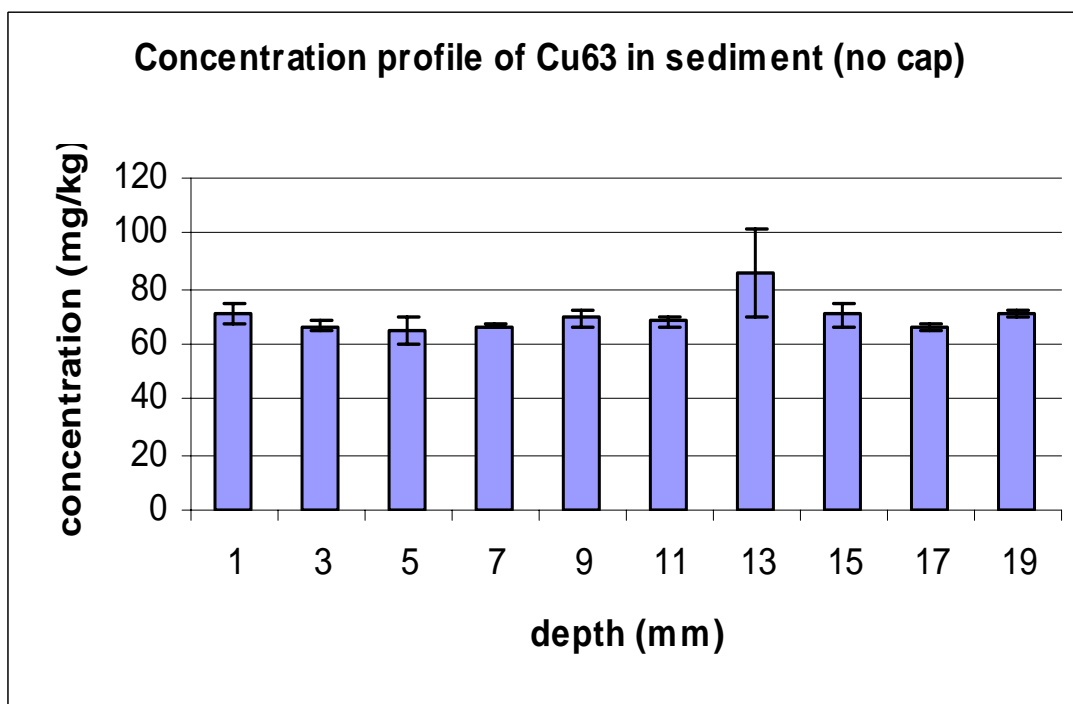


Figure D3.1.6 Concentration profile of Cu63.

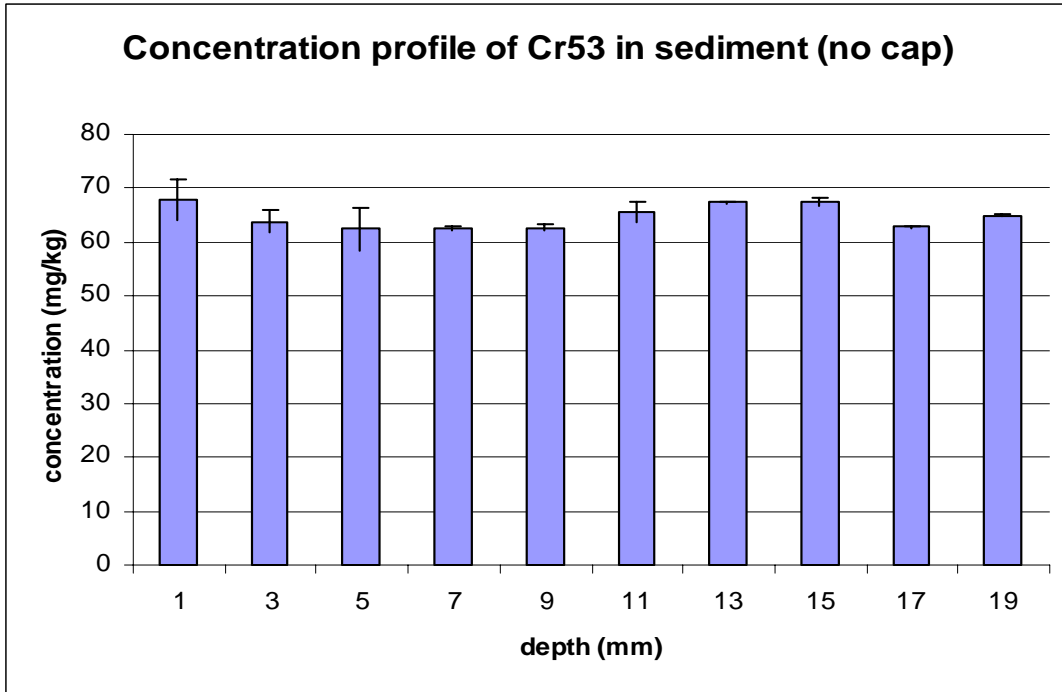


Figure D3.1.7 Concentration profile of Cr53.

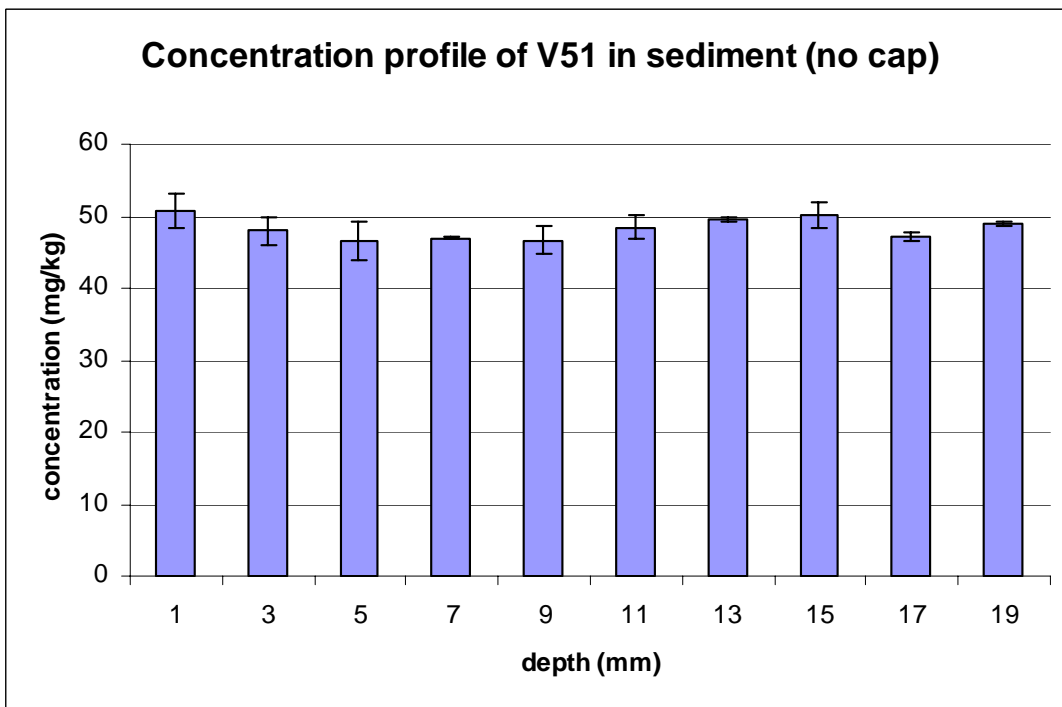


Figure D3.1.8 Concentration profile of V51.

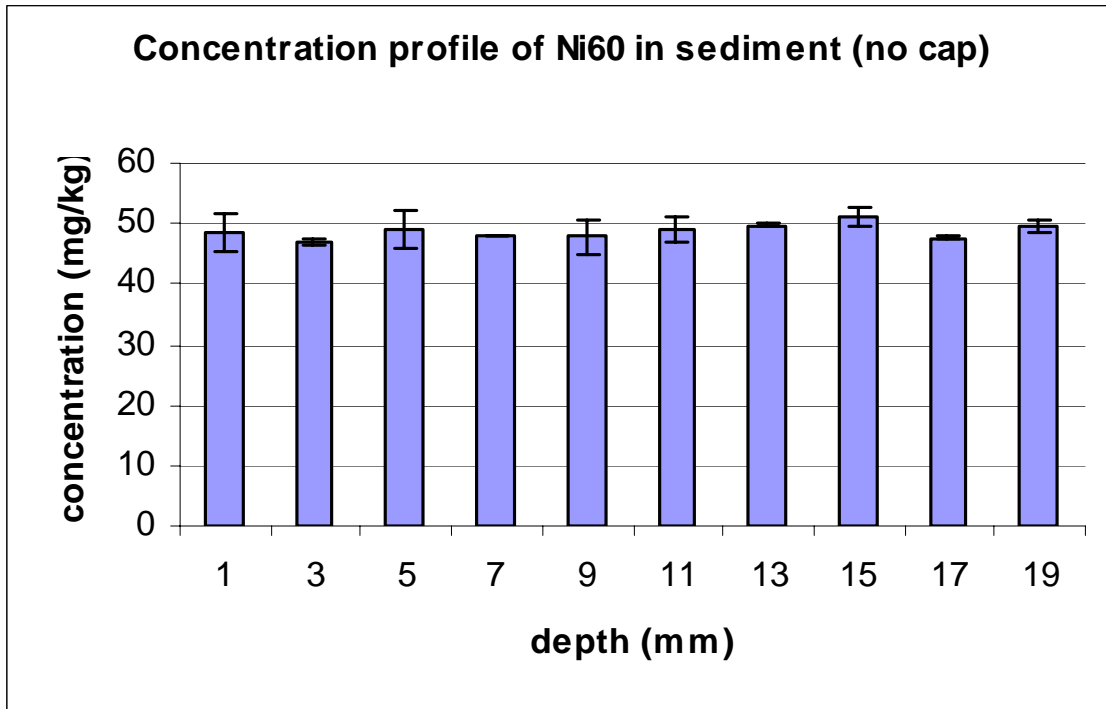


Figure D3.1.9 Concentration profile of Ni60.

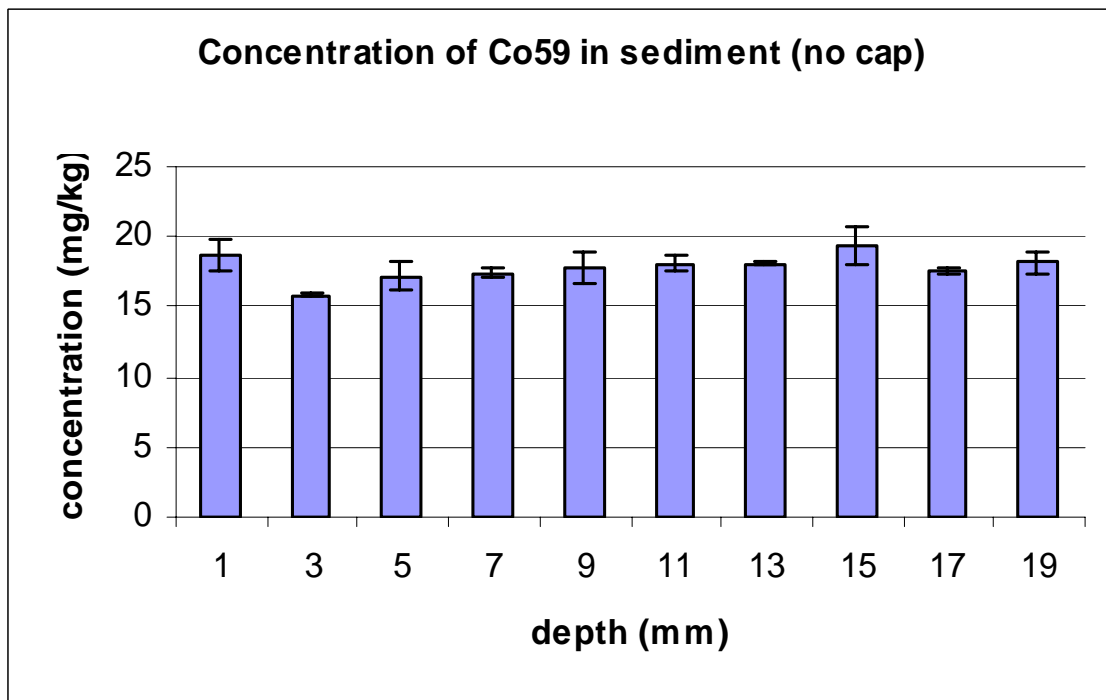


Figure D3.1.10 Concentration profile of Co59.

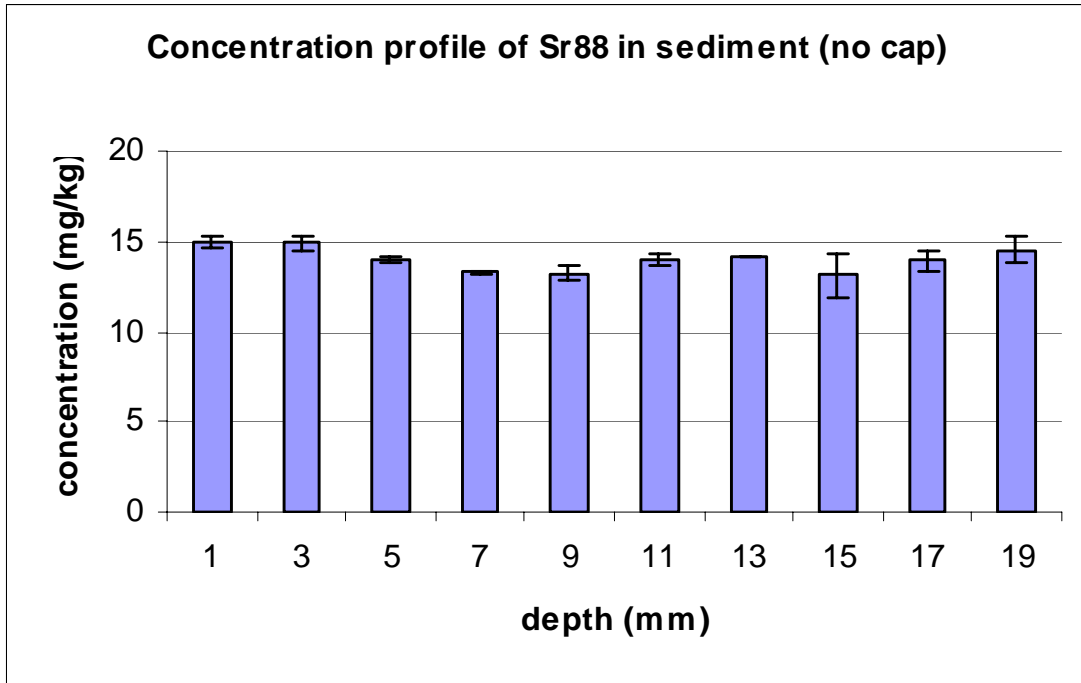


Figure D3.1.11 Concentration profile of Sr88.

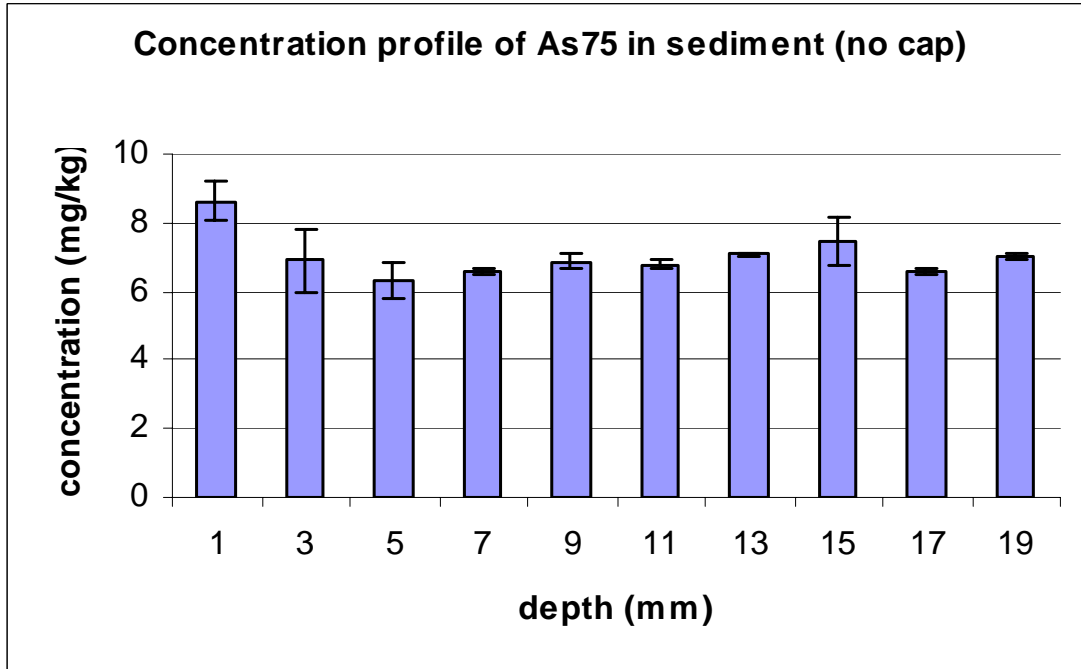


Figure D3.1.12 Concentration profile of As75.

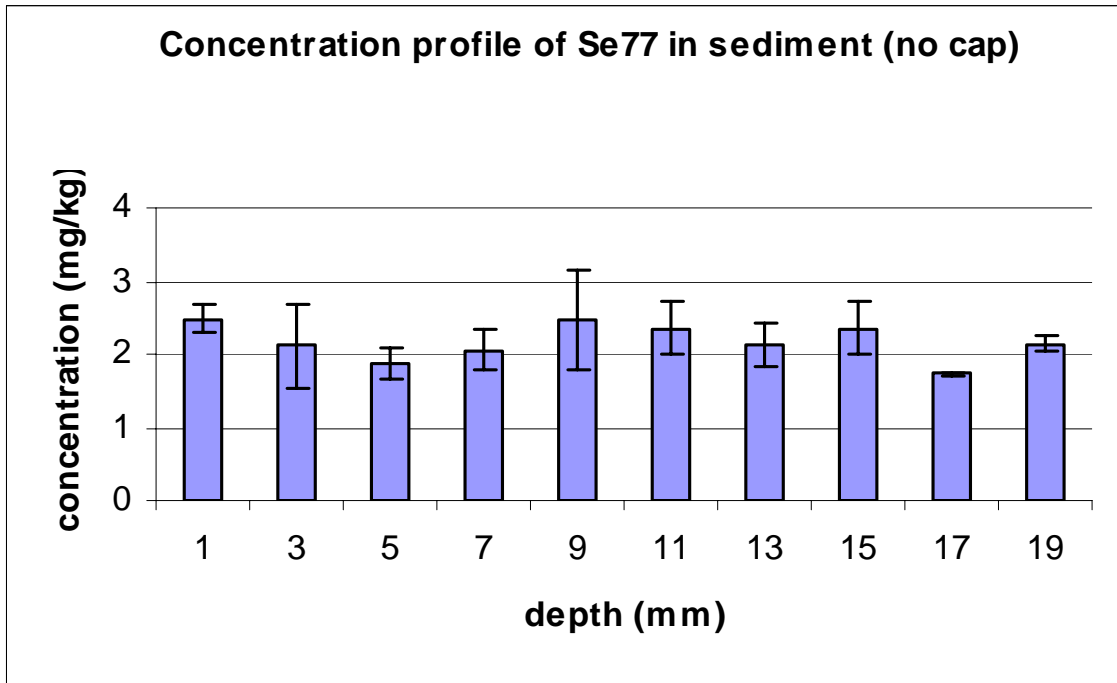


Figure D3.1.13 Concentration profile of Se77.

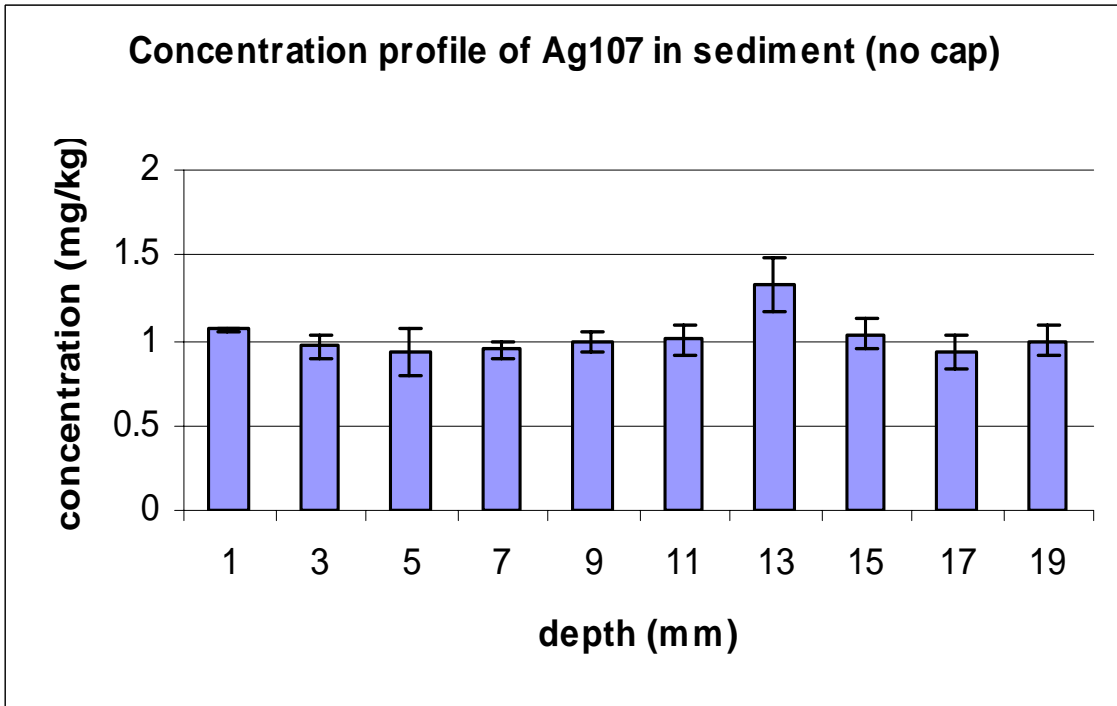


Figure D3.1.14 Concentration profile of Ag107.

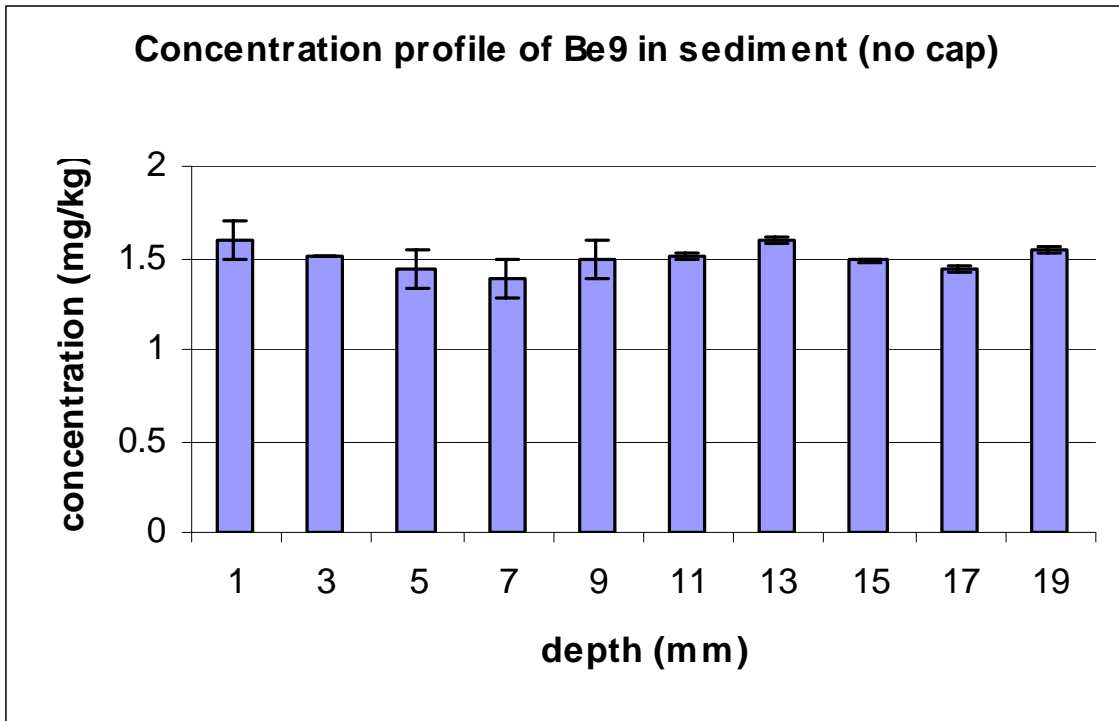


Figure D3.1.15 Concentration profile of Be9.

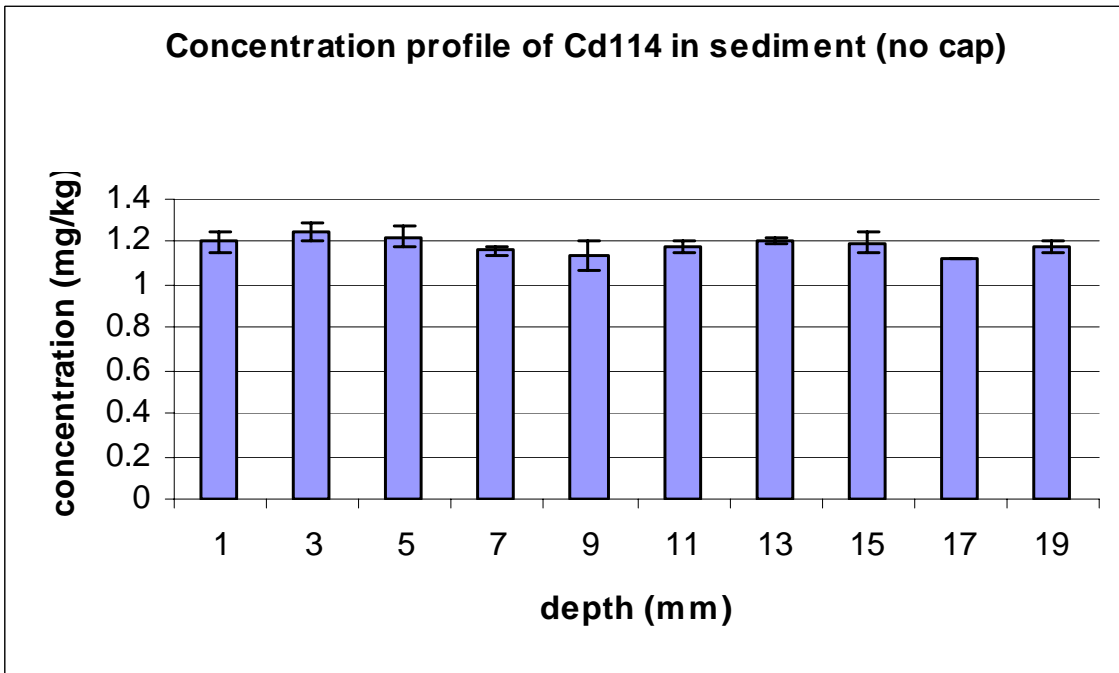


Figure D3.1.16 Concentration profile of Cd114.

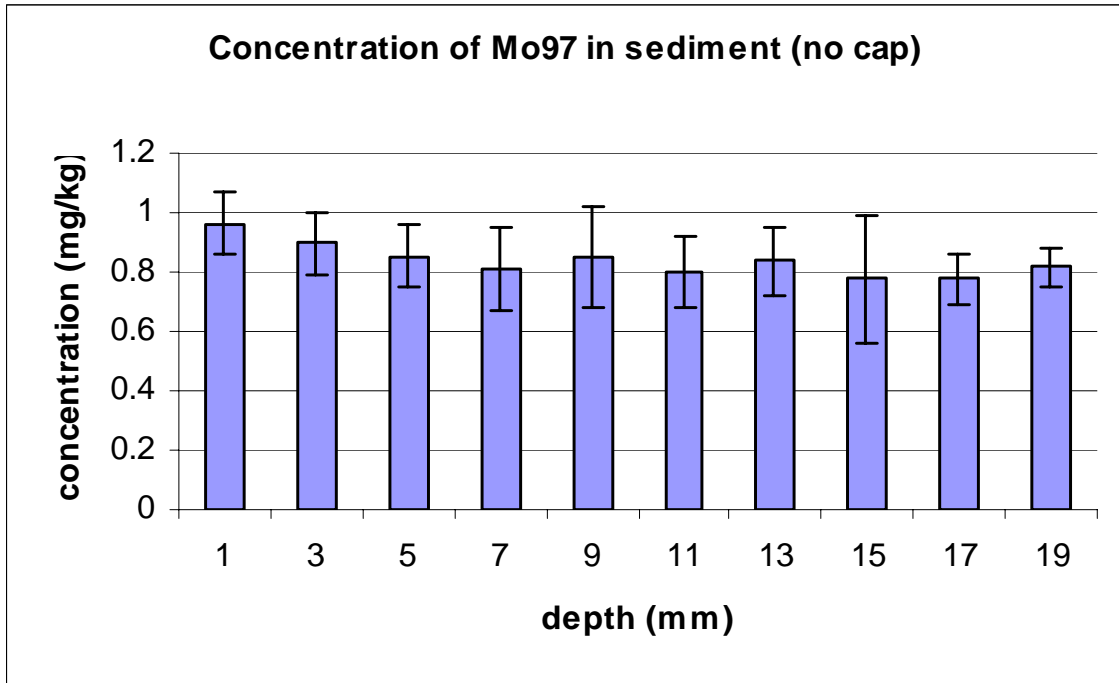


Figure D3.1.17 Concentration profile of Mo97.

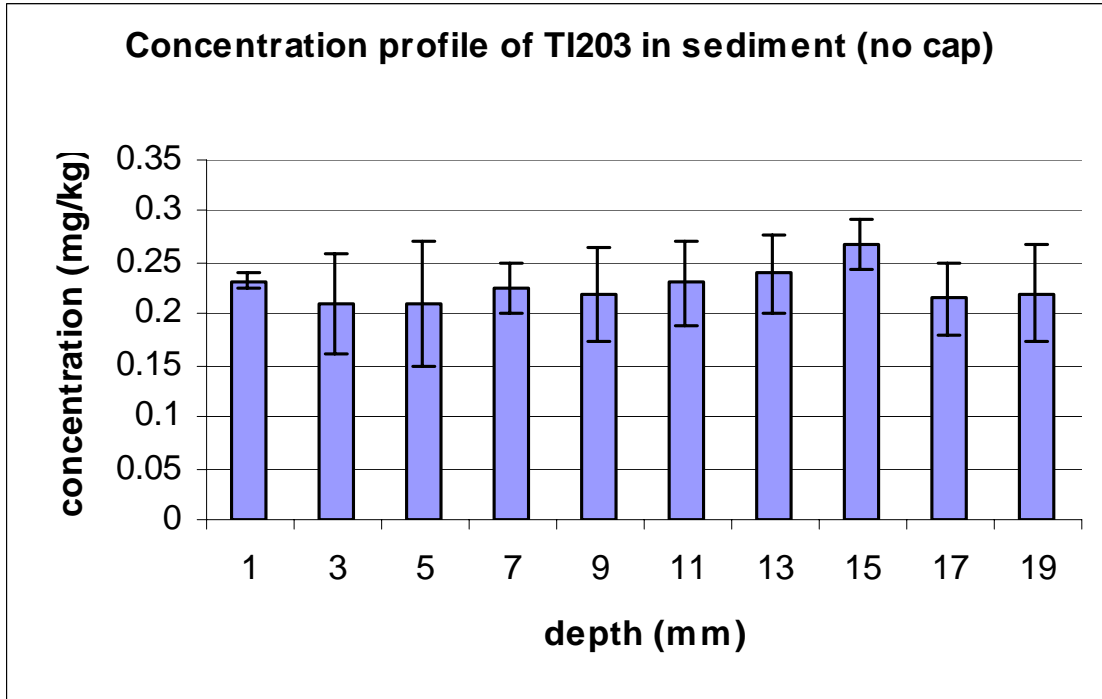


Figure D3.1.18 Concentration profile of TI20.

D3.2 Capped Sediment (4 mm sand cap)

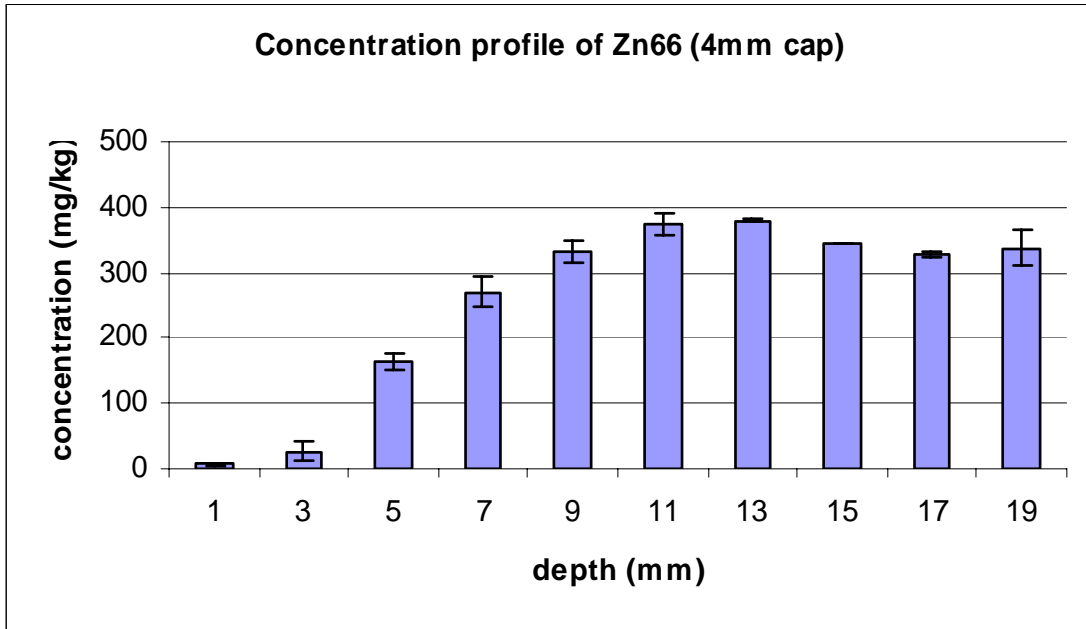


Figure D3.2.1 Concentration profile of Zn66.

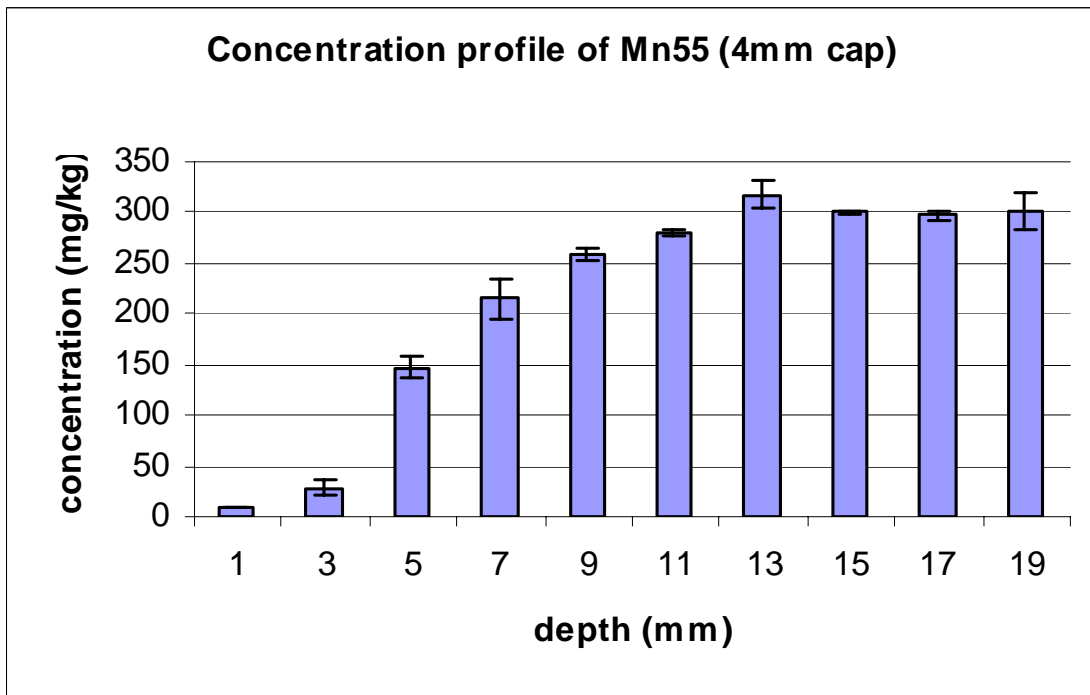


Figure D3.2.2 Concentration profile of Mn55.

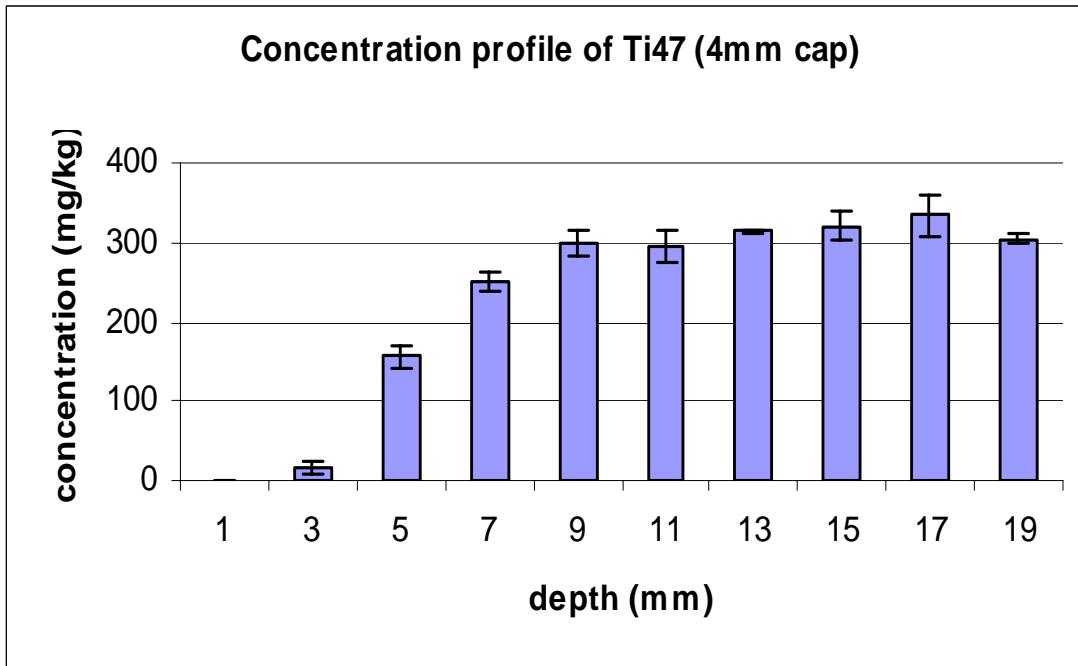


Figure D3.2.3 Concentration profile of Ti47.

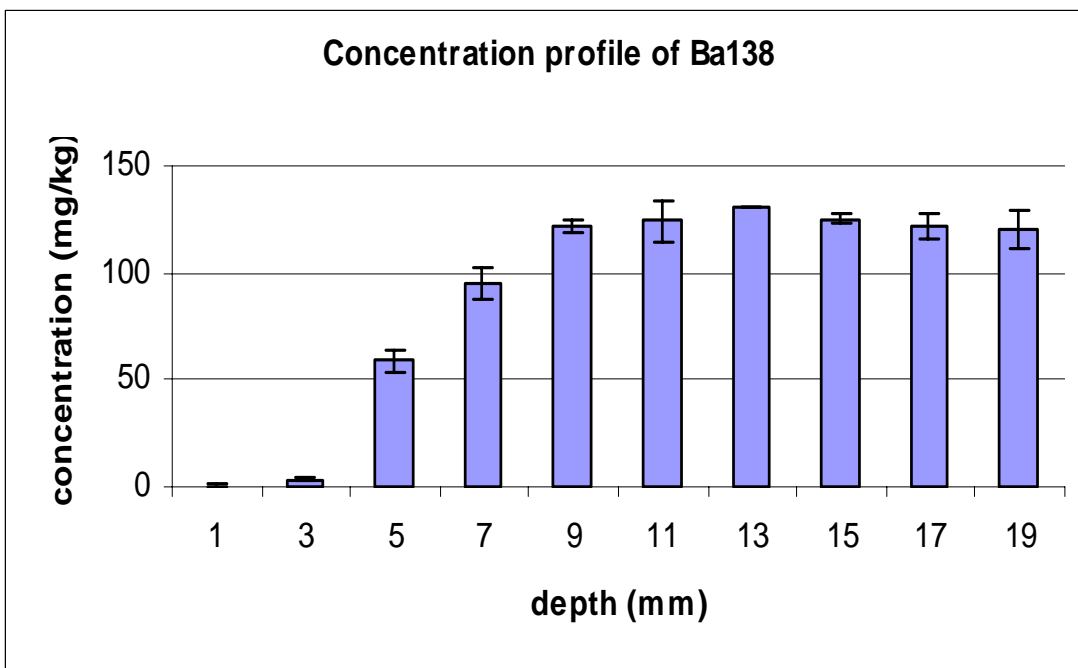


Figure D3.2.4 Concentration profile of Ba138.

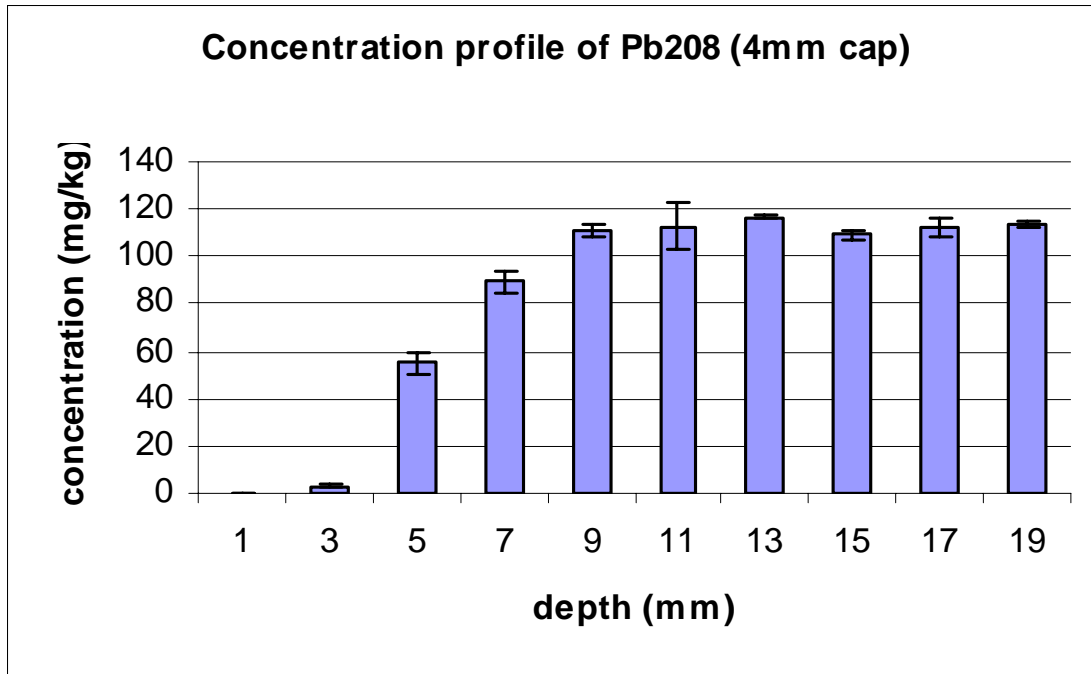


Figure D3.2.5 Concentration profile of Pb208.

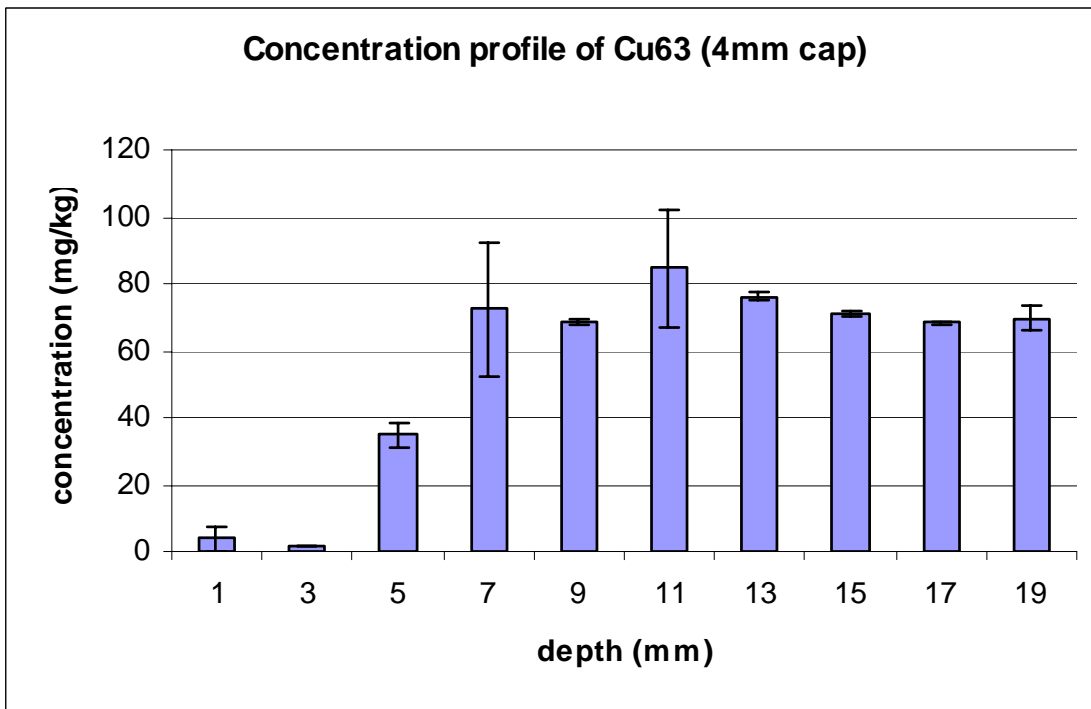


Figure D3.2.6 Concentration profile of Cu63.

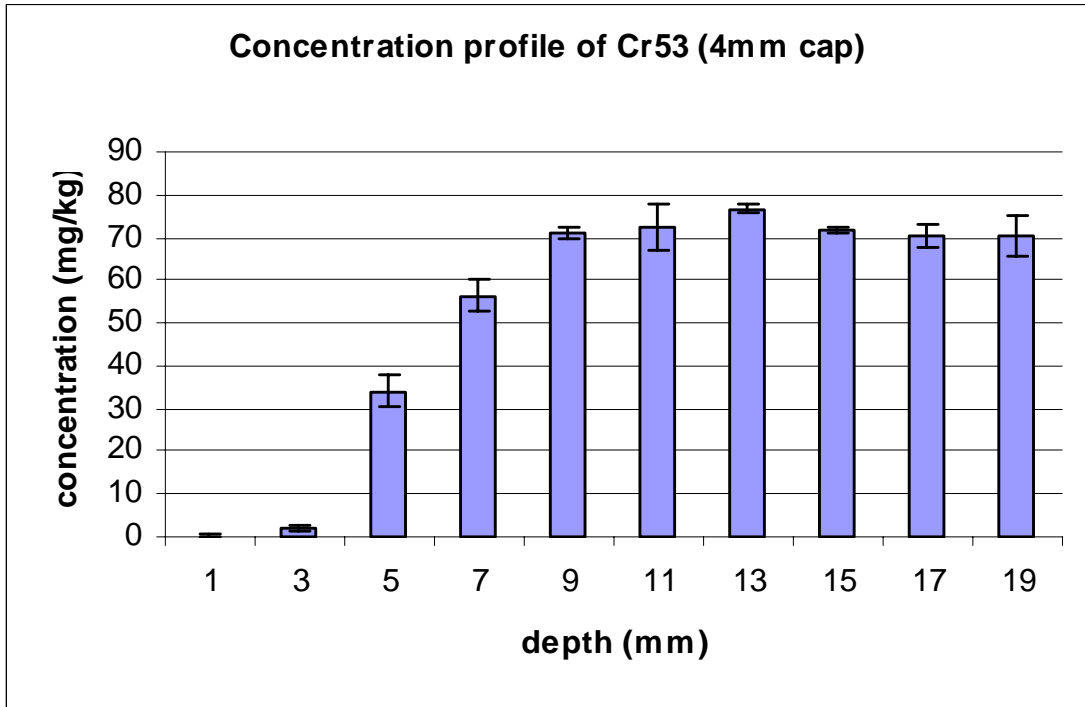


Figure D3.2.7 Concentration profile of Cr53.

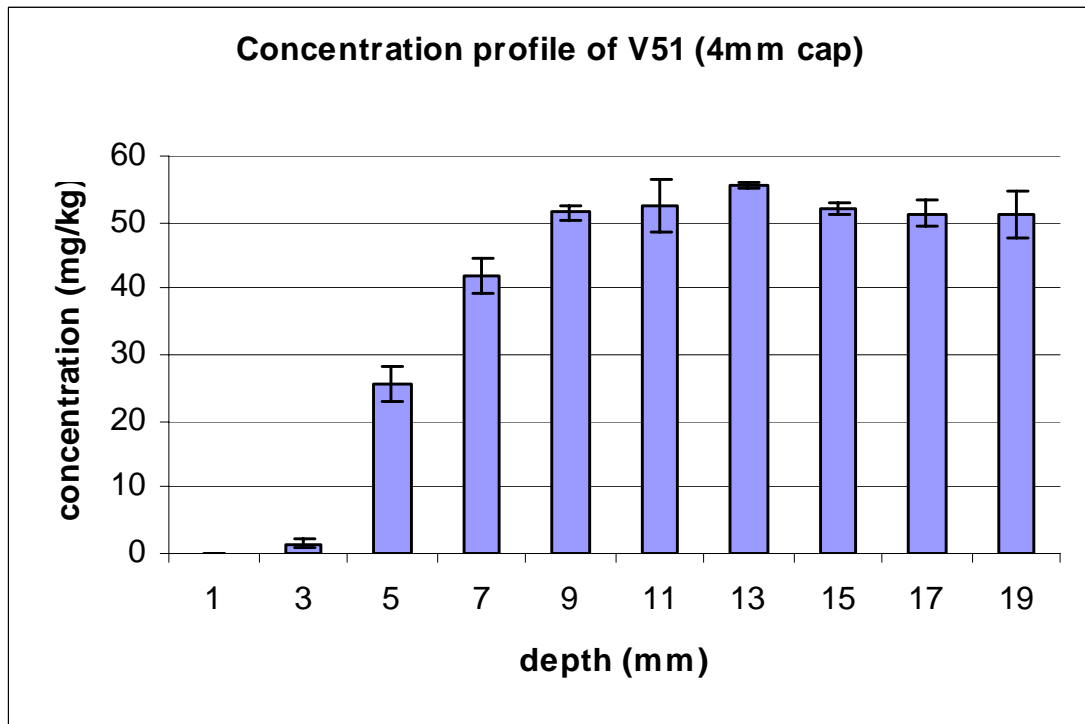


Figure D3.2.8 Concentration profile of V51.

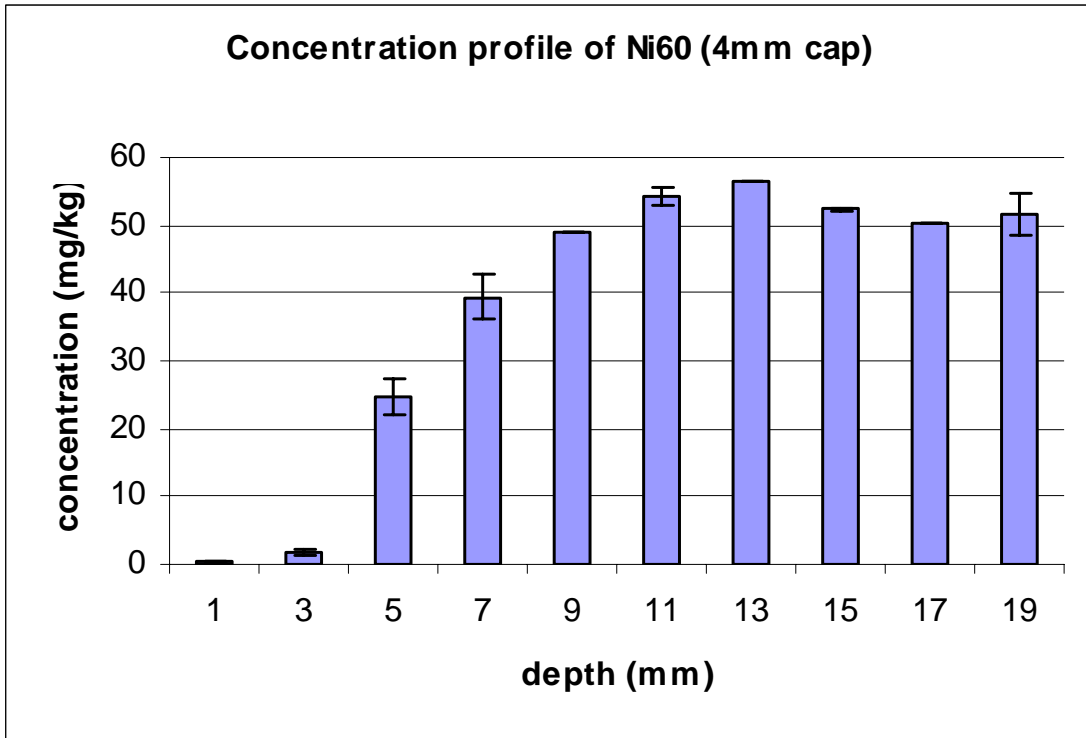


Figure D3.2.9 Concentration profile of Ni60.

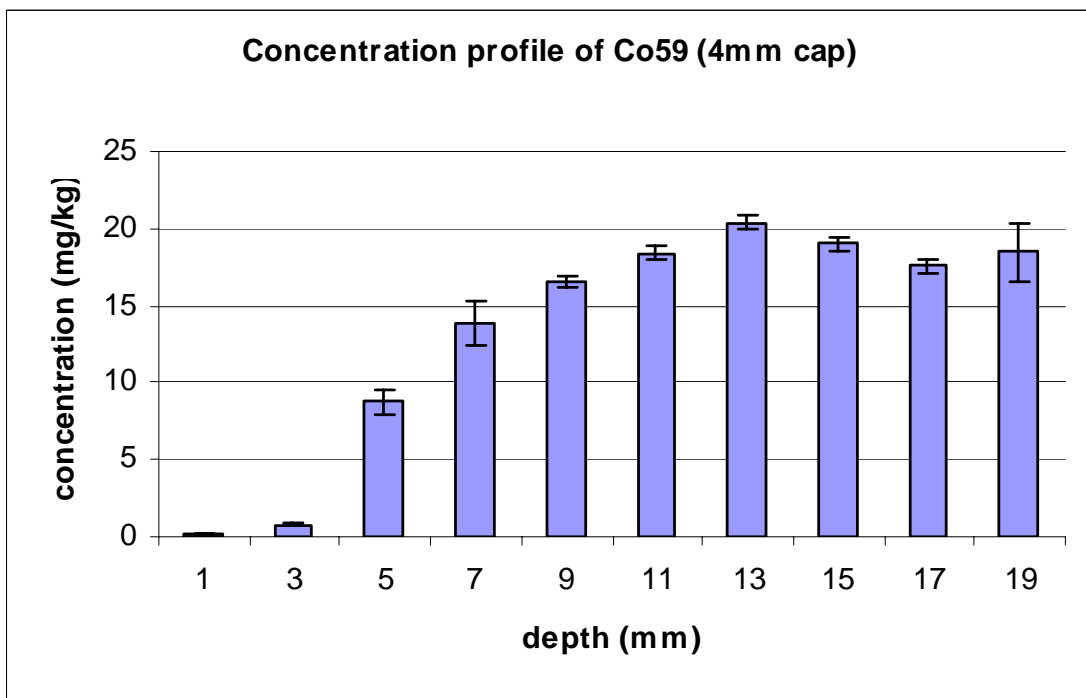


Figure D3.2.10 Concentration profile of Co59.

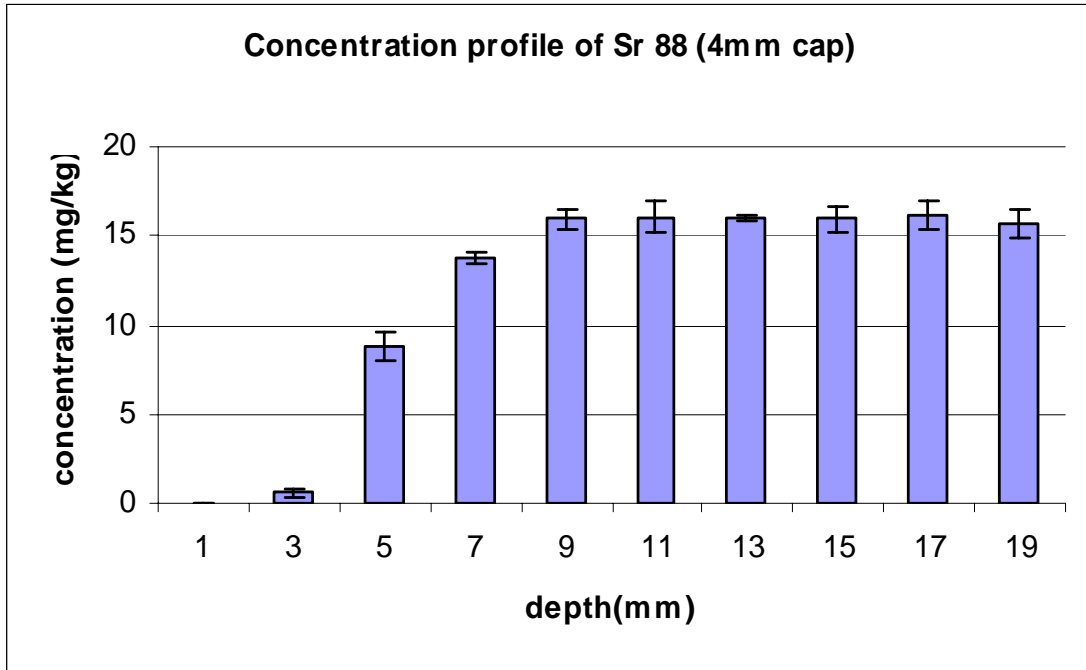


Figure D3.2.11 Concentration profile of Sr88.

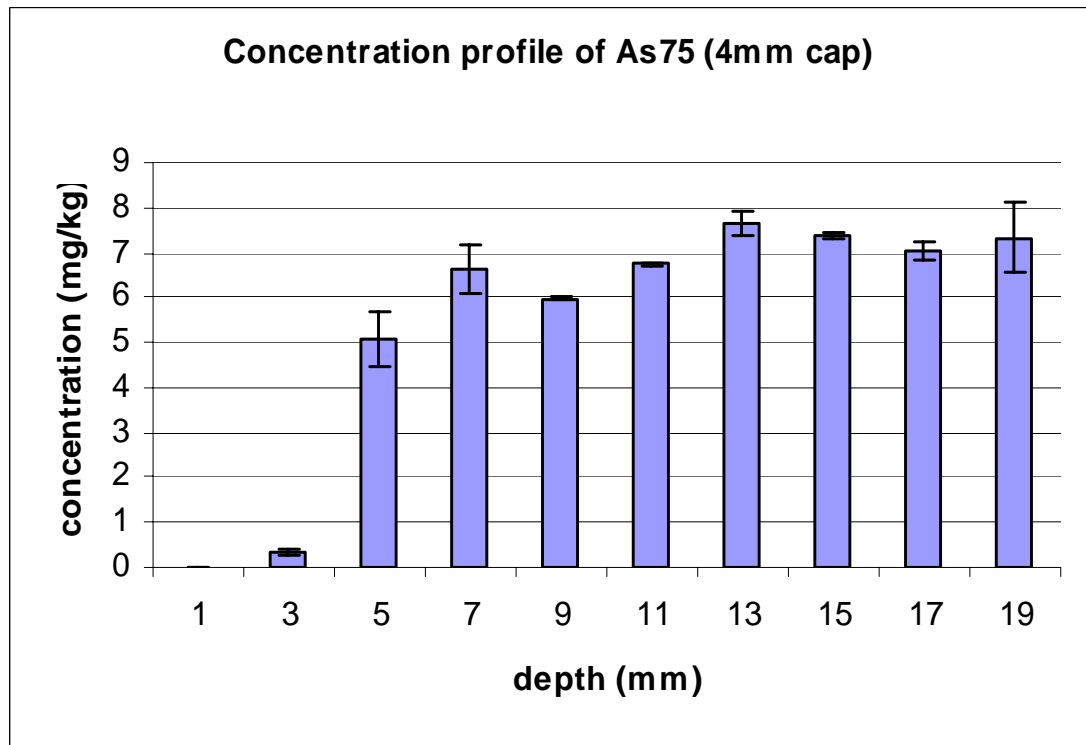


Figure D3.2.12 Concentration profile of As75.

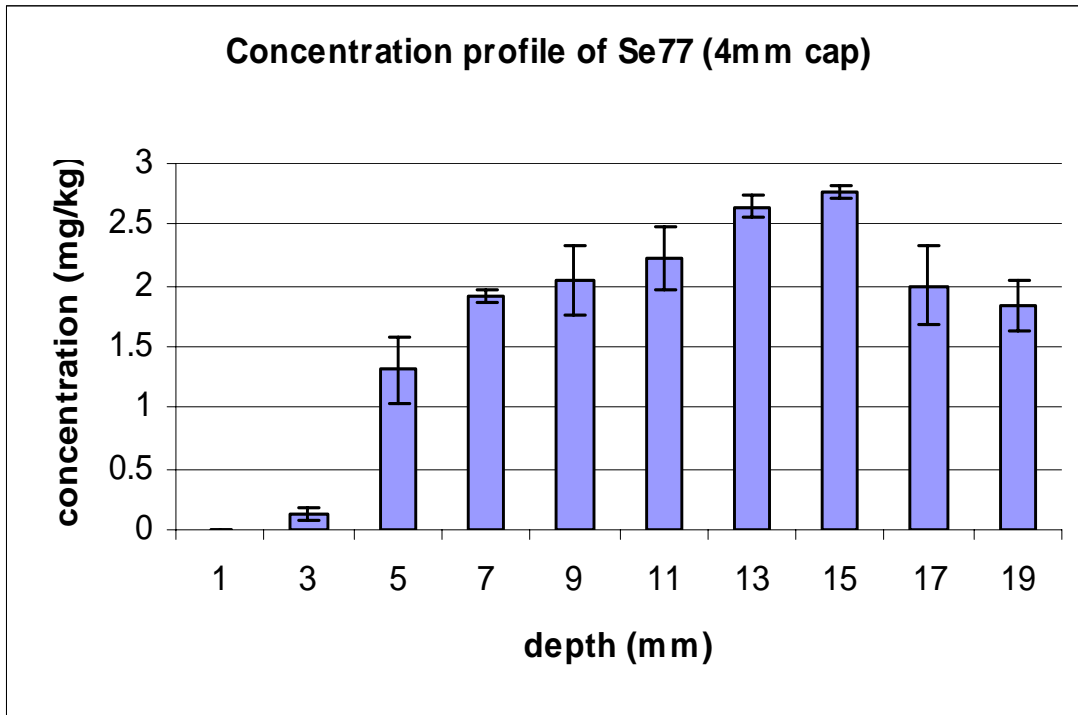


Figure D3.2.13 Concentration profile of Se77.

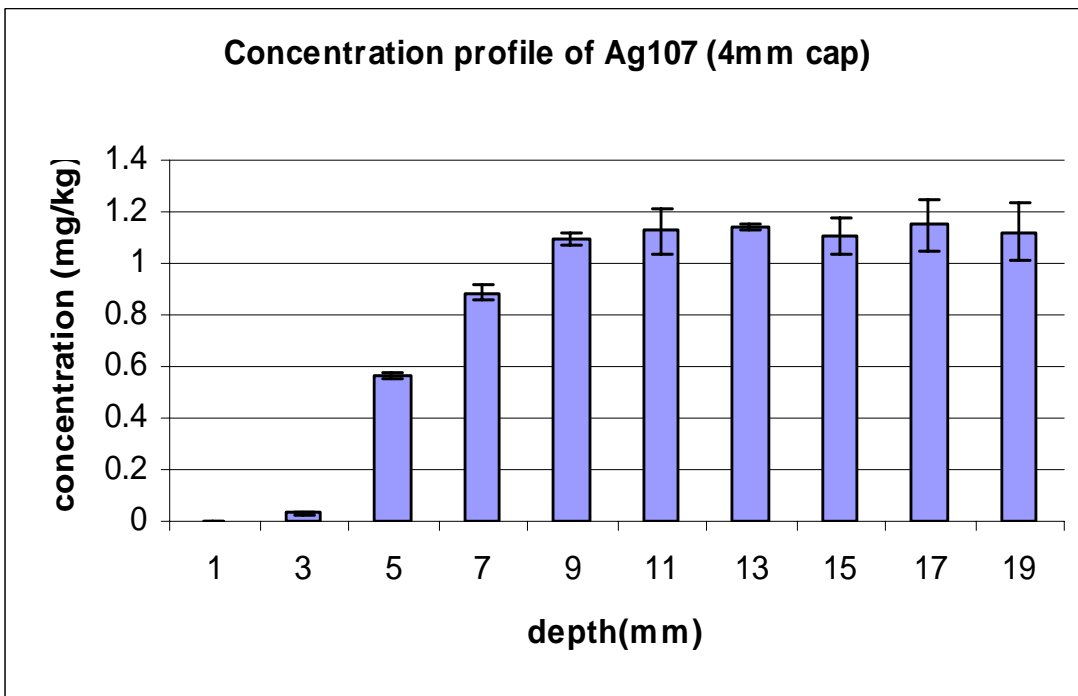


Figure D3.2.14 Concentration profile of Ag107.

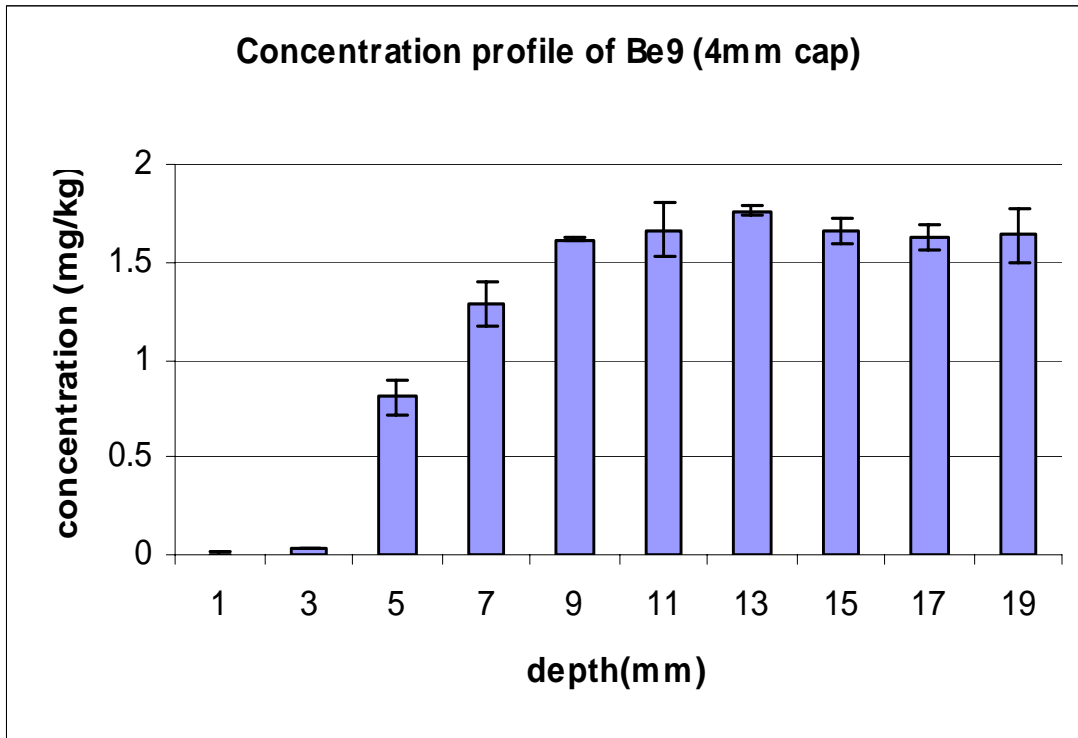


Figure D3.2.15 Concentration profile of Be9.

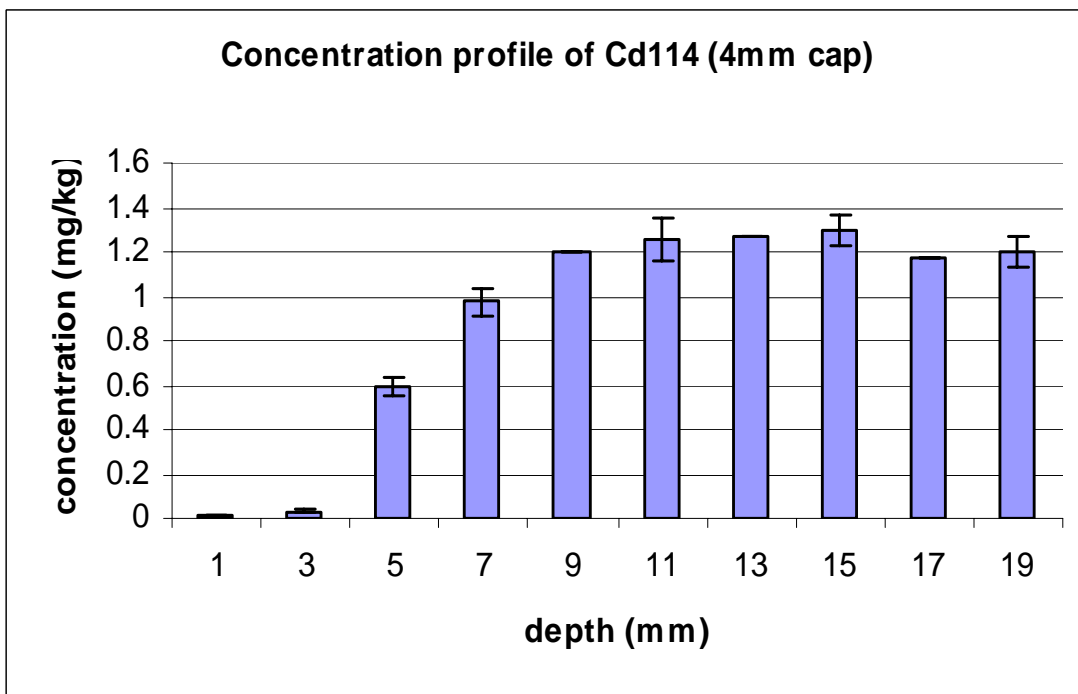


Figure D3.2.16 Concentration profile of Cd114.

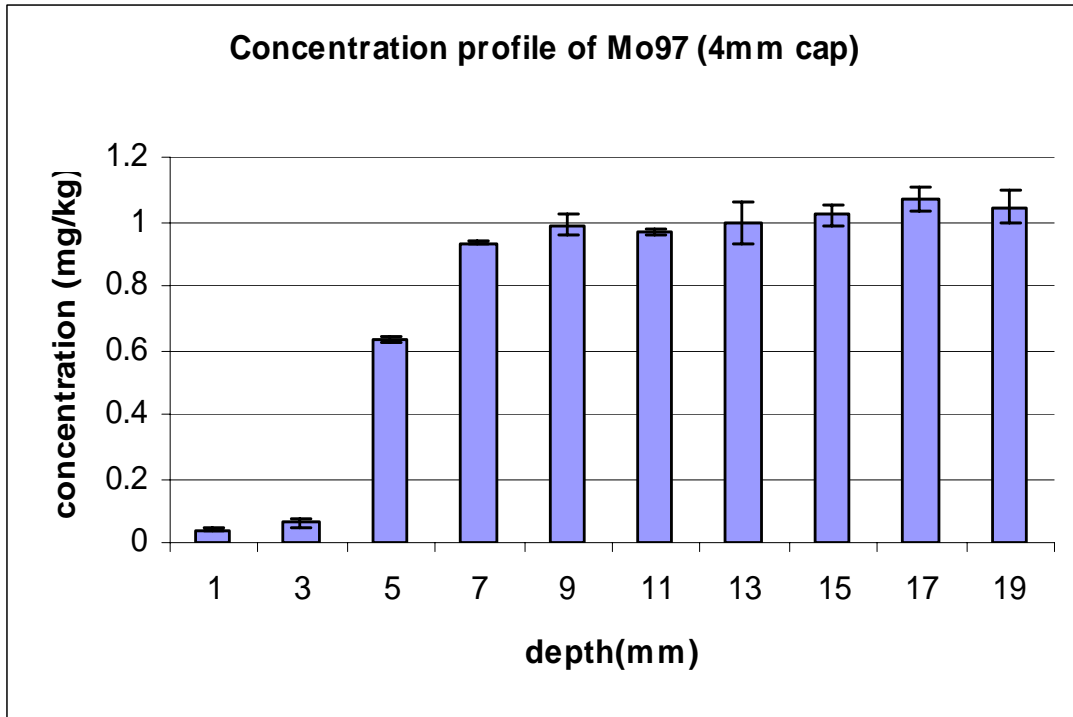


Figure D3.2.17 Concentration profile of Mo97.

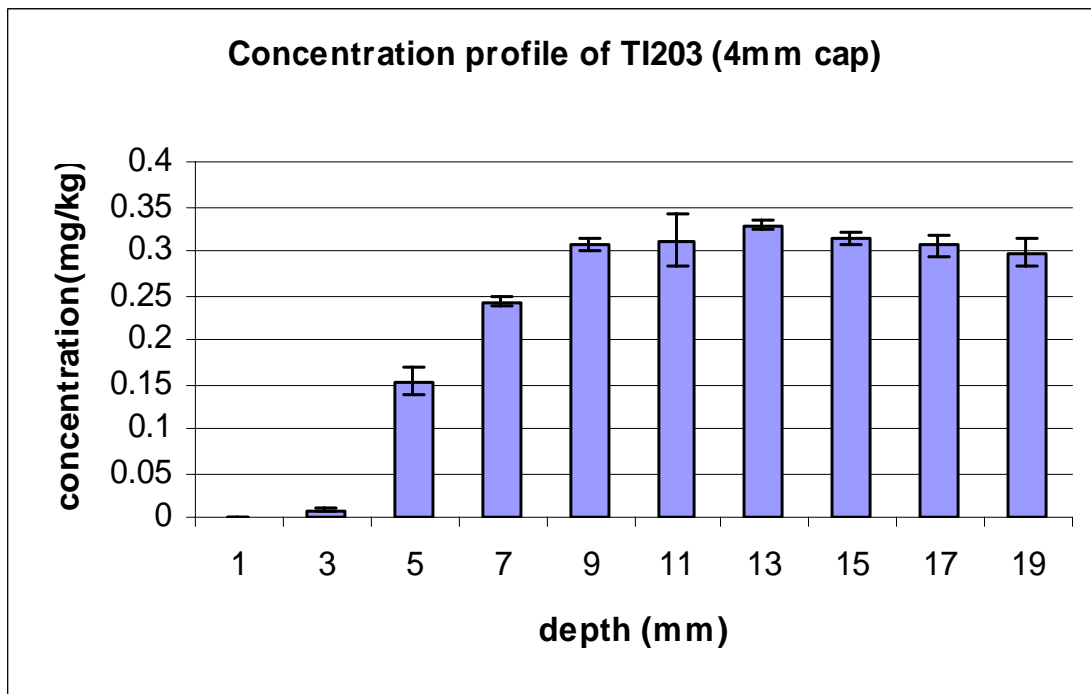


Figure D3.2.18 Concentration profile of TI203.

D3.3 Capped Sediment (8 mm sand cap)

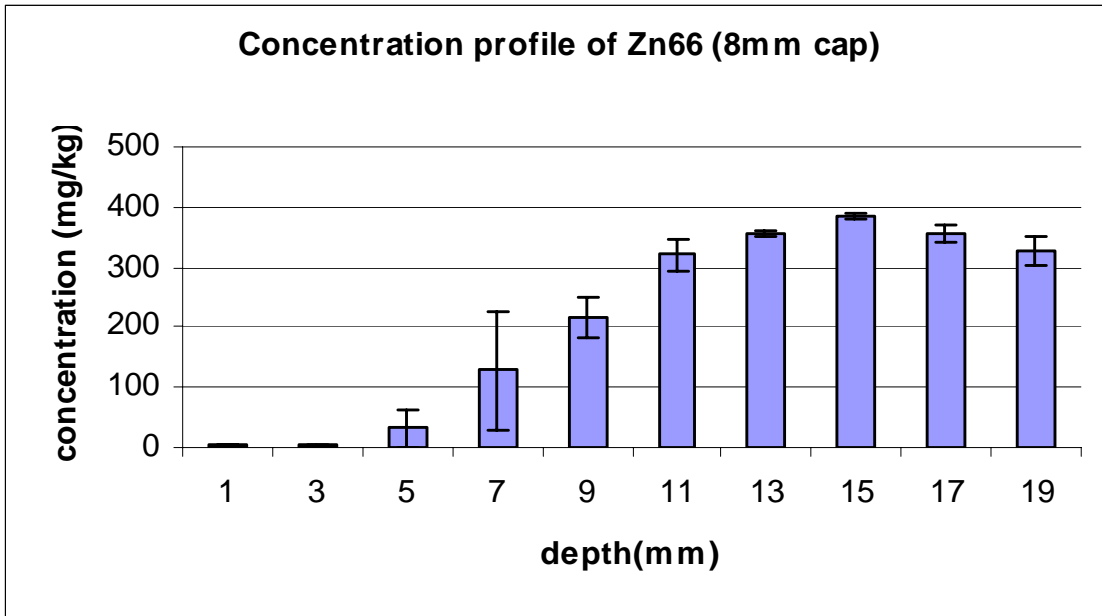


Figure D3.3.1 Concentration profile of Zn66.

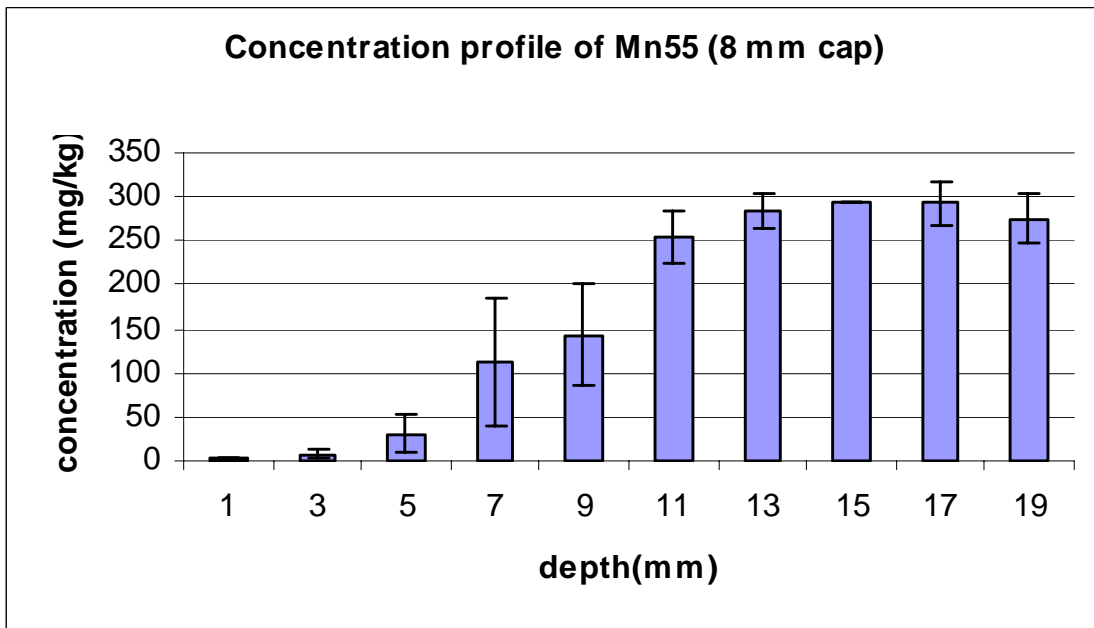


Figure D3.3.2 Concentration profile of Mn55.

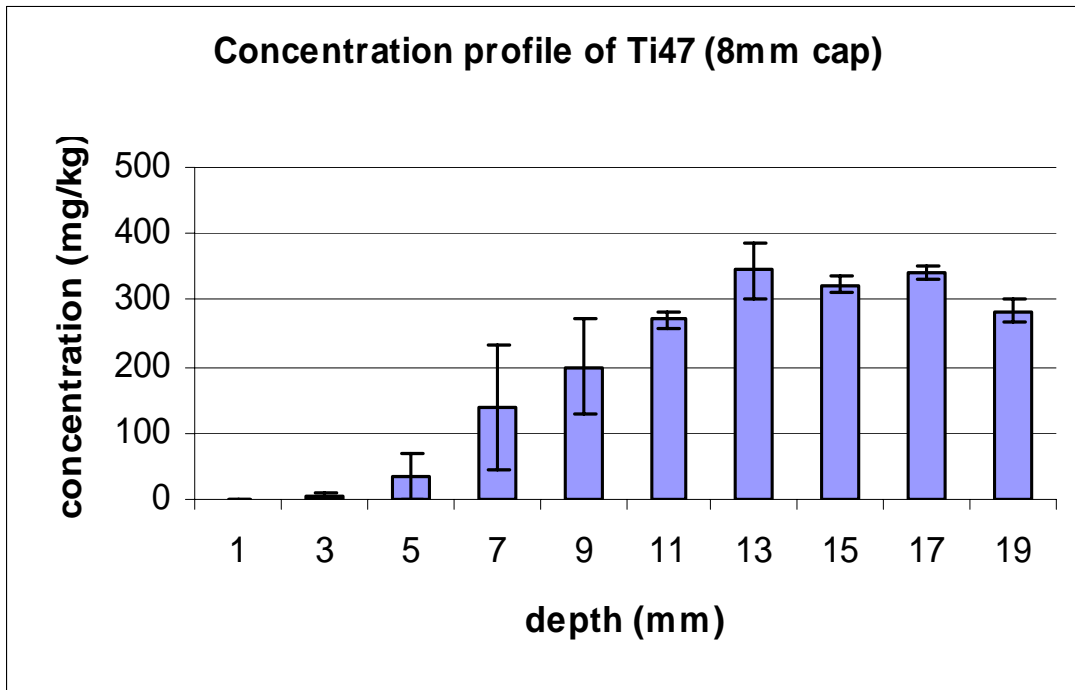


Figure D3.3.3 Concentration profile of Ti47.

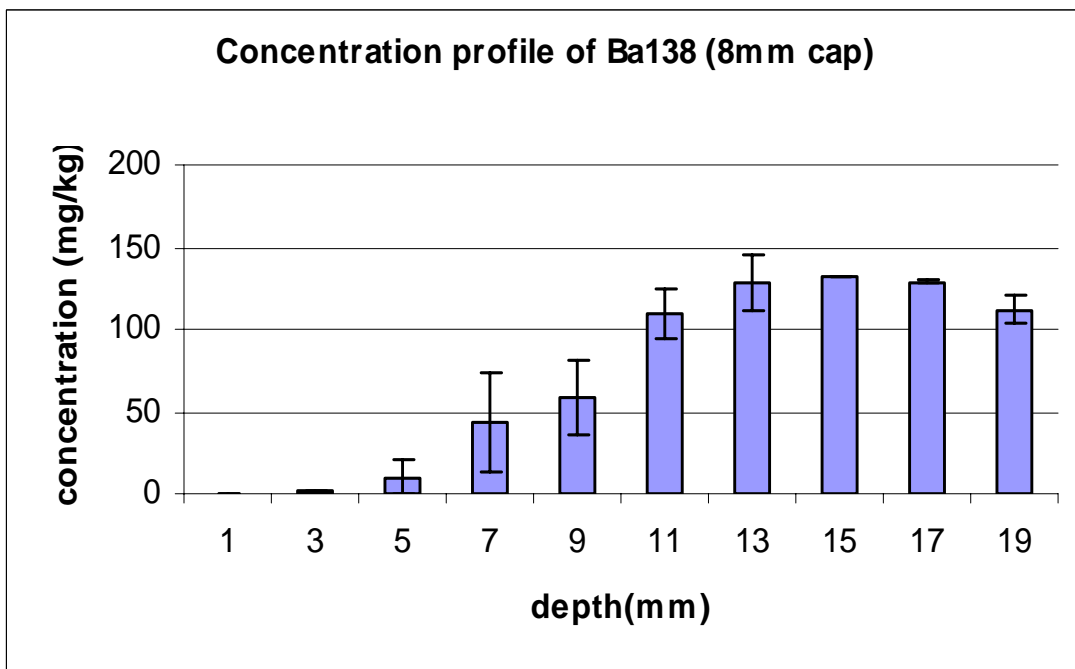


Figure D3.3.4 Concentration profile of Ba138.

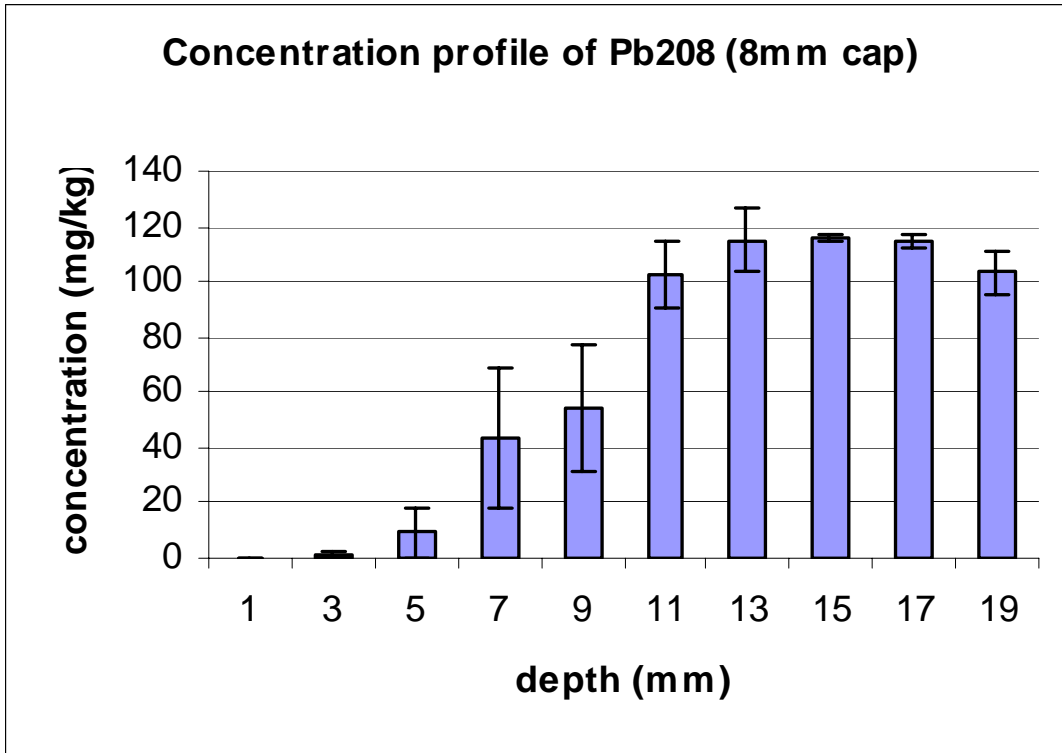


Figure D3.3.5 Concentration profile of Pb208.

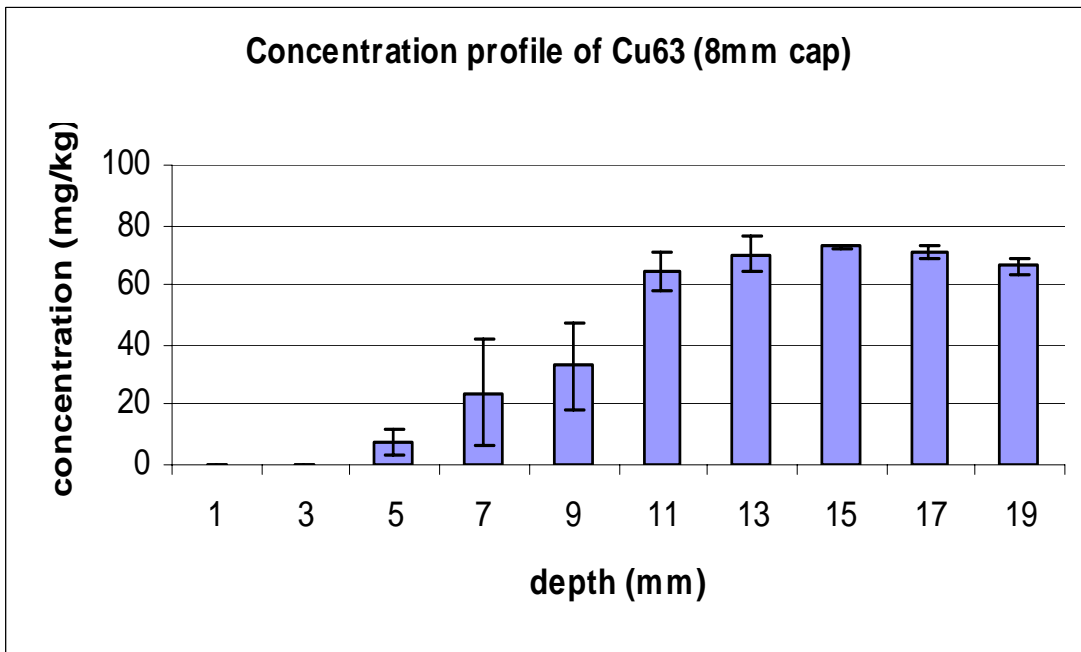


Figure D3.3.6 Concentration profile of Cu63.

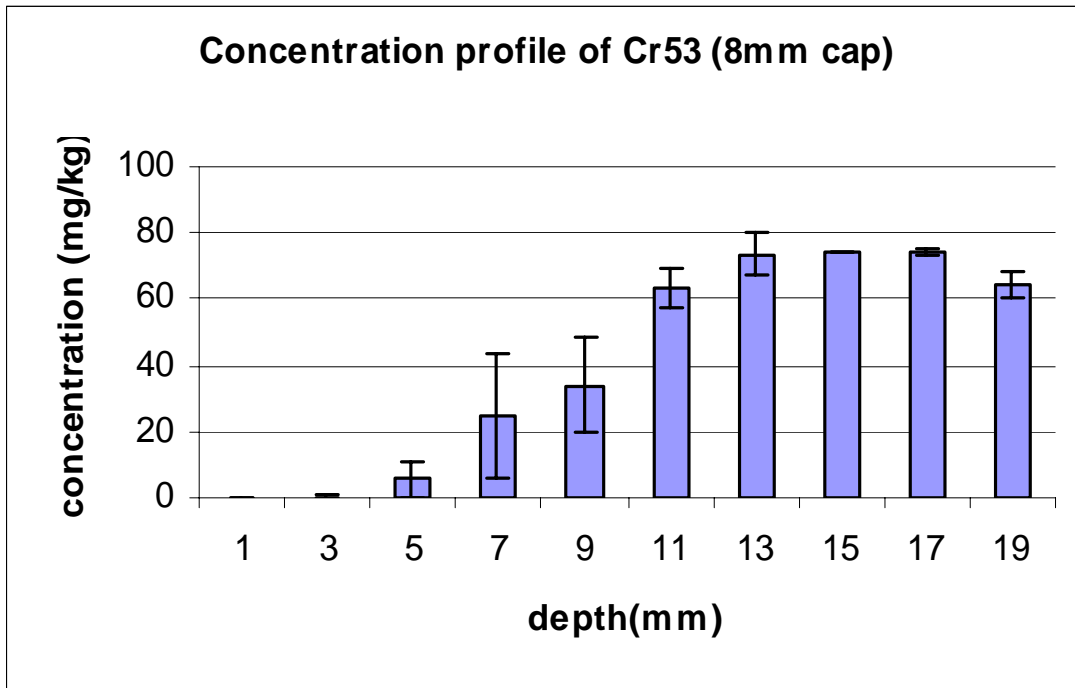


Figure D3.3.7 Concentration profile of Cr53.

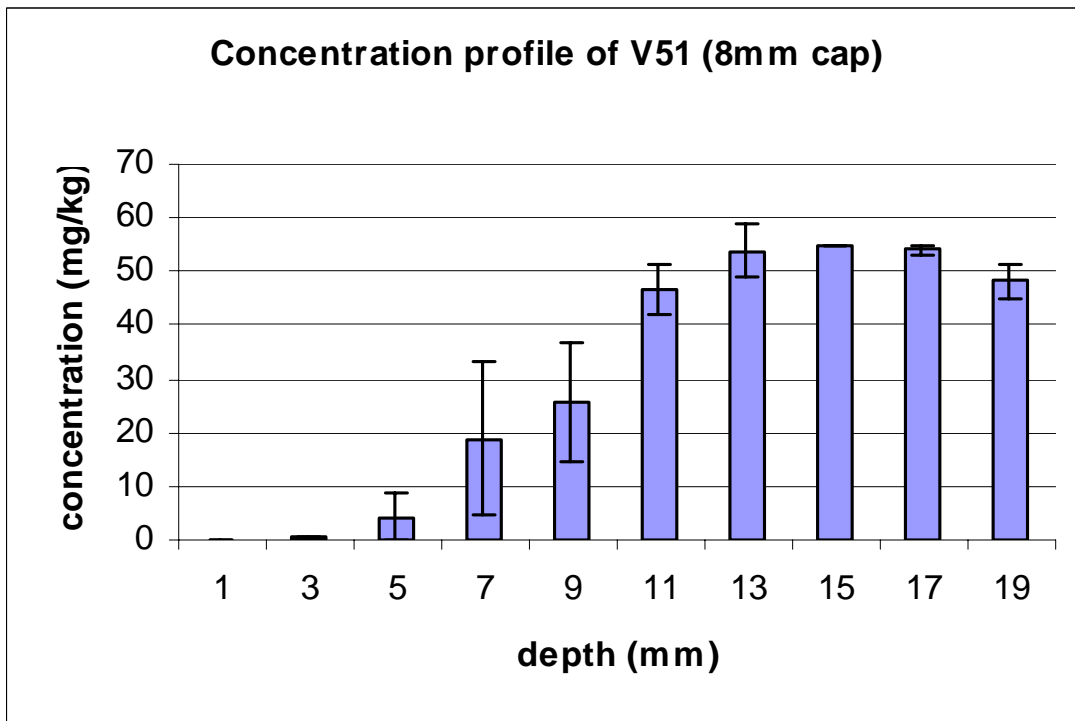


Figure D3.3.8 Concentration profile of V51.

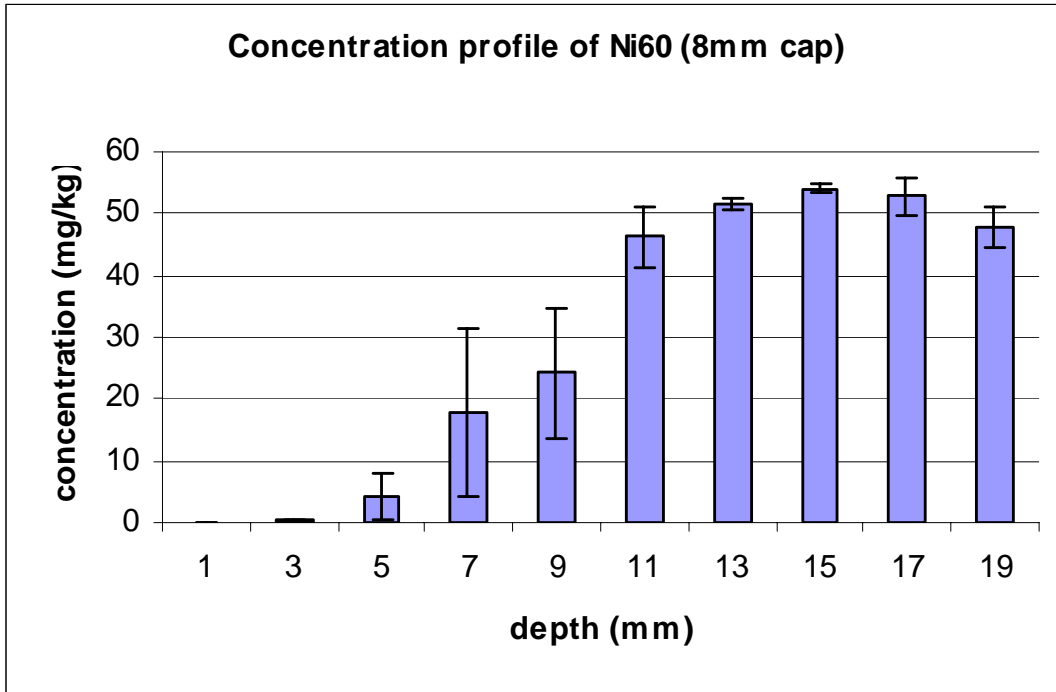


Figure D3.3.9 Concentration profile of Ni60.

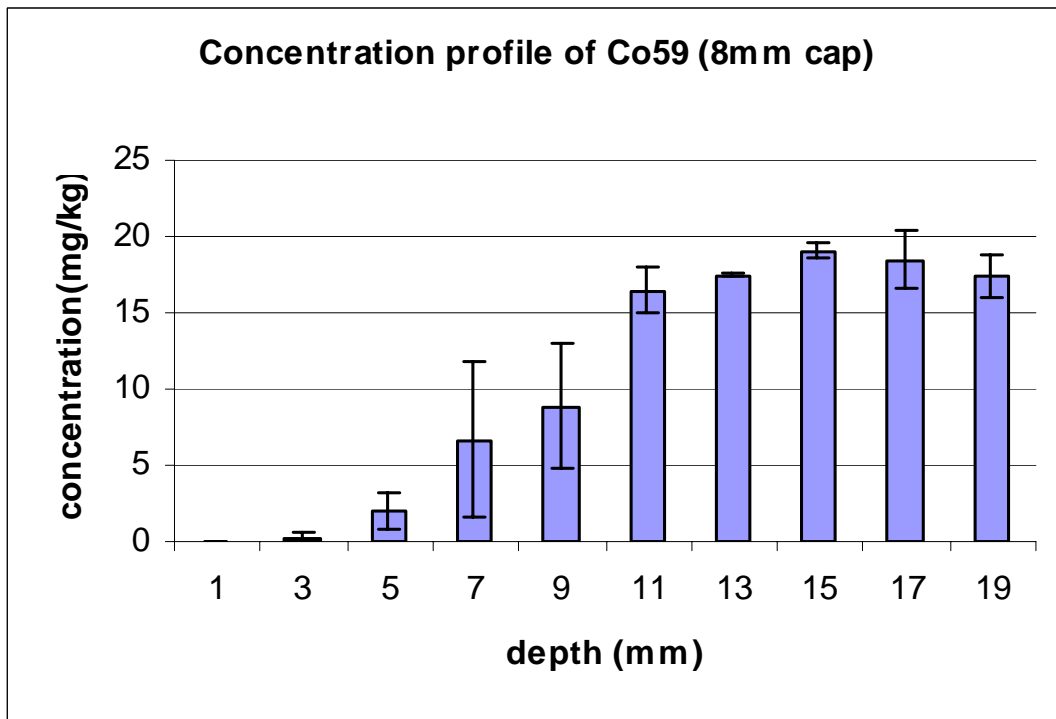


Figure D3.3.10 Concentration profile of Co59.

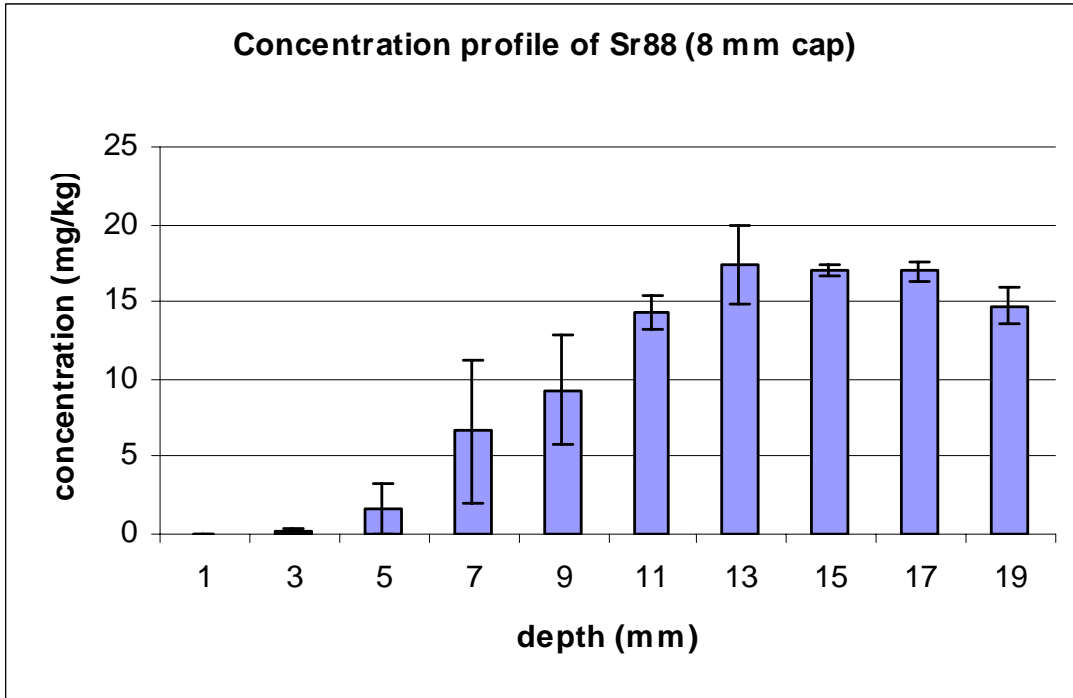


Figure D3.3.11 Concentration profile of Sr88.

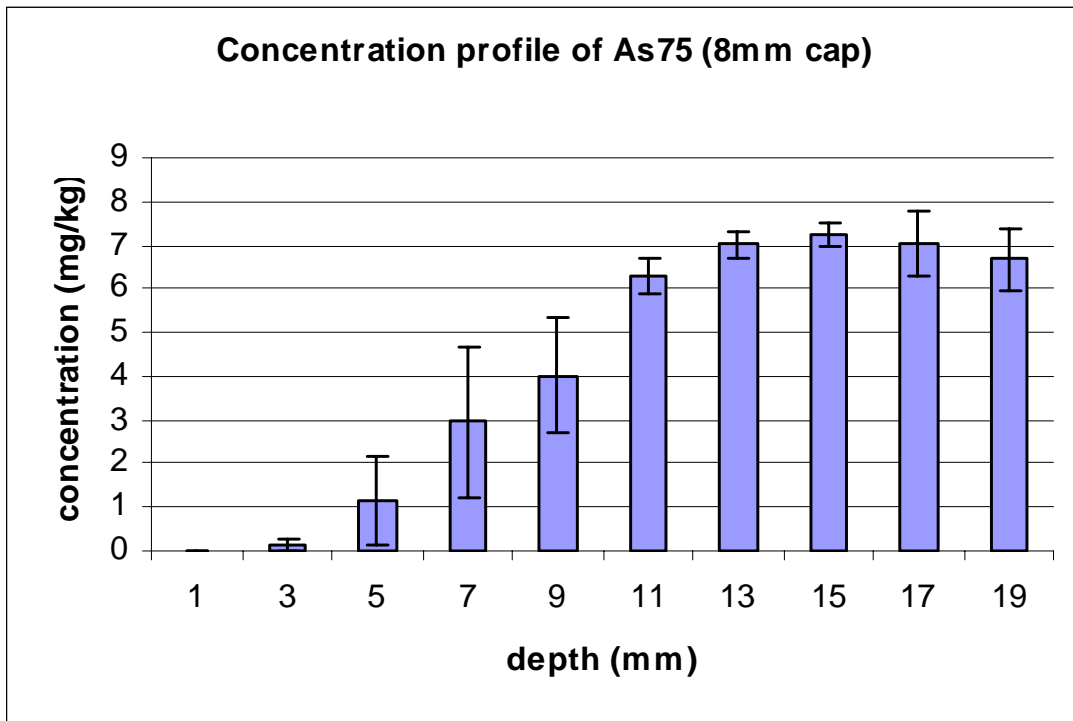


Figure D3.3.12 Concentration profile of As75.

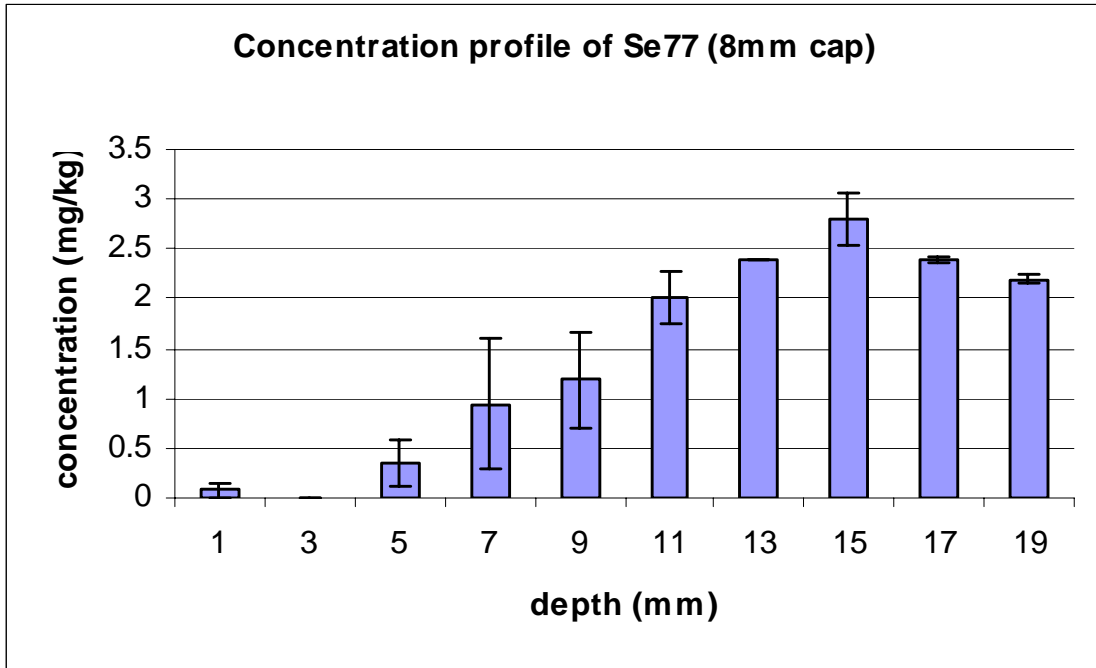


Figure D3.3.13 Concentration profile of Se77.

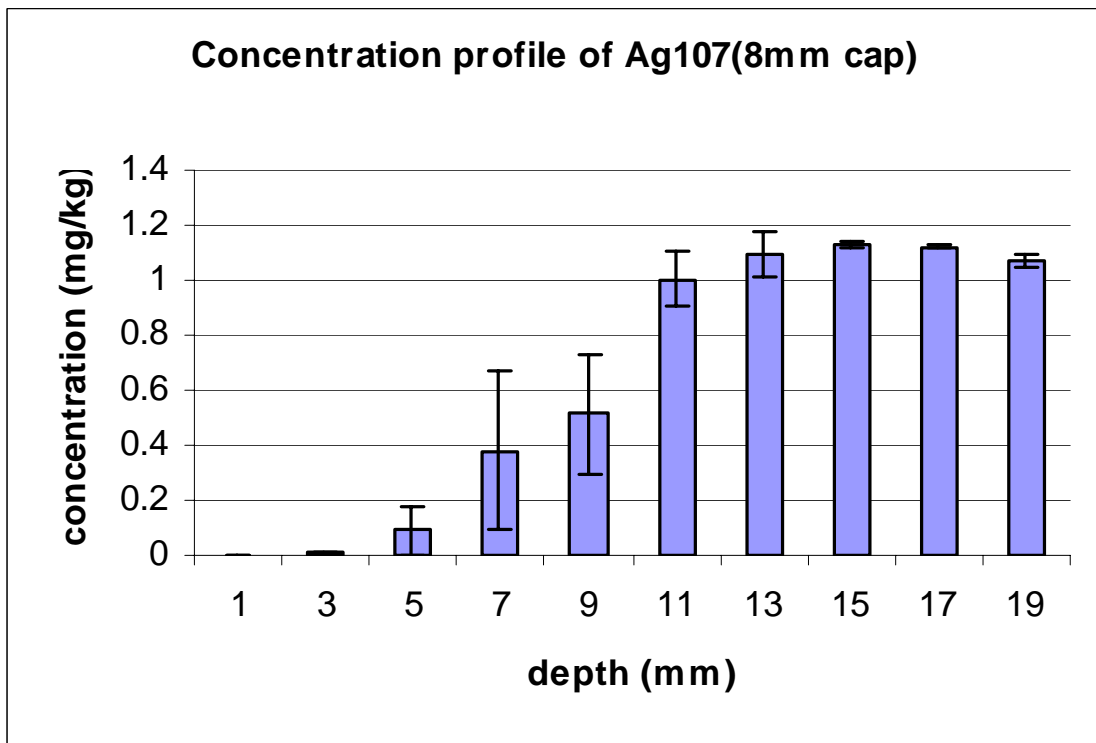


Figure D3.3.14 Concentration profile of Ag107.

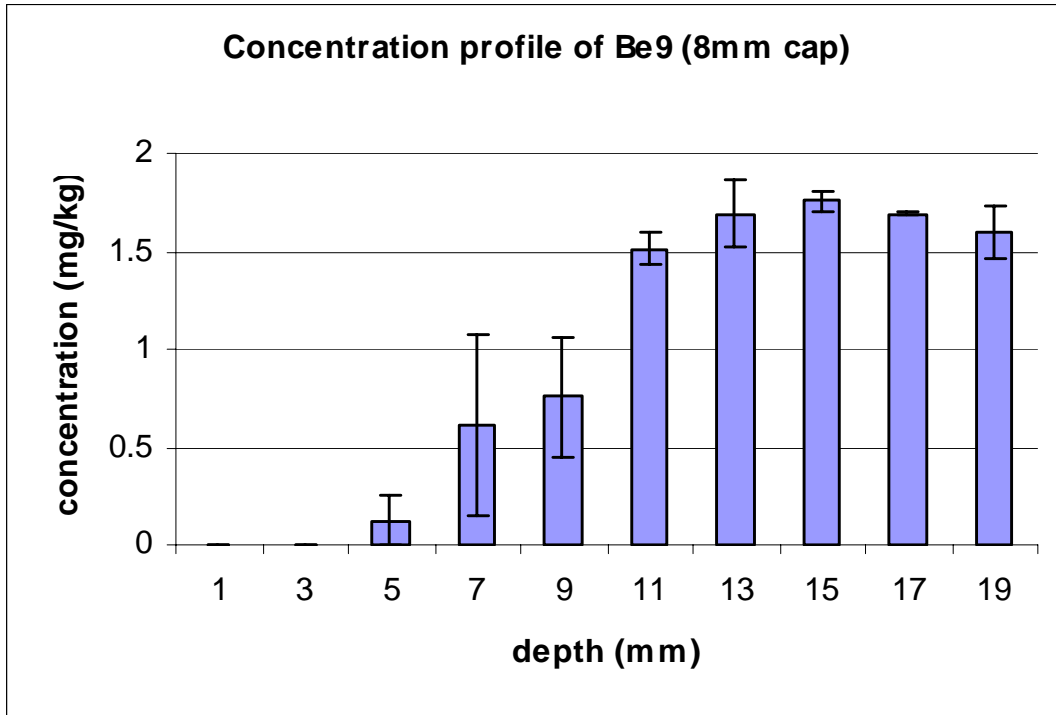


Figure D3.3.15 Concentration profile of Be9.

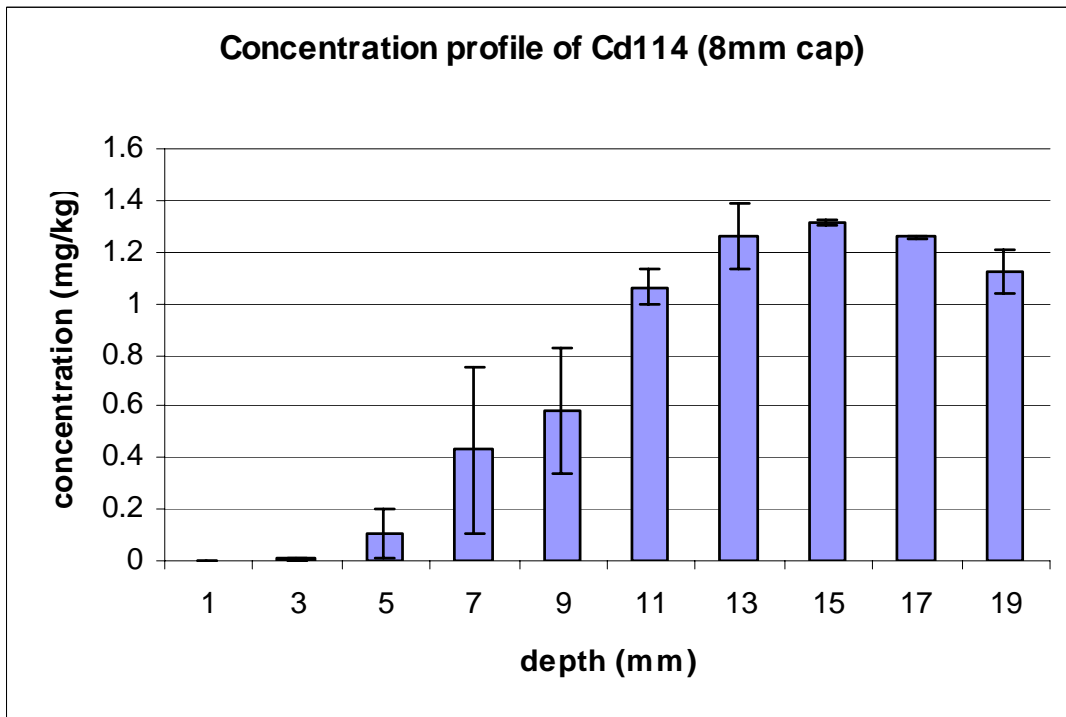


Figure D3.3.16 Concentration profile of Cd114.

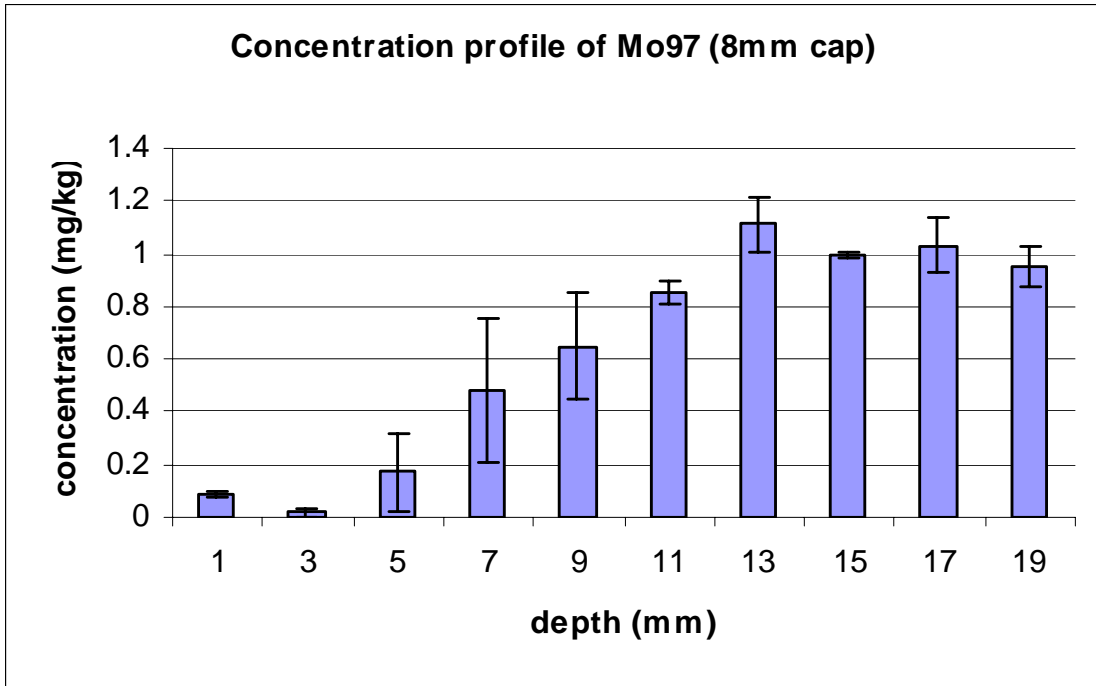


Figure D3.3.17 Concentration profile of Mo97.

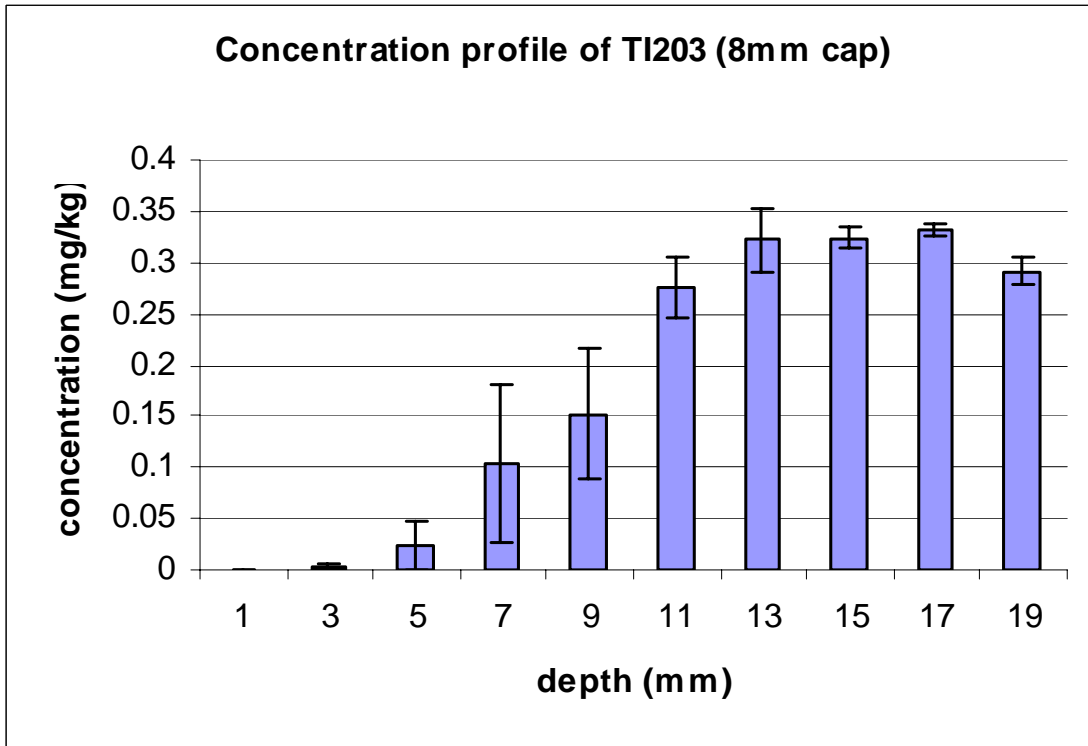


Figure D3.3.18 Concentration profile of TI203.

APPENDIX E: FILTRATION LOSS FACTORS

Phenanthrene redistributes between water and sediment particles after sediment, de-ionized (D.I.) water and phenanthrene water solution are mixed. Mass balance gives

$$C_{sp}V_{sp} + W_{ds}W_s 1000 = C_w \left(V_{sp} + V_{DI} + \frac{W_{ds}w}{\rho_w(1-w)} \right) + C_w K_d W_{ds} 1000 \quad (E1)$$

where C_w is the aqueous phase concentration (ppb), V_{sp} is the spiked solution volume (mL), V_{DI} is the D.I. water volume (mL), W_{ds} is the weight of the dry sediment (g), w is the moisture of the sediment, ρ_w is the water density (g/mL), K_d is the partition coefficient of phenanthrene in the sediment ($1.027 \text{ m}^3/\text{kg}$), C_{sp} is the concentration of the spiked solution, and W_s is the sediment loading (mg/kg).

If the contraction or expansion (excess volume) due to mixing is neglected, total suspended soil (TSS, g/L) can be expressed as

$$TSS = \frac{1000W_{ds}}{V_{DI} + V_{sp} + W_{ds} \left(\frac{1}{\rho_p} + \frac{w}{\rho_w(1-w)} \right)} \quad (E2)$$

where ρ_p is soil particle density (about 2.6 g/cm^3).

The filtration loss factor is defined as

$$f = \frac{C_{w0} - C_w}{C_{w0}} \quad (E3)$$

where C_{w0} is the original concentration in aqueous phase (ppb), and C_w is the measured aqueous concentration after filtration (ppb).

The sediment slurry was made by mixing sediment, D.I. water and phenanthrene solution in a 500 mL glass bottle. The amount of sediment, D.I. water and phenanthrene solution was

determined according to defined TSS and concentration range that were estimated with equation (E1) and (E2). The slurry was filtrated using the same filter (0.7 μm glass fiber filter, Whatman) and syringe (BD 5 mL syringe, Becton Dickinson and Company, Franklin Lakes, NJ) as used in the experiment after it was shaken for more than 24 hours. The filtrate was analyzed with HPLC. The original concentration in aqueous phase was calculated with equation (E1). Then the factor was calculated with equation (E3). Tables and figures below show the experimental results.

Table E1 Factors measured for the experiments with sediment slurry

| TSS (g/L) | Concentration after filtration (ppb) | Factors (%) |
|-----------|--------------------------------------|-------------|
| 0 | 837.07 | 12.99 |
| 0 | 875.41 | 15.47 |
| 0 | 815.02 | 16.14 |
| 0 | 868.9 | 13.97 |
| 0 | 851.31 | 17.97 |
| 0 | 834.56 | 16.67 |
| 0 | 803.67 | 18.95 |
| 0 | 845.98 | 15.15 |
| 0 | 761.2 | 15.19 |
| 2 | 290.33 | 12.05 |
| 2 | 305.76 | 9.89 |
| 2 | 291.13 | 11.15 |
| 9.98 | 57.98 | 32.33 |
| 9.99 | 67.35 | 26.91 |
| 9.96 | 59.88 | 30.96 |
| 19.85 | 29.79 | 37.16 |
| 18.45 | 31.79 | 36.7 |
| 19.85 | 23.28 | 44.86 |

Table E2 Factors for the experiments with sediment

| TSS (g/L) | | Concentration after filtration (ppb) | Factor (%) |
|-----------|-------|--------------------------------------|------------|
| 4.5 | 4.49 | 73.93 | 28.28 |
| | | 77.09 | 25.22 |
| | | 73.99 | 28.22 |
| | 4.49 | 34.97 | 34.82 |
| | | 36.83 | 31.33 |
| | | 36.91 | 31.18 |
| | 4.49 | 12.29 | 40.51 |
| | | 12.62 | 38.9 |
| | | 12.48 | 39.59 |
| | 4.37 | 7.11 | 42.76 |
| | | 6.98 | 43.77 |
| | | 6.68 | 46.19 |
| | 4.39 | 4.82 | 41.69 |
| | | 4.53 | 45.13 |
| | | 4.96 | 39.97 |
| 15 | 15.01 | 30.42 | 44.17 |
| | | 30.60 | 43.82 |
| | | 30.64 | 43.76 |
| | 15.01 | 16.73 | 48.39 |
| | | 17.21 | 46.92 |
| | | 16.51 | 49.07 |
| | 15.00 | 10.49 | 52.64 |
| | | 10.38 | 53.14 |
| | | 10.77 | 51.36 |
| | 15.01 | 3.07 | 70.41 |
| | | 4.20 | 59.43 |
| | | 4.04 | 60.96 |
| 29.2 | 29.22 | 17.29 | 47.39 |
| | | 18.31 | 44.27 |
| | | 16.81 | 48.84 |
| | 29.19 | 13.73 | 49.37 |
| | | 13.21 | 51.29 |
| | | 13.43 | 50.48 |
| | 29.16 | 9.92 | 57.52 |
| | | 9.83 | 55.22 |
| | | 9.45 | 56.94 |
| | 29.23 | 4.38 | 61.55 |
| | | 4.33 | 61.96 |
| | | 4.36 | 61.68 |
| | 29.29 | 2.95 | 65.34 |
| | | 3.03 | 64.41 |
| | | 3.05 | 64.23 |

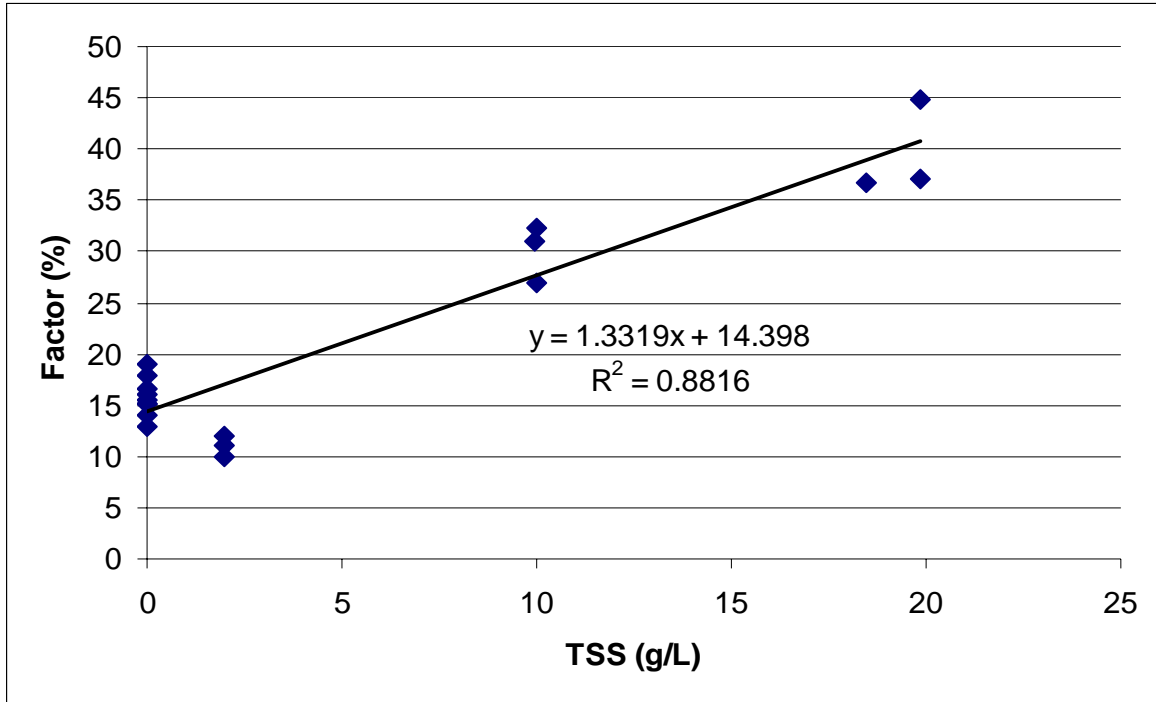


Figure E1 Factors used for the experiments with sediment slurry.

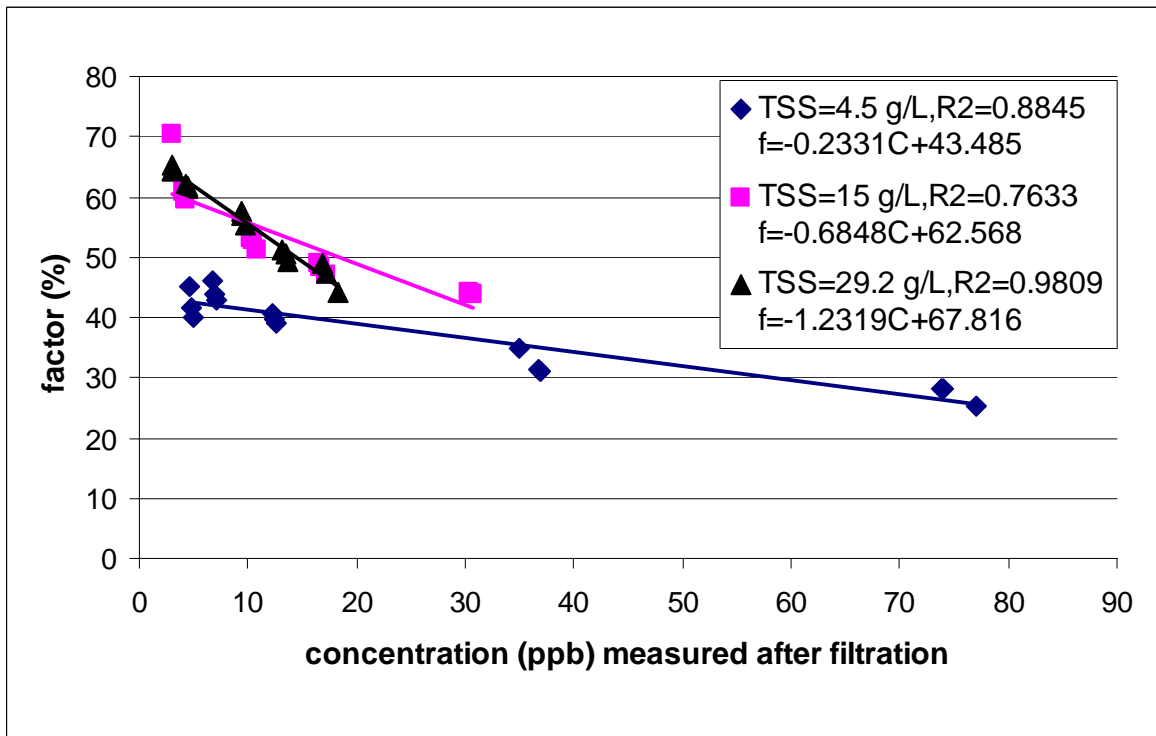


Figure E2 Factors used for the experiments with sediment.

APPENDIX F: MASS TRANSFER COEFFICIENT BETWEEN THE ORGANIC AND AQUEOUS PHASES

As we discussed in 4.1.2.0, there are two important transport mechanisms between the aqueous and solvent (hexane here) phases in the bubble column, i.e., partitioning and bubble-wake entrainment. The former can be estimated by Henry's law and the latter by $\pi r_c^2 k_1 C_w$. Transient mass balance can be carried out to model the solute transport in the bubble column, and k_1 can be determined by the linear regression of the experimental data as follows.

F1 Water Solution

Mass balance in water column yields

$$\frac{d(V_w C_w)}{dt} = -HQ_g C_w(t) - k_1 \pi r_c^2 C_w(t) \quad (\text{F1})$$

with initial condition: $C_w(t=0) = C_{w0}$, where C_w is the solute concentration in water, V_w is the volume of the water solution (m^3), H is the Henry's law constant (dimensionless) and Q_g is the gas volumetric flow rate (m^3/s).

Integrating the above equation gives

$$\ln\left(\frac{C_{w0}}{C_w}\right) = \left(\frac{HQ_g + k_1 \pi r_c^2}{V_w}\right) \cdot t \quad (\text{F2})$$

So $k_1 = \frac{sV_w - HQ_g}{\pi r_c^2}$ where s can be determined by calculating the slope of $\ln\left(\frac{C_{w0}}{C_w}\right)$ vs t .

Mass balance in hexane layer gives

$$\frac{d(V_h C_h)}{dt} = HQ_g C_w(t) + k_1 \pi r_c^2 C_w(t) \quad (\text{F3})$$

with initial condition: $C_h(t=0) = C_{h0} = 0$, where V_h is the volume of hexane, and C_h is the solute concentration in hexane.

Solute mass in water column and hexane layer should be a constant or the initial solute mass in water solution:

$$C_h V_h + C_w V_w = C_{w0} V_{w0} \text{ or } C_w(t) = \frac{C_{w0} V_{w0} - C_h(t) V_h}{V_w}$$

where V_{w0} , C_{w0} are the initial volume and concentration of the water solution, and $V_w \approx V_{w0}$.

Substituting the above into equation (F3) yields

$$\begin{aligned} \frac{d(V_h C_h)}{dt} &= HQ_g C_w(t) + k_1 \pi r_c^2 C_w(t) = (HQ_g + k_1 \pi r_c^2) \left(C_{w0} - \frac{V_h}{V_w} C_h(t) \right) \text{ or} \\ \frac{dC_h}{dt} &= \frac{(HQ_g + k_1 \pi r_c^2)}{V_w} \left(\frac{C_{w0} V_w}{V_h} - C_h(t) \right) \end{aligned} \quad (\text{F3}')$$

An analytical solution to the above equation is

$$\ln \left(\frac{1}{1 - \frac{V_h C_h(t)}{V_w C_{w0}}} \right) = \frac{HQ_g + k_1 \pi r_c^2}{V_w} \cdot t \quad (\text{F4})$$

So k_1 can also be determined by calculating the slope of $\ln \left(\frac{1}{1 - \frac{V_h C_h(t)}{V_w C_{w0}}} \right)$ vs t .

In principle, PHE concentrations from either water or hexane can be used to determine the mass transfer coefficient k_1 , and k_1 obtained from either concentration (C_w or C_h) should be the same. Owing to the experimental errors, the mass transfer coefficient k_1 estimated from PHE concentrations in water and those in hexane are slightly different (Figure F-1 to F-2).

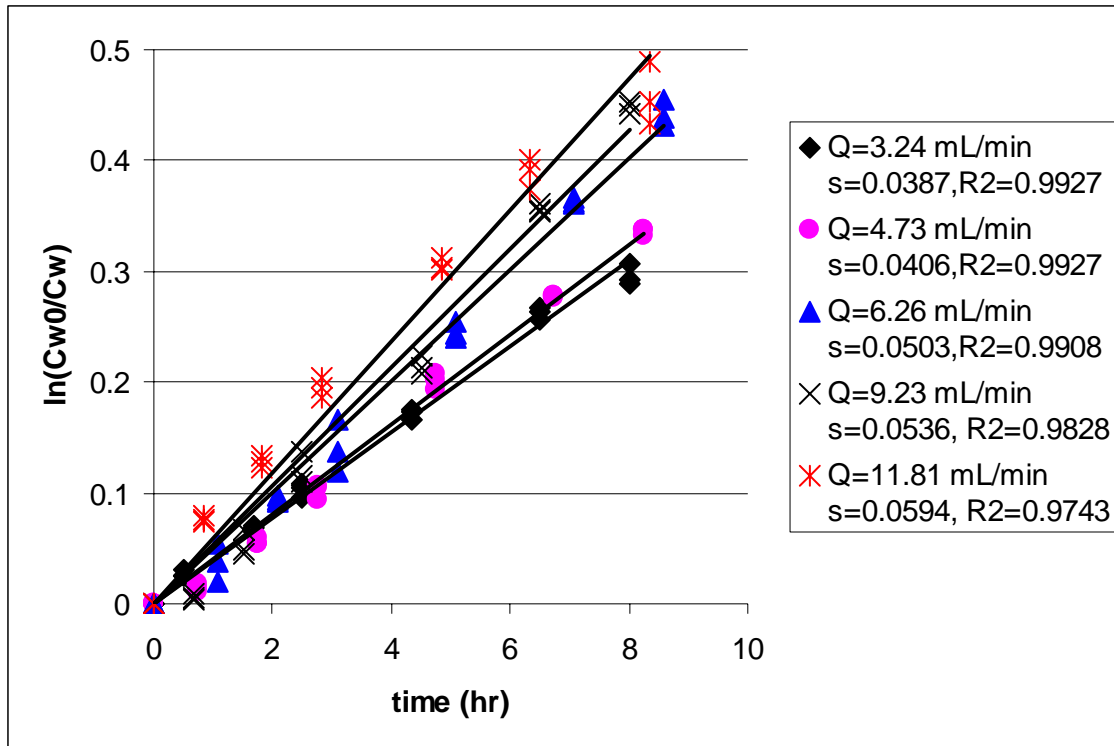


Figure F1 Determination of k_1 with PHE concentration in water.

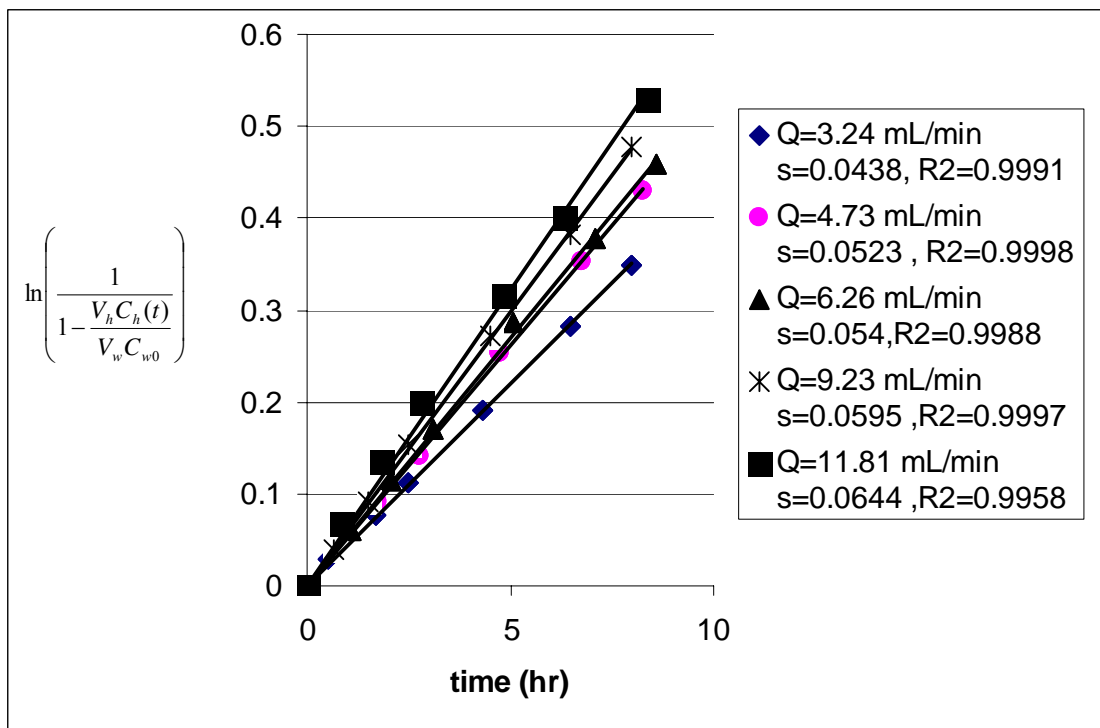


Figure F2 Determination of k_1 with PHE concentration in hexane.

F2 Sediment Slurry

Mass balance in slurry:

$$\frac{d(\rho_{ss} V_w W_s)}{dt} = -HQ_g C_w(t) - k_1 \pi r_c^2 C_w(t) \quad (F5)$$

where ρ_{ss} is the total suspended soil (TSS, kg/m³), V_w here is the volume of the sediment slurry (m³), and W_s is the solute concentration in the slurry (kg/kg).

At equilibrium, solute mass balance in slurry gives

$$\rho_{ss} V_w W_s = V_w C_w + \rho_{ss} V_w K_d C_w \quad (V_w \approx V_{w0})$$

Substituting the above into equation (F5) yields

$$\frac{dC_w}{dt} = -\frac{HQ_g + k_1 \pi r_c^2}{(1 + \rho_{ss} K_d) V_w} \cdot C_w(t) \quad (F5')$$

with initial condition: $C_w(t = 0) = C_{w0}$. Solving the above differential equation gives

$$\ln\left(\frac{C_{w0}}{C_w}\right) = \frac{HQ_g + k_1 \pi r_c^2}{V_w (1 + \rho_{ss} K_d)} \cdot t \quad (F6)$$

So $k_1 = \frac{s V_w (1 + \rho_{ss} K_d) - HQ_g}{\pi r_c^2}$, where s is the slope of $\ln\left(\frac{C_{w0}}{C_w}\right)$ vs t .

Mass balance in hexane:

$$\frac{d(V_h C_h)}{dt} = HQ_g C_w(t) + k_1 \pi r_c^2 C_w(t) \quad (F7)$$

with initial condition: $C_h(t = 0) = C_{h0} = 0$

At equilibrium, we have two mass balance equations:

$$\rho_{ss} V_w W_s = V_w C_w + \rho_{ss} V_w K_d C_w$$

$$C_h V_h + V_w C_w + \rho_{ss} V_w K_d C_w = V_{w0} C_{w0} + \rho_{ss} V_{w0} K_d C_{w0}$$

$$\text{or } C_w(t) = \frac{C_{w0}V_{w0}(1 + \rho_{ss}K_d) - C_h(t)V_h}{V_w(1 + \rho_{ss}K_d)} = C_{w0} - \frac{V_h}{V_w(1 + \rho_{ss}K_d)}C_h(t)$$

Substituting the above equation into equation (F7) gives

$$\begin{aligned} \frac{d(V_h C_h)}{dt} &= HQ_g C_w(t) + k_1 \pi r_c^2 C_w(t) = (HQ_g + k_1 \pi r_c^2) \left(C_{w0} - \frac{V_h}{V_w(1 + \rho_{ss}K_d)} C_h(t) \right) \\ \text{or } \frac{dC_h}{dt} &= \frac{(HQ_g + k_1 \pi r_c^2)}{V_w(1 + \rho_{ss}K_d)} \left(\frac{C_{w0}V_w(1 + \rho_{ss}K_d)}{V_h} - C_h(t) \right) \end{aligned} \quad (\text{F7'})$$

The solution to the above equation is

$$\ln \left(\frac{1}{1 - \frac{V_h C_h(t)}{V_w(1 + \rho_{ss}K_d)C_{w0}}} \right) = \frac{HQ_g + k_1 \pi r_c^2}{V_w(1 + \rho_{ss}K_d)} \cdot t \quad (\text{F8})$$

$$\text{So } k_1 = \frac{sV_w(1 + \rho_{ss}K_d) - HQ_g}{\pi r_c^2}, \text{ where } s \text{ is the slope of } \ln \left(\frac{1}{1 - \frac{V_h C_h(t)}{V_w(1 + \rho_{ss}K_d)C_{w0}}} \right) \text{ vs } t.$$

In order to measure PHE concentration in the aqueous phase of sediment slurry, slurry samples need to be filtrated before HPLC analysis. The adsorption of PHE on the filter is significant (Appendix E). This makes the aqueous concentration data scatter. So PHE concentrations in hexane layer were employed to calculate the mass transfer coefficient, k_1 (Figure F3 to F5). Table F1 lists the k_1 data in all the experiments.

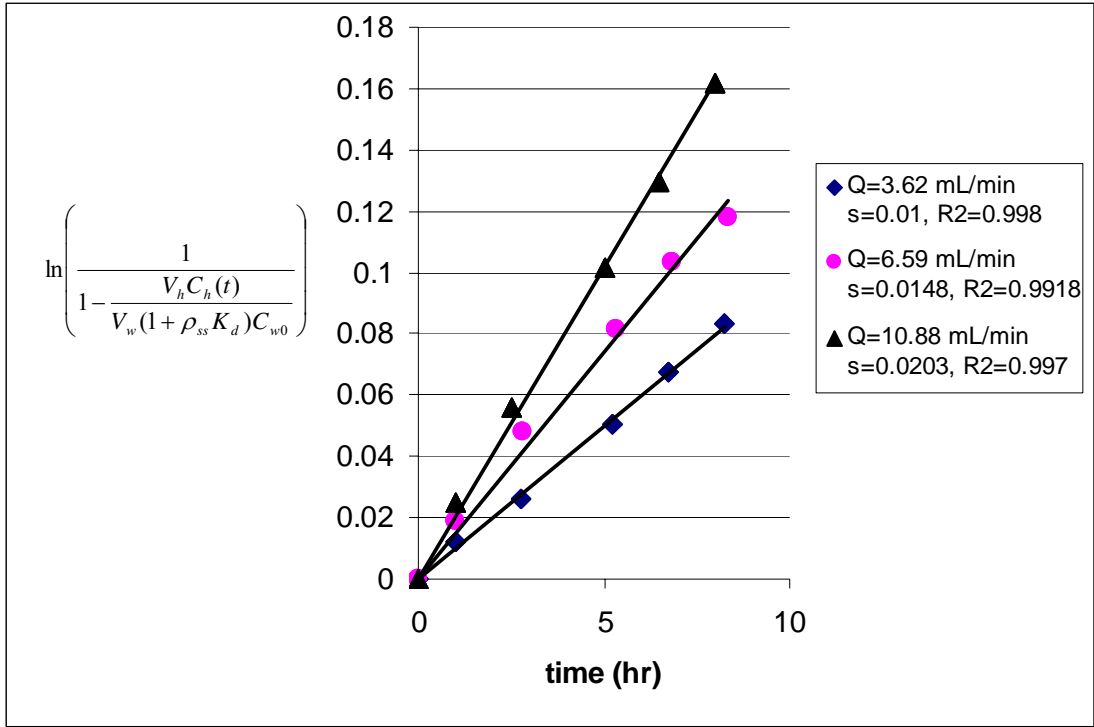


Figure F3 Determination of k1 at TSS=2 g/L.

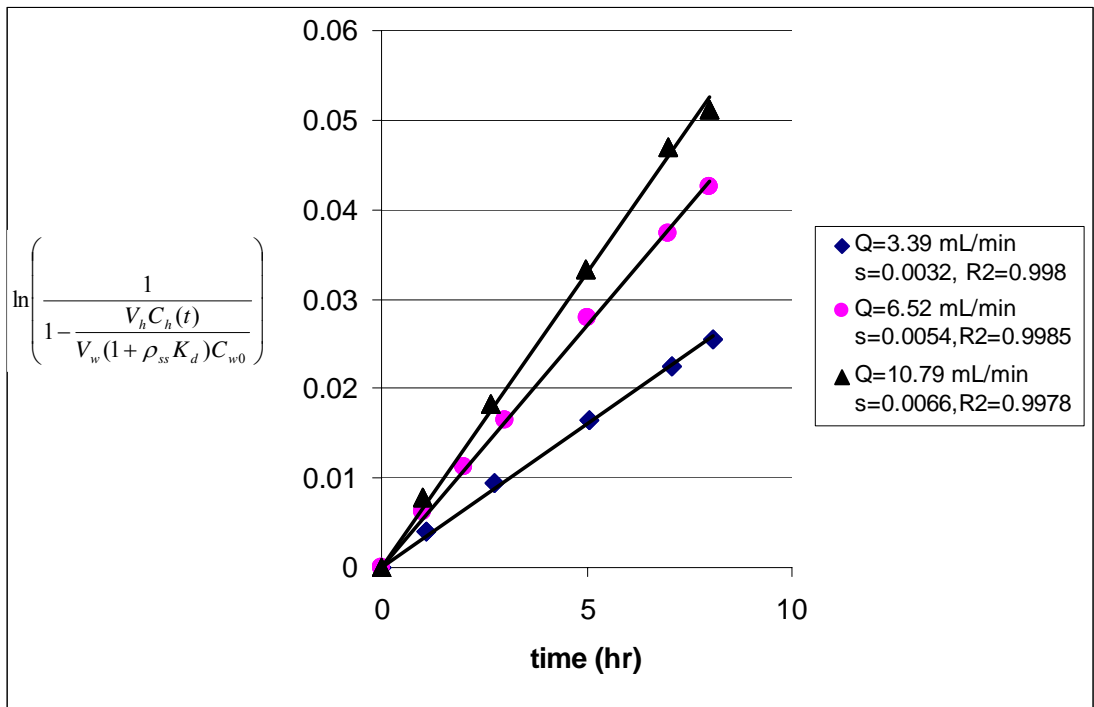


Figure F4 Determination of k1 at TSS=10 g/L.

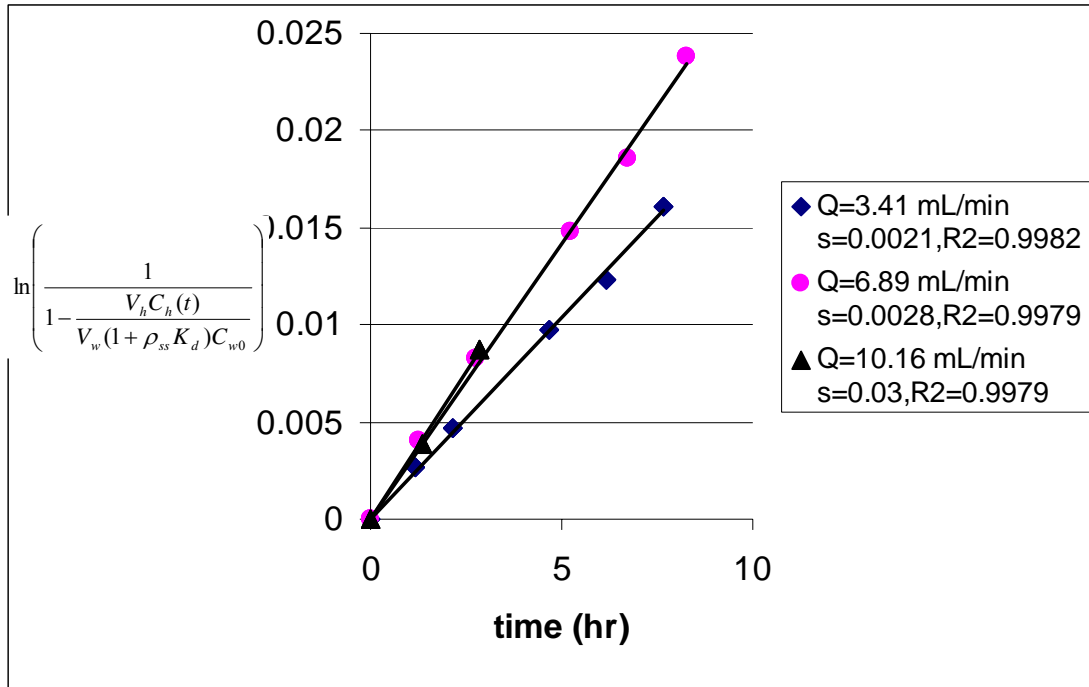


Figure F5 Determination of k1 at TSS=20 g/L.

Table F1 k1 values at different cases

| TSS (g/L) | Q _g , mL/min (L/m ² -day) | Slope (1/h) | k1 (m/s) × 10 ⁶ |
|----------------------------|---|-------------|----------------------------|
| 0 (use C _w) | 3.24 (929) | 0.0387 | 6.86 |
| | 4.73 (1356) | 0.0406 | 7.21 |
| | 6.26 (1794) | 0.0503 | 8.96 |
| | 9.23 (2646) | 0.0536 | 9.54 |
| | 11.81 (3385) | 0.0594 | 10.56 |
| 0 (use C _h) | 3.24 (929) | 0.0438 | 7.77 |
| | 4.73 (1355) | 0.0523 | 9.30 |
| | 6.26 (1794) | 0.054 | 9.62 |
| | 9.23 (2646) | 0.0595 | 10.59 |
| | 11.81 (3385) | 0.0644 | 11.45 |
| 2 | 3.62 (1038) | 0.01 | 5.54 |
| | 6.59 (1889) | 0.0148 | 8.14 |
| | 10.88 (3118) | 0.0203 | 11.15 |
| 10 | 3.39 (972) | 0.0032 | 6.54 |
| | 6.52 (1869) | 0.0054 | 11.04 |
| | 10.79 (3093) | 0.0066 | 13.39 |
| 20 | 3.41 (977) | 0.0021 | 8.29 |
| | 6.89 (1975) | 0.0028 | 11.03 |
| | 10.16 (2912) | 0.003 | 11.77 |

VITA

Qingzhong Yuan was born in Heze, Shandong Province, P. R. China, March 14, 1962. At the age of sixteen, he entered Tianjin Institute of Light Industry (now Tianjin University of Science and Technology), majoring in salt-chemical engineering. He earned a Bachelor of Engineering degree in July 1982, and was assigned to work in Shandong Institute of Salt-Making Industry. There he got married to Jinhui Liu in March 1985, and their daughter Yunan Yuan was born in October 1986.

Through 1982 to 1991, he mainly did research in developing new salt-making techniques for comprehensive utilization of brines and bitterns, and also worked on synthesis, factory design and production of bromides such as Tetrabromobisphene A, Halon 1211, Bromoaminoacid, etc. He became a chemical engineer in 1989.

In November 1991, he joined Shandong Institute of Light Industry as a lecturer. During the next decade, he did research in the field of phase chemistry of salt-water systems. Based on the ion-interaction model of Pitzer, he developed new methods that can accurately predict parameters (such as salt saturation points of brine) in salt-making processes with seawater, salt-lake brines and salt-well brines. During this period of time, he also taught (Courses: Phase Diagram of Salt-water Systems, Chemical Technological Processes, Introduction to the Design of Chemical Factory, etc). In 1995, he became an associate professor.

From August 1999 to August 2000, he did research on photocatalytic treatment of organics in dilute wastewater streams on surface-modified semiconductor particles (TiO_2) at Louisiana State University as a visiting scholar supported by Chinese Government (China Scholar Council, CSC). After finishing the research at LSU, he went back to China to continue

his research and teaching. In November 2000, he became a professor in the Department of Chemical Engineering at Shandong Institute of Light Industry.

In August 2002, he moved to LSU to pursue a doctorate in chemical engineering. While at LSU, he held a Graduate Research Assistantship from the Department of Chemical Engineering, was awarded a Financial Enhancement and an Economic Development Assistantship from the Graduate School, and received John J. Seip Memorial Award (the first place in Ph. D. Qualifying Exam of Chemical Engineering Department, 2003). He passed the defense on October 23, 2006, and the degree of Doctor of Philosophy will be conferred in May 2007.